

**Mid-crustal Cu-Au Mineralisation during Episodic Pluton Emplacement,
Hydrothermal Fluid Flow, and Ductile Deformation at the Minto Deposit, YT, Canada**

by

Shawn Bruce Hood

B.Sc. (Hons.), Carleton University, 2008

A THESIS SUBMITTED IN PARTIAL FULFILLMENT OF
THE REQUIREMENTS FOR THE DEGREE OF

MASTER OF SCIENCE

in

THE FACULTY OF GRADUATE STUDIES

(Geological Studies)

THE UNIVERSITY OF BRITISH COLUMBIA

(Vancouver)

July 2012

© Shawn Bruce Hood, 2012

Abstract

The genesis of the Minto copper-gold deposit, YT, Canada, has been variously interpreted since its discovery although no existing model accounts for ductile deformation as a control on mineralization. Results from this study show that Minto ore is hosted within ductilely deformed granitoid host rocks emplaced as multiple intrusions into an actively deforming environment, with the variably sheared host rocks separated by incipiently deformed granodiorites essentially barren of mineralisation. Contacts between deformed/mineralized rock and incipiently deformed/barren rock range from abrupt to gradational, and are the product of pre-existing igneous contacts, variably partitioned deformation, or a combination of these. Deformation of granitoids is interpreted to have controlled fluid flow, with associated alteration promoting further deformation and fluid flow. Potassic alteration, in the form of biotite-magnetite, is the dominant alteration associated with mineralisation, and analysis of alteration using isocon diagrams indicates that K, Fe, Si, Cu, Au, and Ag have been added during alteration, although mass has been lost overall due to a relative reduction in Na and Ca. Host rock intrusion, mineralization, and deformation are interpreted via geochronology and crosscutting relationships as ongoing over at least 5 m.a., from about 202 Ma until about 197 Ma, based on U-Pb SHRIMP geochronology of zircons in granitoids and Re-Os ICP-MS geochronology of molybdenite. The trend of mineralisation is now coincident with the strike of foliation on short steep limbs and of axial planes of folded foliation. This geometry may not be representative of original processes, but of remobilization of ore during continued deformation.

The above observations, coupled with data from existing studies, strongly suggest Minto is representative of deposit generation within an arc subduction environment at depths not typically considered for copper-gold deposit formation.

Table of Contents

Abstract.....	ii
Table of Contents	iii
List of Tables	vi
List of Figures.....	vii
Acknowledgements	x
Dedication	xi
Chapter 1: Introduction	1
Chapter 2: Body of Thesis.....	7
2.1 Geological Setting.....	7
2.1.1 Regional Geology	7
2.1.2 Deposit Geology	10
2.2 Igneous Host Rocks	14
2.2.1 Intrusive Units.....	16
2.2.1.1 K-Feldspar Granodiorite	16
2.2.1.2 Coarse Grained Tonalite	18
2.2.1.3 Dikes	19
2.2.2 Internal Pluton Fabrics	21
2.2.3 Lithogeochemistry of KGd	32
2.2.3.1 Results.....	34
2.3 Mineralisation and Alteration	38
2.3.1 Ore Assemblage	38
2.3.2 Alteration Assemblages	44

2.3.3	Evaluating Mass Transfer	47
2.3.3.1	Analytical Techniques	47
2.3.3.2	Isocon Plots.....	51
2.4	Structural Geology	60
2.4.1	Solid State Microstructures.....	61
2.4.1.1	Stage 1: Incipient Deformation.....	61
2.4.1.2	Stage 2: Weak Foliation.....	65
2.4.1.3	Stage 3: Well Developed Penetrative Foliation (S_P).....	65
2.4.1.4	Stage 4: Mylonitic Foliation	66
2.4.2	Gneissic Banding	67
2.4.3	Sulphide Deformation Fabrics	70
2.4.4	Foliation and Shear Zone Geometry	73
2.4.5	Late Brittle Deformation.....	99
2.5	Geochronology.....	100
2.5.1	U-Pb SHRIMP Geochronology	101
2.5.1.1	Samples.....	101
2.5.1.2	Analyses.....	102
2.5.1.3	Results.....	112
2.5.1.3.1	Suite One.....	112
2.5.1.3.2	Suite Two	112
2.5.2	Re-Os Molybdenite Geochronology	114
2.5.2.1	Samples.....	114
2.5.2.2	Analyses.....	116

2.5.2.3	Results.....	117
2.6	Summary.....	118
2.6.1	Relationship between Igneous Activity, Alteration, and Deformation.....	118
2.6.2	Geochronology.....	124
2.7	Discussion.....	127
2.7.1	Petrogenesis and Emplacement Depth.....	127
2.7.2	Synopsis of the Crustal Environment During Emplacement of the Minto Pluton 130	
2.7.3	Pluton Emplacement and Ductile Deformation	134
2.7.4	Deformation, Permeability, and Hydrothermal Fluid Flow.....	139
2.7.5	Hydrothermal Alteration.....	142
2.7.6	Comparisons with Other Cu-Au-Magmatic Related Ore Systems	146
Chapter 3: Conclusion.....		153
References.....		155
Appendices.....		169
	Appendix A Field Measurements	170
	Appendix B Pit Maps.....	186
	Appendix C Whole-Rock Geochemical Sample Locations.....	191
	Appendix D Whole-Rock Lithochemical Data.....	193
	Appendix E Isocon Calculations.....	199
	Appendix F Graphical Logs.....	200
	Appendix G U-Pb Geochronology.....	215
	Appendix H Molybdenite Study	217

List of Tables

Table 1: Comparison of lithologies recognized by previous workers at Minto.....	15
Table 2: Geochemical sample information.	33
Table 3: Lithochemical sample information from samples collected during 2009 field season.....	50
Table 4: Results of U-Pb SHRIMP analyses of KGd zircons and age calculations..	104
Table 5: Sample data from molybdenite.....	117
Table 6: Temperature estimates based on observed microtextures	137

List of Figures

Figure 1: Cross section through idealized subduction zone and continental arc	2
Figure 2: Regional geological setting of the Minto pluton and deposit.....	8
Figure 3: Interpretative map of major lithologies and important structures in the Minto deposit, excluding quaternary sediments.	11
Figure 4: Two main granitoids comprising the Minto pluton: K-feldspar megacrystic granodiorite (KGd) and coarse grained tonalite (Tlt)..	17
Figure 5: Photographs of pegmatite dikelets (Pgt) showing the variety of crosscutting relationships with KGd and foliation.....	20
Figure 6: Mafic magmatic enclaves (MMEs) within KGd	23
Figure 7: Photographs of mafic enrichments defining igneous layering.....	25
Figure 8: Crosscutting relationships involving distinct intrusions of KGd indicating multiple stages of intrusion..	28
Figure 9: Photos showing crosscutting relationships involving intrusions of Tlt which indicate multiple stages of intrusion..	30
Figure 10: Whole-rock lithogeochemical granite type discrimination diagram based on total alkalis versus total silica (TAS).	35
Figure 11: Whole rock lithogeochemical characterization of KGd using trace elements.	36
Figure 12: Photographs and photomicrographs of hypogene mineral assemblages related to sulphide mineralization.	40
Figure 13: Plots of metal tenor using company geochemical data (Captone Resources dataset, unpublished).....	43
Figure 14: Photomicrographs showing selected alteration assemblages	45

Figure 16: Spider diagrams comparing samples used in isocon study, samples collected regionally, and samples analysed during previous study	54
Figure 17: Plots to assess chemical immobility within altered/deformed samples of KGd....	55
Figure 18: Isocon diagram illustrating relative enrichment and depletion of major element oxide (wt %) and trace element (ppm) concentrations in the Minto Granodiorite..	57
Figure 19: Photographs showing hand samples of deformed KGd	62
Figure 20: Photographs showing compositional banding in KGd	68
Figure 21: Photomicrograph showing microtextures of typical Cu-sulphide deformation at Minto.....	71
Figure 22: Photomicrograph showing macroscopic deformation of Cu-sulphides at Minto..	72
Figure 23: Stereonets depicting S_P foliations measured at Minto.....	74
Figure 24: Photomicrographs showing examples of structural contacts in KGd.....	75
Figure 25: Photo showing S_P fabric developed in a stoped enclave of deformed and magnetite altered KGd.	78
Figure 26: Downhole variation of S_P in unoriented vertical drillholes.....	79
Figure 27: Schematic diagrams illustrating possible interpretations of geometry from S_P foliation observed in unoriented drillcore.....	82
Figure 28: Orthophoto of the Minto mine showing the locations of logged diamond drill holes, figures with pit photographs and structural data, and cross sections.	83
Figure 29: Examples of shear zones in the Minto open pit.....	85
Figure 30: Stereonets of S_P measured from regions across the Minto deposit.	88
Figure 31: Variation of S_P folding observed within shear zones in the Minto open pit.	91

Figure 32: Graphical log of diamond drill hole 06SWC078 showing a correlation between potassic alteration, sulphide type, and ore grade.	93
Figure 33: Map of the Minto open pit summarising S_P foliation geometry.....	95
Figure 34: Steep foliation and Cu-grade thickness from the Minto deposit.....	97
Figure 35: Concordia diagrams for U-Pb SHRIMP analysis of KGd zircons.	110
Figure 36: Photomicrographs showing textures in molybdenite samples suggestive of relative timing.	115
Figure 37: Cross sections from the Minto deposit showing the continuity of deformation zones, mineralization, and potassic alteration.....	119
Figure 38: Annotated photograph of KGd samples showing summary of U-Pb SHRIMP zircon ages.	125
Figure 39: Schematic of Minto deposit paragenesis.	132
Figure 40: Simplified schematic diagram of magma generation and emplacement within a subduction arc environment.....	151

Acknowledgements

I offer my enduring gratitude to the faculty, staff and my fellow students in the Department of Earth and Ocean Sciences, who made my time at the UBC so fulfilling and who shared my enthusiasm for geology.

I owe particular thanks to my supervisor Dr. Kenneth Hickey, with whom I enjoyed working immensely. I thank my external supervisor Dr. Maurice Colpron of the Yukon Geological Survey for being a grounding influence during my studies and for enlarging my vision Yukon geological history and tectonics. Gratitude also to Brad Mercer, vice-president of exploration from the Capstone Mining Corp., for organizing the project and for giving practical guidance in the field. Much appreciation to Dr. Nancy Joyce and Dr. Nicole Rayner for their assistance producing U-Pb SHRIMP ages and to Dr. Dave Selby for his role in producing Re-Os ages. Many thanks to Dr. Jim Mortensen and Dr. James Scoates who sat on my defence committee and posed many penetrating and thought provoking questions.

I am grateful to the Capstone Mining Corp. and the Yukon Geological Survey for funding this research project in its entirety.

Dani Aldrich, Taras Nahnybida, and Vivienne McLennan from Capstone were very helpful contributors as field partners, data providers, and proof readers.

To Hickeylab and friends: I could not imagine my M.Sc. experience without any of you. Thank you for everything.

Special thanks to my lovely and patient fiancé Ayesha, who is the transporting ligand to my aqueous metal ion. Thanks for helping me through, love.

Dedication

Dedicated to my family, especially Grandma and Grandpa Hood, and Oma and Gramps Koens, for their love and encouragement over the years.

Chapter 1: Introduction

The majority of Earth's economic copper deposits are associated with felsic magmatism in arc-environments. In particular, the porphyry-Cu class of deposits hosts approximately 75% of the world's copper supply (Sillitoe, 2010). Mineralisation in porphyry deposits is hydrothermal in origin and is spatially and temporally associated with porphyritic granitoid stocks and dikes of calc-alkaline to alkaline composition, in many cases being hosted by them (Cloos, 2001; Richards, 2005). Such granitoid intrusions and coincident mineralisation are typically emplaced at 1-4 km depth, but may occur as deep as 9 km (Singer et al., 2008). In contrast, the magma forming these intrusions and the metalliferous hydrothermal fluids responsible for mineralisation are typically sourced from large parental magma chambers 5 to 15 km below the granitoid stocks (Figure 1) (Cloos, 2001; Richards, 2005; Singer et al., 2008). The fluid is exsolved from the cooling and fractionating parental magma during magma convection as well as during magma crystallization (Shinohara and Hedenquist, 1997). The granitoid stocks and dikes of porphyry systems, while not necessarily major contributors of metalliferous magmatic fluids, act to channel these fluids upwards towards the site of their deposition (Shinohara et al., 1995; Cloos, 2001; Richards, 2005). Historically, the majority of research involving Cu metallogenesis has been focussed on porphyry-Cu systems in the upper 9 km of the crust, with a paucity of data and research involving deeper magmatic environments. This higher crustal focus is linked to the limited exposure of deep systems that can be clearly linked to porphyry deposits. Nevertheless, workers interpreting a deeper fluid source for porphyry deposits have long

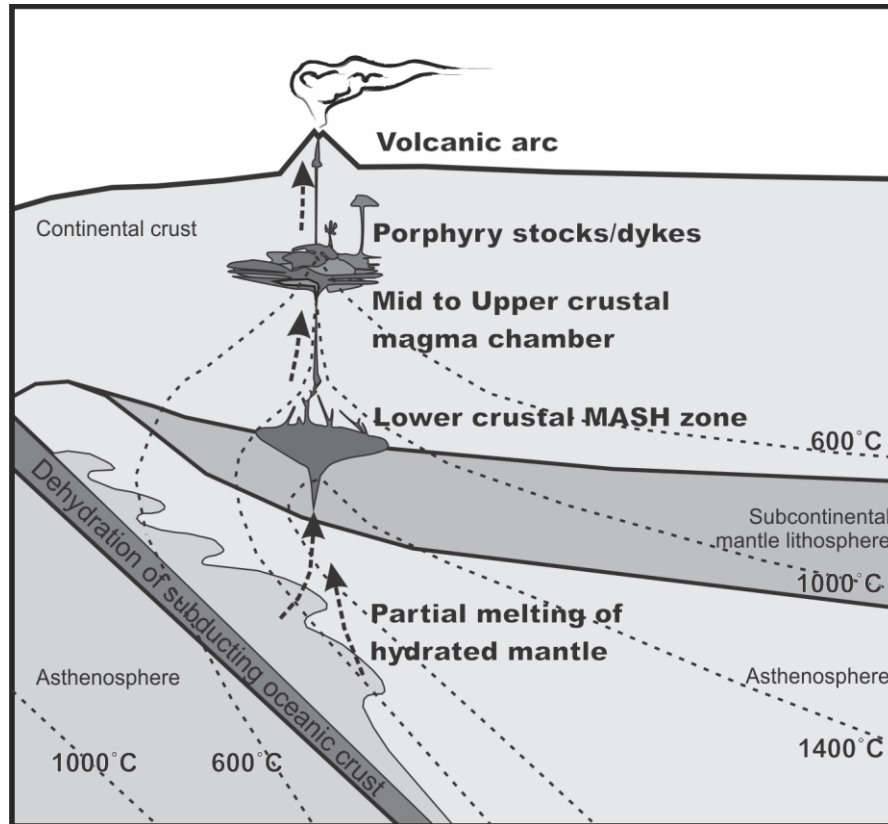


Figure 1: Cross section through a subduction zone and continental arc (modified from Richards, 2003). Dehydration of the subducting oceanic crust leads to hydration of the overlying mantle. Partial melting occurs as hydrated material is convected to hotter regions of the asthenospheric mantle wedge. Evolved, more buoyant magmas rise away from this zone of melting, assimilation, storage, and homogenisation (i.e., MASH zone, Hildreth and Moorbath, 1988) through the crust dominantly via fractures/dikes. Porphyry fluids are thought to originate from mid to upper crustal batholiths and be emplaced at shallower levels via overlying stocks/dikes (Cloos, 2001). Diagram is not to scale.

hypothesized that the large parental “roots” to porphyry systems are an underexplored prospect for magmatic related Cu-Au mineralisation (Sillitoe, 1973; Seedorff et al., 2008). This raises the question of how any such mineralisation might be manifest in large mid to upper crustal magma chambers and how might it relate to their initiation, growth and crystallization?

Porphyry deposits have long been associated with subduction zones, and workers have successively refined the tectono-magmatic controls on mineralisation using the context of convergent arc environments (Sillitoe, 1973; Richards, 2003; Sillitoe and Hedenquist, 2003). According to this model, fertile calc-alkaline magmas are generated in the MASH zone, a zone of melting, assimilation, storage, and homogenisation (Hildreth and Moorbath, 1988). The initial ascent of hydrous magmas generated in deep crustal MASH zones (DePaolo and Wasserburg, 1977; Hawkesworth, 1982; Brown et al., 1984; Hildreth and Moorbath, 1988) is likely controlled by grain scale percolative flow of melt during ductile deformation (Collins and Sawyer, 1996; Brown and Solar, 1999; Schilling and Partzsch, 2001). Melt progressively gathers to feed larger conduits, dikes or diapirs that go on to form larger magma chambers at shallower depths (Collins and Sawyer, 1996; Brown and Solar, 1999).

The initiation and growth of large magma chambers commonly involves the emplacement of multiple batches of magma via some combination of dyking and diapirism (Weinberg and Podladchikov, 1994; Petford, 1996; Brown and Solar, 1998; Petford et al., 2000a; Pignotta et al., 2010;). At higher crustal levels magma chambers tend to grow by vertical inflation and roof uplift through the intrusion of multiple shallow dipping sheet-like intrusions along rheological heterogeneities, and/or by magmatic stoping of country rocks (Brown and Solar, 1998; Cruden, 1998; Morgan et al., 1998; Becker et al., 2000; Zak and Paterson, 2006; Miller

et al., 2009; Clemens and Benn, 2010). Although the growth of such magma chambers commonly involves significant internal flow and deformation of melt, resulting in the formation of mafic schlieren and magmatic foliations and lineations (e.g., Paterson, 2009), there is little syn-intrusive development of pervasive solid-state foliations within the country rock or earlier solidified intrusive phases. However, with increasing crustal depth and higher country rock temperatures the emplacement of magma and the growth of large magma chambers involves a greater degree of ductile deformation of wall rocks and earlier emplaced magma pulses. Vertical growth of magma chambers is dominated by floor depression via solid state ductile return flow of the country rock rather than roof uplift (Cruden, 1998; Wiebe and Collins, 1998; Cruden and McCaffrey, 2001; Žák and Paterson, 2005). Lateral growth of magma chambers can occur via radial flattening and vertical elongation of the hot country rocks in the thermal aureole surrounding the magma chamber, and/or of earlier magma pulses within the magma chamber itself (Siegesmund and Becker, 2000; Johnson et al., 2003). Such flattening is driven by magma pressure and is accomplished by thermally activated solid-state intracrystalline deformation (of country rock and sub-solidus intrusive rocks) and/or magmatic flow (of earlier intrusive phases still in a supra-solidus state). Regional deformation of country rocks controlled by forces external to the emplacing magma can also play a significant role in the growth of mid-crustal magma chambers.

Several studies have documented the preference for magma to be emplaced in dilatant sites within and adjacent to large crustal shear zones in convergent tectonic settings (Vigneresse, 1995; Brown and Solar, 1998; Koukouvelas et al., 2002; Weinberg et al., 2004; Weinberg et al., 2009). Owing to changing patterns of regional deformation partitioning, magmas intruded into such tectonically active regions are commonly overprinted by deformation prior to and

after they have cooled below the solidus resulting in solid state and /or magmatic foliations in plutons that are parallel to regional fabrics (Brown and Solar, 1998; Weinberg et al., 2004; Weinberg et al., 2009; Pignotta et al., 2010). Given their mid to upper crustal depth and convergent arc setting, the growth initiation and growth of the large parental magma chambers that feed upper crustal porphyry-Cu deposits should, in many cases, have involved synchronous ductile deformation of country rock and/or earlier emplaced magma pulses. It seems likely that such deformation might also influence the evolution, and passage of magmatic derived metalliferous fluids within, and out from, mid-crustal magma chambers that feed porphyry-Cu deposits. Deformation should have a first order influence on permeability and on the extent of fluid rock interaction (Dipple and Ferry, 1992; Cox, 2005) and this should directly affect the spatial distribution of alteration and mineralisation associated with the hydrothermal fluid exsolved from a crystallizing melt.

The Minto pluton in the Yukon Territory, Canada, is a ductilely deformed calc-alkaline granitic intrusion hosting a Cu-Au deposit that may represent an example of a mid-crustal metalliferous magma body like that thought to underlie and feed porphyry-Cu systems. Although previous studies have suggested the deposit has many characteristics of a porphyry system (Tafti, 2005), thermobarometry places the intrusion of Minto host rocks at 15-25 km (Tafti, 2005), far deeper than the deepest published porphyry systems (Singer et al., 1989) but within depths proposed for magma chambers thought to feed porphyry systems (Cloos, 2001; Richards, 2003; Brown, 2007). To better understand the interaction of deformation and magmatic related Cu-Au mineralisation at sub-porphyry depths, this study examines the geometric patterns and kinematic history of ductile deformation in the Minto pluton and assesses its genetic relationship to mineralisation. The specific goals of this study are to

assess the relationship between felsic calc-alkaline intrusions, contemporaneous ductile deformation, and hydrothermal mineralisation to understand whether the Minto deposit is a product of a magmatic system analogous to those inferred to feed porphyry systems. Key observations and interpretations made in this study include: (i) calc-alkalic arc granitoids have been emplaced in the ductile regime as episodic intrusions, (ii) the range in timing for hypogene sulphide mineralisation is contemporaneous with episodic granitoid intrusion, (iii) a positive feedback relationship between ductile deformation and hydrothermal alteration is likely responsible for the observed geometry at Minto, and finally (iv) the Minto deposit represents an intrusion related hydrothermal Cu-Au-Ag deposit located within a convergent arc framework where magma emplacement and mineralisation occurred in the ductile regime at depths below deep porphyry-Cu deposits. As such, Minto represents mineralisation in a parental magma chamber, such as those described to feed porphyry stocks and dikes, and a new potential for exploration arc settings.

Chapter 2: Body of Thesis

2.1 Geological Setting

2.1.1 Regional Geology

The Minto pluton is part of the Aishihik plutonic suite (Figure 2) which also includes the Aishihik batholith to the south, and the Walhalla Creek pluton, McGregor Creek pluton, Tatchun batholith, and Granite Mountain batholith. The Aishihik suite forms a belt of Early Jurassic calc-alkaline intrusions extending from west of Whitehorse to east-central Alaska that define a continental arc within the Yukon-Tanana terrane (Johnston et al., 1996a; Mortensen et al., 1999). The Minto pluton (Figure 2) intrudes the Upper Triassic augite-phyric basalts of Stikinia (the Lewes River Group) to the east and north, and Late Devonian-Early Mississippian meta-plutonic rocks of Yukon-Tanana terrane (Simpson Range plutonic suite) to the west (Tempelman-Kluit, 1984; Gordey and Makepeace, 1999; Colpron, 2006).

The northern end of the Minto pluton is covered by Pliocene and younger basalt flows of the Selkirk Group. The eastern contact of the Minto pluton with Triassic rocks is locally faulted. Geological relationships at the southern end of the Minto pluton are obscured by the Cretaceous Carmacks Group which unconformably overlies the Early Jurassic Aishihik plutonic suite, represented in the southeast of the Minto deposit by a clast-supported cobble to boulder conglomerate comprised of Minto lithologies (Figure 3). Minto may link to the south, under the Carmacks Group, with the Granite Mountain batholith (Tafti, 2005).

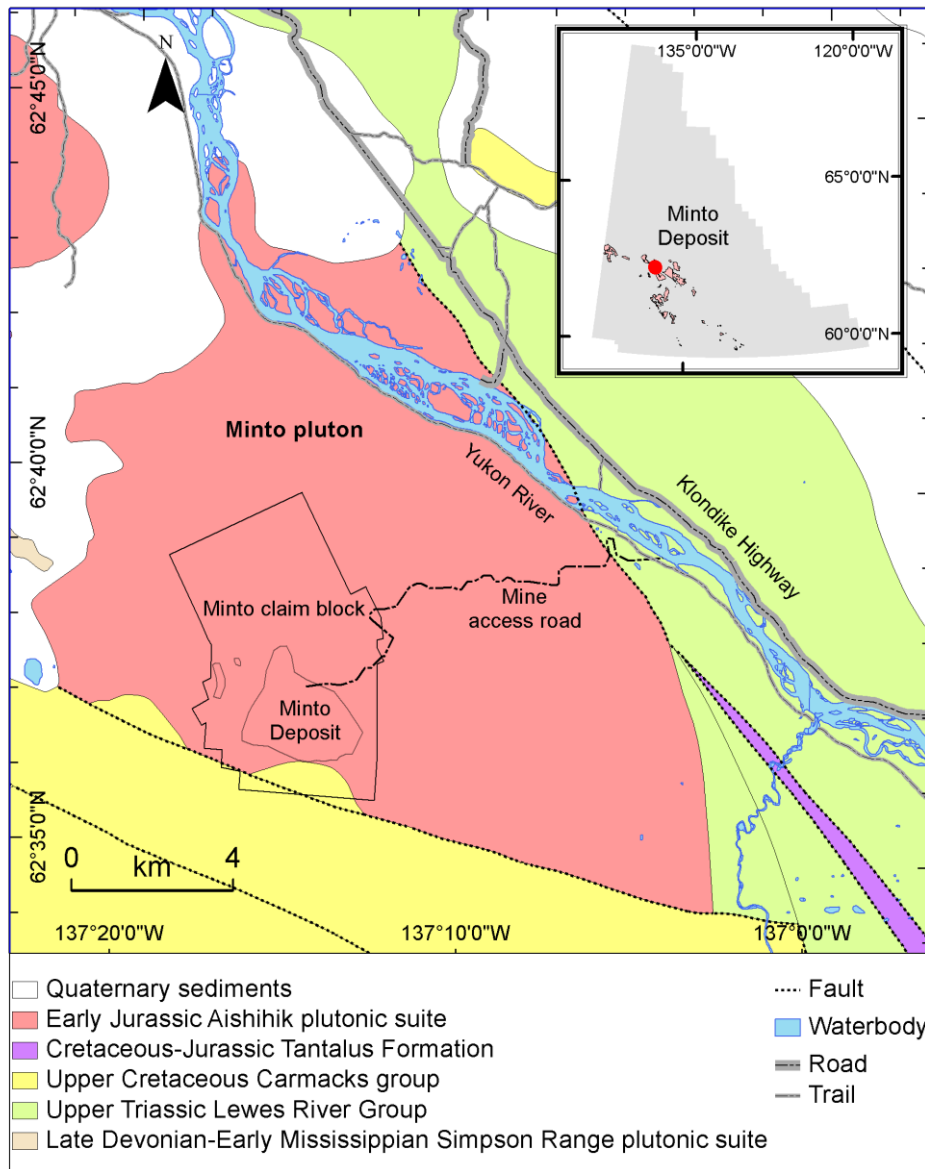


Figure 2: Regional geological setting of the Minto pluton and deposit. The Minto pluton is part of the Aishihik plutonic suite, a northwest trending belt of Jurassic-Cretaceous aged felsic intrusions in southwest Yukon extending into Alaska (marked in black on inset map) interpreted as the result of arc subduction. Fault contacts to the east and south obscure the contact relationship between the pluton and country rocks of the Yukon-Tanana terrane. Younger quaternary sediments and Upper Cretaceous Carmacks Group unconformably overlie older rocks, further obscuring geologic relationships. Deposit margins are inferred from Capstone Resources' exploration drilling. Figure modified from Colpron, 2006.

Existing geochronologic U-Pb zircon measurements using Laser Ablation Inductively Coupled Plasma Mass Spectrometry (LA-ICP-MS) by Tafti (unpublished M.Sc. thesis data) suggest the Minto pluton was emplaced at approximately between 197 Ma and 201 Ma. Hornblende geobarometry and geothermometry by Tafti (unpublished M.Sc. thesis data) suggests emplacement of Minto granodiorite at depths greater than 15 km. Detrital zircons taken from a cobble conglomerate composed of Minto deposit lithologies indicate a maximum age of 77 Ma for this overlying sediment, indicating that the deposit was subaerial by the Late Cretaceous.

Within the area encompassing the Minto deposit, the otherwise massive Minto pluton is transected by numerous ductile shear zones with well-developed foliation and a generally shallow orientation. These zones are millimetres to hundreds of metres wide and up to ~1 km in lateral extent. The zones of foliated rock are spatially associated with Cu-Au mineralisation manifested as disseminated chalcopyrite and/or bornite with locally occurring stringers or massive sulphide. Measured and indicated resources as of 2010 were 29.9 Mt @ 1.2% Cu, with 365 Kt Cu, 12t Au, and 122t Ag (Annual Technical Report, 2009), with the tenor of hypogene gold and silver mineralisation coincident with copper assay values. Scanning Electron Microprobe (SEM) scans indicate that gold and silver are contained within bornite and chalcopyrite (pers. Comm., Capstone mine staff, 2010). Gold is typically microscopic although native gold has been observed in fractures and epidote veins (pers. comm., Capstone mine staff, 2010).

Brittle faulting is common at the deposit and dissects the foliated deformation zones. The largest fault on the property is the DEF fault (Figure 3), an approximately east-west trending fault dipping about 60° to the north. This fault zone is defined by well-developed breccia,

gouge, and low temperature clay alteration minerals several metres in thickness. Although slip along the fault is unknown, abundant cataclasite and offset between mineralized zones on either side of the fault suggest displacement on a scale of hundreds of metres. The main ore bodies within the Minto pit are truncated by the DEF fault, although smaller zones of mineralization are present within the hangingwall.

2.1.2 **Deposit Geology**

Interpretations of ore genesis at the Minto deposit have been widely debated since its discovery in 1973. Gale (1976) posited direct precipitation of Cu-Fe sulphides from a melt. Pearson (1977) was first to recognize the association between deformation and ore grade, but interpreted the system as a pre-existing sedimentary hosted copper deposit or hydrothermal deposit that had been metamorphosed and intruded by later granitoids. Mortensen et al. (1999) believed that the Minto deposit is a porphyry-style deposit pre-dating deformation and occurring before the intrusion of granitoids interpreted as part of the Granite Mountain batholith. Gordey and Makepeace (2001) proposed that the deformed host rocks containing Minto mineralisation were roof pendants within the Granite Mountain Batholith. This concept and the early work by Pearson (1977) was extended by Tafti (2005) using Thermal Ionization Mass Spectrometry (TIMS) dating of zircons, whole-rock geochemistry, and sulphur/lead isotope characterization.

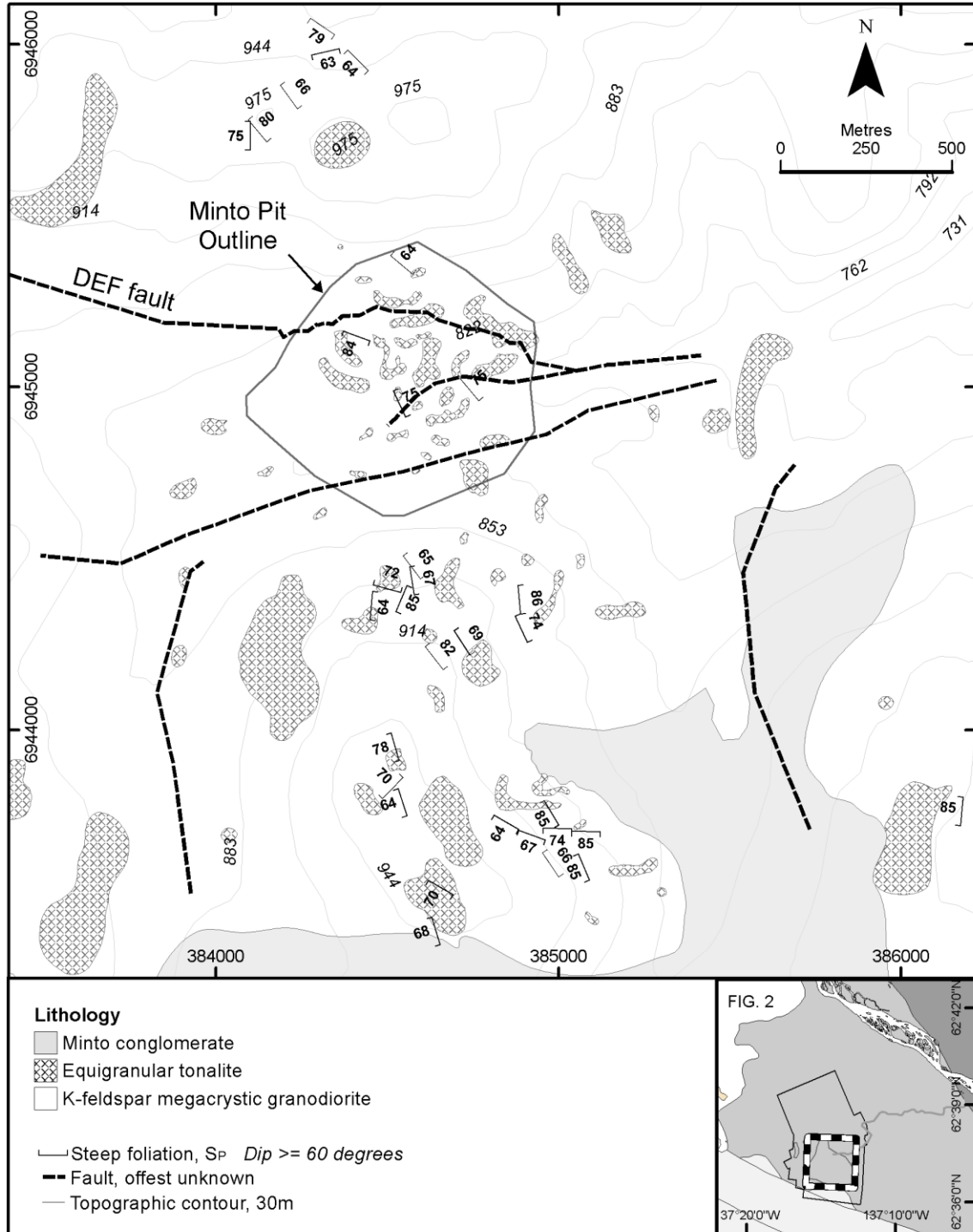


Figure 3: Interpretative map of major lithologies and important structures in the Minto deposit, excluding quaternary sediments. The distribution of lithologies and their contacts is interpreted from surface mapping undertaken in 2008 and bedrock intersections from company drilling. K-feldspar

granodiorite and equigranular tonalite are part of the Minto pluton. Minto Conglomerate is interpreted as basal Carmacks Group (shown in Figure 2) (Tempelman-Kluit, 1974, Tempelman-Kluit, 1984).

Important structures include zones where foliation (S_p) is steep ($\geq 60^\circ$) and major faults. Steep foliation measurements were recorded from outcrops or from oriented drill holes. The trend of steep foliation, NNW-SSE, is coincident with the main mineralization trend of the Minto deposit. Shallow foliations are omitted on this map for the sake of clarity. Fault locations are inferred from outcrop exposure, drill intersections, and airborne magnetic data.

Using these results, Tafti (2005) interpreted Minto as a partially formed porphyry deposit wherein hydrothermal activity stalled and the deposit was buried, metamorphosed, and partially digested within a granitic diapir. This model contrasts with slightly earlier work by McCausland et al. (2002) who interpreted ages, intrusion depths, and geological relations observed in the Granite Mountain Batholith as evidence that it was emplaced into deformed gneiss as the youngest magmatic product in an active shear zone, and that magmatic fabric along the west margin of the batholith may indicate the nearby presence of the shear zone's northwest trending wall within the Early Jurassic continental magmatic arc.

2.2 Igneous Host Rocks

The Minto deposit is hosted within the Minto pluton, a body mainly comprised of calc-alkalic K-feldspar megacrystic granodiorite (Bostock, 1936; Pearson, 1977). Because of extensive deformation and alteration at the Minto deposit, previous workers describe a range of pseudolithologies representing a mix of protolith mineralogy, alteration mineralogy and deformation textures (Table 1). In this study, igneous rock types are defined using protolith mineralogy and chemistry. The effects of overprinting alteration and ductile deformation are considered separately.

Table 1: Comparison of lithologies recognized by previous workers at Minto

Hood (2010)	Bostock (1936)	Pearson (1976)	Tafti (2005)
K-feldspar Granodiorite (KGd)	Granodiorite Granite/diorite gneiss Foliated granodiorite	Klotassin Granodiorite (granodiorite, diorite, qz-monzodiorite) Quartzofeldspathic gneiss (Kfs- or Qz-rich) Biotite-rich gneiss Siliceous ore Foliated Biotite Granodiorite Biotite--quartz-feldspar gneiss Blotchy-textured hornblende biotite granodiorite	Granodiorite (granodiorite, syenite, tonalite) Quartzofeldspathic gneiss Biotite-rich gneiss Siliceous ore
Hornblende-biotite diorite (KGd sub-unit)		fine-grained foliated hornblende diorite	Diorite (quartz diorite, quartz monzodiorite, and diorite)
Coarse Grained Tonalite (Et)		Foliated hornblende diorite	
Granite pegmatite		Granite pegmatite K-feldspar-quartz pegmatite	Granitic Pegmatite
Aplite		Aplite	Foliated Grey biotite Aplite
Not observed		foliated to non-foliated biotite microgranite	
Not observed		Alaskite	
Not observed		Augite andesite	

2.2.1 Intrusive Units

2.2.1.1 K-Feldspar Granodiorite

K-feldspar megacrystic granodiorite (KGd, Figure 3 and Figure 4A) is the dominant rock type within the Minto Pluton and within the study area. This variety of granitoid actually composes a continuum of granitoid variants, grading from crowded K-feldspar megacrystic syenite to equigranular tonalite or quartz diorite (Pearson, 1977; Tempelman-Kluit, 1984; Tafti, 2005), based on classification using modal abundance of total quartz-alkali feldspar-plagioclase (from Streckeisen, 1974). In general, KGd contains approximately 30% to 50% plagioclase, 10% to 50% K-feldspar, 20% to 25% quartz, and total biotite \pm hornblende 10% to 15%. Accessory minerals include magnetite, epidote, titanite, apatite, and zircon. These minerals display sharp euhedral crystal faces in thin section. K-feldspar occurs most commonly as megacrysts 1 to 3 cm long with internal oscillatory zoning. Inclusions of biotite, plagioclase, hornblende, epidote, and zircon are common along growth zones. KGd tending to tonalite or diorite compositions typically contains anhedral K-feldspar rather than K-feldspar megacrysts. Plagioclase occurs up to 1 cm in length and occurs as euhedral to anhedral equigranular crystals evenly distributed throughout the rock mass. Igneous growth textures such as stepped twins and oscillatory zoning are common in plagioclase. Quartz forms anhedral masses interstitial to feldspars, but it locally forms glomeroporphyritic masses (henceforth referred to as “quartz eyes”) up to 1 cm in diameter. Randomly oriented biotite crystals up to 5 mm and/or euhedral hornblende up to 7 mm compose up to ~15% of KGd.

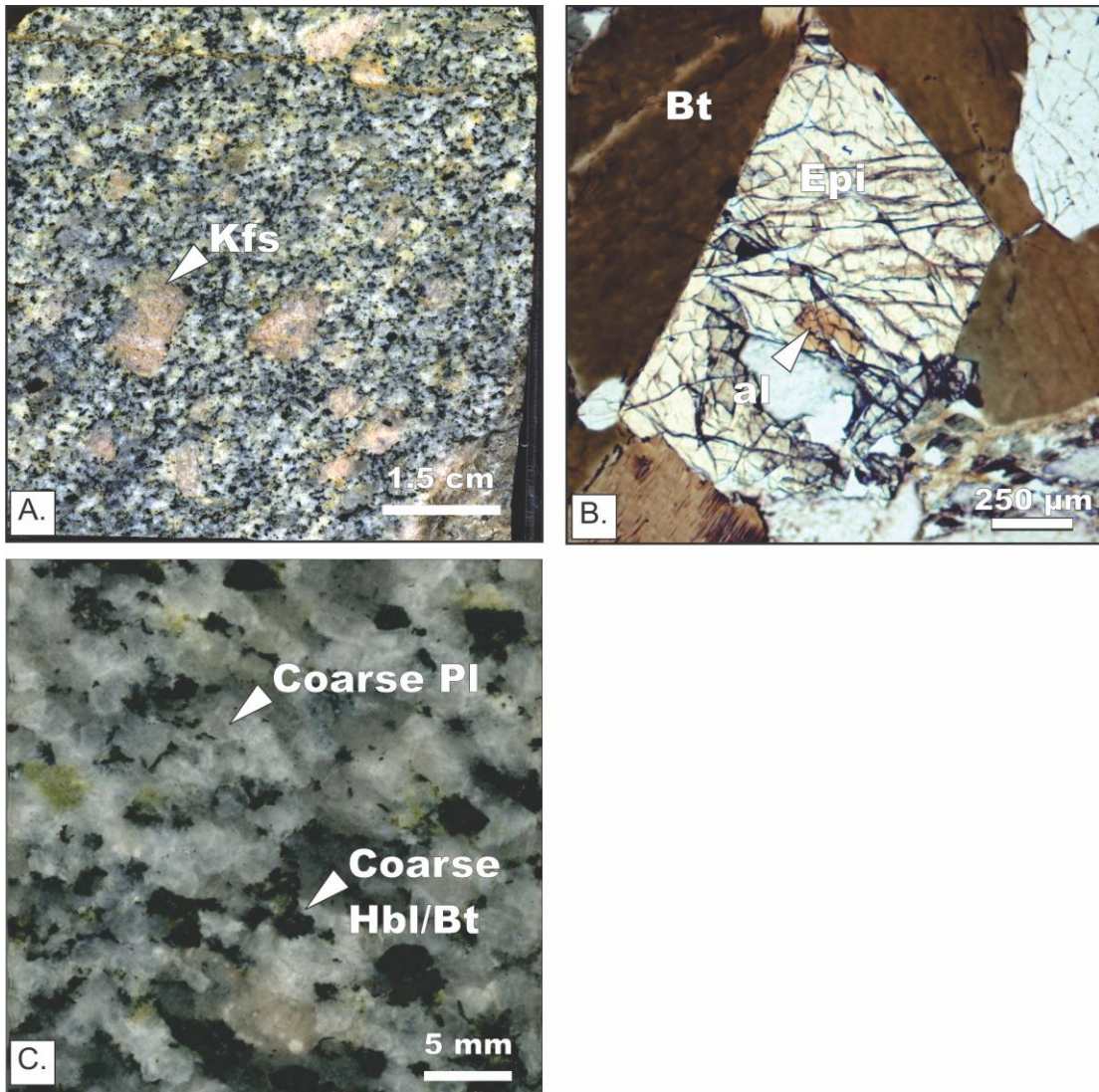


Figure 4: Two main granitoids comprise the Minto pluton: K-feldspar megacrystic granodiorite (KGd) and coarse grained tonalite (Tlt). Sample locations given in Appendix C A. KGd is the most common variant and is typically medium-grained with centimetre-scale K-feldspar megacrysts. The modal mineral composition ranges from syenite to quartz monzodiorite to diorite to tonalite (classification after Streckeisen, 1974). Kfs = K-feldspar. Sample S09-13-03A. B. KGd contains abundant magmatic epidote (Epi) with characteristic euhedral crystallinity, sharp grain boundaries with plagioclase and biotite, growth zoning, and allanite (al) cores. Bt = biotite. Sample SBH-C009. C. Coarse grained tonalite (Tlt) contains plagioclase (Pl) and euhedral hornblende (Hbl) that are typically approximately 5mm, in contrast with the more medium grained KGd. K-feldspar megacrysts are not present within this unit. Tlt was not observed to vary appreciably in bulk mineralogy. Sample H424-251.6.

Mafic component varies from 100% biotite to 100% hornblende but in most areas these minerals are both present. Magmatic epidote (Figure 4B) is a potentially important indicator of crystallization depth and occurs as both inclusions in feldspar and as individual grains. Secondary epidote is common at Minto, and magmatic epidote was identified using the following criteria (as described by Zen and Hammarstrom, 1984; Liu et al., 1999; Schmidt and Poli, 2004b): sharp euhedral boundaries with mafic phases, growth zoning, and allanite cores. Inclusions of magmatic epidote within K-feldspar and plagioclase are < 0.15 mm, highly birefringent, zoned, and euhedral to subhedral. Individual magmatic epidote grains interstitial to other minerals are 0.5 to 2 mm, euhedral to subhedral, zoned, and contain brown-green allanite cores visible in thin section (B).

2.2.1.2 Coarse Grained Tonalite

Intrusions of coarse-grained tonalite (Figure 4C) at the Minto deposit are typically less than a metre in thickness and crosscut KGd. Modal composition is approximately 75% plagioclase, 20% quartz, <10% biotite +/- hornblende. Plagioclase and hornblende are up to 6 mm, notably larger than their counterparts in KGd. Plagioclase is euhedral to subhedral with growth zoning or lamellae. Quartz is interstitial to feldspar. Mafic minerals include biotite +/- hornblende and epidote. Zircons are present as an accessory and display complex overgrowths. Enclaves of this unit were observed most frequently within strongly deformed and altered zones of KGd and are themselves weakly boudinaged and folded, although growth textures in igneous phenocrysts, such as oscillatory zoning and growth lamellae, are largely preserved.

2.2.1.3 Dikes

Five types of dikes were observed crosscutting the granitoids of the Minto Pluton, from youngest to oldest: (i) hornblende diorite dikes, (ii) Andesite dikes, (iii) aplite dikes, (iv) granitoid pegmatites, and (v) quartzofeldspathic lets (Figure 5).

Hornblende diorite dikes crosscut all units and do not exhibit evidence of alteration or ductile deformation, even at microscale. This is in contrast with all other observed dike varieties. Andesite and aplite dikes are observed as individual intrusions within massive and deformed rocks, intruding along or within pegmatites, or as angular breccia clasts within deformation zones. Plagioclase is typically moderately weathered or altered to sericite. Aplite crosscutting mineralized rock locally carries sulphides, possibly mobilized from mineralized hostrock.

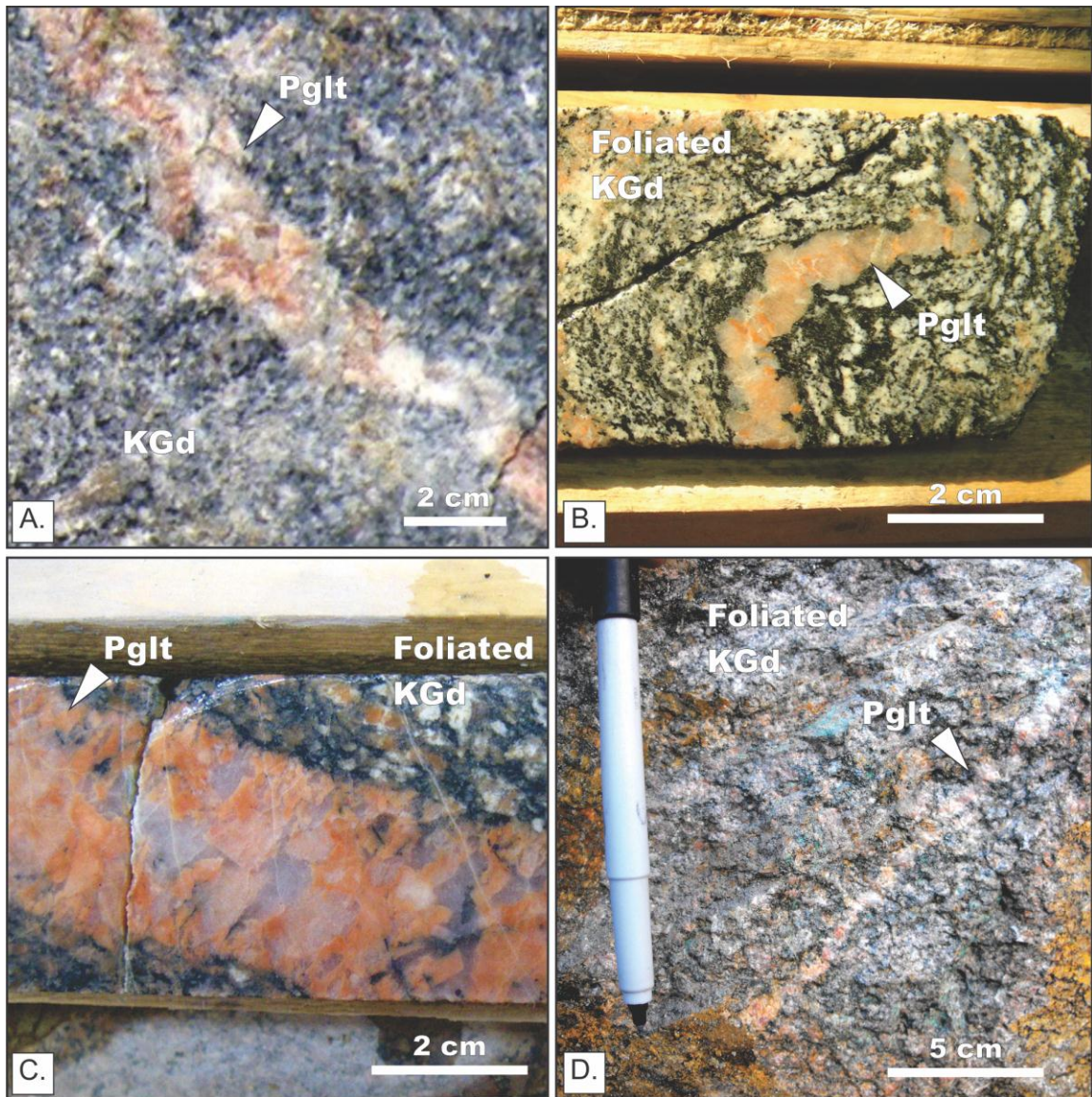


Figure 5: Photographs of pegmatite dikelets (Pglt) showing the variety of crosscutting relationships with KGd and foliation. These relationships suggest several episodes of intrusion and varying timing relative to regional deformation. A. Pegmatite dikelets crosscutting KGd indicating intrusion after KGd. B. Deformed pegmatite dikelet intruded and deformed along biotite foliation in deformed and altered KGd. This relationship indicates intrusion before cessation of deformation accommodated along foliation. C. Undeformed planar pegmatite dikelet intruded along biotite foliation in deformed and altered KGd. Relationship suggests intrusion after the cessation of deformation accommodated along foliation. D. Undeformed pegmatite dikelet crosscutting biotite foliation. This relationship indicates intrusion after the cessation of deformation accommodated along biotite foliation.

Large granitoid pegmatite dikes up to 1 m in thickness are present throughout the Minto deposit and have been dated using U-Pb isotope dilution–thermal ionisation mass spectrometry (ID-TIMS) techniques on zircons at 195.5 (+/- 0.7) Ma (Tafti, 2005). Contacts with wallrock are sharp, with no observable thermal effects, such as grain size reduction along pegmatite margins or deformation in wallrock. Plagioclase, K-feldspar, quartz, and biotite are typically coarse- to very coarse-grained. Inclusions of sulphides are locally present in intervals that crosscut mineralized hostrock. Orientations of dikes vary and crosscutting relationships between pegmatite dikes suggests multiple intrusion events.

Finally, quartzofeldspathic dikelets exhibit pegmatitic K-feldspar, plagioclase, and quartz. These pegmatite dikelets are up to several centimetres in thickness with sharp margins. Quartzofeldspathic dikelets crosscut both massive (Figure 5A) and deformed rocks (Figure 5B, C, and D). In deformation zones, these dikelets may intrude along foliation (Figure 5B and C) or crosscut it (Figure 5C). The range of textures and crosscutting relationships suggests that quartzofeldspathic dikelets were emplaced during several episodes relative to deformation.

2.2.2 Internal Pluton Fabrics

Foliations in granitoids can form by magmatic flow, ‘submagmatic flow’, high-temperature solid-state deformation and moderate- to low-temperature solid-state deformation (Paterson et al., 1989). Magmatic fabrics within the Minto pluton occur within, and between, individual intrusions of KGd and Tlt and are separate from the solid-state deformation textures, i.e., foliation and gneissic banding, discussed below. Fabrics include mafic magmatic enclaves, mafic mineral accumulations or schlieren, igneous emplacement contacts, and magmatic mineral lineation.

Mafic magmatic enclaves (MMEs, after Barbarin, 1999) are observed regionally in KGd (Figure 6) as centimetre to metre scale rock masses composed of biotite, magnetite, titanite and epidote. These xenoliths are locally impinged by euhedral K-feldspar (Figure 6A), suggesting they predate feldspar growth. Mafic-rich zones were observed with a variety of habits: sharply bounded enclaves (Figure 6A), enclaves with irregular boundaries with KGd (Figure 6B), and as mafic enclaves with gradational boundaries with KGd (Figure 7A). Mafic magmatic enclaves are common in calc-alkaline granitoids (Didier, 1991) and are abundant in most of the Cordilleran granitoids (e.g., Pitcher, 1982; Barbarin, 1999). Mafic enclaves in granitoids have been postulated as related to restite material from resorbed fragments of country rock (Chappell et al., 1987), basaltic magma injections into granitoid magma chambers (Huppert and Sparks, 1988; Wiebe and Collins, 1998; Wiebe et al., 2002), mixing/mingling between mafic and felsic magma within magma chambers (Furman and Spera, 1985; Vernon et al., 1988), and as the product of late mineral coarsening during crystallization of granitoid magma chambers (Boudreau, 2011).

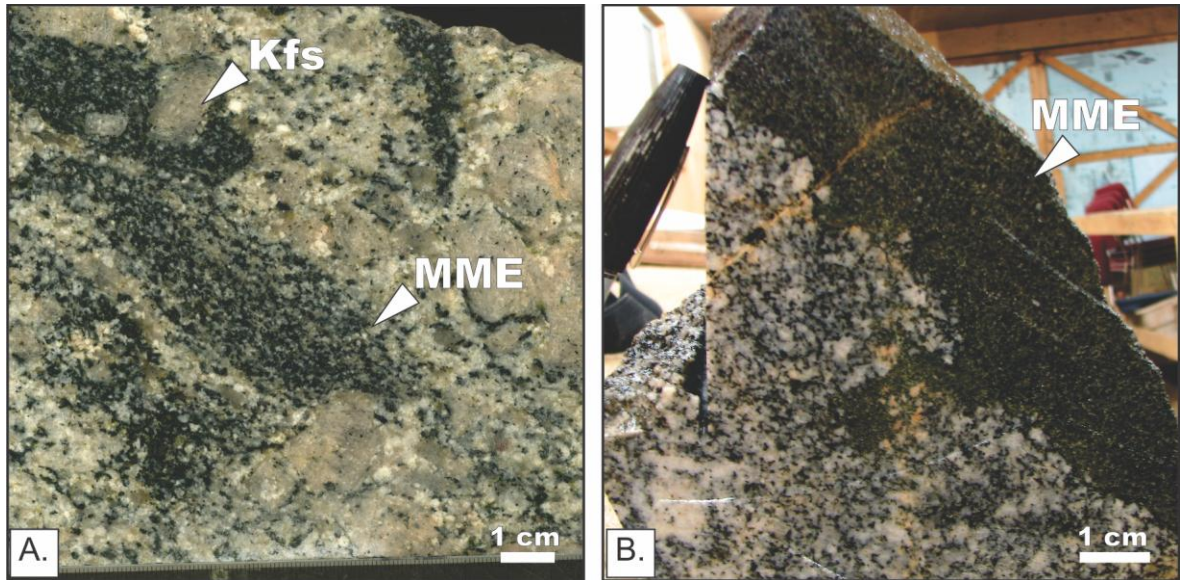


Figure 6: Mafic magmatic enclaves (MMEs) within KGd may indicate pre-solidus intrusion of mafic magma into the KGd magma chamber or mineral differentiation within the Minto pluton. MMEs were observed with both regular and irregular boundaries. A. MMEs, tens of centimetres in scale, locally appear to be impinged by K-feldspar megacrysts, possibly indicating the late growth of K-feldspar with enough local liquid magma to settle into xenoliths (Clemens and Wall, 1981; Vernon and Paterson, 2008). B. MME sharing irregular boundary with KGd, suggesting KGd had not completely solidified at the time enclaves were emplaced.

Mafic accumulations are especially common in the margins of intrusions, adjacent to contacts with other granitoids or with country rocks (Barbarin, 1999). Mafic aggregates can form schlieren layering (Barbarin, 1999), and contacts between mafic aggregates and granitoids can be either sharp or diffuse (Barbarin, 1999), meaning that gradational contact shown in Figure 7A, defined by an aggregation of minerals also observed within enclaves, may represent schlieren layering within KGd. Schlieren layering was also observed in Tlt cropping out in road cuts east of the main deposit (Figure 7B). These rhythmic successions of layers are composed of millimetre thick layers of moderately aligned biotite, hornblende, epidote, magnetite, and titanite separated by felsic layers 1 – 50 cm thick of medium- to coarse-grained quartz and plagioclase with lesser amounts of biotite, hornblende, epidote, magnetite, and titanite (Figure 7C). This zone of schlieren layering is tens of metres wide and appears to have been intruded by a layer parallel tonalite sill (Figure 7A and B). Only weak ductile deformation microfabrics are present in these layers, supporting interpretation as an igneous foliation. These schlieren have a subvertical eastward dip in outcrop. Regional paleomagnetic studies by McCausland et al. (2002) suggest that plutonic rocks in the Aishihik plutonic suite have not been reoriented from the horizontal by more than 3° since formation, therefore the steep orientation of schlieren could be due to processes within the forming pluton, e.g., due to sinking wall rock rafts (after Wiebe et al., 2007). However, varying dip of the Minto conglomerate observed by Tafti (2005) and Mortensen (pers. comm.) may be evidence of greater reorientation, e.g., due to fault block rotation.

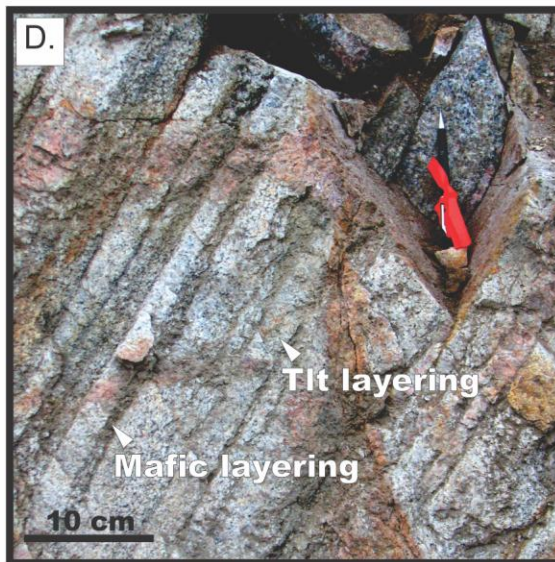
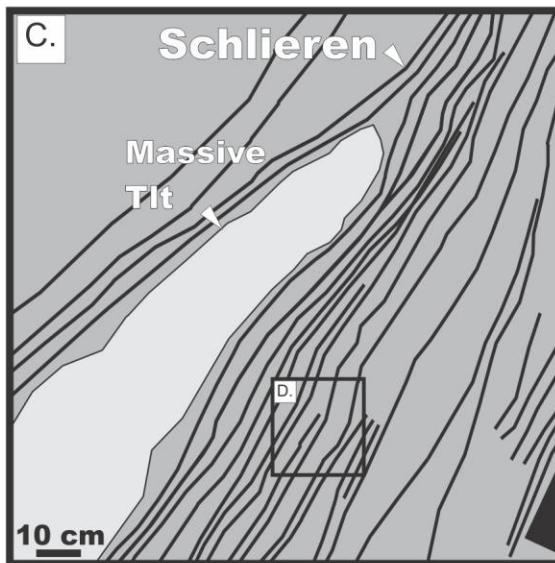
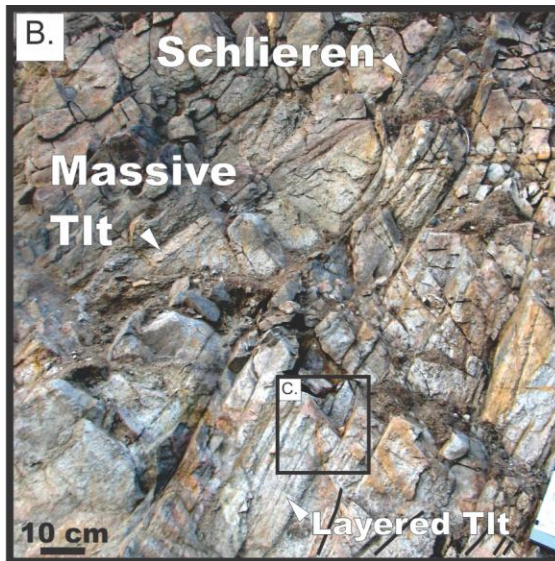
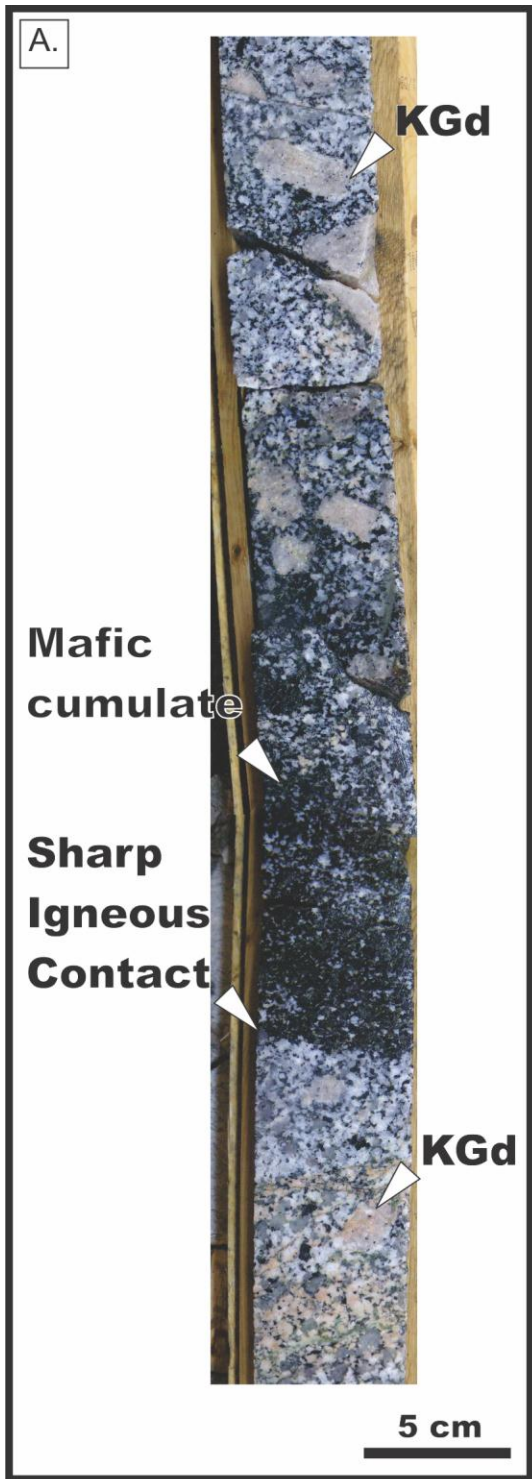


Figure 7: Photographs of mafic enrichments defining igneous layering. A. Gradational contact into mafic enrichment with sharply bounded basal contact with KGd, indicating mineral differentiation within the forming Minto pluton through settling of mafic minerals as a cumulate or through “filter pressing”. B. Mafic layering in tonalite interpreted as schlieren (after Didier and Barbarin, 1991) occurring as a zone of layered Tlt in outcrop at the scale of tens of metres. C. Enlarged view of alternating mafic- and felsic-rich layering. Mafic phases include biotite, hornblende, epidote, magnetite, and titanite. Felsic layers are interpreted as Tlt. D. Schematic representation of outcrop illustrating the layer-parallel lobe of Tlt, interpreted as a sill. Such a cross cutting relationship indicates igneous emplacement occurring after host rock crystallisation to the degree that schlieren are able to form.

Igneous contacts between intrusions of granitoid were identified using the criteria of Streckeisen (1974), i.e., common crystal alignment along contacts, phaneritic crystal texture in adjacent rocks, and igneous mineral textures (e.g., straight intermineral crystal faces or growth zoning) without strong deformation microtexture overprints. Contacts between granitoids at Minto are sometimes difficult to distinguish because of gradation between variants within individual masses, or because granitoids in igneous bodies may have similar grain size and mineralogy. Crowded K-feldspar porphyry KGd was observed across the Minto pluton and is useful for delineating igneous contacts, e.g., due to the abrupt termination of the porphyritic rock with other granitoids and due to the tendency for magmatic flow alignment of megacrysts along contacts (Figure 8A). Igneous contacts between pulses of KGd were observed between masses of KGd at the scale of metres (Figure 8A) and on the order of centimetres involving stoped enclaves (Figure 8B). Igneous KGd contacts are also exemplified by the crosscutting of pre-existing deformation fabrics such as biotite foliation (Figure 8C). Only single contacts were observed, meaning the thickness of individual pulses could not be determined. Similar igneous contacts were observed involving Tlt (Figure 9). Igneous Tlt contacts are recognized due to the more coarse-grained nature of plagioclase, bioite, and hornblende. Four igneous contacts between Tlt and KGd were observed in unoriented vertical drillholes and were shallowly dipping, i.e., less than 40 degrees.

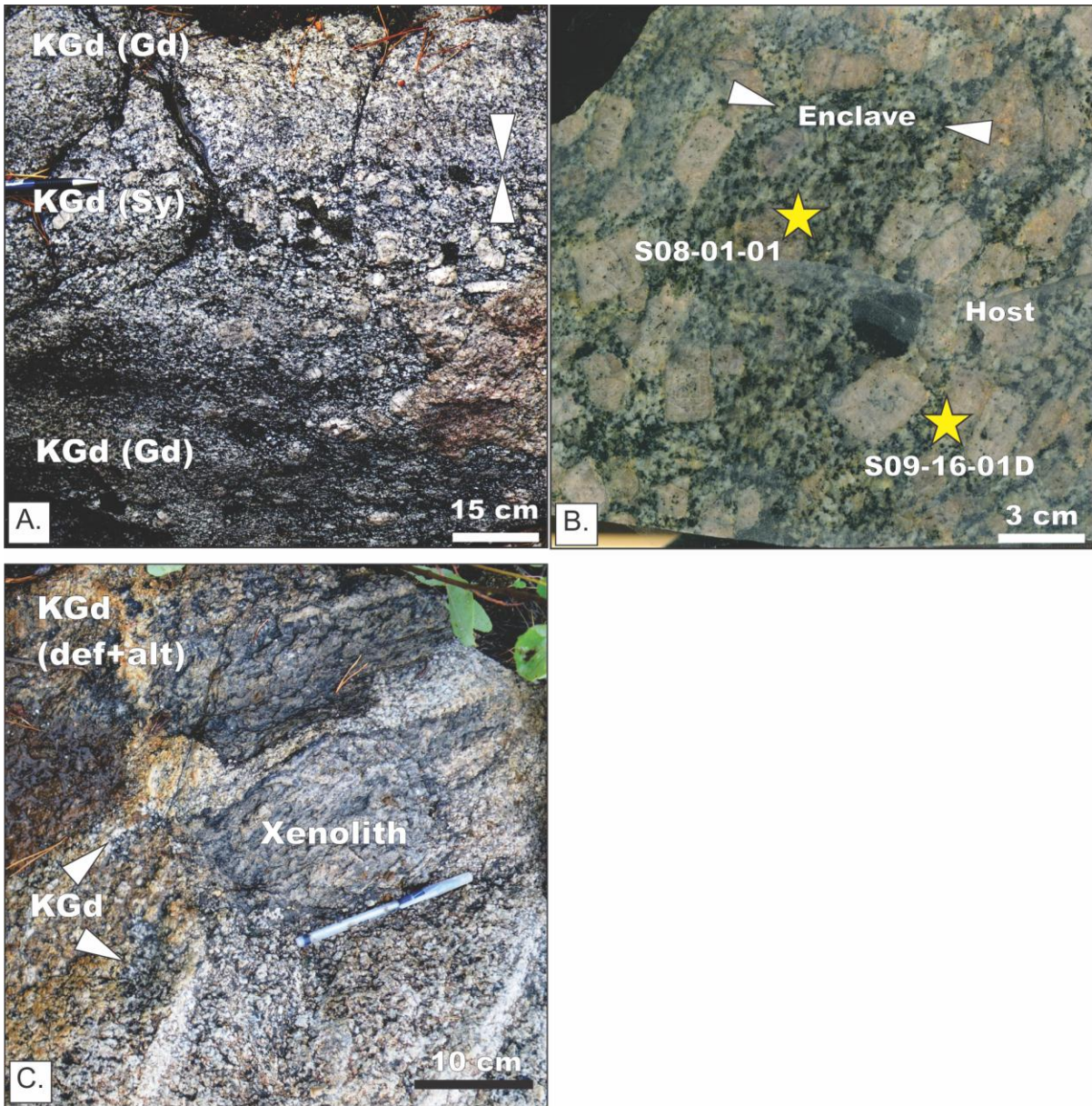


Figure 8: Crosscutting relationships involving distinct intrusions of KGd indicating multiple stages of intrusion. A. Planar igneous contact between two intrusions of massive KGd. The contact is marked by a gradational increase of K-feldspar megacrysts upwards towards the contact and with an abrupt reduction of K-feldspar phenocrysts across the contact. The long axes of K-feldspars are aligned parallel to the contact, interpreted as magmatic alignment. Photo also exemplifies the local heterogeneity of the Minto pluton, with KGd varying from granodiorite (Gd) at the bottom of the photograph upwards to syenite (Sy), then abruptly back into granodiorite. B. A weakly chlorite-epidote-magnetite-pyrite altered enclave of KGd within an unaltered KGd host, suggesting a history of intrusion interspersed with

hydrothermal alteration. Note the magmatic alignment of K-feldspar along the enclave margin. U-Pb dating of zircon using the SHRIMP indicates crystallization ages of 200.1 +/- 1.1 Ma for the enclave and 197.6 +/- 1.6 Ma for the host (see Geochronology). C. KGd intruded along a strongly deformed and altered KGd. This intrusion has stopped an enclave of the pre-existing deformed KGd into the younger KGd. Pre-existing structural fabrics were also crosscut by Tlt, e.g., biotite foliation (Figure 9C) and gneissic layering (Figure 9D). Pre-existing structural fabrics were also crosscut by Tlt, e.g., biotite foliation (Figure 9C) and gneissic layering (Figure 9D).

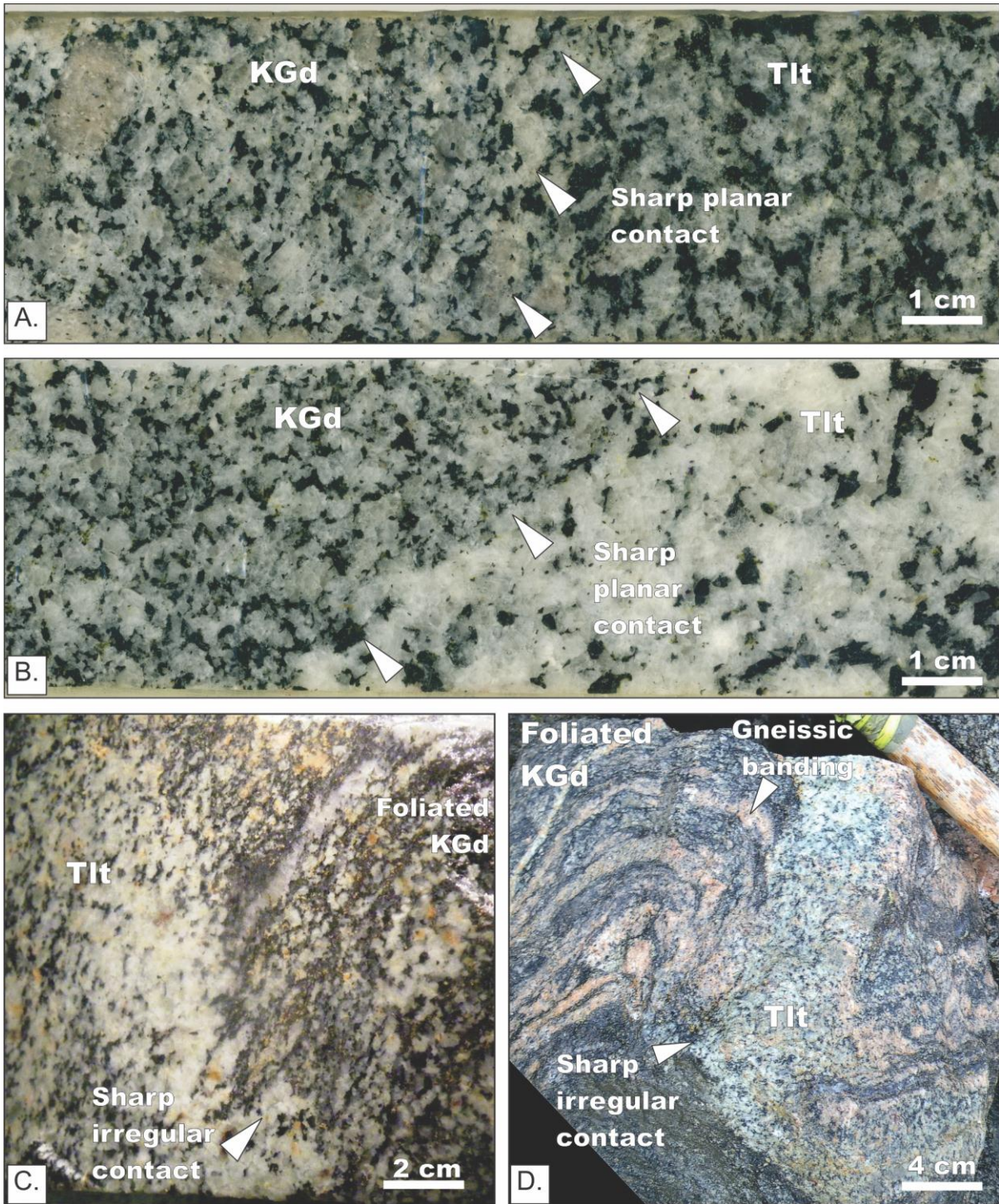


Figure 9: Photos showing crosscutting relationships involving intrusions of Tlt which indicate multiple stages of intrusion. A. Subtle igneous contact between KGD and Tlt marked by a contrast in bulk mineralogy and grainsize, i.e., lack of K-feldspar, abundant hornblende, and coarser grainsize within Tlt. Sample H587-252.5. B. Apparent igneous contact between KGD and Tlt marked by a contrast in bulk

mineralogy and grain size. Sample H424-252(c). C. Igneous contact between Tlt and a deformed and altered granitoid indicating intrusion after the development of biotite foliation. Note that the igneous contact in this case is irregular and marked by short intrusions along foliation planes. This enclave of Tlt is a boudin within a larger section of foliated KGd, indicating intrusion before the cessation of ductile deformation. Boulder taken from blast heave in the Minto pit. D. Igneous contact between Tlt and a strongly deformed, compositionally banded granitoid. The Tlt host rock is folded, indicating intrusion after multiple stages of deformation, and altered (quartz-magnetite-chalcopyrite-bornite). Boulder is from high grade stockpile, mined from the Minto pit.

2.2.3 Lithochemistry of KGd

The bulk chemistry and trace element concentrations of granitoids are a useful means of interpreting the tectonic setting and conditions during granitoid petrogenesis. In this study whole rock lithochemistry also serves as a protolith benchmark to assess the metasomatism associated with the Cu-Au mineralisation at Minto. A suite of ten KGd samples was collected across the Minto pluton (Table 2, Appendix C) for lithochemical analysis along a roughly East-West transect. KGd was chosen because it is interpreted as the most common protolith for deformed ore-bearing rocks at the Minto deposit. The sample suite consists of five fresh samples collected from drillcore and five samples taken from surface. Weathering effects for surface samples were reduced by removing weathering rinds using a rotary saw. Samples were analysed using a combination of lithium metaborite/tetraborate fusion inductively coupled plasma mass spectrometry (FUS-ICP) and instrumental neutron activation analysis (INAA) by Actlabs (Ancaster, Ontario; method 4LITHORESEARCHQUANT). Results and detection limits for this assay package are listed within Appendix B and are typically in the low ppm and ppb range for trace elements. In addition to the use of laboratory standards, selected samples were split and both aliquots were analysed as a means of quality control. Quality control for analyses are also given in Appendix C .

Table 2: Geochemical sample information. Geochemical data in Appendix C . ND = not described by

Tafti (2005)

Researcher	Sample	Weathering	UTM E	UTM N
Hood (this study)	H424-212	Fresh	384531.1	6944491
	H424-252	Fresh	384531.1	6944491
	H424-323	Fresh	384531.1	6944491
	H510-64	Fresh	383202.1	6945821
	H587-253	Fresh	384140.5	6945938
	S09-02-9A	Weathered	383776	6945758
	S09-08-01A	Weathered	382654	6944715
	S09-15-04A	Weathered	387024	6946222
	S09-16-01D	Weathered	384724	6945250
	S09-22-01C	Fresh	384535	6945018
Tafti (2005)	01-12-282.5-283	ND	ND	ND
	01-13-162-163	ND	ND	ND
	01-8-113-114	ND	ND	ND
	01-9-256	ND	ND	ND
	02-RT-2	ND	ND	ND
	93-A-169-170	ND	ND	ND
	93-A-205.3	ND	ND	ND
	93-A-326-327	ND	ND	ND
	93-B-302-304	ND	ND	ND
	93-E-476-477	ND	ND	ND
	93-G-236-237	ND	ND	ND
	96-4-285-286	ND	ND	ND
	99-6-108-109	ND	ND	ND

2.2.3.1 Results

The weight percentage of major rock forming elements for KGd in this study are within the range of values described by Tafti (2005, figure 10), e.g., in terms of total $\text{Na}_2\text{O} + \text{K}_2\text{O}$ versus SiO_2 (as per Cox et al., 1979)

Concentrations of Y+Nb vs. Rb (Figure 11A) suggest granitoids were generated in a continental magmatic arc, i.e., volcanic arc granite field (after Pearce and Norry, 1979). Alumina saturation plots (Figure 11B) indicate Minto granitoids are strongly peraluminous. Modified alkali-lime saturation plots (MALI, Figure 11C) of KGd show most rocks within the calc-alkalic zone, with several surface samples within the calcic field, possibly attributable to weathering. KGd plots within the magnesian region of a Fe Index plot (Figure 11D).

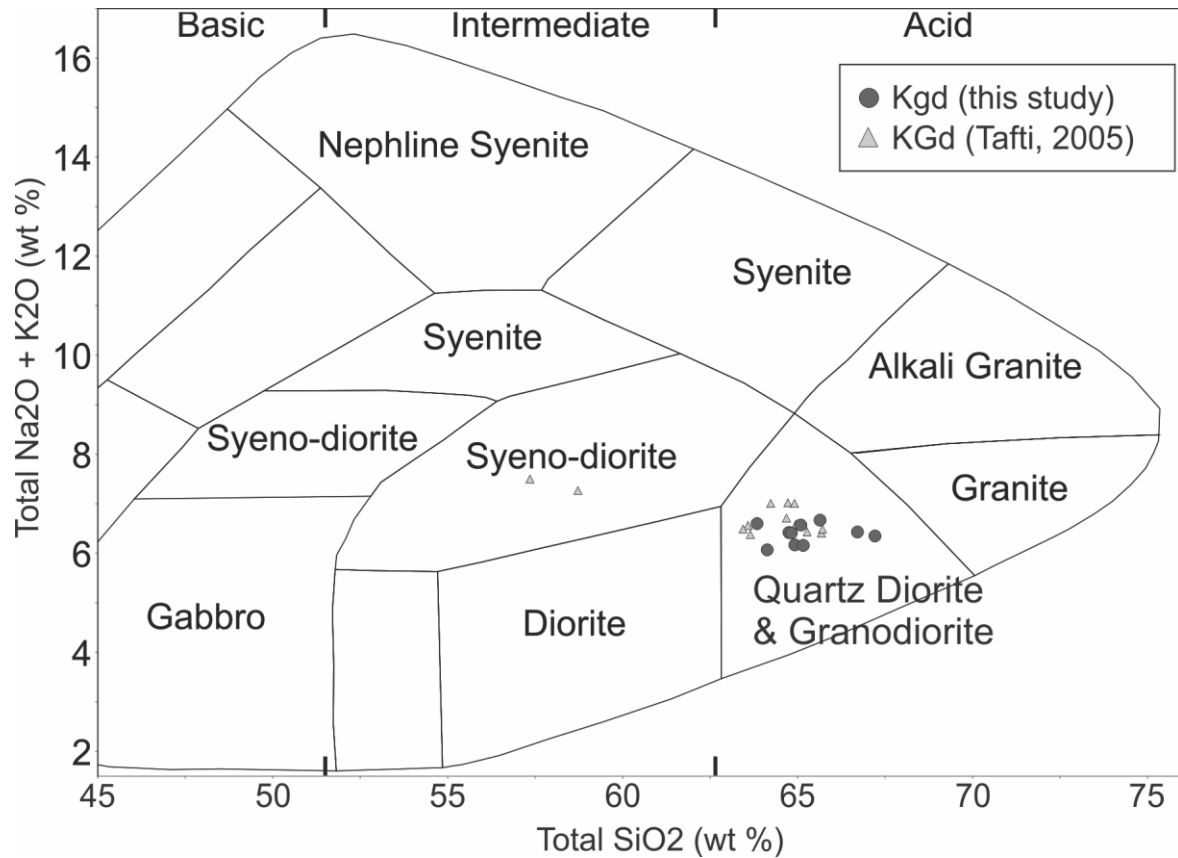


Figure 10: Whole-rock lithogeochemical granite type discrimination diagram based on total alkalis versus total silica (TAS) (Cox et al., 1979) modified after (Middlemost, 1994) placing KGd within the quartz diorite/granodiorite field. Quartz diorite and granodiorite are grouped because the geochemical classification of volcanic rocks using total alkali versus silica cannot reproduce QAPF parameters (Bas et al., 1986; Le Maitre, 1989). Classification is on a non-genetic basis and intended to be consistent with classification of volcanic rocks using modal mineral content, i.e., quartz-alkali feldspar-plagioclase-foiidite (QAPF, after Streckeisen, 1974). Two samples from Tafti (2005) plot as syenodiorite, while the remainder plot in a similar location to KGd sampled in this study.

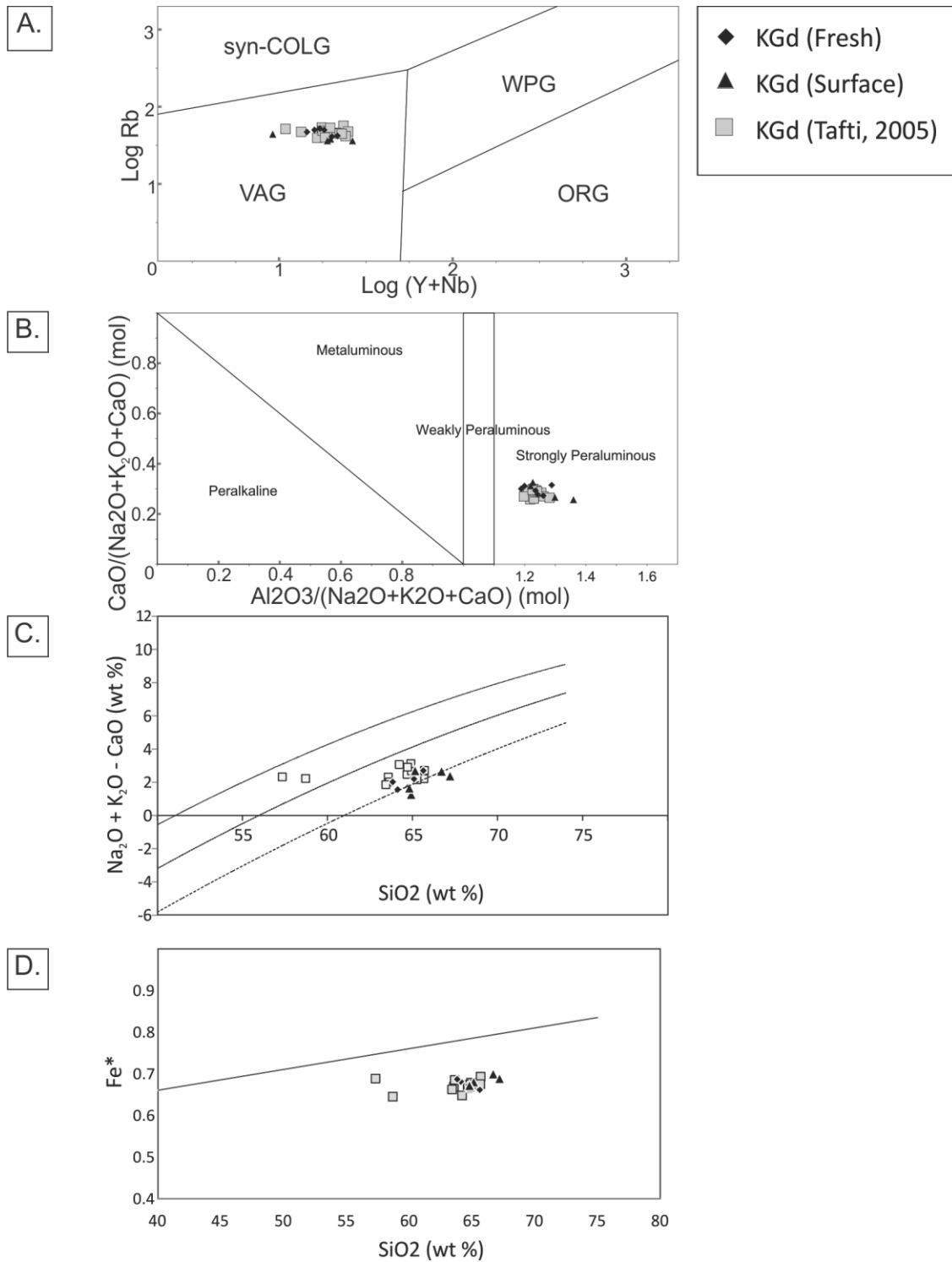


Figure 11: Whole rock lithochemical characterization of KGd using trace elements. A. Tectonic discrimination diagram (Pearce et al., 1984) indicating KGd plots within the volcanic arc granite field (VAG). Other abbreviations represent orogenic granites (ORG), syncollision granites (syn-COLG), and

postcollision granites (post-COLG) granitoids. B. Aluminum saturation plot (Roser and Korsch, 1988) placing KGd within the strongly peraluminous field. C. Peraluminous rocks may be calcic, alkali-calcic, or calc-alkalic (Frost et al., 2001). Modified alkali-lime (MALI) plot of $\text{Na}_2\text{O} + \text{K}_2\text{O} - \text{CaO}$ vs. SiO_2 (after Frost et al., 2001; Frost and Frost, 2008) indicates KGd from this study clusters near the Calc-alkalic to Calcic boundary but is dominantly calc-alkalic. D. KGd from this study plots as magnesian according to the Fe Index plot (after Frost et al., 2001; Frost and Frost, 2008), and therefore oxidized. Fe^* is defined as $[\text{Fe}^{\text{Tot}}/(\text{Fe}^{\text{Tot}} + \text{MgO})]$. Boundary line (modified Fe^* trend) is a continuous line defined by $\text{Fe}^* = 0.46 + 0.005 \text{SiO}_2$ (Frost and Frost, 2008).

2.3 Mineralisation and Alteration

Mineralisation and associated alteration at Minto is mainly coincident with variably developed shear zones. For this study field mapping, core logging, petrographic observation, and geochemical analysis are used to characterize hydrothermal alteration in the Minto deposit. Samples for study were collected from regional outcrop, the open pit, and from exploration drillcore.

2.3.1 Ore Assemblage

The hypogene ore minerals of the Minto deposit are bornite and/or chalcopyrite, with Au and Ag occurring as microscopic inclusions within Cu-sulphides. These economic minerals occur in the following assemblages : (i) bornite, (ii) bornite-chalcopyrite, (iii) chalcopyrite, (iv) chalcopyrite-pyrite, and (v) pyrite. Assemblages grade laterally and vertically, a feature first noted and mapped by Pearson (1979).

Chalcopyrite and bornite are fine- to medium-grained and disseminated amongst biotite (Figure 12A). Contacts between Cu-sulphides and biotite or magnetite are typically straight (Figure 12B), although the interpretation of sulphide textures as evidence of relative timing between sulphide types, exsolution conditions, metasomatism, or remobilization is extremely unreliable owing to the overprint of ductile deformation and thermal re-equilibration. Exsolution textures of chalcopyrite from bornite, and possibly vice-versa, are present in approximately 75% of mineralized samples. Sharp, wedge-shaped lamellae are interpreted as having not been deformed, although a genetic cause is not clear, as they may form during sulphide precipitation, during cooling, as a result of re-heating, due to replacement, or due to metamorphism (Brett, 1964; Gill, 1969; Durazzo and Taylor, 1982). These exsolution lamellae may also have a vermicular or myrmekitic geometry, a texture suggestive of thermal

annealing and re-equilibration (Brett, 1964; Durazzo and Taylor, 1982). Mineralisation tends to occur within biotite-dominated foliation, but biotite-chalcopyrite-bornite also occur as stringers or veins (Figure 12C) with little evidence of deformation. Pyrite (Figure 12D) is present as fine to coarse grains disseminated or as anhedral masses. Quartz veins (Figure 12E.) are rare and chalcopyrite and bornite tend to occur along margins. More common are silicified zones (Figure 12F) bearing sulphides, magnetite, and biotite. Chalcopyrite and bornite are locally present as inclusions within weakly zoned Mn-Ca-Fe garnets (Figure 12G), although chalcopyrite was also observed to overprint garnets (Figure 12H).

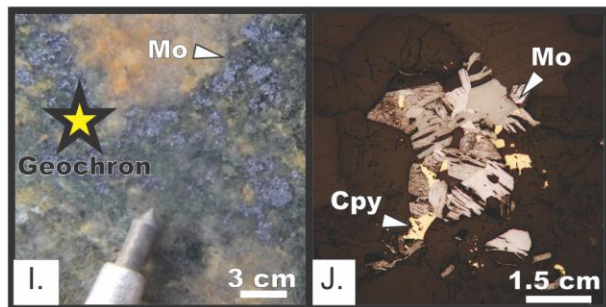
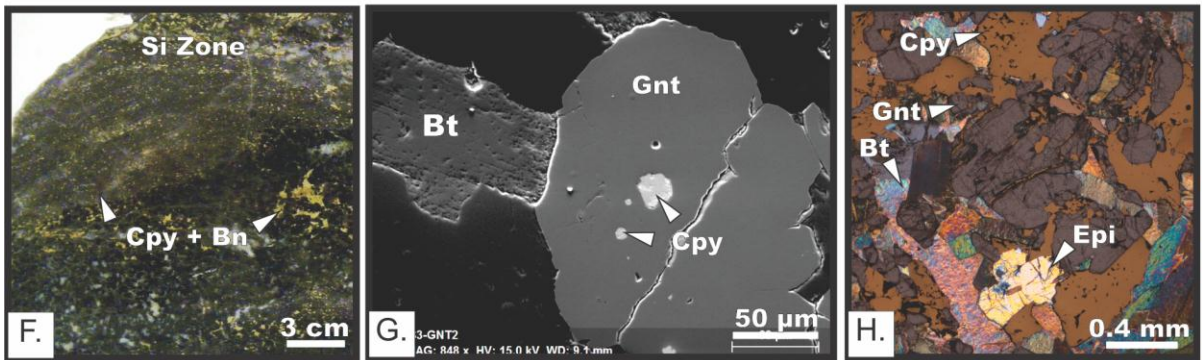
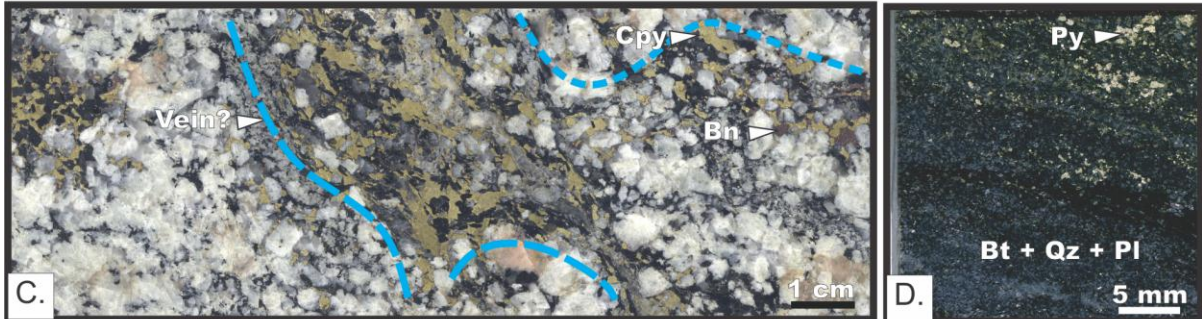
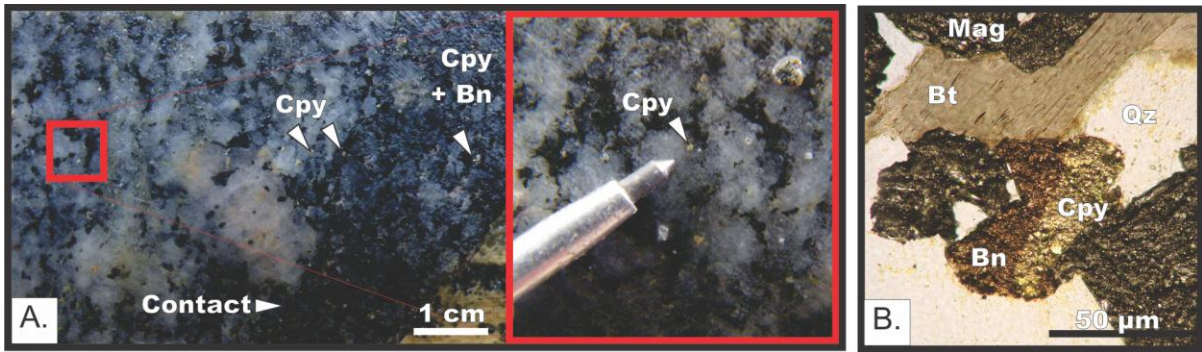


Figure 12: Photographs and photomicrographs of hypogene mineral assemblages related to sulphide mineralization. A. Fine to medium grained chalcopyrite and/or bornite is the most common and widespread mineralization style at Minto. Mineralization tends to terminate abruptly at structural contacts, although millimeter-scale blebs of chalcopyrite and bornite were observed within massive rocks up to several centimetres from contacts (inset). B. Micrograph of contact between chalcopyrite, bornite, biotite, and magnetite showing sharp intermineral boundaries. Plane polarized plus incident light. Sample SBH-C042B-B. C. Photograph of chalcopyrite with minor bornite occurring as coarse grained blebs coincident with medium-coarse grained biotite-magnetite alteration. Sulphides are also present as disseminated fine grains throughout the rest of the sample. Sample SBH-C039. D. Pyrite at Minto is relatively uncommon compared to chalcopyrite and bornite. Pyrite may occur alone or with chalcopyrite, generally correlated with biotite alteration. Sample H510-276. E. Quartz vein with coarse grained chalcopyrite-bornite and epidote-hematite along margins. Quartz veins are uncommon at Minto and are not obviously correlated to mineralization. F. Folded and boudinaged zone of silicified rock hosting disseminated chalcopyrite-bornite-magnetite. Siliceous Cu-sulphide zones are associated with chalcopyrite-bornite rich regions and strong biotite-magnetite alteration. G. SEM backscatter micrograph of Ca-Mn-Fe garnet with rounded chalcopyrite inclusions. Magnetite is also a common inclusion in these garnets. Sample H587-233. H. Chalcopyrite overprinting fractured Ca-Mn-Fe garnet. Sample H510-276. I. Disseminated molybdenite overprinted by propylitic alteration, manifested as chloritization of biotite and pervasive pink hematite staining of plagioclase. The molybdenite in this sample was dated at 197.4 (+/- 0.8) Ma using Re-Os geochronology and is discussed in the Geochronology section of this thesis. Sample H429-153. J. Weakly deformed molybdenite with inclusions of chalcopyrite. Molybdenite at Minto appears to post-date Cu-sulphide mineralization. Micrograph taken under reflected light. Sample 08SH-C028.

Minor molybdenite was observed in drill core across the Minto deposit as fine- to coarse-grained blebs. Molybdenite was most commonly disseminated within granitoid host-rocks (Figure 12I), although it was also observed as hosted within quartz-gypsum veins or quartzofeldspathic dikelets. Regardless of the mineralization style, molybdenite consistently crosscut bornite, chalcopyrite (Figure 12J), and pyrite, and is in turn overprinted by propylitic alteration. Three samples for Re-Os geochronology were chosen from across the deposit and are described further in 2.4.5, Geochronology.

Based on copper, gold, and silver assays from the across the Minto deposit, hypogene mineralisation appears to be approximately collinear (Figure 13). Whether this relationship between elements is due from co-genetic precipitation or from multiple overprinting mineralisation events was not determined, but the relationship indicates copper grade as a useful proxy for gold and silver when mapping mineralisation.

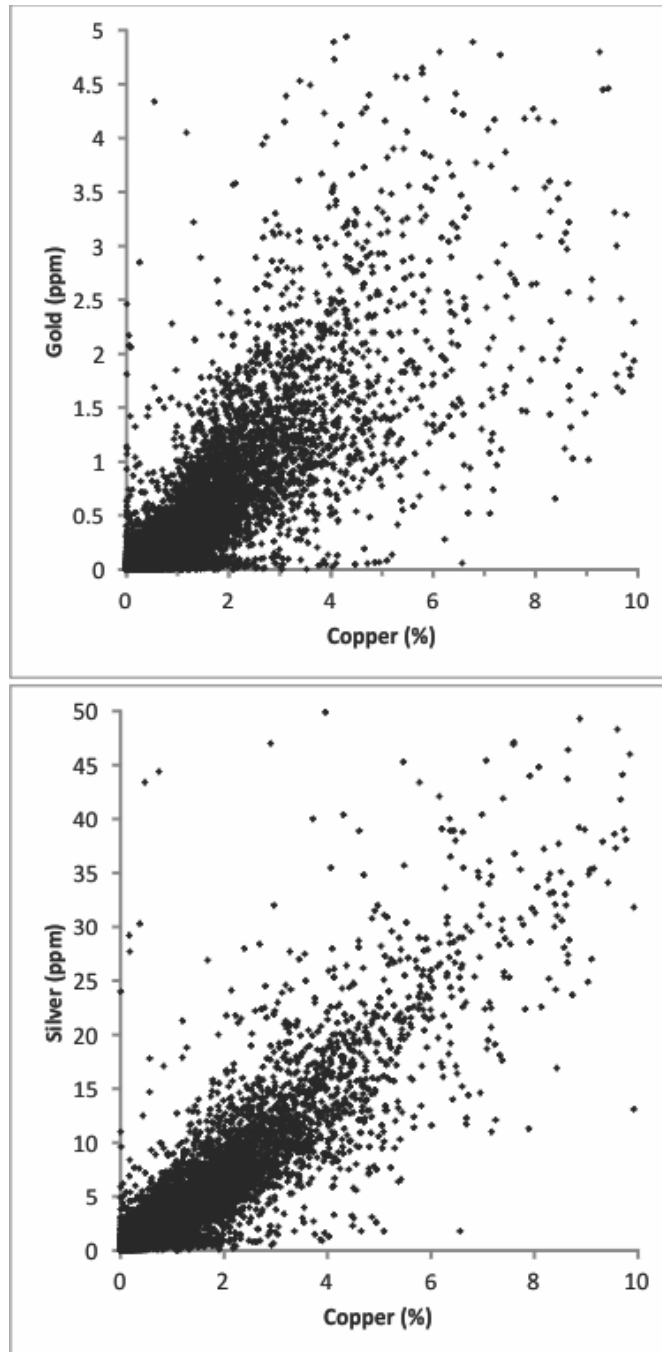


Figure 13: Plots of metal tenor using company geochemical data (Captone Resources dataset, unpublished) suggest an approximately linear correlation between Cu and Au (A.), and Cu and Ag (B.), making copper a useful proxy for other economic metals at Minto when mapping or creating cross sections. Data has been filtered in an attempt to show only assays where hypogene mineralization is present. Intervals have removed where metals are not present and when the ratio between Cu NS (non-sulphide hosted copper) and Cu is greater than 0.15, i.e., zones of supergene enrichment.

2.3.2 Alteration Assemblages

Potassic alteration is the most common alteration type present at Minto. It is largely defined by secondary biotite and magnetite. This potassic alteration is present in essentially all foliated granitoids and may constitute up to 10-25% of the rock, usually as anastomosing folia (Figure 12A) but locally as foliation parallel veinlets (Figure 14A). Biotite crystals range in size from sub-millimetre to several millimetres and shows sharp crystal faces with euhedral to subhedral fine- to medium- grained magnetite (Figure 14B). Quartz associated with biotite-magnetite occurs as siliceous zones. Chalcopyrite + bornite can comprise up to 10% of these zones, magnetite and biotite up to 1%, with minor plagioclase also present.

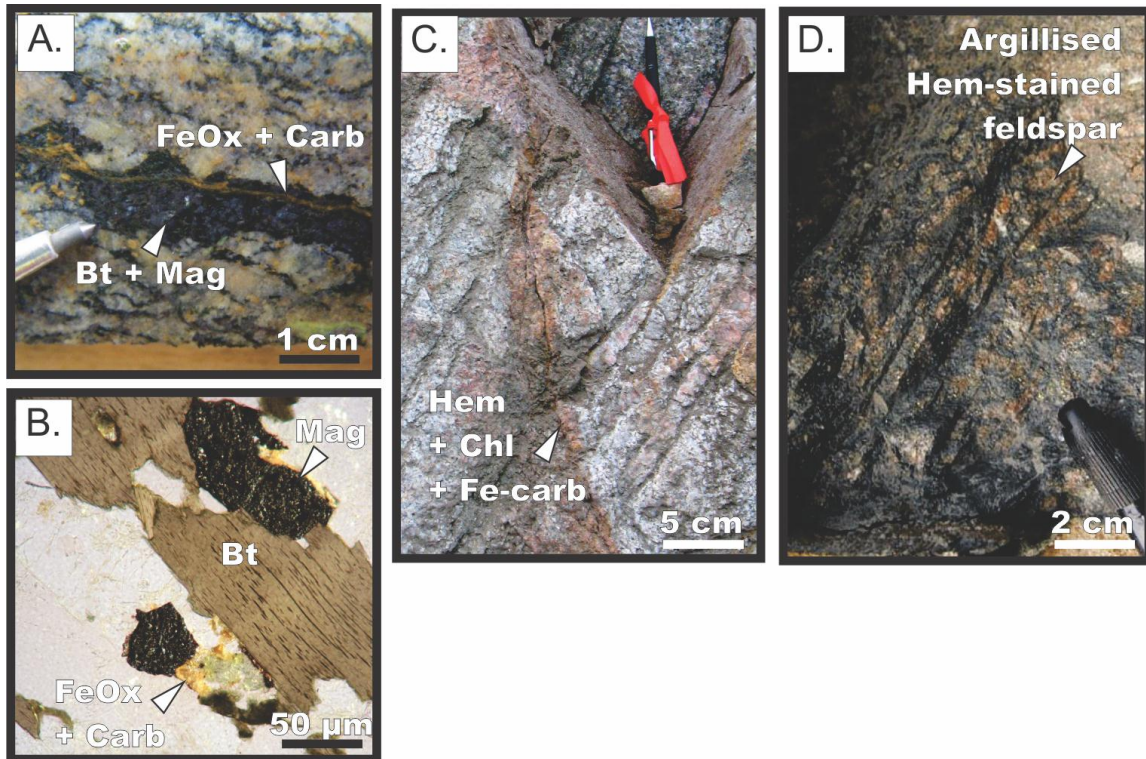


Figure 14: Photomicrographs showing selected alteration assemblages. A. Foliation parallel veinlet of biotite-magnetite alteration crosscut by veinlet of iron oxide-carbonate. B. Biotite-magnetite alteration showing sharp contacts between phases. Sample SBH-C100-C. C. Fracture controlled propylitic alteration (marked with a white arrow). Pink selvage is hematite-stained plagioclase. Biotite and hornblende within selvage margin are altered to chlorite. D. Pervasive propylitic alteration consisting of chlorite-hematite-Fe carbonate assemblage crosscutting copper sulphides and controlled by brittle deformation.

Secondary magnetite within potassically altered zones increases the magnetic volume susceptibility of rocks, typically to the hundreds of kappa (dimensionless SI units of $\text{Am}^{-1} / \text{Am}^{-1} \cdot 10^{-3}$) range. In contrast, a typical magnetic volume susceptibility measurement for KGd is between 0 and 5 kappa. Thus magnetic-susceptibility is a useful quantitative proxy for the degree of potassic alteration.

Relatively late propylitic alteration is widely distributed across the Minto deposit and is characterized by chlorite +/- epidote +/- calcite +/- hematite dusting of feldspars +/- fine hematite veining. Hornblende and/or biotite are variably converted to chlorite +/- epidote +/- titanite +/- hematite +/- pyrite. Hematite dusting of plagioclase is extremely common, and the resulting pink to pink-orange colouration may lead to easy misidentification as K-feldspar. Propylitic alteration is controlled by fractures, i.e., joints and microfractures. The scale and pervasiveness of this alteration ranges from micrometre sized intergranular fluid pathways, to millimetre/centimetre selvages along fractures (Figure 14C), to several metres of pervasive alteration (Figure 14D). Fractures crosscut massive KGd, shear zones, shear zone boundaries, and igneous contacts. An earlier stage of propylitic alteration has locally been crosscut by later granodiorite intrusions (Figure 8B). Crosscutting and intergranular carbonate veining is present throughout the Minto deposit. Habit ranges from intra-biotite grain infill to <0.25 - 1 mm veins. Crystals are blocky, equigranular, and polygonal up 0.2 mm, to equigranular fine-grained anhedral crystals 10 μm . Rarely, both phenotypes of crystal are present in a vein, finer-grained crystals being restricted to one margin of the vein and grading to coarser size. Veins tend to be oriented parallel to foliation in foliated zones, and in various sub-parallel orientations oblique to foliated/non-foliated contacts in massive granitoids. Fine-grained sericite is locally developed with plagioclase and ranges in intensity from weak to nearly

complete. Moderately to strongly saussuritized plagioclase appears blue-green in hand specimen. Epidote veining was observed in all igneous rocktypes. Veins range from sub-millimetre to several millimetres. “Bleached” selvages are common, possibly due to argillization of plagioclase, and contain chloritized biotite/hornblende and hematite dusting of plagioclase. Minor pyrite was locally observed within the margins of the vein.

Late supergene alteration has locally altered Cu-sulphides to chalcocite, tenorite, malachite, and azurite. This alteration has produced economic supergene mineralisation in areas of Minto, but is not discussed further in this text.

2.3.3 Evaluating Mass Transfer

The nature and scale of mass transfer associated with Cu-Au mineralisation was evaluated using whole rock litho-geochemistry on a suite of mineralized foliated to massive non-mineralized and non-altered granitoids from across the Minto property. Questions to be examined include whether the foliated-mineralized rocks could be derived from the massive units through progressive foliation development and hydrothermal alteration/metasomatism, whether mineral assemblages interpreted as hydrothermal could have indeed arisen from mass addition or mass subtraction, whether there has been mass increase or decrease in altered rocks, and whether there is a variation in mass transfer patterns between samples representing different ore mineralogy.

2.3.3.1 Analytical Techniques

Thirty-eight samples were collected from regional outcrops, pit benches, and drill core for whole-rock geochemical analyses of major, trace, and rare earth elements (Figure 15). Samples represent a variety of Minto granitoids and include examples of massive, variously deformed, and variously altered rocks. All samples were trimmed using a rotary saw to

minimize the effects of weathering and were analysed at Activation Laboratories Ltd. in Ancaster, Ontario. Fusion inductively coupled plasma (FUS-ICP) was used for the following elements and oxides: SiO₂, Al₂O₃, Fe₂O₃ (T), MnO, MgO, CaO, Na₂O, K₂O, TiO₂, P₂O₅, Sc, Be, V, Sr, Ba. Fusion mass spectroscopy (FUS-MS) was used for the following elements: Cr, Co, Ni, Cu, Zn, Ga, Ge, As, Rb, Y, Zr, Nb, Mo, Ag, In, Sn, Sb, Cs, La, Ce, Pr, Nd, Sm, Eu, Gd, Tb, Dy, Ho, Er, Tm, Yb, Lu, Hf, Ta, W, Tl, Pb, Bi, Th, U. Instrumental Neutron Activation Analysis (INAA) was used for the following elements: Au, As, Br, Cr, Ir, Sc, Se, Sb. Finally, percent copper was measured using Inductively Coupled Plasma Optical Emission Spectroscopy (ICP-OES). Geochemical results are presented in (Table 3).

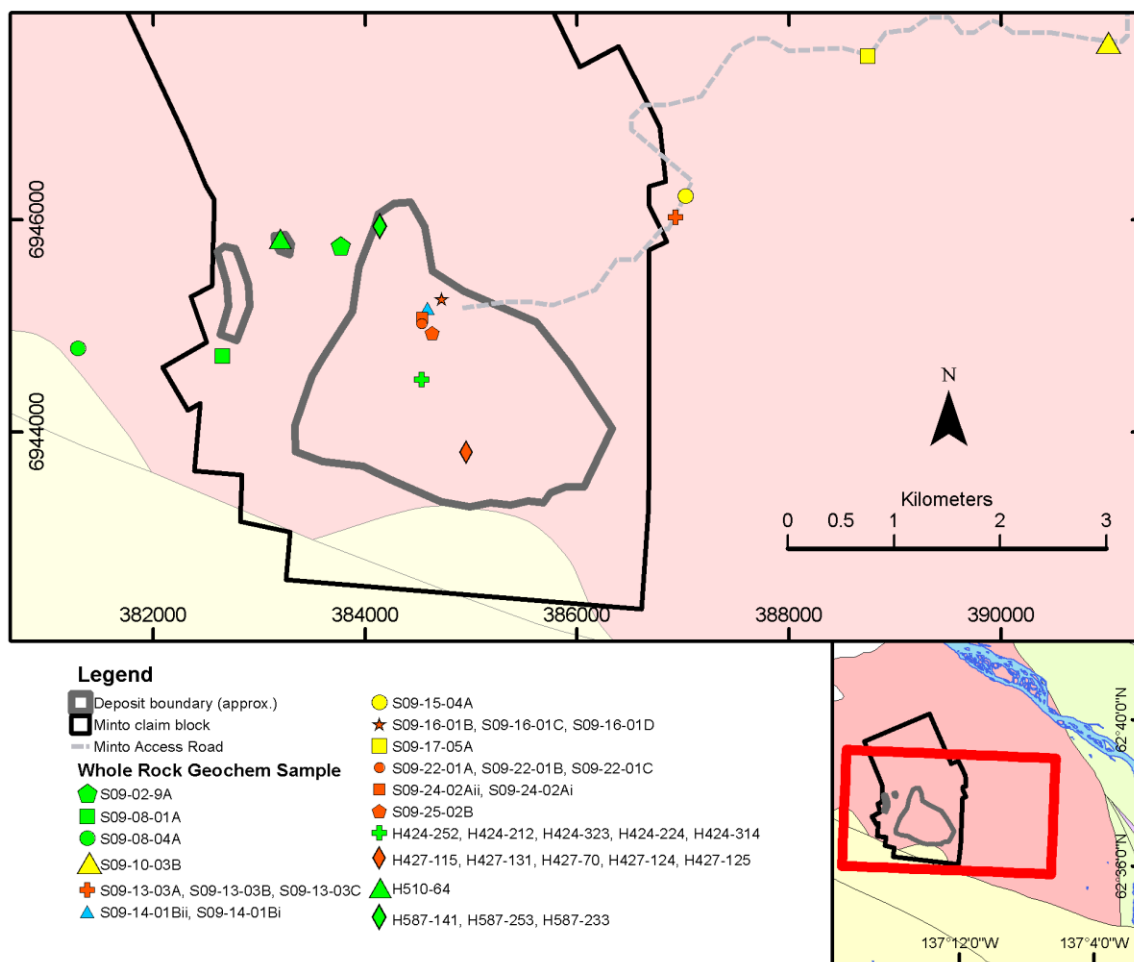


Figure 15: Location of regional and drillhole samples selected for geochemical comparison. Transect A-A' geochemical samples overlaid on orthophoto of the Minto deposit. Base photo sourced from Capstone Resources database.

Table 3: Lithogeochemical sample information from samples collected during 2009 field season. Geochemical data listed in Appendix D . KGd = K-feldspar granodiorite, Tlt = tonalite, BGn = banded gneiss, unk = unknown, Bt = biotite, Mag = magnetite, Cpy = chalcopyrite, Bn = bornite, Py = pyrite, Gnt = garnet, Qtz = quartz, Si = silicification, Weath = weathered.

Sample	UTM E	UTM N	Elev	Lith	Def'd	Alteration
H424-212	384531	6944491		KGd	No	NA
H424-224	384531	6944491		KGd	Typical	Bt, Mag, Cpy
H424-252	384531	6944491		KGd	No	NA
H424-314	384531	6944491		KGd	Typical	Bt, Mag, Cpy, Bn
H424-323	384531	6944491		KGd	No	NA
H427-115	384956	6943813		KGd	Typical	Bt, Mag, Cpy
H427-124	384956	6943813		KGd	No	NA
H427-125	384956	6943813		KGd	Typical	Bt, Mag, Cpy, Py
H427-131	384956	6943813		KGd	No	NA
H427-70	384956	6943813		KGd	Typical	Bt, Mag, Cpy, Bn
H510-64	383202	6945821		KGd	No	NA
H587-141	384141	6945938		KGd	No	NA
H587-233	384141	6945938		KGd	Typical	Bt, Cpy, Gnt
H587-253	384141	6945938		KGd	No	NA
S09-02-9A	383776	6945758	960	KGd	No	NA
S09-08-01A	382654	6944715	1007	KGd	No	NA
S09-08-04A	381289	6944784	884	KGd	No	NA
S09-10-03B	391014	6947669	625	KGd	No	NA
S09-13-03A	386926	6946023	760	KGd	No	NA
S09-13-03B	386926	6946023	760	KGd	No	NA
S09-13-03C	386926	6946023	760	KGd	No	NA
S09-14-01Bi	384590	6945165	730	KGd	BGn	Qtz vein? Si, Bt, Mag, Cpy, Bn
S09-14-01Bii	384590	6945165	730	KGd	Def	Bt, Mag, Si, Cpy, Bn
S09-15-04A	387024	6946222	767	KGd	No	NA
S09-16-01A	384724	6945250	825	KGd	BGn	Weath. Bt, Mag, Cpy, Bn, Si
S09-16-01B	384724	6945250	825	KGd	No	NA
S09-16-01C	384724	6945250	825	KGd	Typical	Bt, Mag, Cpy, Bn
S09-16-01D	384724	6945250	825	KGd	No	NA
S09-17-05A	388739	6947539	747	KGd	No	NA
S09-22-01A	384535	6945018	730	Tlt	BGn	Bt, Mag, Cpy, Bn
S09-22-01B	384535	6945018	730	KGd	unk	Bt, Mag, Cpy, Bn
S09-22-01C	384535	6945018	730	KGd	No	NA
S09-24-02Ai	384539	6945075	730	Tlt	unk	Bt, Mag, Cpy, Bn
S09-24-02Aii	384539	6945075	730	Tlt	unk	Qtz vein? Si, Bt, Mag, Cpy, Bn
S09-25-02B	384633	6944928	730	KGd	BGn	Bt, Mag, Cpy, Bn

2.3.3.2 Isocon Plots

Whole rock geochemical data only show relative changes in bulk rock chemistry (Gresens, 1967). For example, a rock that has been extremely enriched in SiO_2 during deformation will show much larger concentrations of all other elements relative to its protolith. This can be corrected by normalizing element concentrations to the inferred immobile elements in the protolith. Some elements can be essentially immobile during deformation and alteration depending on factors such as fluid composition, host rock composition, and deformation environment (e.g., Streit and Cox, 2002).

Gresens (1967) designed a mathematical method to estimate changes in rock volume and concentrations of elements during metasomatism. In Gresens' (1967) method the likely immobile components during alteration are used to identify any volume change associated with the alteration. If it is assumed that volume change is a factor common to the behavior of all components, it is possible to calculate gains or losses of the other components. Mass gains and losses are calculated using the following relationship: $X_n = [F_v(S^b/S^a)C_n^b - C_n^a] \times 100$, where X_n = is the mass gain or loss for component n, F_v is the volume factor, S^b is the specific gravity of the altered sample, S^a is the specific gravity of the unaltered sample (i.e., protolith), C_n^b is the concentration of component n in the altered sample, and C_n^a is the concentration of component n in the unaltered sample.

Grant (1986) presented a mathematically similar graphical method to solve Gresens' (1967) equation called the isocon method. A review of the isocon method was published by Grant (2005) and is applied in this thesis. The isocon method uses a plot of the geochemical composition of an altered rock against that of its protolith. In the ideal case, immobile elements will define a straight line through the origin, the isocon, defined by: $C^A =$

$(M^0/M^A)C^0$, where C^A is the element concentration in the altered rock, C^0 the element concentration in the fresh rock, and the slope is defined by the ratio of equivalent masses (M^0/M^A) in the fresh and the altered rock (Grant, 1986). Hence, the slope indicates mass gain (slope > 1) or mass loss (slope < 1) during alteration of the protolith.

Three suites of KGd and altered KGd were selected from drill core and the open pit. Seven samples of KGd in these suites are interpreted as representative least-altered protoliths for adjacent altered rocks. To assess this interpretation these samples were compared to other KGd sampled across the Minto pluton and from a pre-existing study (Tafti, 2005) and all exhibit similar normalized chondrite plots of KGd (Figure 16). KGd from sample suites was then averaged, as per Grant (2005), to reduce the effects of protolith heterogeneity, minor alteration, or weathering effects. This averaged protolith serves as the geochemical baseline for nine samples of deformed sulphide bearing granodiorite with potassic alteration, further subdivided based on sulphide assemblages into bornite-chalcopyrite, chalcopyrite, and chalcopyrite-pyrite groups.

Elements to be plotted on the isocon diagram were chosen by (i) selecting elements that appear to be least mobile based on plots of elements against each other (Figure 17), and (ii) elements characteristic of the main mineral assemblages described above. Element values were then scaled as described by Grant (2005) to best produce a clear representation of the data, i.e., elements with small values will plot close to the origin relative to elements with high concentrations. Grant (1986) selected the isocon by arbitrarily scaling the concentration values for each element so as to obtain a reasonable distribution of the data points on the isocon plot. The slope of the isocon may be determined as described by Grant (2005) from: (a) clustering of C_i^A/C_i^O data, (b) the best fit of data forming a linear array through the origin

on an isocon diagram (the graphical equivalent of the first method), (c) the a priori assumption that certain elements are immobile, (d) the assumption of constant mass during alteration, or (e) the assumption of constant volume during alteration. Certain elements are more commonly more immobile than others (Grant, 1986; O'Hara and Blackburn, 1989; Glazner and Bartley, 1991; Tobisch et al., 1991; Marquer and Burkhard, 1992; Prochaska et al., 1992), however it is necessary to confirm relative immobility on a case by case basis. High field strength elements (HFSE) like Al_2O_3 , TiO_2 , Zr and Hf and most REE, like La and Yb, are considered immobile in most hydrothermal systems (e.g. Leitch and Lentz, 1994).

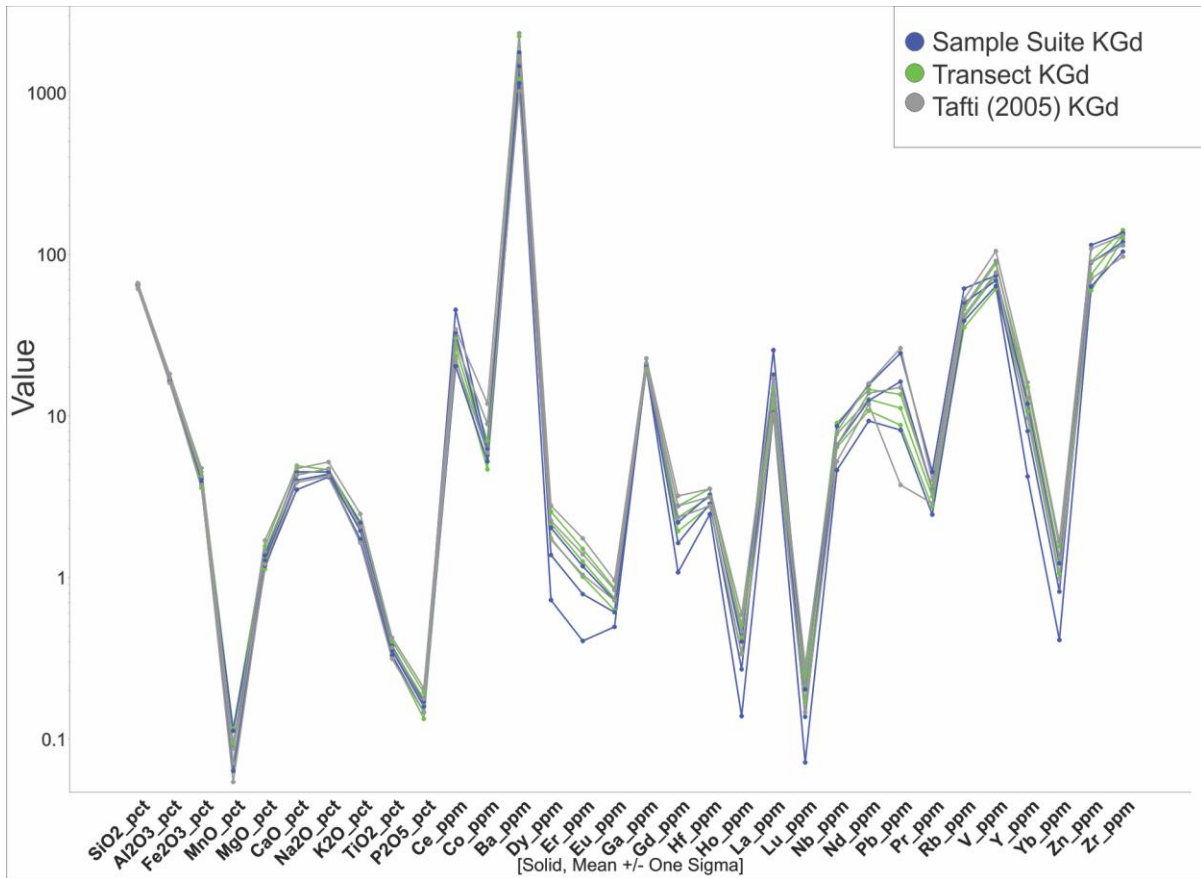


Figure 16: Spider diagrams comparing samples used in isocon study, samples collected regionally, and samples previously analysed by Tafti (2005) showing that the averaged bulk geochemistry of each sample suite is within 1-sigma overlap of one another. This similarity suggests that the averaged protolith suite used for isocon analysis is representative of averaged KGd composition across the Minto pluton even though there is local mineral heterogeneity within the pluton. Element values have been normalized to the CI chondrite values of McDonough and Sun (1995). Blue points represent seven samples of KGd taken proximal to altered samples used for isocon study. Green points represent samples taken from across an east-west transect of the Minto pluton. Grey points represent thirteen samples taken from unpublished thesis data (Tafti, 2005) and represent a mix of fresh and weathered rocks.

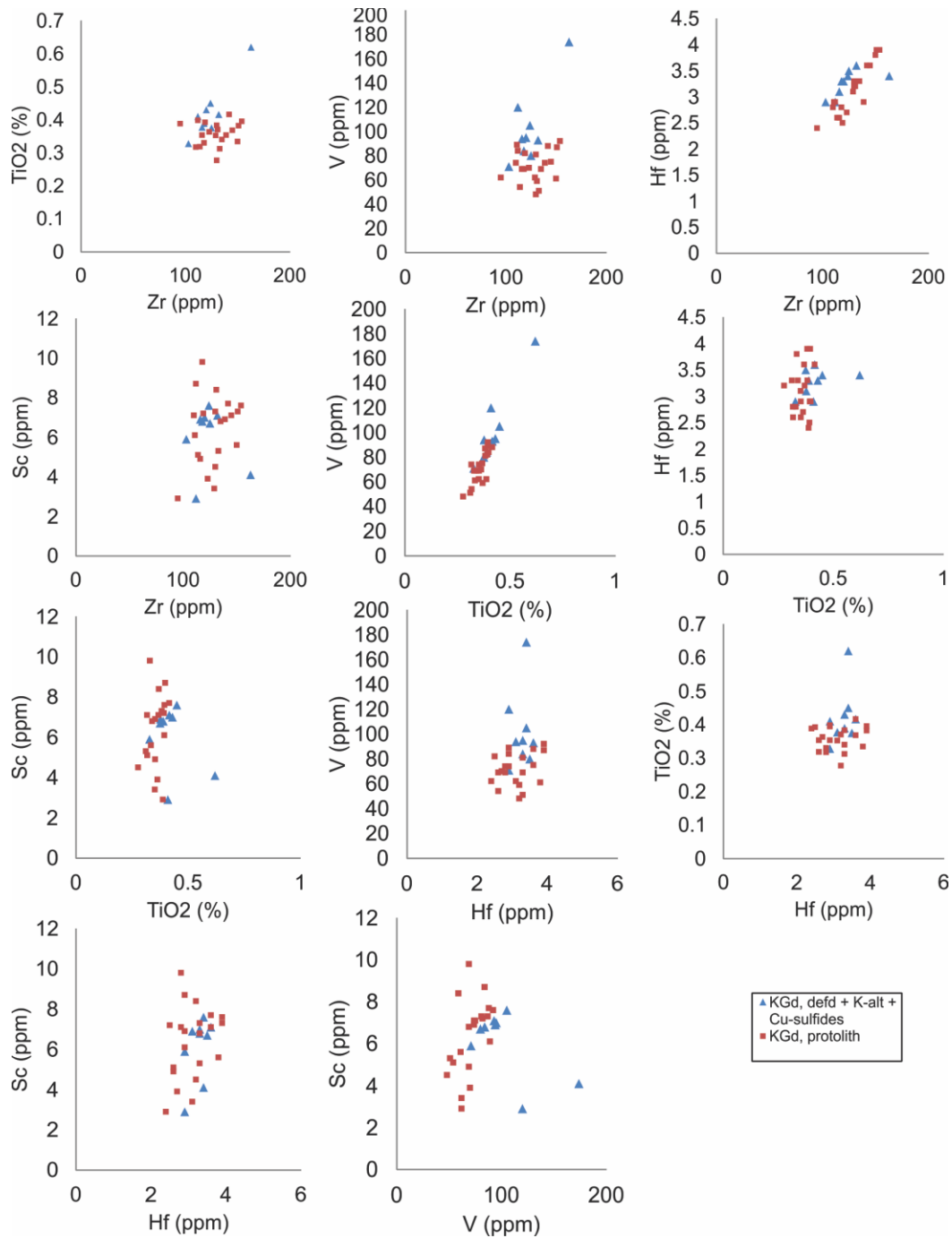


Figure 17: Plots for altered and protolith samples of KGd, measured using whole rock lithochemistry (Table 2), were plotted with Ti, Hf, Zr, and V being interpreted as the most likely candidates for immobility during alteration/deformation. Assessment of immobility is based on elements with consistent relative abundances in the protoliths and altered/deformed rocks plot as clusters or overlapping linear trends (after Finlow-Bates and Stumpfl, 1981). Analytical uncertainties are given in Appendix D

For this study, concentrations of elements in protolith and biotite-magnetite-sulphide samples were plotted against each other to determine potential immobility (Figure 17, following Finlow-Bates and Stumpfl 1981), with Hf, Zr, V, and Ti emerging as the most likely candidates. These elements then served as the basis for an isocon, with results shown in Figure 18. Elements that have been enriched plot above the isocon, and those that have been depleted plot below the isocon. For the Cu-sulphide, biotite-magnetite bearing granodiorites in this study, K_2O , Fe_2O_3 , P_2O_3 , U, Th, and Pb appear to have been added. Depleted elements include SiO_2 , Al_2O_3 , CaO, Na_2O , and Sr. The addition of K and reduction of Na and Ca in these samples is consistent with literature involving potassically altered rocks (Giggenbach, 1984). Mn generally appears to have been depleted from these rocks, although one sample containing Mn-rich garnet plots above the isocon. The remaining plotted elements MgO, Pb, Lu, Gd, Sc, Ce, and La plot both above and below the isocon. This may be due to variation of these elements in the protolith or varying enrichment or depletion in the samples.

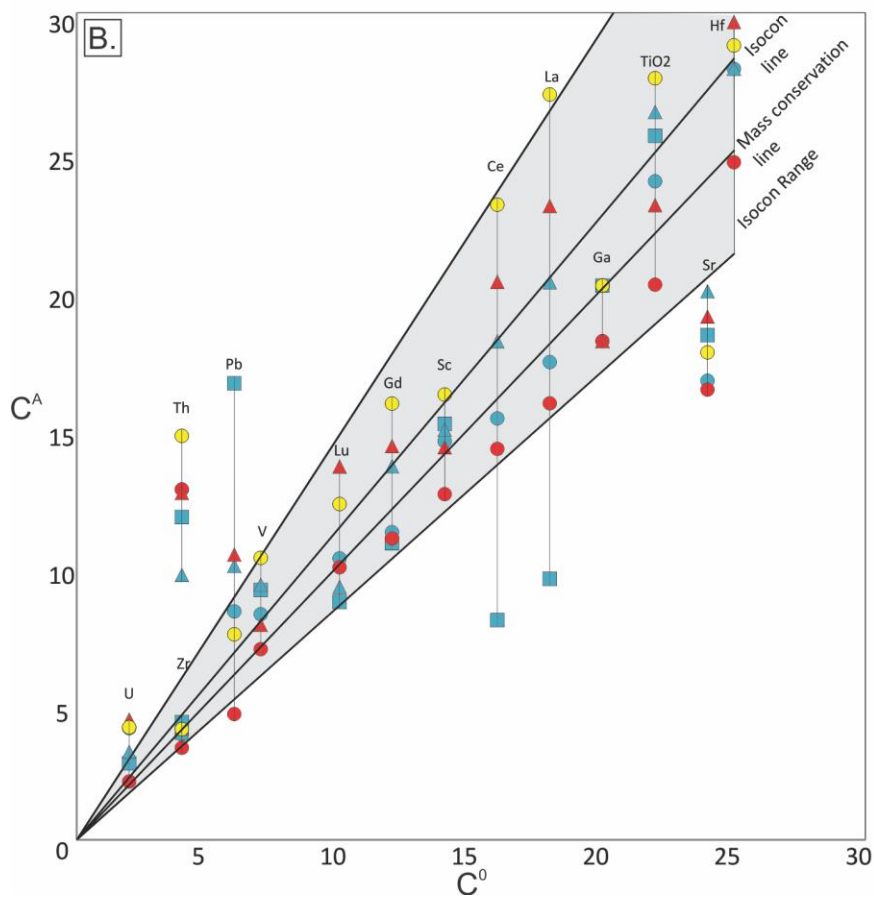
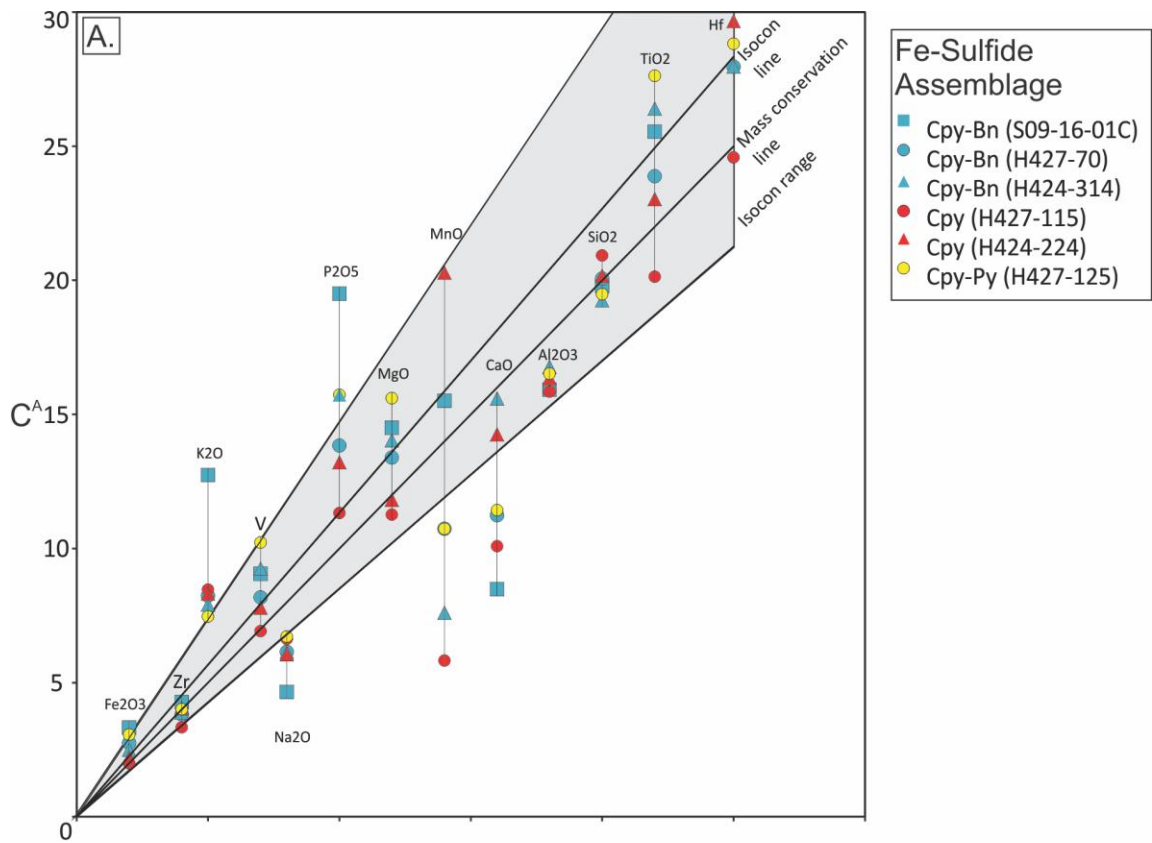


Figure 18: Isocon diagram illustrating relative enrichment and depletion of major element oxide (wt %) and trace element (ppm) concentrations in the Minto Granodiorite. X-axis = representative least altered sample averaged from twenty-one samples of least-altered KGd, Y-axis = altered sample. Altered samples are all deformed versions of KGd with sulphide mineralization plus magnetite-biotite (potassic) alteration. Data are scaled for portrayal as described by Grant (2005). The mass conservation line has slope = 1 and is a reference isocon indicating equal concentrations in least altered and altered rock. Isocon line is a reference isocon assuming Ti, Hf, Zr, and V have been immobile during alteration (Grant, 1986; O'Hara and Blackburn, 1989; Glazner and Bartley, 1991; Tobisch et al., 1991; Marquer and Burkhard, 1992; Prochaska et al., 1992). Data above this line may represent element enrichment, and data below this line may represent element depletion to least-altered rock. The grey zone is bounded by the greatest spread of immobile element values and represents the spread of potential isocon slope error due to element heterogeneity in the least-altered sample.

There has been debate about the most accurate method for isocon placement, e.g., fitting by eye (Grant, 1986, 2005), least-squared regression (Baumgartner and Olsen, 1995), or error bars (Baumgartner and Olsen, 1995). This debate is centered around the difficulty in choosing an accurate isocon due to natural variation, e.g., heterogeneity of immobile elements amongst samples of a protolith. This effect is pronounced when examining granitoid rocks, where minerals may be fractionated within rocks although overall geochemistry is similar. Immobile elements in this study do vary within the protolith, illustrated by points not plotting in the same position. A conservative interpretation of what elements have been enriched or depleted may be made if an “isocon region” is constructed by including the area covered by the greatest spread in immobile element concentrations. In theory, any elements plotting above or below the isocon region show variation due to mass transfer to an extent greater than any variation inherent to the protoliths. In this case it appears that K_2O and Th have definitely been added to rocks, while Na_2O and Sr have definitely been depleted.

2.4 Structural Geology

The Minto pluton comprises multiple intrusive phases as observed through cross-cutting relationships between granitoids and granitoid dikes. Magmatic flow fabrics are common and developed heterogeneously within granitoids through the pluton. In addition, all granitoids show fabrics indicating solid state deformation, varying from incipient recrystallization microtextures to the development of mylonitic foliations. This ductile deformation is concentrated into discrete shear zones coincident with hypogene Cu-Au-Ag mineralisation and associated alteration.

At least two varieties of rock fabric are recognized within Minto granodiorites and represent end members of fabric development: magmatic fabrics (discussed in Section 2.2.2) and solid-state recrystallization fabrics. Purely magmatic fabrics are developed within intrusive rocks above the solidus, e.g., dimensional-preferred orientation of K-feldspar megacrysts in KGd as the result of non-hydrostatic stress in flowing magma (Vernon and Paterson, 2008). Magmatic fabrics involve the rotation and/or settling of crystals in a melt matrix, and filter pressing of melt from between crystals, however these physical processes are only possible where the melt to crystal fraction is high; above 60-80% crystals it is difficult to rotate crystals and magmatic foliation can be “frozen in”.

Interpreting the relative timing between pluton crystallization and regional deformation is a complex problem because of the changing rheology of magma as it crystallizes, and because of the incomplete understanding of the range of fabric development created during the transition from magma to crystalline solid and during emplacement (e.g., Paterson, 1989). For example, crystallization dynamics and related igneous fabrics have been modeled for magma chambers where regional stress is absent (e.g., Bea, 2010), although it is widely

believed that regional deformation is a common factor during pluton emplacement (e.g., Brown and Solar, 1998).

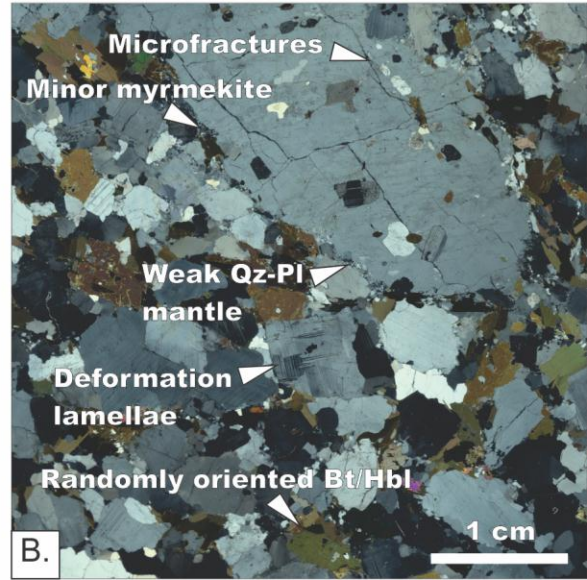
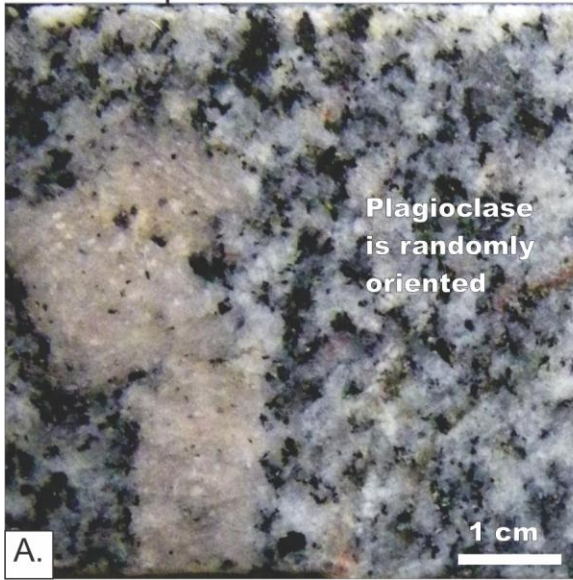
2.4.1 Solid State Microstructures

The most prominent structural feature of host rocks at Minto is a typically shallow dipping (0° - 30°) penetrative solid state foliation (S_P) that occurs in discrete shear zones bounded by granitoids that appear massive in hand specimen. The intensity of solid state deformation and the associated development of the S_P foliation grades out from the shear zones into the relatively non-deformed massive granitoids. This gradient in strain intensity is largely unaffected by any overprinting penetrative deformation and provides a spatial analogue for progressive foliation development. The gradient in the intensity of S_P has been divided into four stages on the basis of relative degrees of solid state recrystallization of quartz, plagioclase, and K-feldspar. The four levels of deformation are (i) incipient deformation, (ii) weak foliation, (iii) typical penetrative foliation, and (iv) mylonitic, i.e., highly deformed.

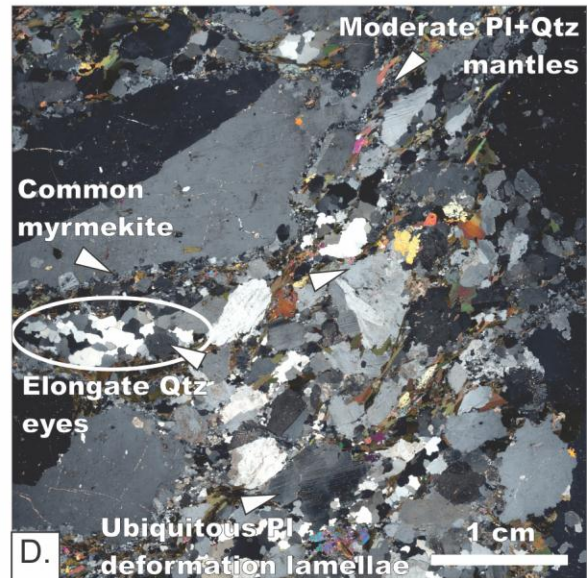
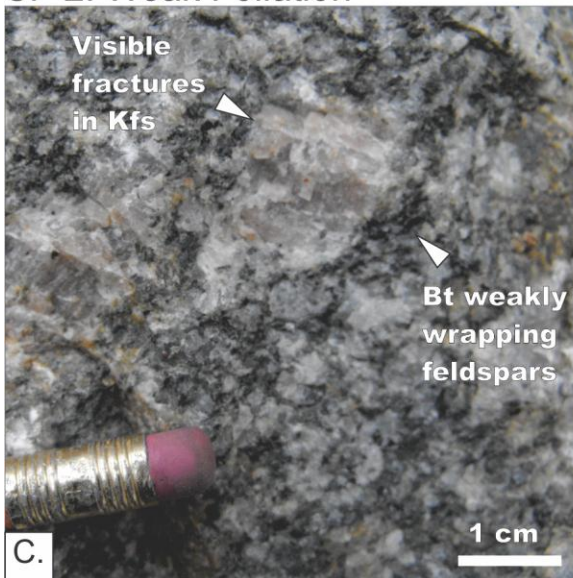
2.4.1.1 Stage 1: Incipient Deformation

“Massive” granitoids that make up much of the Minto pluton are incipiently deformed and exhibit textures indicative of intracrystalline deformation and recovery/recrystallization that overprint primary igneous textures. These textures, though visible in thin section, are not evident in hand specimen (Figure 19A and B). K-feldspar, plagioclase, quartz, and biotite, all have textures indicative of incipient solid state deformation, including deformation lamellae and twins, grain boundary bulges, and marginal K-feldspar myrmekite development (Simpson and Wintsch, 1989).

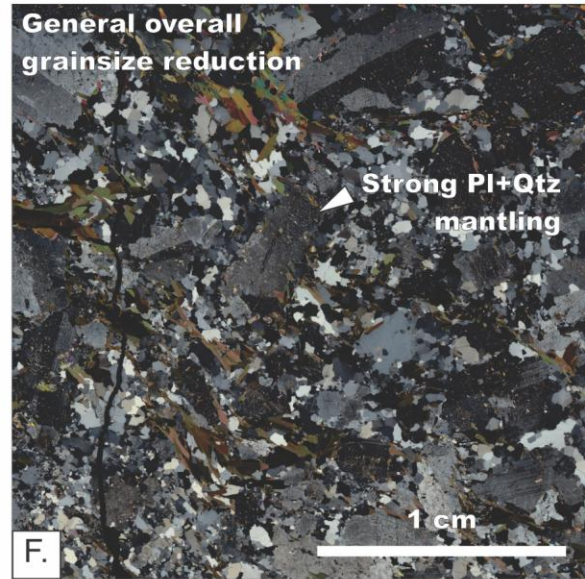
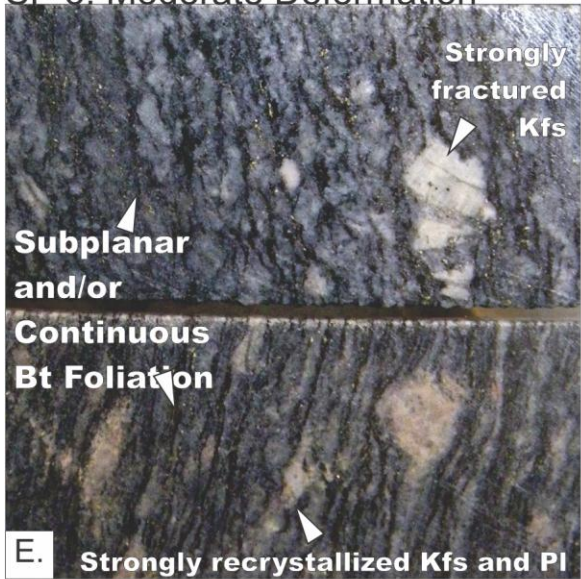
SP 1: Incipient Deformation



SP 2: Weak Foliation



SP 3: Moderate Deformation



SP 4: Strong Deformation

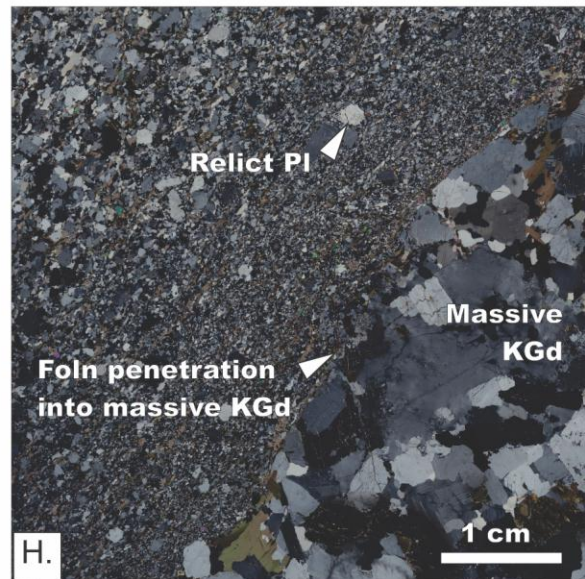
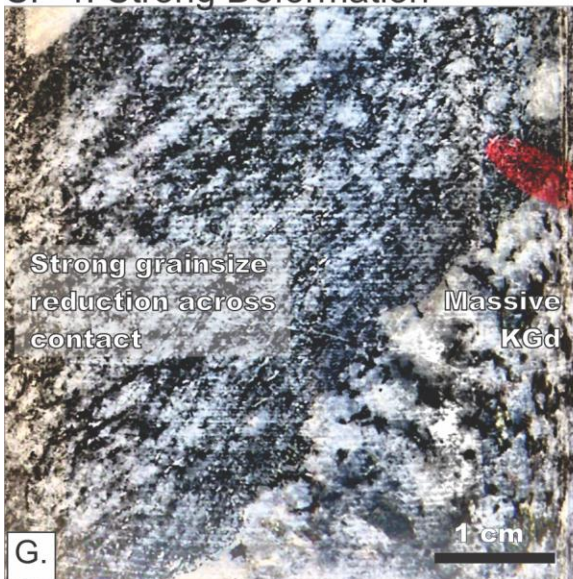


Figure 19: Photographs showing hand samples of deformed KGd where grainsize is progressively less. Thin sections show an increasing amount of deformation textures with decreasing grain size. A. Incipient deformation is not observable in KGd at hand specimen scale. B. Minor solid-state recrystallization microtextures characterize incipient deformation and are evidence of strain accommodated by the Minto pluton as a whole. Microtextures include the beginning of core-and-mantle textures, minor myrmekite

development along K-feldspar margins, slight undulose extinction in quartz and feldspars, and tapered lamellae in plagioclase slightly overprinting growth lamellae. C. Weakly deformed KGd exhibits discontinuous and disjunctive biotite foliation that anastomoses around feldspar grains. K-feldspar is commonly fractured. Quartz may form flattened masses, especially where quartz eyes are present. D. In thin section weak deformation is also exemplified by moderate myrmekite development along K-feldspar margins. Minor recrystallization of quartz and plagioclase creates fine-grained mantles of recrystallized material around cores of larger relict feldspars. E. Moderately deformed KGd is the most common structural unit at Minto. Ductile deformation textures are more strongly developed and relict internal igneous textures in igneous minerals are rare. Quartz and plagioclase have undergone significant grain size reduction. Quartz and plagioclase exhibit solid state intracrystalline deformation textures with weak lenticular shapes aligned with S_p , whereas K-feldspar tends to experience grain size reduction by fracture first, then ductile deformation. G. and H. Strongly deformed KGd sharing a structural contact with incipiently deformed KGd, defined by an abrupt reduction in grain size. Deformation intensity is highest near the contact, and the deformation zone partially penetrates massive rock. Very fine grained chalcopyrite and magnetite are present in the high strain zone but not in the incipiently deformed rock.

2.4.1.2 Stage 2: Weak Foliation

As the intensity of S_P progresses, solid state deformation fabrics are more pronounced and become visible in hand specimen (Figure 19C and D). Stage 2 deformation is considered to begin when structural fabrics are recognizable in the field. In this stage biotite becomes progressively aligned into discontinuous to continuous anastomosing folia. Marginal recrystallization of plagioclase and quartz into the foliation plane gives these porphyroclasts a slightly lenticular shape. K-feldspar is commonly fringed by fine-grained myrmekite and crosscut by parallel, “domino” style, fractures oblique to the surrounding foliation. Quartz eyes are recrystallized to quartz ribbons that become progressively flatter in tandem with more strongly developed solid state deformation microstructures described above. Fine-grained plagioclase and quartz mantle larger plagioclase and K-feldspar grains creating a core-and-mantle texture. Undulose extinction within quartz and biotite is also more common, and the boundaries between these minerals are more undulatory.

2.4.1.3 Stage 3: Well Developed Penetrative Foliation (S_P)

Progressive foliation development eventually leads to the near total recrystallization and variable degrees of grain size reduction of all the primary igneous minerals (Figure 19E and F). This stage is considered to begin where deformation, i.e., S_P , is readily measurable in the field. K-feldspar augens, representing relict K-feldspar megacrysts, are typically similar in grain size to plagioclase and quartz grains and deform entirely by recrystallization. This may be due to previous grain size reduction by brittle fracture to a point at which recovery and recrystallization can relieve internal strain energy at the strain rate and temperature conditions of the shear zone (e.g., Vernon et al., 1983). Additionally, hydrothermal fluids channelled through the deformation zones may hydrolytically weaken K-feldspar (Yund and

Tullis, 1980; Tullis and Yund, 1985). Plagioclase and quartz also deform ductilely, and grain boundaries are increasingly undulatory with prominent grain boundary bulge development. Biotite is progressively more aligned, resulting in more continuous folia, and anastomoses feldspar rich microlithons. Unlike feldspars and quartz, the grain size of biotite does not appreciably decrease at this stage. Individual grains within foliation are not necessarily foliation parallel, and extinction angles also vary. The degree of biotite foliation development is linked to its relative abundance, and it should be noted that rocks with abundant hydrothermal biotite are preferentially deformed. Interestingly, hornblende was not observed in deformed rocks, suggesting that deformation zones are coincident with zones of hydrothermal alteration and that hornblende is no longer stable.

2.4.1.4 Stage 4: Mylonitic Foliation

Mylonitic foliation is developed both within larger deformation zones and crosscutting otherwise massive granitoids. This stage is separated from previously described stages based on abrupt strain transitions juxtaposing very fine-grained mylonite with more coarsely grained rocks, and by the consistent grain size reduction of bulk minerals (Figure 19G and H), typically quartz, feldspars, epidote, and magnetite. Deformation microtextures are identical to those in S_p , i.e., textures arising from solid state recrystallization of constituent minerals. This is consistent with interpretations by Hickey and Bell (1996) that mylonitic foliations represent a final metastable grain size substantially smaller than that in less highly strained rocks.

Mylonitic zones are present as bands up to several centimetres in scale. These zones are generally within larger, less deformed zones and parallel to the adjacent foliation. Less commonly mylonite foliation was observed to crosscut massive of deformed granitoids at

moderate to steep orientation. In otherwise massive host rocks, grain size reduction of original mineralogy is significant. Small zones of steeply oriented (50° - 80°) mylonitic zones crosscut massive and deformed granitoids. When cutting deformed zones, S_P is rotated into the overprinting zone of mylonitic foliation. Disseminated and deformed magnetite and sulphide minerals, including chalcopyrite and bornite, are common in mylonite zones, including mylonitic zones crosscutting massive unmineralized granitoids.

2.4.2 **Gneissic Banding**

Granitoid gneisses (Figure 20) exhibit compositional layering of light bands of dominantly quartz +/- hematite-stained plagioclase +/- K-feldspar, and dark bands comprising dominantly quartz +/- magnetite +/- biotite. Chalcopyrite and bornite are common accessory minerals in the rock, mainly within dark bands, and are either disseminated or variously deformed. Zones of this banded rock occur bounded by massive KGd, as discrete zones within larger zones of deformed KGd, and as small zones sharing gradational contacts with surrounding deformed KGd. These banded rocks are interpreted as a product of deformation overprinting KGd, where the host has been altered and likely intruded by felsic dikelets, as shown in Figure 5. Compositional segregation and a well developed foliation observed at hand specimen scale suggest banded rocks are equivalent to Stage 3, described above. Quartz and plagioclase grains tend to be larger than those in strongly deformed rocks, and all grains are anhedral.

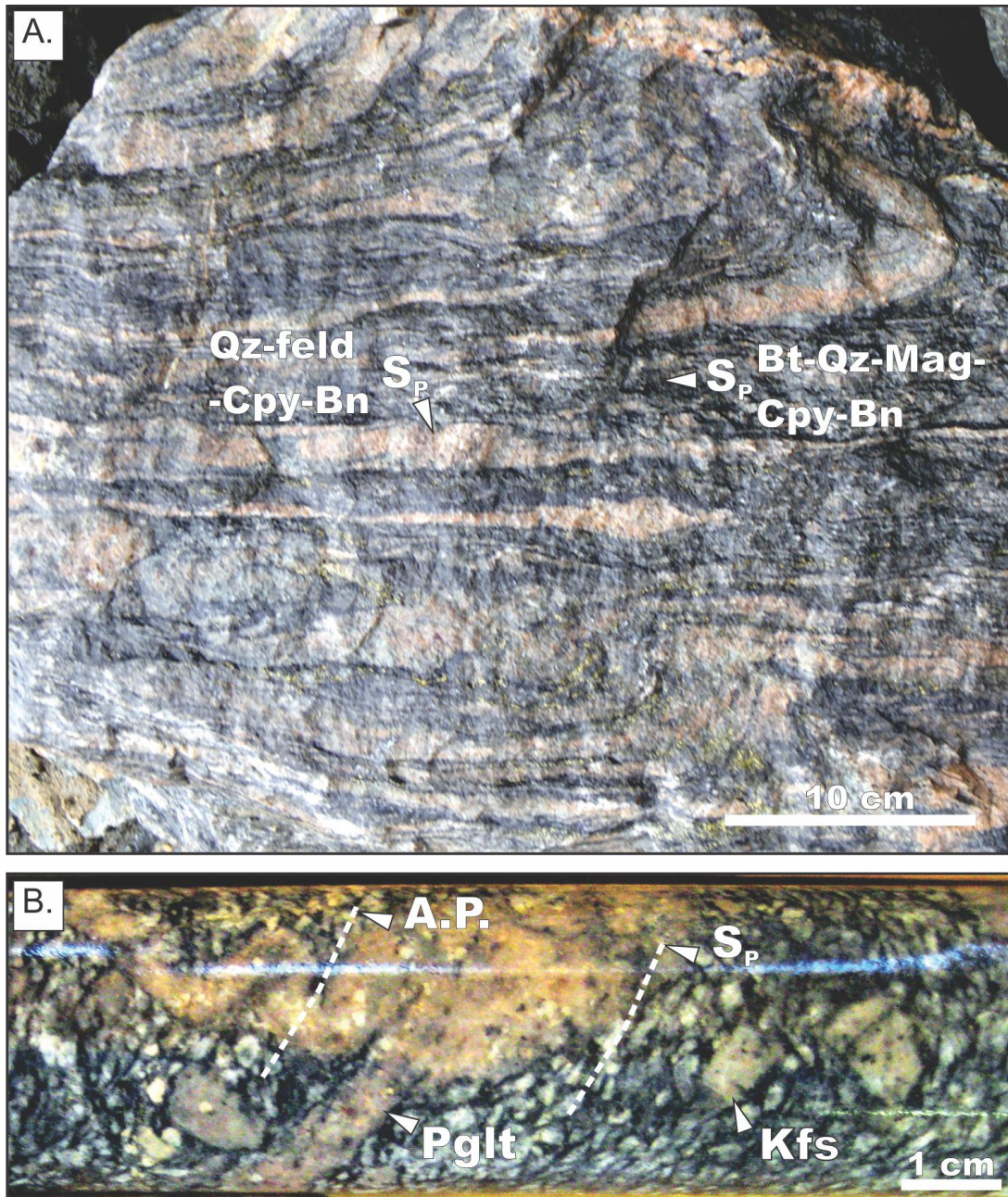


Figure 20: Photographs showing compositional banding in KGd. A. A typical sample of gneissic banding at Minto taken from a high-grade zone in the Minto open pit. S_P is defined by mainly by compositional banding and biotite foliation is minor, in contrast with other deformed rocks. Bands are typically pink and black, composing recrystallized quartz (Qz), plagioclase and K-feldspar (feld), magnetite (Mag), chalcopyrite (Cpy), and bornite (Bn). Feldspar is volumetrically higher in pink bands, whereas quartz, magnetite, and sulphides are dominant within black bands. B. Compositional banding is interpreted as produced by the rotation and folding of pegmatite dikelets (Def'd Pglt) into the plane of the foliation, plus

recrystallization of primary minerals (quartz and feldspar) and secondary alteration minerals (quartz, biotite, magnetite, and sulphides). Folded dikelets have axial planes (AP) parallel to S_p . Gradational boundaries between zones of gneissic banding and variably deformed KGd strongly suggest KGd is the protolith of gneissic zones.

2.4.3 Sulphide Deformation Fabrics

Bornite and chalcopyrite are present as disseminated grains up to several millimeters in diameter, as thin discontinuous veinlets and/or interconnected elongate blebs, and as massive “web” or “net” textures enveloping other minerals. Deformation has variably overprinted sulphides bearing each of these textures.

Chalcopyrite and bornite appear to be ubiquitously deformed at the microscale, with sulphides sharing cusped grain boundaries with internally deformed quartz or feldspar (Figure 21). Ductile deformation and potential re-equilibration and thermal annealing of sulphides, possible at temperatures as low as 100 °C (Brett, 1964; Durazzo and Taylor, 1982), precludes sulphide textures from being useful as indicator of original mineralisation habit.

At hand-scale “web” textures are associated with mineralization in strongly folded rocks (Figure 22A and B), especially within fold hinges. The geometry of cusp structures at hand specimen and larger appears may be approaching boudin necks or mullions, interpreted to form under high-grade metamorphic conditions where sulphides are rheologically much weaker compared to their wall rocks, i.e., formed during layer-parallel shortening where relatively less competent sulphide layer deform into cusps protruding into more competent wall-rocks (e.g., Sokoutis, 1987; Sokoutis, 1990; Talbot and Sokoutis, 1992). Sulphide mullions are common within deformed sulphide deposits, e.g., the Selebi Pikwe Cu-Ni deposit in Botswana (Osterman and Hutchinson, 1994), the Trojan Ni deposit in Zimbabwe (Maiden et al., 1986), the Matchless Cu deposit in South-West Africa (Maiden et al., 1986), and the Broken Hill Ag-Pb-Zn deposit in Australia (Maiden et al., 1986).

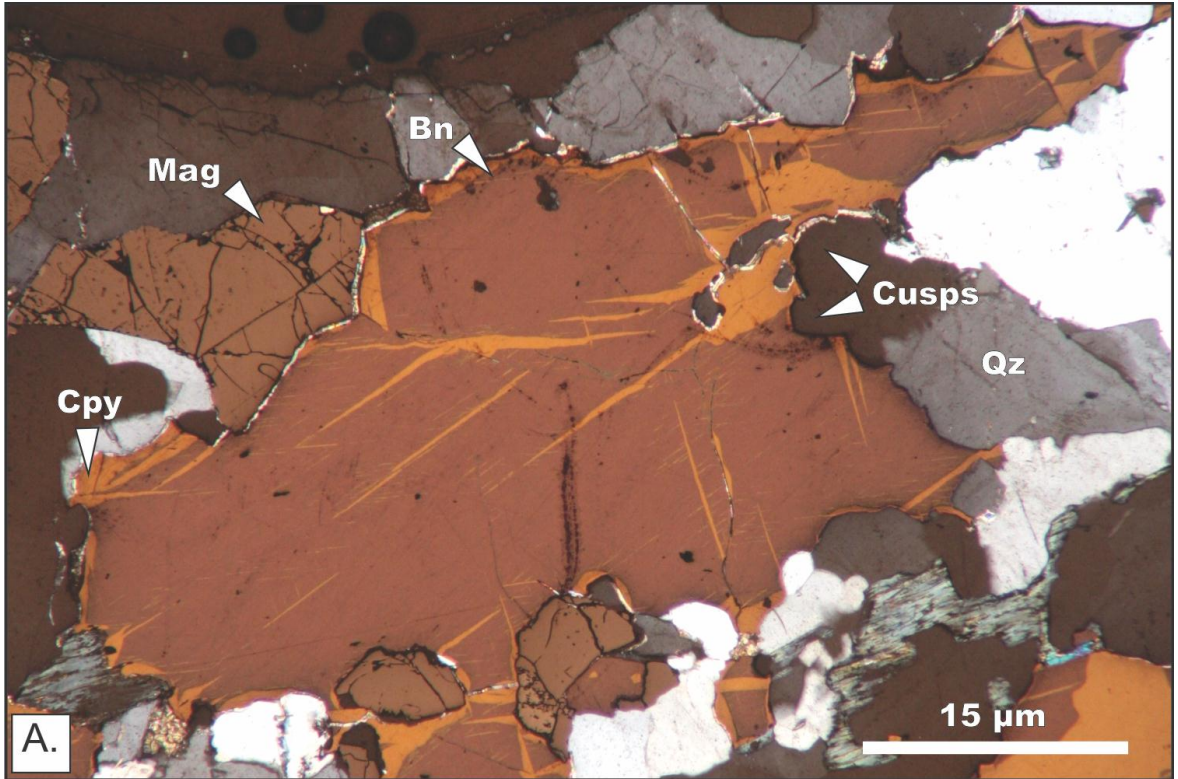


Figure 21: Photomicrograph showing microtextures of typical Cu-sulphide deformation at Minto. Bornite with chalcopyrite exsolution lamellae. Cusped contact with silicates are interpreted as reflecting the deformation of a silicate-sulphide mass where sulphides are less competent than the silicate, producing cusped shapes. Chalcopyrite exsolution lamellae indicate chemical re-equilibration after bornite precipitation, and the sharp, tapered, undeformed texture indicates formation after ductile deformation (Brett, 1964; Durazzo and Taylor, 1982).

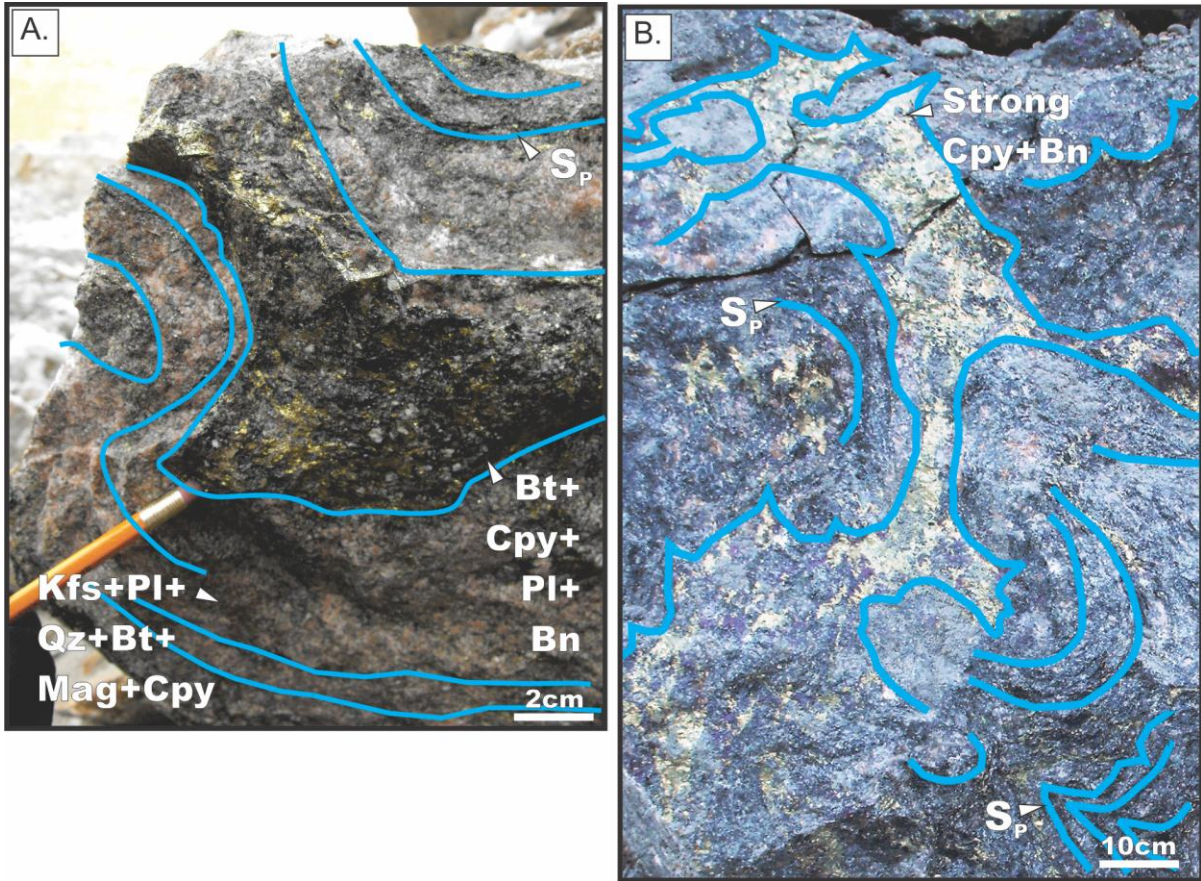


Figure 22: Photomicrograph showing macroscopic deformation of Cu-sulphides at Minto. A. Cu-sulphides are most associated with biotite foliation or quartz alteration, and these regions are observed to deform more readily than surrounding feldspar-rich rocks. Deforming sulphide-rich zones tend to form cusp and lobate structures, essentially analogous to the texture shown in Figure 21. Sulphides within folded deformation zones appear to be enriched within hinges. Hand specimen taken from the Minto pit at 730 m elevation. B. Web or net textured chalcopyrite-bornite mineralization is typical of high grade Cu-sulphide zones at Minto. Remobilisation of sulphides into low strain areas of fold hinges may be responsible for upgrading hydrothermal ore grades. Outcrop is located in the west of the Minto pit at 730 m elevation.

2.4.4 Foliation and Shear Zone Geometry

There is limited outcrop available outside of the Minto pit and much of that is of massive rock due to preferential weathering of foliated rock. Extensive diamond drilling has been performed across the property, but most of it is not oriented. Such core is useful for assessing progressive foliation development but provides limited information on foliation orientation, although the vertical orientation of most of the holes does help to constrain possible foliation orientation. To gain an understanding of the mesoscopic to macroscopic geometry of foliated rocks, accessible pit faces and all natural surface exposure were mapped and structurally assessed. Six oriented drill holes across the property provided some 3D constraints on foliation geometry in the subsurface.

S_P measured from regional outcrop, the open pit, and oriented drill holes indicates that foliation throughout the Minto property dips predominately northeast or southwest, with dip varying from shallow to steep orientation (Figure 23A). However, the orientation of S_P is most likely to be subhorizontal (Figure 23B). S_P is localized into shear zones ranging in scale from millimetres to metres, and with structural contacts grading into massive rock over distances from millimetres to metres (Figure 24A, B, C, D, and E). These structural contacts between massive and deformed rocks are interpreted to arise from partitioned deformation. Structural contacts are through evidence of strain related recrystallization, e.g., abrupt grain size reductions of quartz, plagioclase, K-feldspar, epidote, and biotite (Tullis and Yund, 1985; Ree et al., 2005), tapered deformation twins in plagioclase, myrmekite development in K-feldspar, and lobate to amoeboid quartz and feldspar inter-grain boundaries (Poirier and Guillopé, 1979; Urai et al., 1986).

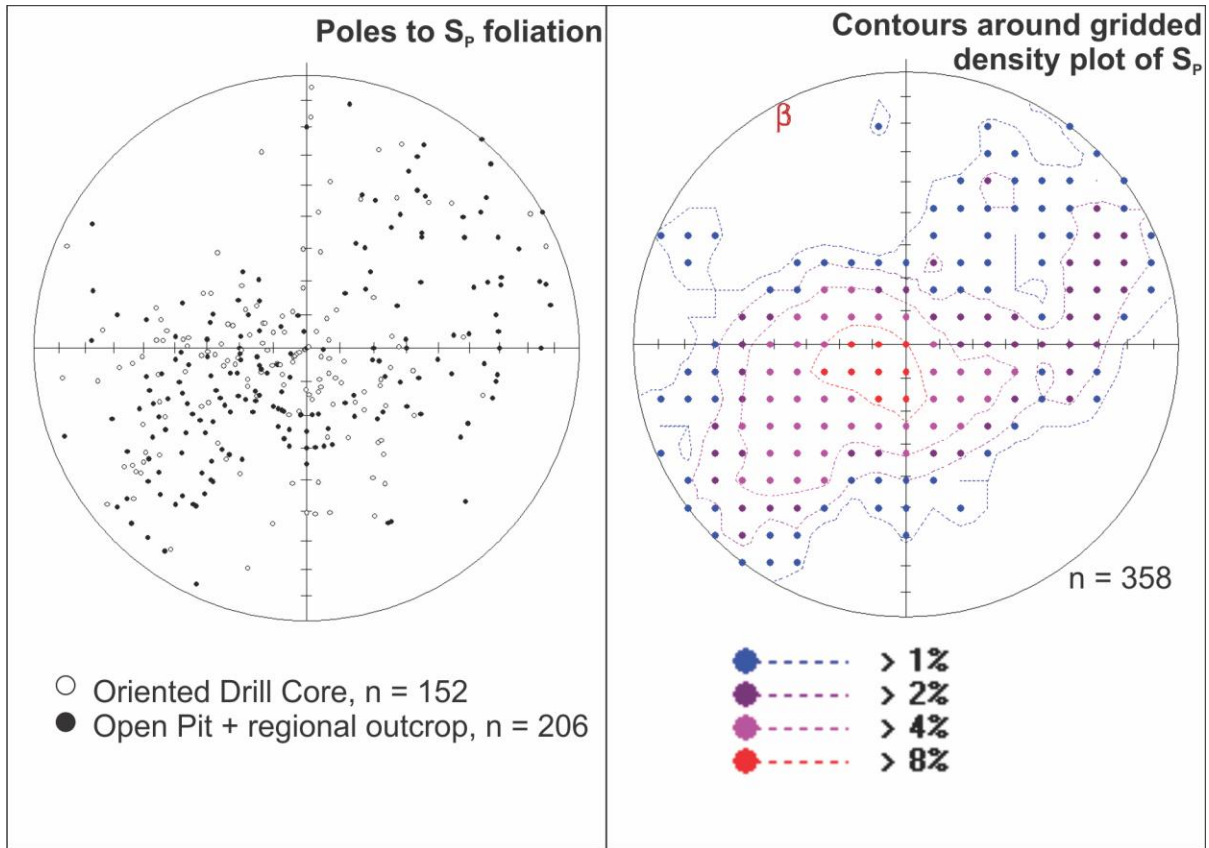


Figure 23: Stereonets depicting S_P foliations measured at Minto. A. Equal area stereonet showing the distribution of S_P measured during study of the Minto deposit. Measurements from outcrop (solid dots) overlap measurements from drillcore (open dots) indicating lateral variation of S_P across the deposit is approximately similar to vertical variation. B. Equal area stereonet with gridded contours representing density of poles to S_P foliation. The dominant cluster of poles in each diagram occurs near the center, representing the high prevalence of shallow foliation. Lesser clusters occur near stereonet margins, representing areas of steeply dipping S_P .

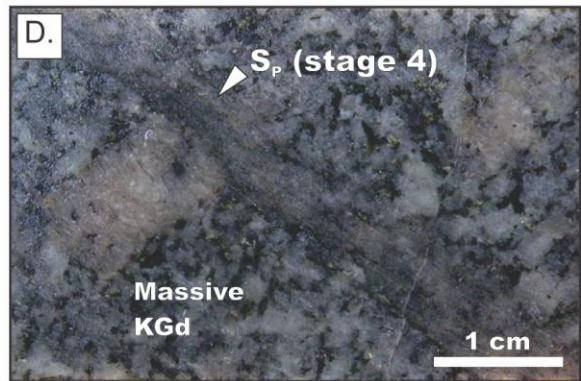
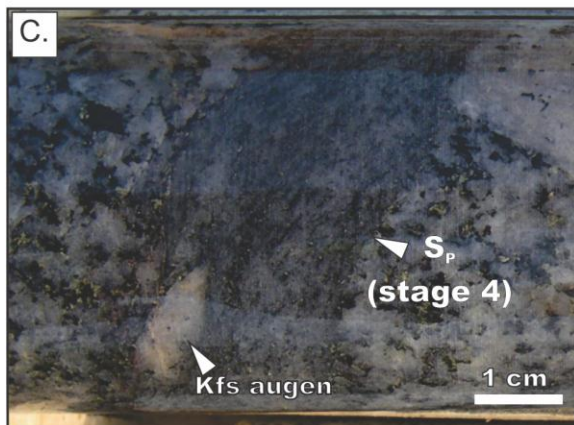
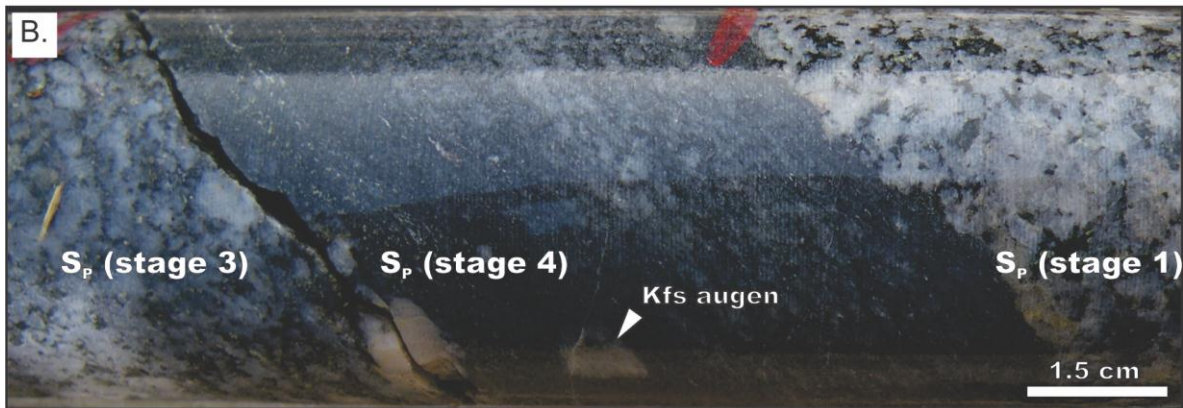
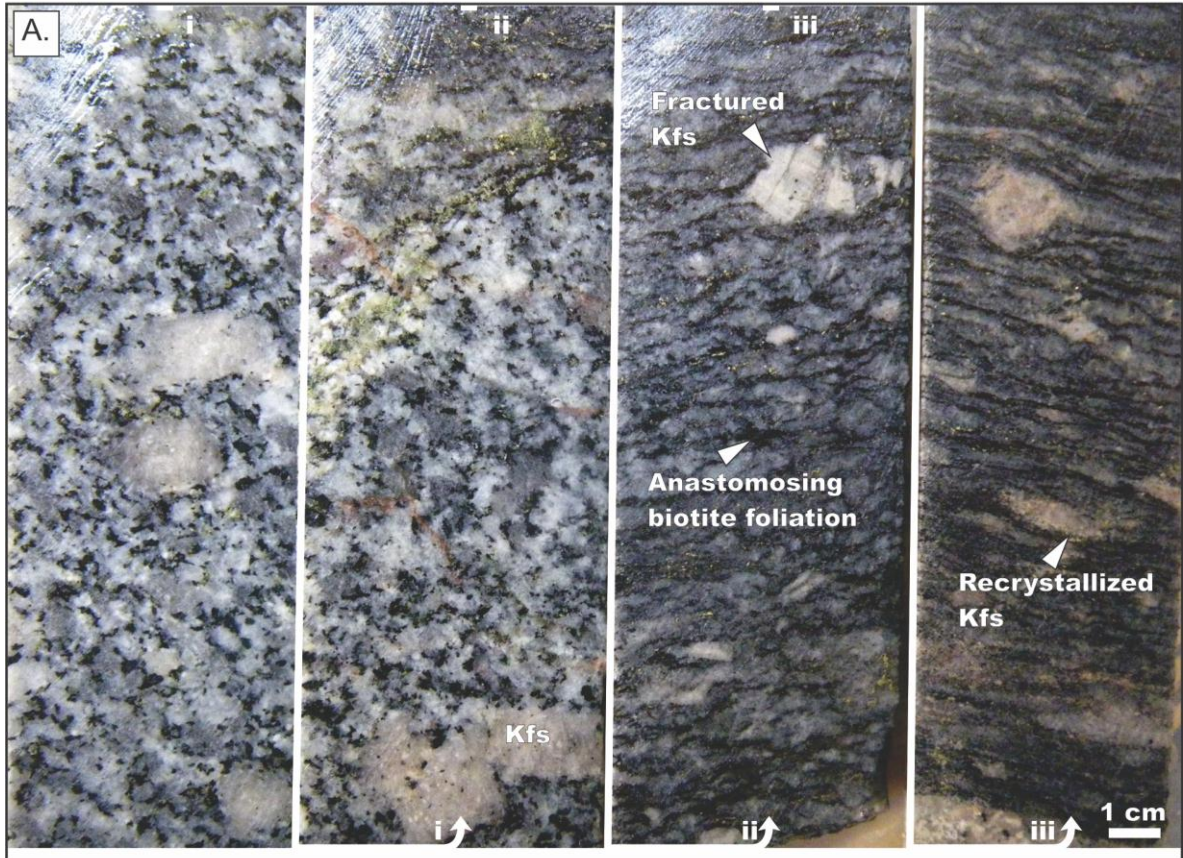


Figure 24: Photomicrographs showing examples of structural contacts in KGd, where fine grained disseminated chalcopyrite is present within deformation zones but not incipiently deformed wallrock. A. Gradational contact showing progressive deformation increasing into shear zone, downhole. Shear zone is metres thick and bounded above and below by massive KGd. B. Sharply bound shear zone at the scale of centimetres crosscutting KGd. Quartz and plagioclase are nearly completely recrystallized, while K-feldspar remains as augens. C. Centimetre scale deformation zone crosscutting massive KGd. D. Millimetre scale shear zone crosscutting large block of KGd.

Core-and-mantle textures of feldspar cores mantled by fine to medium recrystallized quartz are also common at massive-deformed rock contacts, suggesting ongoing grain size reduction played a role in development of S_P foliation (White, 1975; Lister and Price, 1978; Tullis and Yund, 1985). At the scale of millimetres to tens of centimetres, these contacts are generally cusped or penetrative at the expense of massive rocks. In many cases the contact between massive and deformed rocks represents a real strain gradient where deformation has affected a single protolith. However, it is not always possible to discern crosscutting shear zones from granitoid emplaced along pre-existing foliation (as shown in Figure 8C), especially when continued deformation overprints igneous contacts (Figure 25). Recognizing igneous contacts at Minto can be difficult because of ductile deformation fabrics are developed to some extent in all granitoids. A clear example of an igneous relationship occurs when massive intrusions cut pre-existing foliations at high angles, or enclaves of deformed rock occur (Figure 25) in later intrusions. These relationships are observed to be overprinted by macroscopic strain, e.g., S_P foliation, a clear case of deformation overprinting igneous contacts. In situations where magma was emplaced parallel to shear zones, continued deformation will have made it near impossible to recognize the primary intrusive contact. Continued deformation after the development of massive-deformed contacts is also interpreted based on the common cusped geometry between deformed and massive granitoids at Minto at the expense of massive rocks, i.e., piercement of deformed rock into massive rock. This mullion type geometry is especially developed where secondary quartz, biotite, and/or sulphide alteration is strongest.

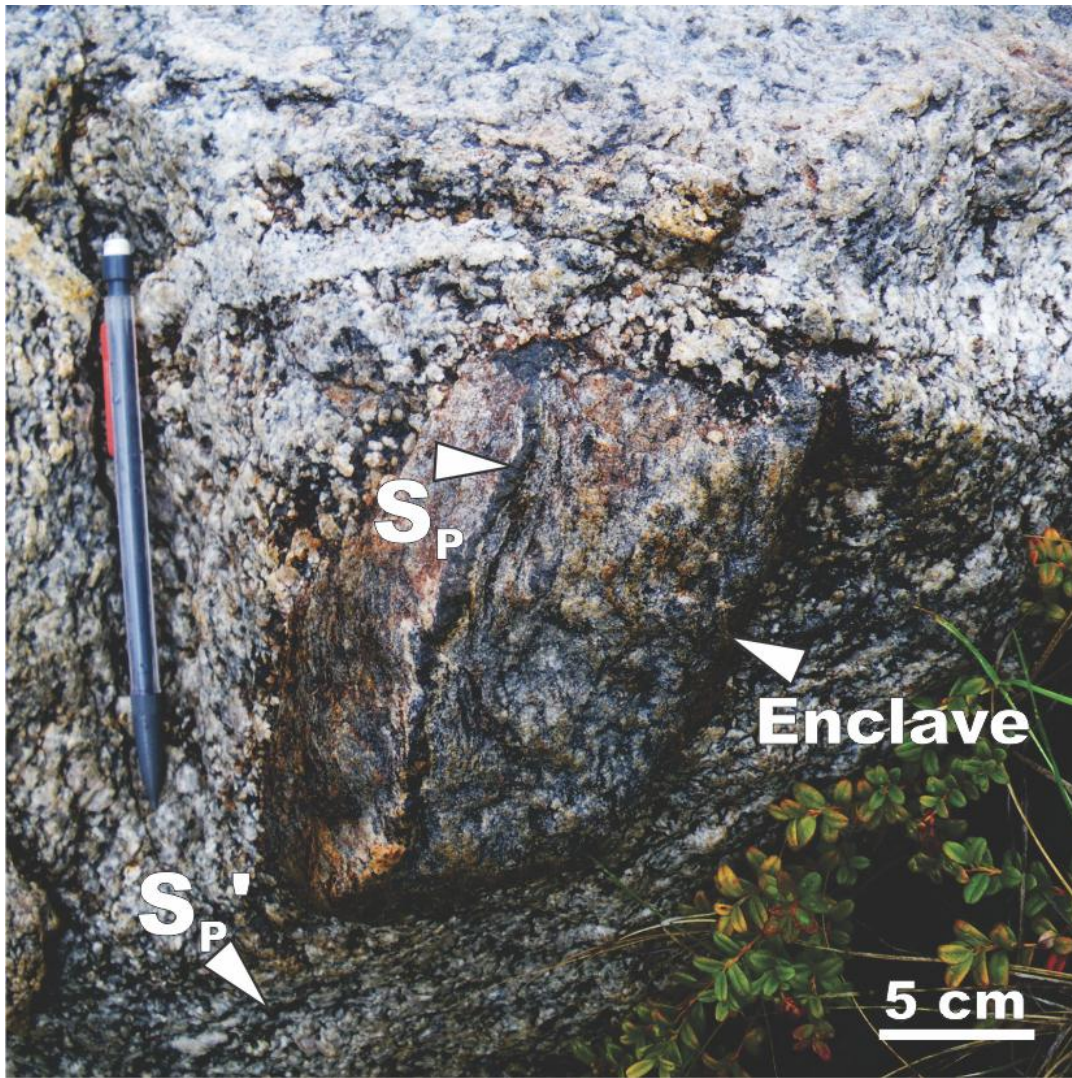


Figure 25: Photo showing S_P fabric developed in a stopped enclave of deformed and magnetite altered KGd. S_P has also developed separately in the younger surrounding KGd, suggesting continuous deformation affecting volumes of magma solidifying at different times, perhaps representing more than one phase of magma emplacement.

These regions are generally the most deformed, next to regions with strongly developed planar fabrics. Cuspate or mullion geometry has been interpreted to arise where a less-rheologically competent rock deforms more readily than its adjacent rock unit (Sokoutis, 1987; Talbot, 1982), and is a feature inherent in metamorphosed sulphide deposits (e.g., Trojan nickel deposit, Matchless copper deposit, and Broken Hill silver-lead-zinc deposit; Maiden et al., 1986; Talbot and Sokoutis, 1992).

The variation of S_P orientation at Minto has been observed predominately in unoriented vertical drillholes, e.g., as shown in Figure 26. The typical observed pattern is of alternating intervals of massive and variably deformed granitoids. The orientation of S_P within deformed intervals is most commonly consistent throughout the interval, approximately parallel to upper and lower contacts with massive rocks. Less common are instances where S_P is truncated at massive contacts, where S_P changes orientation gradually or abruptly within a deformed interval, or where S_P abruptly changes orientation at contacts.

There are several possible geometric interpretations to explain the varying orientation of S_P and the alternating intervals of massive and deformed rock observed in drill core. These explanations are based on observation of episodic igneous activity and ongoing ductile deformation, namely that the observed foliation orientations in drillholes can be explained using mostly structural or mostly igneous processes, although the true nature of the geometry is likely related to interplay between both end members (Figure 27).

Foliation measurements from oriented drillholes and exposure of shear zones in the open pit (Figure 28) support a hypothesis of mainly structural creation, as per Figure 27D. The common metre to tens of metres long intervals of shallowly oriented S_P foliation in drillcore are interpreted as thick, laterally continuous shear zones, as shown in Figure 29A and B.

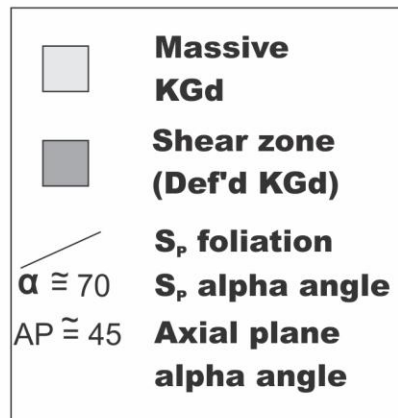
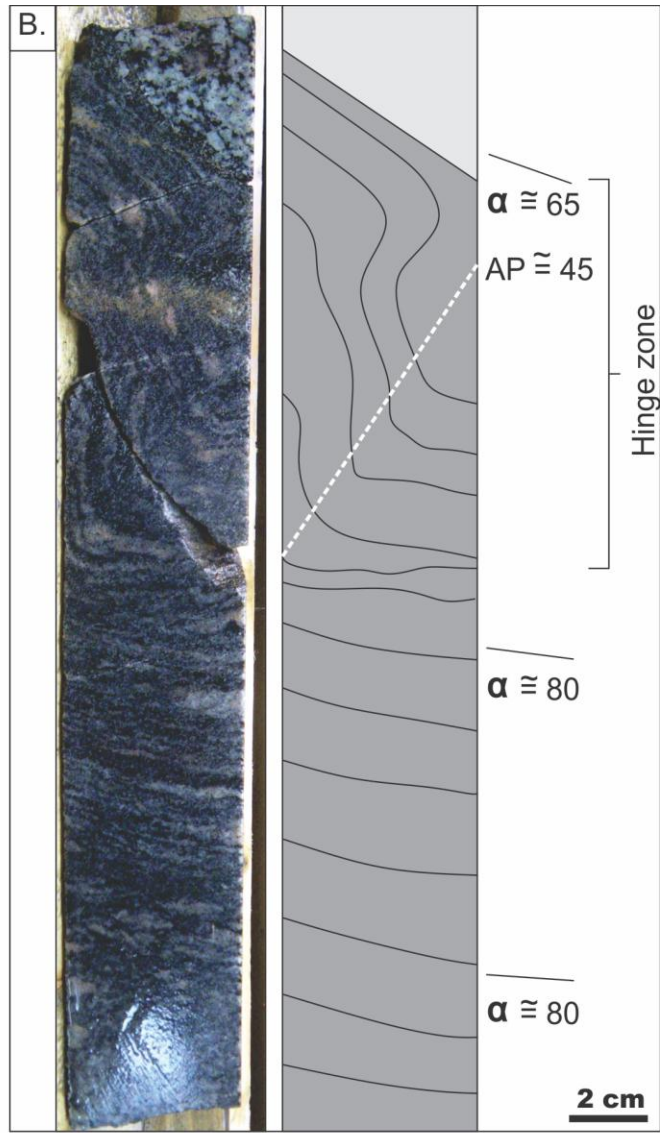
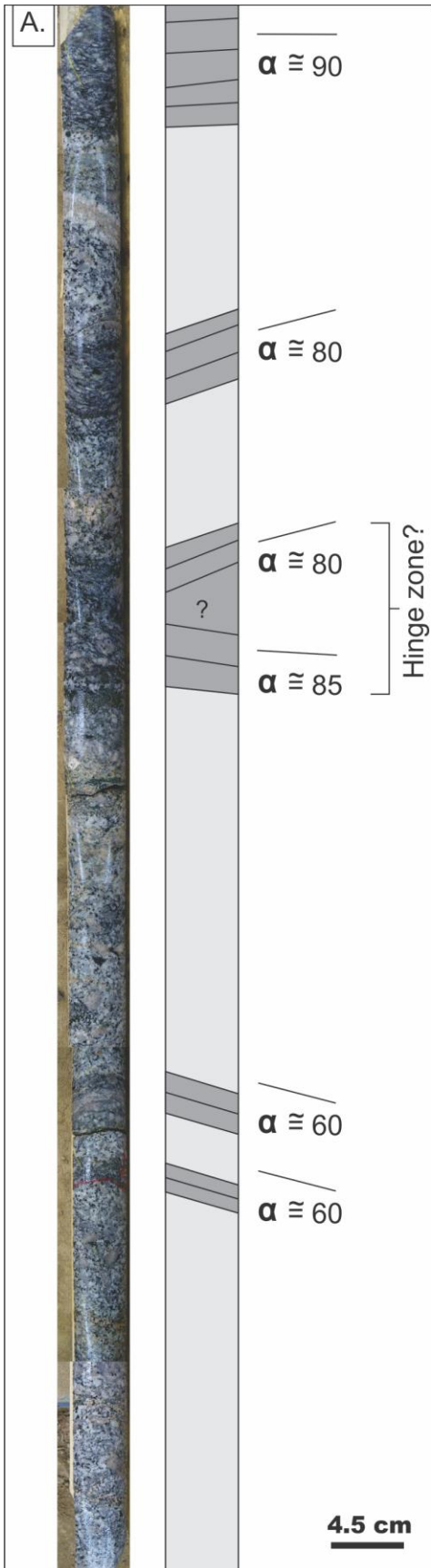


Figure 26: Downhole variation of S_p in unoriented vertical drillholes. Foliation angle is given by α angles, the angle between the core axis and the apex of foliation ellipses in core. Note that in vertical drillcore, foliation approaches horizontal as alpha approaches 90 degrees. A. Length of drill core displaying the typical alternating vertical pattern of deformed and undeformed granitoid. Foliation in vertical drill core most commonly had α oriented ~45 to 90 degrees. Foliation angles swinging through the horizontal may represent hinge zones. Foliation is poorly defined within these features and generally not possible to measure. These foliation transitions were noted most commonly in the midst of shear zones. B. Length of drill core showing short fold limb. In general, foliation transitions from sub-horizontal to sub-vertical orientation occur over several centimetres, with sub-vertical sections being tens of centimetres to metres in length. These hinge zones were noted most commonly near shear zone contacts.

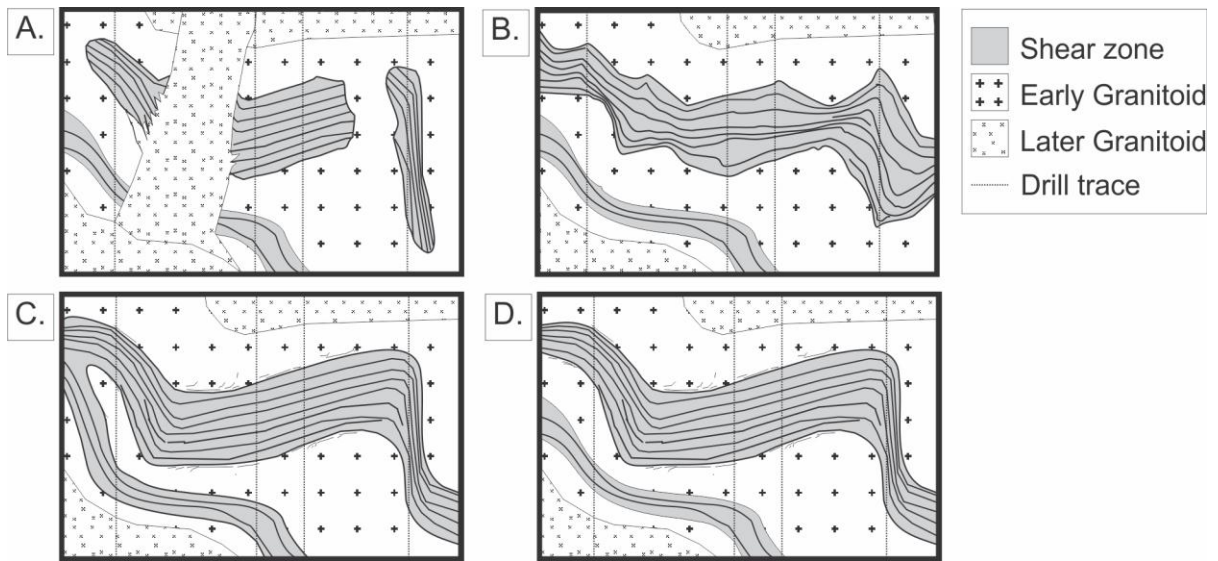
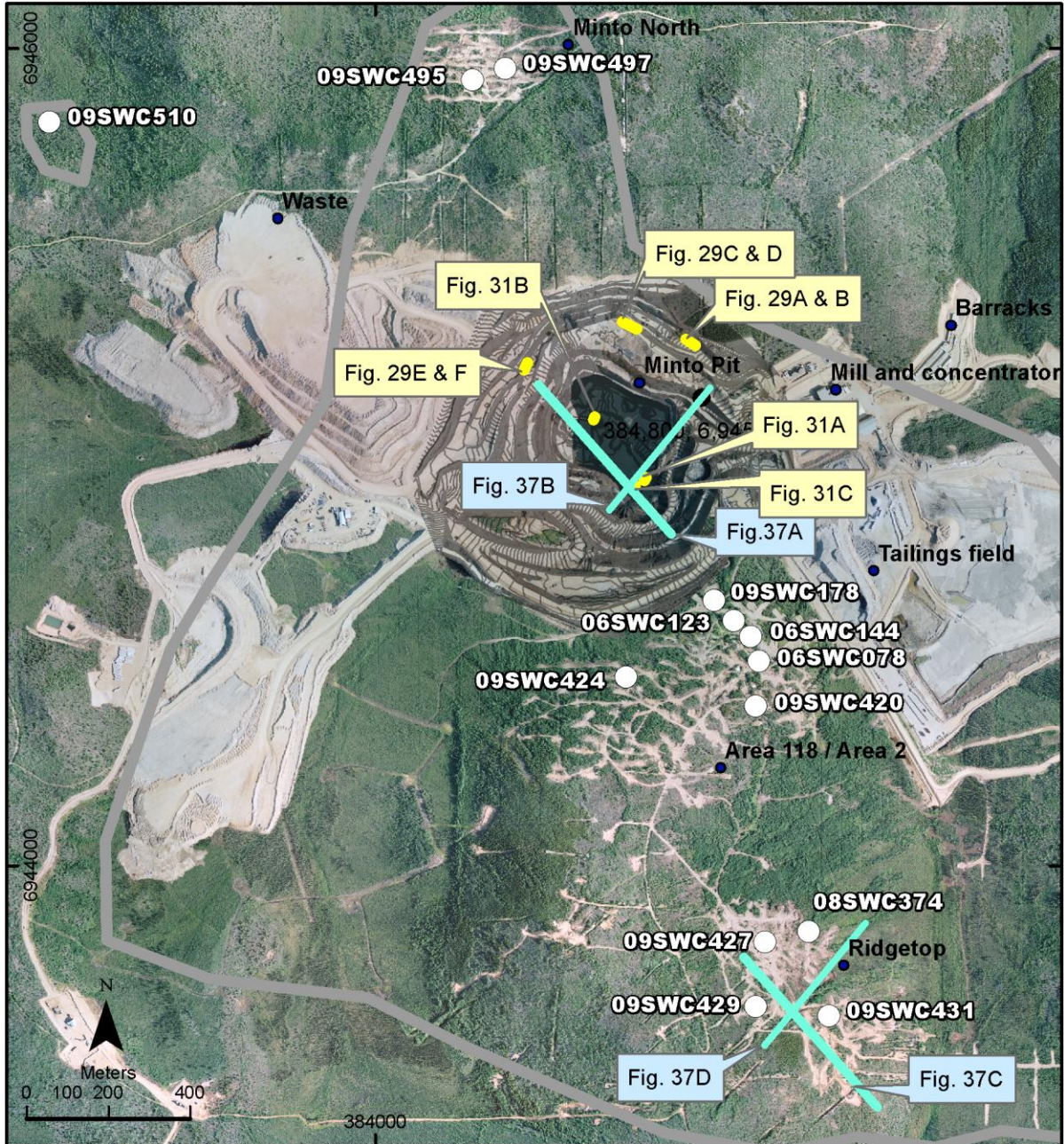


Figure 27: Schematic diagrams illustrating possible interpretations of geometry from S_P foliation observed in unoriented drillcore. **A.** Deformed rocks are rafts stopped into later granitoid intrusions, as per Tafti (2005). Foliation orientation would mainly be a product of raft reorientation into the younger magma intrusions. **B.** Deformation has been partitioned into a block of granitoids as shear zones, with continued deformation accommodated mainly by already deformed and altered rock. Steeply oriented foliation could be a product of mullion development. In this case, accommodated deformation in massive rocks could be evidenced by the narrow, spaced cross-cutting shear zones observed in outcrop. **C.** Foliation has been partitioned into a granitoid block as anastomosing shear zones with varying S_P orientation due to shear zone development around more cohesive blocks of granitoid. **D.** Deformation has been partitioned into a granitoid block as parallel shear zones, with changes in foliation orientation due to later folding of the shear zones.



- Location of logged drillholes
- Fig. X Outcrop represented in figure
- Fig. X Cross section
- Deposit boundary (approx.)
- Pit contour (Nov. 2009)
- Regions

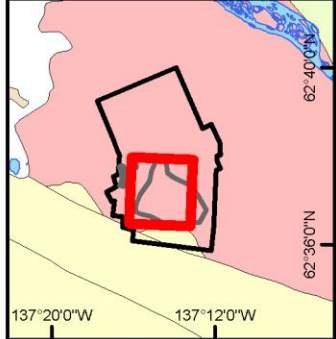
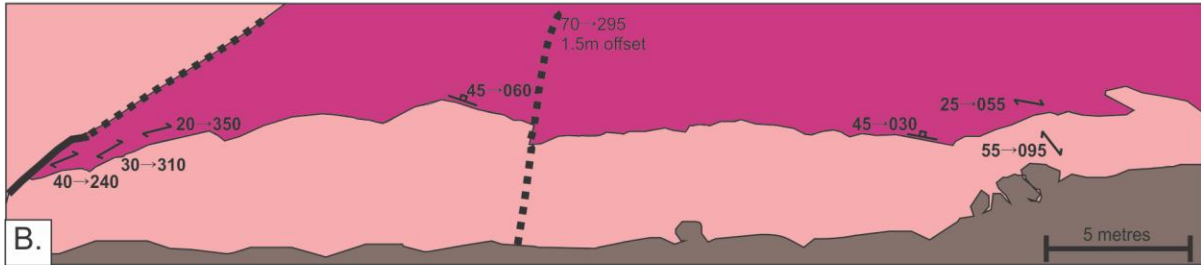


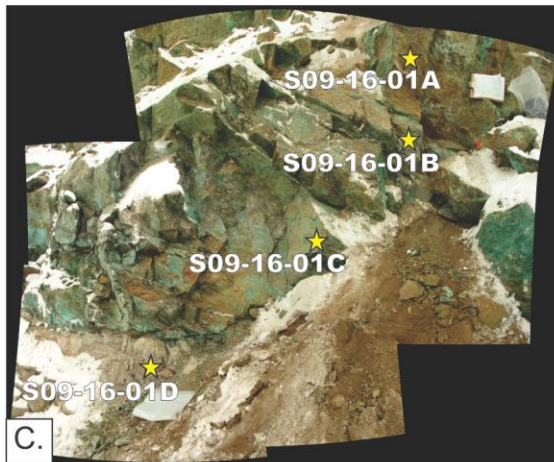
Figure 28: Orthophoto of the Minto mine showing the locations of logged diamond drill holes, figures with pit photographs and structural data, and cross sections.



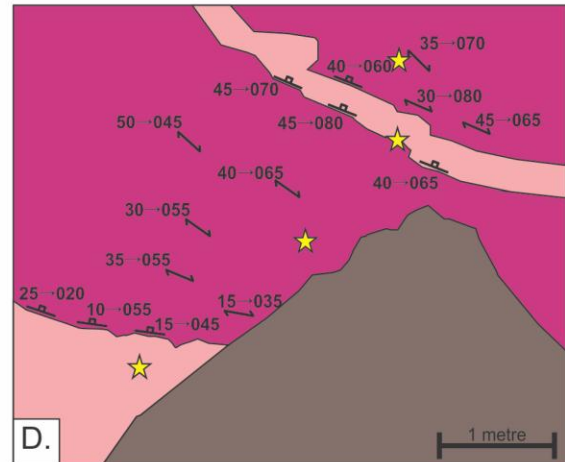
A.



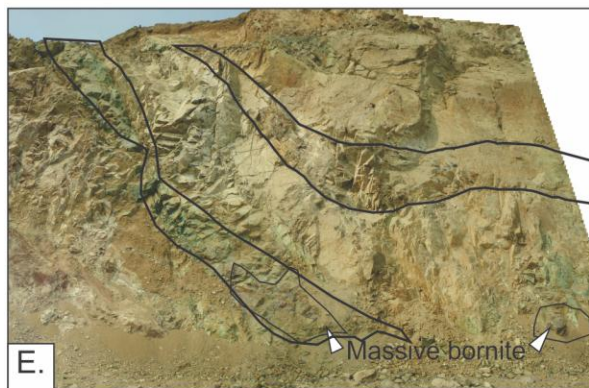
B.



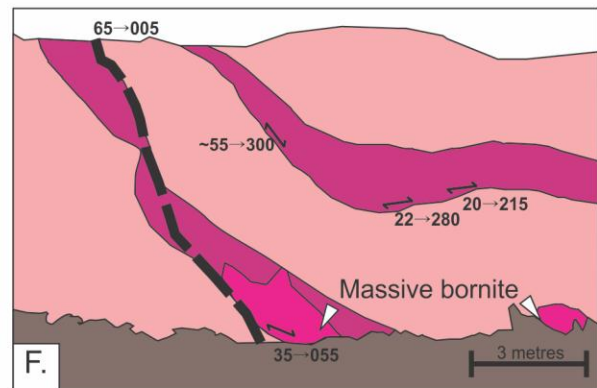
C.



D.



E.



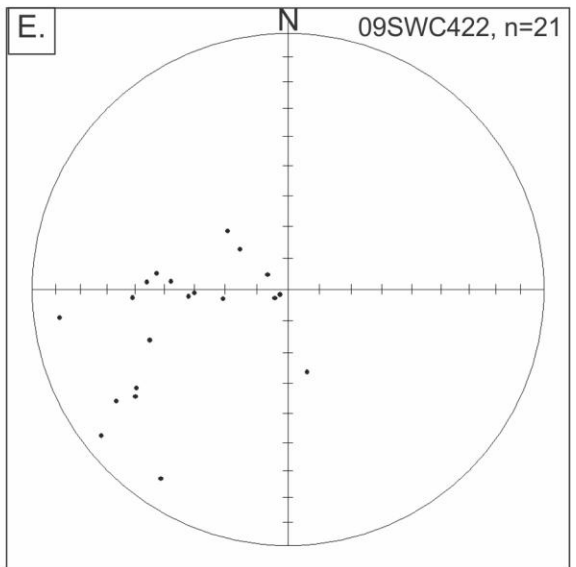
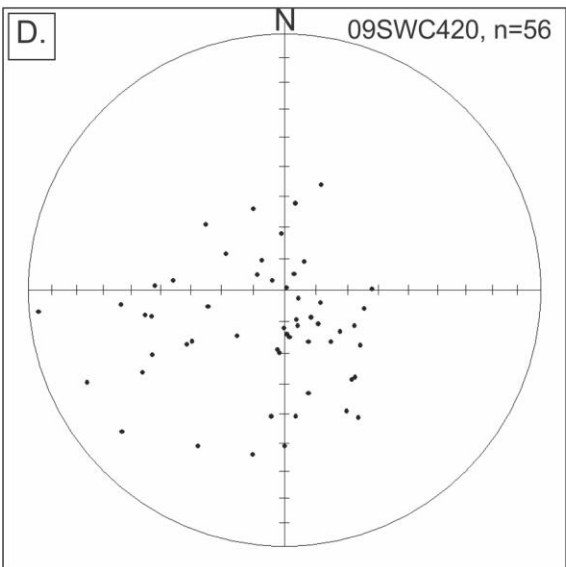
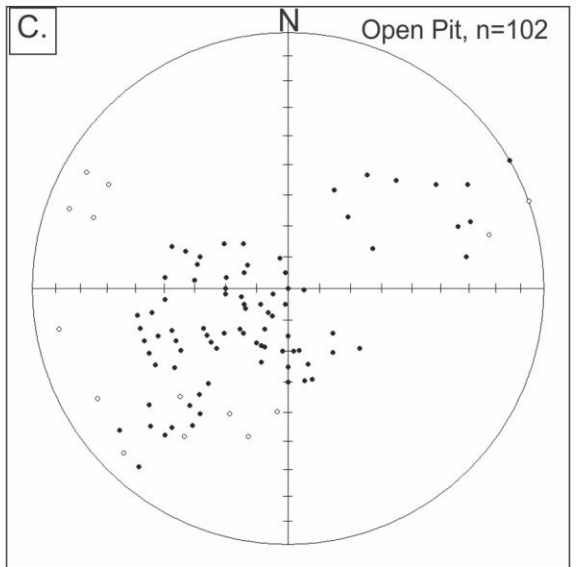
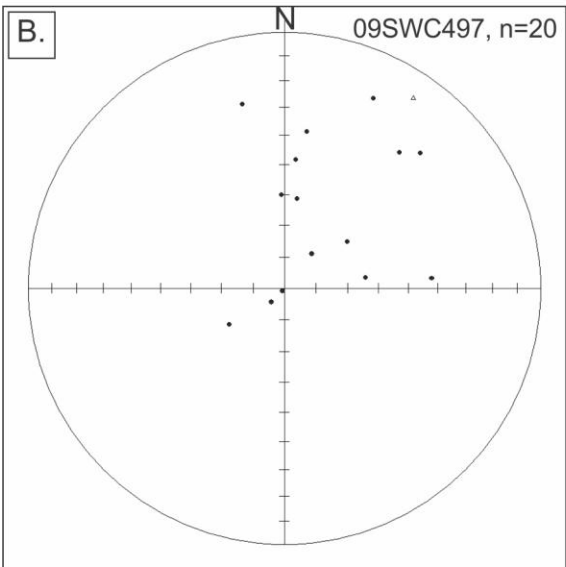
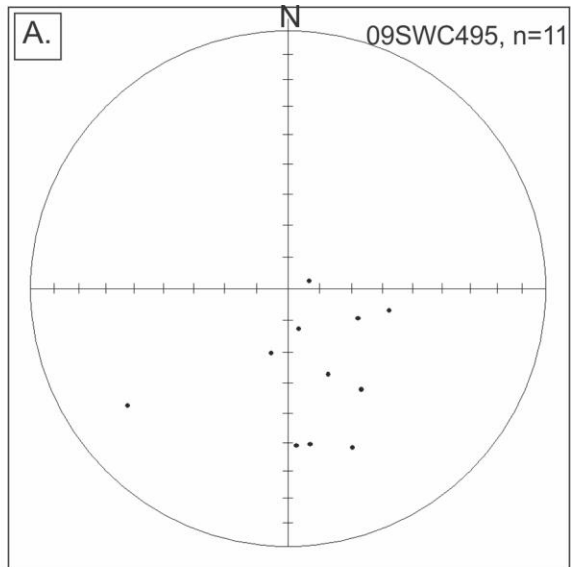
F.

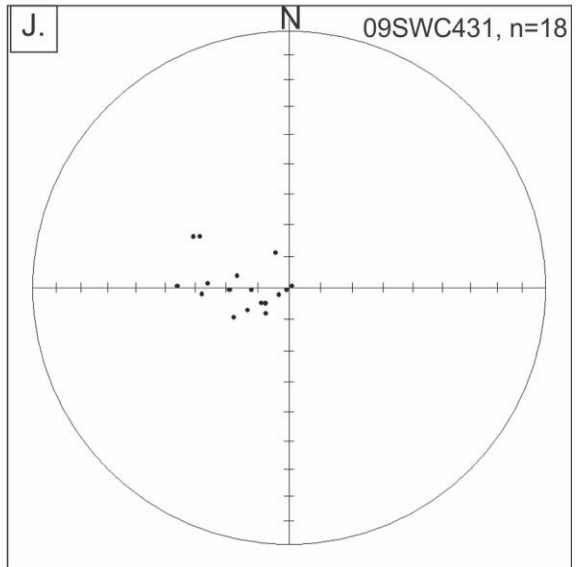
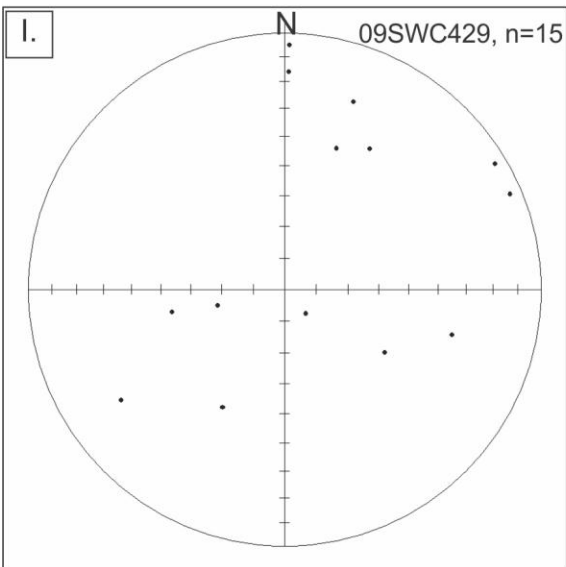
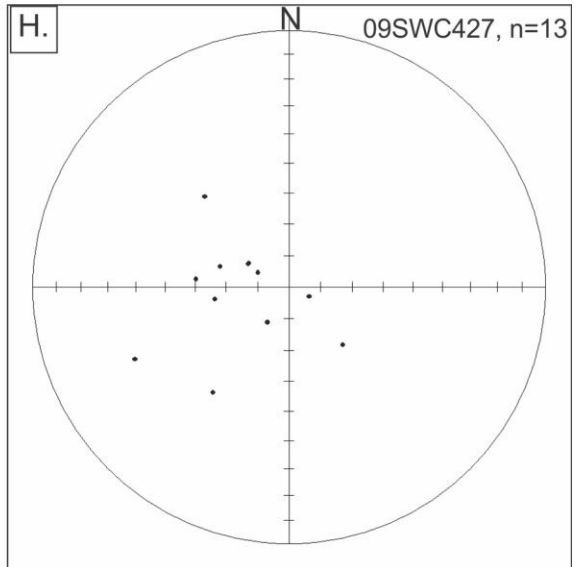
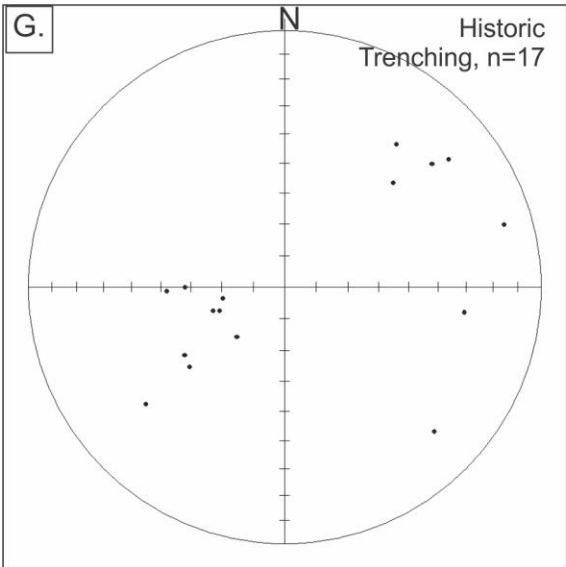
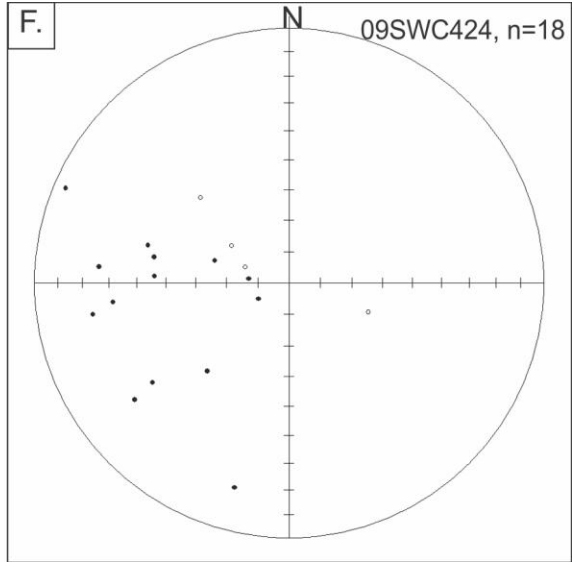
Legend

Pit slough	Dip → Dip Az. S ₁ Foliation
"Massive"/incipiently deformed granodiorite	Dip → Dip Az. Rock contact
Variably deformed/alterred granodiorite	--- Fault
	★ U-Pb SHRIMP sample

Figure 29: Examples of shear zones in the Minto open pit. A. & B. Panoramic photo and schematic diagram of foliation, contacts, and faults in laterally continuous shear zones. The west edge of the deformation zone is terminated by a younger brittle fault, the eastern edge is obscured by strong surficial weathering, and the top of the zone is obscured by sloughed rock. The vertical thickness of the shear zone is at least 5 metres. The basal contact is abrupt, but a gradient margin of about 10 centimetres of stage 1 deformation is present within the massive block. Section is 90-212, looking north. C. & D. Mosaic photo and schematic diagram showing foliation, structural contacts, and sample locations. Four structural domains are defined by variable deformation intensity and are, from top to bottom, gneissic banding, stage 3 deformation, stage 2 deformation, and stage 1 deformation. Deformation along contacts precludes interpreting whether pre-existing igneous contacts are present, or whether deformation has been partitioned into a single rock mass. U-Pb analyses using a SHRIMP from zircons representing each of the four structural domains indicate all rocks are similar in age, approximately 197.0 Ma – 197.8 Ma. Section is 90-210, looking north. E. & F. Panoramic photo and schematic diagram showing foliation and structural contacts. This shear zone represents interpreted asymmetric folding of short steep limbs and long shallow limbs. Section is oriented 90-155, looking west.

Alternating zones of variably strained KGd in drillcore, with or without foliation variation, are interpreted as separated shear zones of varying width, pictured in Figure 29C and D. Intervals of drillcore containing vertical successions in which foliation abruptly swings from horizontal orientation to relatively shorter intervals of steeply oriented foliation are interpreted as intersections with fold hinges, as exhibited in Figure 29E. and F. The interpretation of folded shear zones with asymmetric geometry is roughly consistent with separate interpretations from stereonet plots of regionally measured S_P (Figure 30). A complication of this interpretation comes from folding internal to shear zones, especially where shear zone boundaries are not exposed and thus not available for comparison. Internal folding of S_P within shear zones is common, and fold geometries vary (Figure 31A, B, and C.). The orientation of folds measured at the Minto property mainly dip northeast to southwest with varying steepness (Figure 31D.) and with hinges plunging shallowly northwest to southeast (Figure 31E.). It is not clear based on the data within this thesis what relationship various folds have with the intensity of mineralization, although there are coincidences between the strike of axial planes of folded shear zones (e.g., those shown in Figure 32) and the trend of high grade mineralisation (Figure 33 and Figure 34).





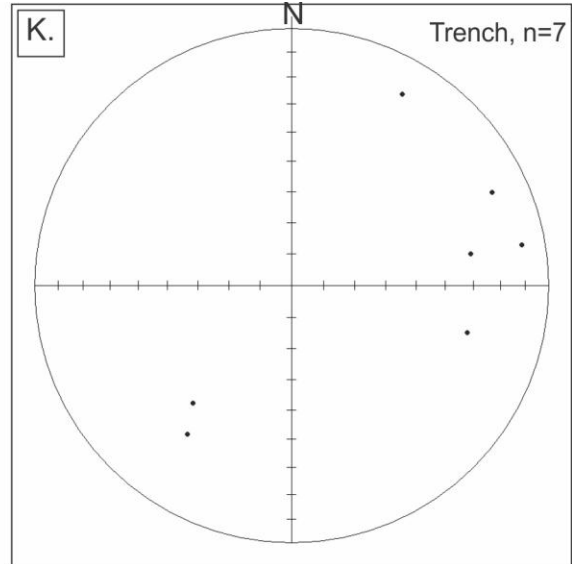
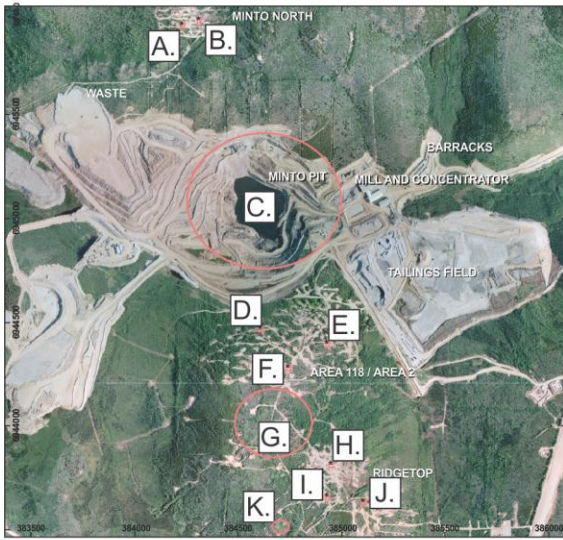


Figure 30: Stereonets of S_P measured from regions across the Minto deposit. Foliation is consistent across the deposit in that orientations are most commonly subhorizontal, and that foliation varies in dip essentially from northeast to southwest. Stereonets C., G., and K. exhibit bimodal clustering of poles to foliation, possibly indicative of asymmetric folding and consistent with folds with short-limb long-limb asymmetric geometry, as observed in drillcore and outcrop.

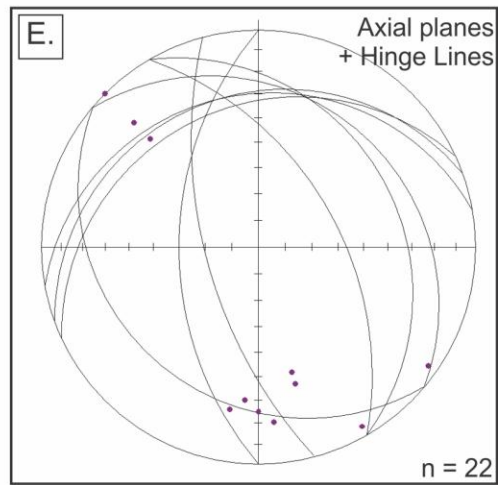
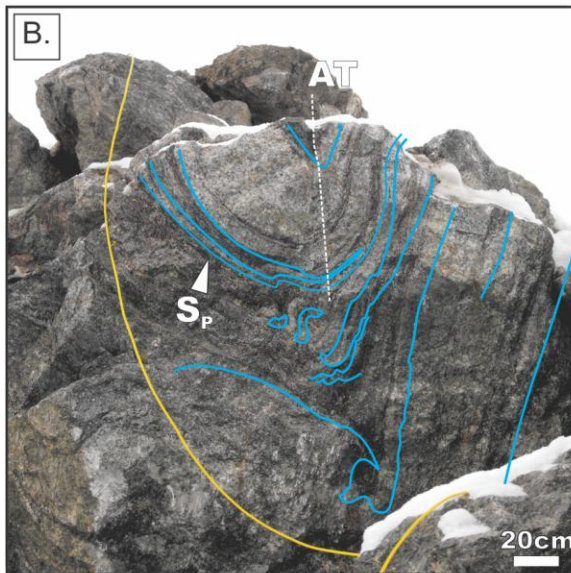
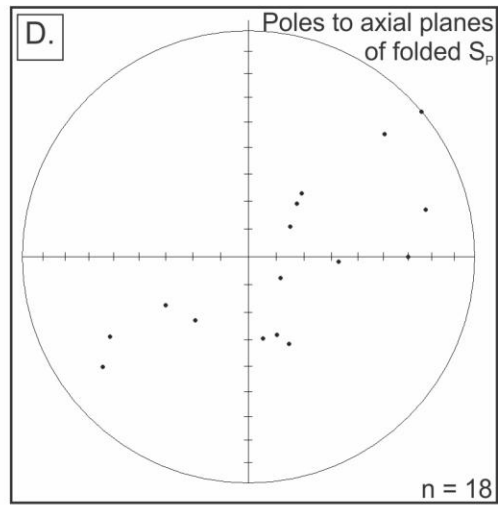
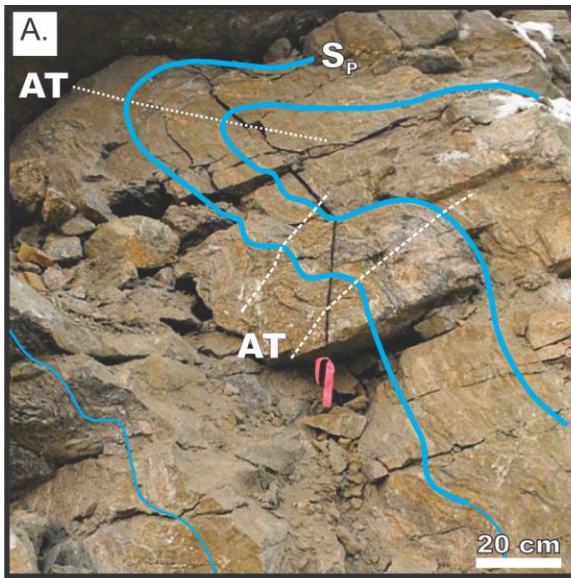


Figure 31: Variation of S_p folding observed within shear zones in the Minto open pit. AT = axial trace. A. Asymmetric folds with moderately dipping axial plane possibly overprinted by open folding with more steeply dipping axial plane. Location shown on Figure 28. B. Folded and boudinaged interval of medium grained tonalite within strongly mineralized pit outcrop. Igneous textures within tonalite are preserved, a possible indication that the unit was still molten during deformation. Axial plane of fold dips 60 degrees and strikes ~ 330 degrees to the northwest Location shown on Figure 28. Rock contains greater than 3% Cu as chalcopyrite-bornite. C. Asymmetric folds with angular hinges in moderately deformed KGd. Axial plane of fold dips 70 degrees and strikes ~330 degrees to the northwest. Sub-metre intervals of gneissic banding are present and grade into stage 3 deformed KGd with abundant folded pegmatite dikelets (red). Rock contains greater than 3% Cu as chalcopyrite-bornite. Location shown on Figure 28 D. Equal area stereonet of poles to fold axial planes measured across the Minto deposit in oriented drillcore and outcrop. Dip of axial planes varies from shallow to steep, with strike most commonly northwest or southeast. E. Equal area stereonet of fold axial planes, plus hinge line plunges. Hinges typically plunge shallowly to the southeast or northwest.

**Drill hole
07SWC178**

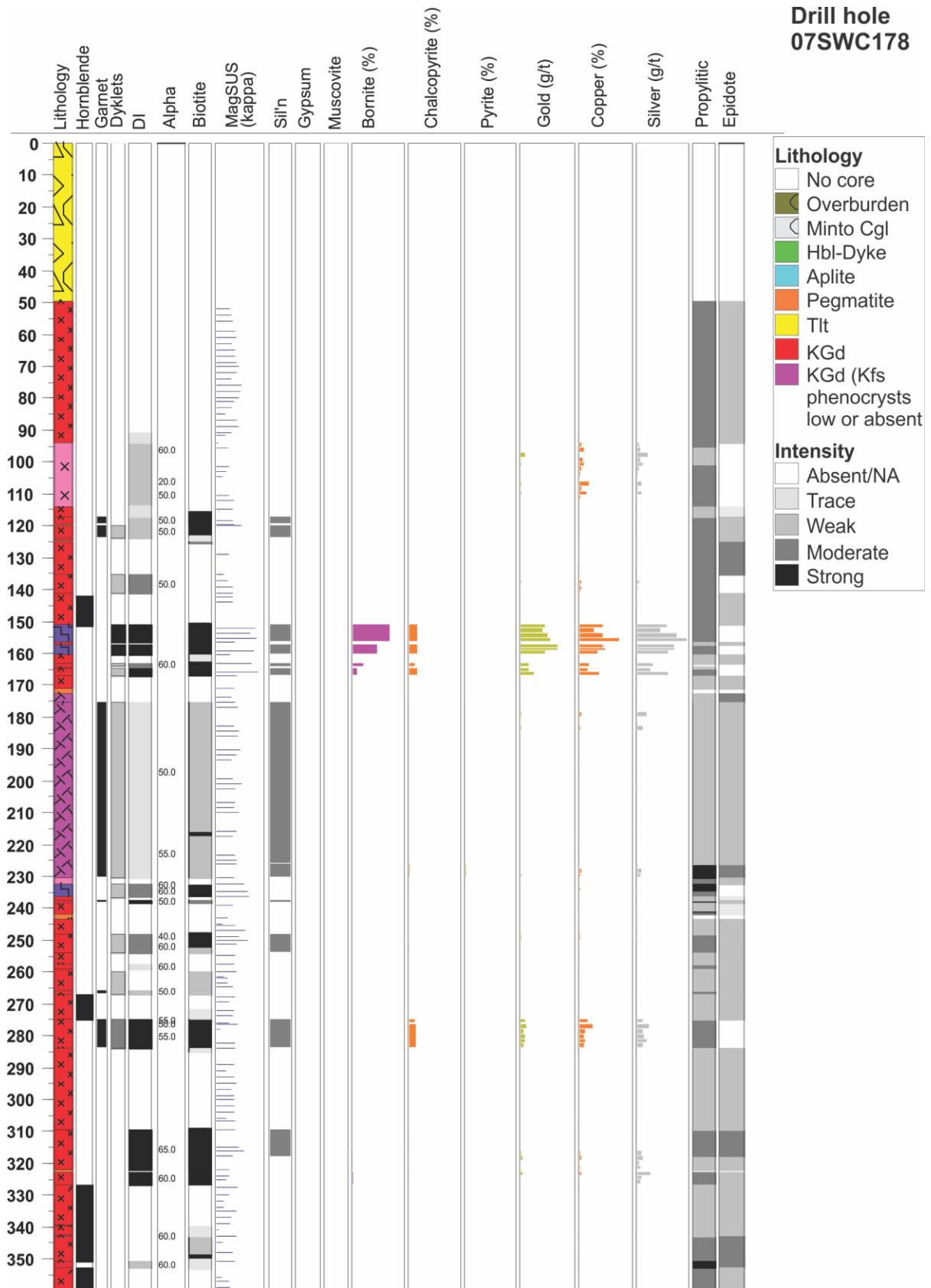
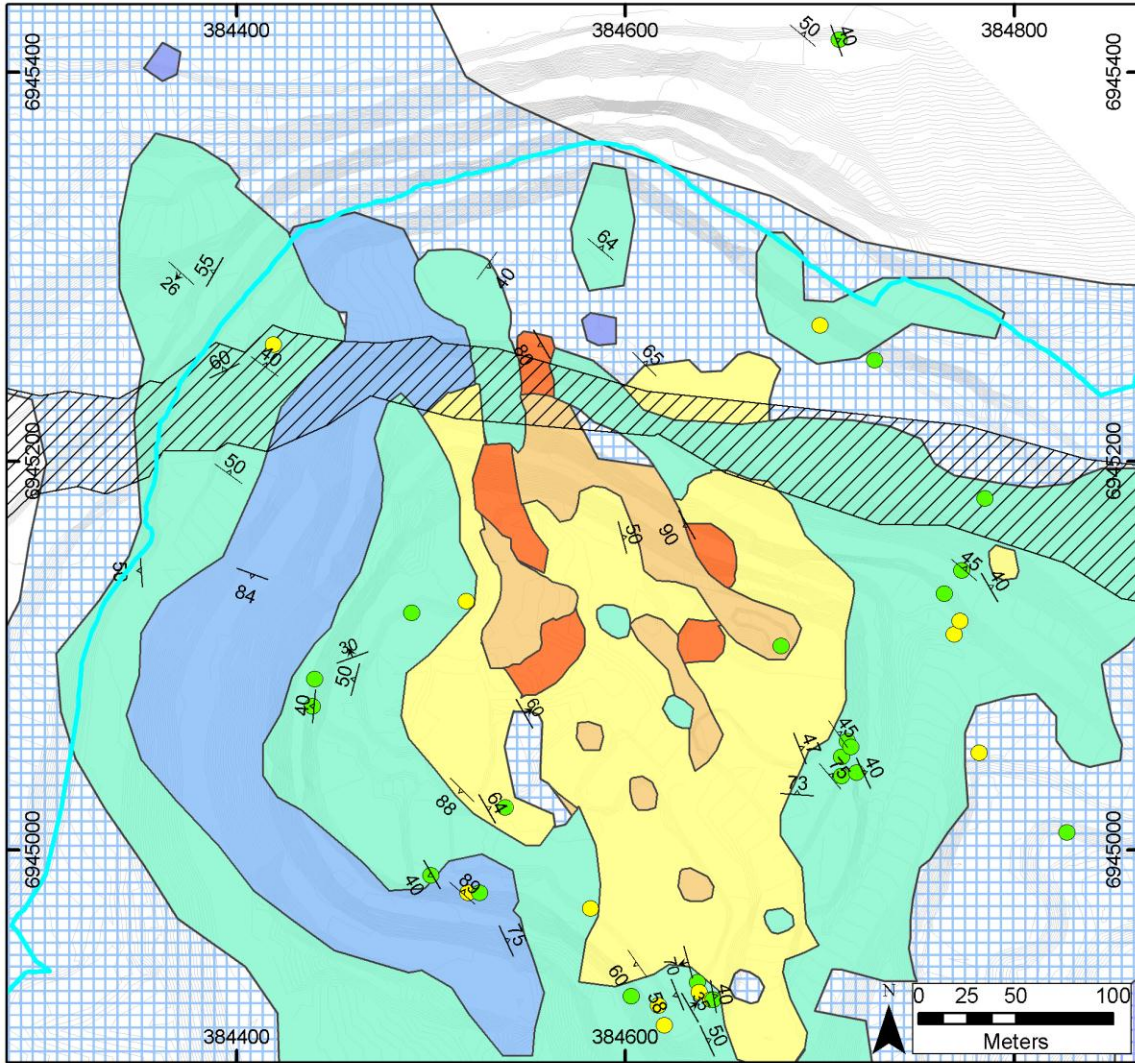


Figure 32: Graphical log of diamond drill hole 06SWC078 showing a correlation between potassic alteration, sulphide type, and ore grade. Additional graphical logs and locations of drillhoels are given in Appendix F . Intensity of potassic alteration is represented by magnetite content (magnetic susceptibility as a proxy), plus biotite content (visual estimation of weak/moderate/strong). Relative deformation intensity (DI) is indicated by the degree on recrystallization of quartz/plagioclase/K-feldspar as described earlier in the text. Deformation intensity, presence of garnet or hornblende, quartzofeldspathic dikelets, silicification, or gypsum are not obviously spatially correlated to mineralization. Propylitic alteration and potentially associated epidote veining overprint massive and deformed/mineralized zones. Alpha = angle between core axis and S_p foliation, Sil'n = silicification, Kfs = K-feldspar.



— Open Pit Contours (Nov. 2009)

▨ Strongly weathered DEF fault-related cataclastic rocks

Foliation

● Foliation, 00 > dip > 20

● Foliation, 20 > dip > 40

▲ Foliation, dip >= 40 degrees

▲ Axial plane of folded SP

Copper Grade Thickness

■ Greater than 120 Kg/t m

■ 90 to 120 Kg/t m

■ 45 to 90 Kg/t m

■ 10 to 45 Kg/t m

■ 10 to 45 Kg/t m (scarce data)

■ 1 to 10 Kg/t m

■ 1 to 10 Kg/t m (scarce data)

■ Copper absent or background

■ Copper absent or background (scarce data)

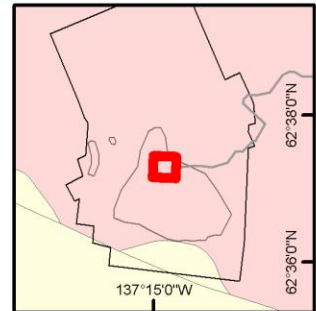
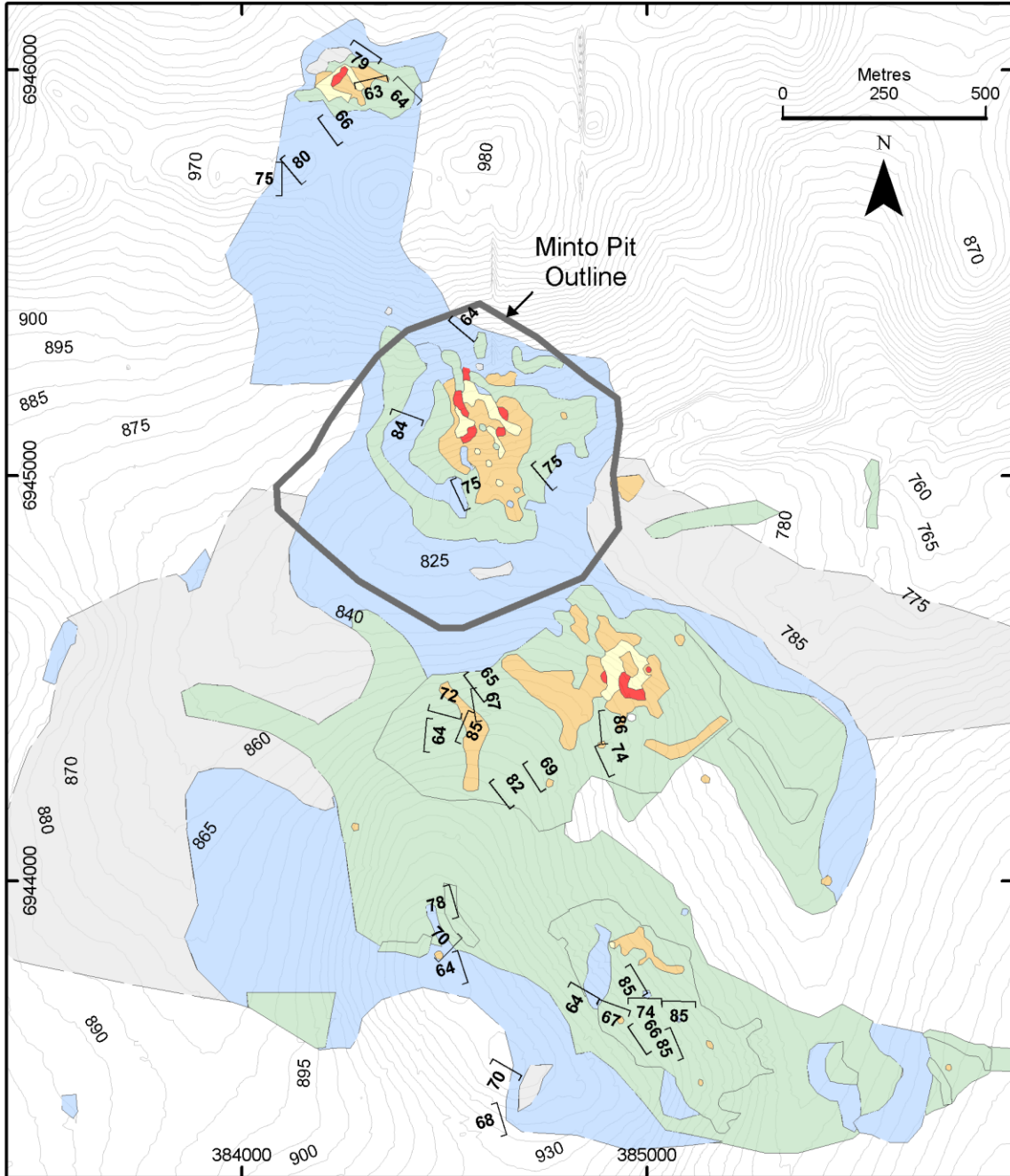


Figure 33: Map of the Minto open pit summarising S_p foliation geometry. Main trend of steeply dipping foliation and axial planes of folded S_p is approximately 330 degrees. There is also a second foliation trend at approximately 200 degrees. Note that the 300 degree trend approximately parallels the high grade core of the open pit. Property foliation, S_p , measurements have been binned into groups representing shallow, moderate, and steep foliation: 0- 30 degrees, 30- 60 degrees, and 60-90 degrees, respectively. Copper grade thickness is calculated from drill hole assays as the sum of (copper grade) x (grade intercept length), and is contoured to show regions of the most mineralisation, inclusive of rock removed during mining. The northeast trend of grade-thickness shown is interpreted as correlated to the similar strike of steep foliation. The trend of grade-thickness also corresponds to Capstone's block model of mineralisation at 730m elevation, i.e., within the main mineralised shear zone targeted in the Minto open pit (Capstone Geologists, pers. comm.). Trends of grade thickness are thus considered an approximation for zones of high mineralisation.



Foliation, SP
 — Dip ≥ 60 degrees
 — Topographic Contours (5m)

Grade Thickness (via drill log)
 ■ Greater than 120 Kg/t m
 ■ 90 to 120 Kg/t m
 ■ 45 to 90 Kg/t m
 ■ 10 to 45 Kg/t m
 ■ 1 to 10 Kg/t m
 ■ Copper absent or background

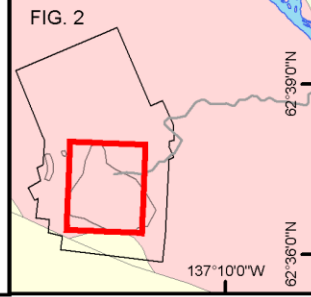


Figure 34: Steep foliation and Cu-grade thickness from the Minto deposit. Steeply dipping foliation dominantly trends northwest-southeast represents relatively narrow zones of overprinting deformation where S_p has been rotated to a steeper dip. The dip direction of shallow to moderate foliation is varied and no major trends are observed. A (copper-grade) x (grade intercept thickness) contour map is given to show the main mineralization trend of the deposit. This corridor of higher grade thickness values is developed subparallel to the northwest-southeast enveloping trend of steeply dipping S_p . Shallow foliations are removed for clarity.

2.4.5 Late Brittle Deformation

Brittle fractures are observed throughout the Minto pluton at scales ranging from microscopic to regional. Microfractures locally crosscut igneous contacts, and magmatic and solid state foliation. Propylitic alteration is typically controlled by brittle fractures that also crosscut igneous and structural contacts. More relevant to exploration are late brittle faults that dissect mineralisation zones. These faults mainly trend approximately east-west, with the largest being the DEF fault (Figure 3).

2.5 Geochronology

There have been four previous studies to constrain the timing of intrusion for granodiorites at the Minto deposit. Pearson (1977) reported two K-Ar biotite ages of 180 (+/- 9) Ma and 177 (+/- 9) Ma for samples of granodiorite and altered granodiorite (“biotite gneiss”). Tempelman-Kluit et al. (1980) reported a $^{206}\text{Pb}/^{238}\text{U}$ age of 191 (+/- 3) Ma and a $^{207}\text{Pb}/^{235}\text{U}$ age of 192 (+/- 3) Ma for a hornblende-bearing granodiorite from the Minto discovery outcrop and a K-Ar biotite age of 174 (+/- 6 Ma) for a foliated granodiorite. More recent dating by Mortensen and Tafti (2002) and Tafti (2005) worked to refine intrusion ages using U-Pb Isotope Dilution-Thermal Ionization Mass Spectrometry techniques. Most samples of granodiorite and deformed/foliated granitoid yielded ages that were variably discordant, reflecting multiple stages of zircon inheritance and post-crystallization lead-loss (Tafti, 2005). No ages for undeformed/altered granitoids are reported; however a zircon age of 197.2 (+/-) 2.1 Ma is assigned to one sample of “garnet-bearing mineralized orthogneiss” (Tafti, 2005), interpreted in this thesis as a strongly deformed granodiorite with quartzofeldspathic banding and Cu-sulphide alteration. Another age of 197.8 +/- 2.5 Ma was assigned to a sample of “siliceous ore” (Tafti, 2005), interpreted here as a strongly deformed quartz + Cu-sulphide occurring in deformed and altered granodiorite. Both of these samples were taken from drill core around the main Minto deposit. U-Pb titanite age dates for a suite of variably deformed and altered Minto granodiorites were reported by Tafti (2005) and range between 194.0 Ma to 185.1 Ma, consistently younger than U-Pb zircon ages. This effect may be attributed to thermal resetting (Tafti, 2005) or reactivity of titanite in high temperature environments with Ti or Ca bearing fluids (Scott and St-Onge, 1995).

This study constrains the age of pluton emplacement, and the age of mineralisation, for the Minto Pluton using U-Pb geochronology on zircon and Re-Os geochronology on molybdenite. In situ U-Pb dating was done using the Sensitive High Resolution Ion Microprobe (SHRIMP II) at the Geological Survey of Canada Geochronology Laboratories in Ottawa, Canada. The SHRIMP II was chosen to limit inheritance issues and lead-loss along internal fractures documented in earlier studies where whole grain digestion of zircons was used. Contact relationships between granodiorite phases at Minto suggest a history of multiple magma batches, overprinted by partitioned deformation and hydrothermal alteration. Samples for geochronology were chosen from the open pit and drill core to represent igneous contacts and partitioned deformation.

2.5.1 U-Pb SHRIMP Geochronology

2.5.1.1 Samples

Two suites of granodiorite samples were collected to constrain intrusion ages and to complement cross-cutting relationships that constrain the relative timing of pluton emplacement, deformation, and alteration/mineralisation (Appendix 4).

The first suite of two samples comprises a moderately altered granodiorite enclave within a fresh granodiorite host (Figure 6B). Sample S08-01-01 is an enclave of altered granodiorite within a body of unaltered granodioritic host represented by sample S09-13-03A. Samples were collected from a well-exposed road cut along the Minto access road near the Minto Dam. KGd exposure in the sample area consists mainly of typical Minto granodiorites, fault bounded at the east of the outcrop with weakly propylitically altered granodiorites. Host KGd in this area is commonly includes crowded K-feldspar porphyry, enclaves of altered KGd,

and mafic magmatic enclaves. This suite was samples to examine the timing relationship between batches of KGd.

The second suite of four samples were collected from a sequence of vertically stacked deformed and massive granodiorites within the hangingwall of the DEF fault in the Minto pit (Figure 28C and D). This interval is interpreted to represent shear zones cross-cutting a single, relatively undeformed, phase of intrusion..

2.5.1.2 Analyses

U-Pb SHRIMP II analyses were conducted at the Geological Survey of Canada (GSC) in Ottawa using analytical procedures described by Stern (1997), with standards and U-Pb calibration methods following Stern and Amelin (2003). Heavy minerals were separated from six samples using standard methods (crushing, Wilfley table, heavy liquids) and sorted according to magnetic susceptibility using a Frantz isodynamic separator. Zircons for all but sample S09-16-03C were recovered by Apatite to Zircon, Inc. Zircons separated from the six samples show signs of inheritance in backscatter and reflected light (photographs of hand specimen and micrographs of analysed grains are provided in Appendix G). Xenocrystic cores with younger overgrowth were identified by geometrically irregular surfaces truncating internal zoning, or by observing growth zoned rims around cores that were subrounded or euhedral, unzoned, or chaotically zoned (Corfu et al., 2003). The rims of zircons were targeted in this study as a means of identifying the last phase of zircon growth, i.e., the age of host rock intrusion.

Zircons were cast in 2.5 cm diameter epoxy mounts along with fragments of the GSC laboratory standard zircons (z6266, with $^{206}\text{Pb}/^{238}\text{U}$ age = 559 Ma, and z8539 Temora, with $^{206}\text{Pb}/^{238}\text{U}$ age 417 Ma). The mid-sections of the zircons were exposed using 9, 6, and 1 μm

diamond compound, and the internal features of the zircons (such as zoning, structures, alteration, etc.) were characterized in reflected light and back-scattered electron mode (BSE) utilizing a Zeiss Evo 50 scanning electron microscope. Mount surfaces were evaporatively coated with 10 nm of high purity Au. Analyses were conducted using a ^{16}O - primary beam, projected onto the zircons at 10 kV. The sputtered area used for analysis was ca. 35 μm in diameter with a beam current of ca. 15 nA. The count rates at ten masses including background were sequentially measured over 5 scans with a single electron multiplier and a pulse counting system with deadtime of 23 ns. Off-line data processing was accomplished using customized in-house software. The 1σ external errors of $^{206}\text{Pb}/^{238}\text{U}$ ratios reported in the data table incorporate a $\pm 1.0\%$ error in calibrating the standard zircon (see Stern and Amelin 2003). No fractionation correction was applied to the Pb-isotope data; common Pb correction utilized the Pb composition of the surface blank (Stern, 1997). Weighted average ages are given at 95% confidence level (2σ), determined using Isoplot (Ludwig, 1998).

Uranium-lead analyses are presented numerically in Table 4 and graphically on concordia plots (Figure 35). The majority of Minto zircons yielded $^{206}\text{Pb}/^{238}\text{U}$ ages between approximately 197 Ma and 200 Ma. Zircons with $^{206}\text{Pb}/^{238}\text{U}$ ages around 300 Ma, observed within samples S09-13-03A, S09-16-01B, and S09-16-01D, are interpreted as inherited zircons from the Yukon Tanana Terrane, country rock to the granodiorite intrusions.

Individual analyses were culled from $^{206}\text{U}/^{238}\text{Pb}$ age calculations based on inheritance, Pb-loss, high common Pb, analyses with $\%^{206}\text{Pb}$ greater than 2%, anomalously high/low UO/U, or when spot locations included cracks or zircon grain boundaries (Nicole Rayner, pers. comm.).

Table 4: Results of U-Pb SHRIMP analyses of KGd zircons and age calculations. Calculated ages are shown graphically on concordia diagrams in

Figure 35.

Sample	Spot	ppm U	Th/U	Y ppm	Hf ppm	ppm 206*	%f206207	Atomic Ratios														Ages (Ma)			
								Uncorrected							204 Corrected (1)							204	207		
								204Pb /206Pb	±%	208Pb /206Pb	±%	238U /206Pb	±%	207Pb /206Pb	±%	207Pb* /235U	±%	206Pb* /238U	±%	err corr	206Pb/238U Calibration Error %	206Pb* /238U Age	206Pb* /238U Age		
S09-13-03A	10265-33.2	536.41	0.30	549	12676	13.94	1.01	5.8E-04	40	0.118	10.1	32.73	1.34	0.050	3.3	0.171	9.46	0.0302	1.40	0.148	1.27	192.1	3	194.1	3
S09-13-03A	10265-53.1	256.65	0.50	638	9668	6.69	1.87	1.1E-03	58	0.209	10.0	32.36	1.64	0.063	8.8	0.197	23.18	0.0303	1.98	0.085	1.27	192.6	4	193.2	3
S09-13-03A	10265-46.1	767.08	0.28	1284	11924	20.16	0.38	2.2E-04	19	0.082	9.4	32.56	1.30	0.051	2.6	0.201	3.33	0.0306	1.30	0.392	1.27	194.3	2	194.8	3
S09-13-03A	10265-33.3	438.29	0.22	581	11561	11.53	1.30	7.5E-04	26	0.087	12.4	32.24	1.35	0.066	3.1	0.233	6.66	0.0306	1.40	0.210	1.27	194.4	3	193.2	3
S09-13-03A	10265-94.1	552.59	0.26	460	12822	14.58	0.93	5.3E-04	31	0.048	21.3	32.26	1.49	0.055	3.2	0.199	6.64	0.0307	1.52	0.229	1.27	195.0	3	195.7	3
S09-13-03A	10265-81.1	836.32	0.31	1427	12261	22.14	0.37	2.2E-04	85	0.091	8.5	32.32	1.30	0.051	2.5	0.203	6.38	0.0308	1.34	0.210	1.27	195.7	3	196.2	3
S09-13-03A	10265-87.1	586.99	0.25	940	11098	15.67	1.65	9.5E-04	31	0.085	11.1	31.65	1.33	0.053	3.1	0.167	12.34	0.0311	1.43	0.116	1.27	197.3	3	199.8	3
S09-13-03A	10265-69.1	654.41	0.35	1334	11596	17.48	1.54	8.9E-04	28	0.120	9.3	31.65	1.34	0.057	3.0	0.188	9.50	0.0311	1.41	0.148	1.27	197.5	3	198.9	3
S09-13-03A	10265-11.1	529.47	0.37	414	10861	14.16	0.24	1.4E-04	29	0.121	7.7	32.03	1.30	0.052	2.6	0.216	3.22	0.0311	1.30	0.404	1.27	197.7	3	197.6	3
S09-13-03A	10265-32.1	389.22	0.28	555	11474	10.45	0.98	5.6E-04	33	0.102	14.4	31.67	1.66	0.050	4.6	0.178	8.92	0.0313	1.69	0.189	1.27	198.5	3	200.5	3
S09-13-03A	10265-29.1	722.46	0.33	1017	10952	19.47	0.44	2.5E-04	127	0.107	7.7	31.74	1.44	0.052	2.5	0.209	10.31	0.0314	1.54	0.150	1.27	199.1	3	199.5	3
S09-13-03A	10265-80.1	404.64	0.28	520	10777	10.96	1.40	8.1E-04	33	0.112	11.3	31.26	1.33	0.053	3.6	0.179	10.96	0.0315	1.41	0.129	1.27	200.2	3	202.3	3
S09-13-03A	10265-18.1	589.48	0.26	882	12209	15.98	0.86	5.0E-04	151	0.082	8.6	31.42	1.56	0.053	2.4	0.197	24.91	0.0316	2.04	0.082	1.27	200.3	4	201.4	3
S09-13-03A	10265-91.1	612.08	0.30	849	11553	16.59	0.29	1.7E-04	34	0.115	9.0	31.59	1.61	0.054	2.9	0.223	3.85	0.0316	1.61	0.418	1.27	200.3	3	200.0	3
S09-13-03A	10265-79.1	751.75	0.40	1627	11924	20.40	0.71	4.1E-04	56	0.110	9.0	31.43	1.33	0.049	3.0	0.188	8.74	0.0316	1.39	0.158	1.27	200.5	3	202.1	3
S09-13-03A	10265-86.1	473.75	0.29	800	11586	12.91	0.25	1.4E-04	54	0.109	10.5	31.44	1.69	0.053	3.3	0.222	4.48	0.0317	1.70	0.379	1.27	201.4	3	201.2	3
S09-13-03A	10265-63.1	658.64	0.29	926	11424	18.04	0.82	4.7E-04	20	0.087	11.4	31.10	1.99	0.051	3.2	0.196	5.28	0.0319	2.00	0.378	1.27	202.4	4	203.7	4
S09-13-03A	10265-25.1	405.28	0.44	1085	10327	11.10	1.61	9.3E-04	26	0.136	8.2	30.85	1.35	0.054	2.9	0.179	9.94	0.0319	1.41	0.142	1.27	202.4	3	204.7	3
S09-13-03A	10265-7.1	652.84	0.27	804	12328	17.90	0.29	1.7E-04	20	0.084	8.8	31.23	1.49	0.050	2.5	0.208	3.20	0.0319	1.49	0.466	1.27	202.6	3	203.3	3
S09-13-03A	10265-4.1	708.48	0.43	908	11349	19.52	0.47	2.7E-04	24	0.137	7.6	31.03	1.61	0.053	2.7	0.216	3.88	0.0321	1.61	0.416	1.27	203.5	3	203.8	3
S09-13-03A	10265-24.1	941.73	0.42	1145	11779	26.13	0.45	2.6E-04	101	0.134	7.2	30.82	1.30	0.049	3.3	0.200	9.51	0.0323	1.38	0.146	1.27	204.9	3	206.2	3
S09-13-03A	10265-2.1	300.06	0.39	481	10868	8.43	0.61	3.5E-04	48	0.123	10.4	30.38	1.50	0.053	3.5	0.214	6.74	0.0327	1.53	0.227	1.27	207.5	3	208.2	3
S09-13-03A	10265-10.1	787.06	0.27	1172	12417	22.33	0.20	1.2E-04	106	0.095	6.9	30.21	1.30	0.050	2.1	0.219	4.54	0.0330	1.32	0.290	1.27	209.5	3	210.0	3
S09-13-03A	10265-8.1	690.08	0.28	1718	8981	20.09	0.00	1.0E-32	100	0.093	8.9	29.50	1.33	0.052	2.6	0.245	2.94	0.0339	1.33	0.450	1.27	214.9	3	214.4	3
S09-13-03A	10265-15.1	511.89	0.30	540	13172	15.53	0.00	1.0E-32	100	0.108	9.1	28.32	1.57	0.053	2.9	0.258	3.28	0.0353	1.57	0.478	1.27	223.7	3	223.1	3
S09-13-03A	10265-12.1	513.80	0.35	664	11766	17.08	0.19	1.1E-04	24	0.098	8.0	25.79	1.35	0.053	2.4	0.275	2.90	0.0387	1.35	0.465	1.27	244.7	3	244.6	3
S09-13-03A	10265-55.1	466.04	0.31	859	11469	18.21	1.69	9.7E-04	31	0.106	9.3	21.61	1.37	0.058	2.8	0.271	11.31	0.0455	1.47	0.130	1.27	286.8	4	289.7	4
S09-13-03A	10265-33.1	173.42	0.47	1448	9849	7.23	2.43	1.4E-03	34	0.169	11.1	20.09	1.78	0.070	3.8	0.329	15.61	0.0486	1.96	0.126	1.27	305.7	6	306.9	5
S09-13-03A	10265-85.1	340.64	0.40	1283	10224	14.87	1.90	1.1E-03	28	0.129	9.3	19.30	1.50	0.055	3.2	0.274	12.60	0.0508	1.59	0.126	1.27	319.6	5	324.7	5
S09-13-03A	10265-64.2	139.26	0.37	2030	9593	6.21	3.29	1.9E-03	40	0.179	11.4	18.62	1.68	0.084	6.9	0.402	22.81	0.0519	2.15	0.094	1.27	326.5	7	325.3	6

Sample	Spot	ppm Σ	Th/U	Y ppm	Hf ppm	ppm 206*	% Σ 206207	Atomic Ratios														Ages (Ma)			
								Uncorrected							204 Corrected (1)							204		207	
								204Pb /206Pb	$\pm\%$	208Pb /206Pb	$\pm\%$	238U/ 206Pb	$\pm\%$	207Pb /206Pb	$\pm\%$	207Pb* /235U	$\pm\%$	206Pb* /238U	$\pm\%$	err corr	206Pb/238U Calibration Error %	206Pb* /238U Age	206Pb* /238U Age		
S08-01-01	10266-22.1	139.22	0.38	523	10442	3.55	2.40	1.4E-03	33	0.138	13.2	32.86	1.12	0.057	4.6	0.149	20.58	0.0297	1.38	0.067	1.00	188.7	3	191.7	2
S08-01-01	10266-53.1	255.45	0.32	242	10513	6.57	2.99	1.7E-03	26	0.123	10.8	32.41	1.12	0.065	3.3	0.164	18.13	0.0299	1.38	0.076	1.00	190.1	3	192.3	2
S08-01-01	10266-81.1	184.87	0.34	561	10239	4.79	1.98	1.1E-03	31	0.121	12.3	32.53	1.10	0.059	3.9	0.176	13.69	0.0301	1.26	0.092	1.00	191.4	2	193.1	2
S08-01-01	10266-1.1	399.05	0.35	687	10325	10.34	0.86	5.0E-04	114	0.117	8.6	32.87	1.10	0.054	2.8	0.196	18.13	0.0302	1.48	0.082	1.00	191.5	3	192.2	2
S08-01-01	10266-23.1	281.14	0.31	439	10092	7.28	1.14	6.5E-04	52	0.152	8.7	32.18	1.06	0.054	4.2	0.183	12.66	0.0302	1.22	0.096	1.00	191.6	2	192.9	2
S08-01-01	10266-39.1	218.71	0.36	702	10260	5.69	1.94	1.1E-03	33	0.164	9.7	32.38	1.08	0.070	7.8	0.226	14.54	0.0303	1.26	0.087	1.00	192.3	2	191.3	2
S08-01-01	10266-42.1	185.70	0.48	847	9589	4.84	4.35	2.5E-03	23	0.205	9.4	31.53	1.10	0.060	3.9	0.093	42.43	0.0303	1.51	0.036	1.00	192.6	3	198.9	2
S08-01-01	10266-8.1	310.04	0.30	491	10073	8.13	1.21	7.0E-04	64	0.089	11.6	32.38	1.67	0.061	3.2	0.216	13.66	0.0305	1.85	0.135	1.00	193.8	4	193.5	3
S08-01-01	10266-37.1	329.12	0.42	407	10361	8.67	0.37	2.1E-04	235	0.152	8.1	32.50	1.12	0.057	3.0	0.228	13.85	0.0307	1.41	0.102	1.00	194.7	3	193.7	2
S08-01-01	10266-43.1	352.35	0.33	444	10256	9.33	1.12	6.4E-04	30	0.087	10.8	32.09	1.06	0.057	3.0	0.203	7.10	0.0308	1.11	0.156	1.00	195.6	2	196.2	2
S08-01-01	10266-18.1	589.15	0.51	409	10736	15.60	0.34	1.9E-04	39	0.180	5.6	32.34	1.14	0.052	2.3	0.211	3.51	0.0308	1.14	0.326	1.00	195.7	2	195.8	2
S08-01-01	10266-41.1	296.33	0.34	532	10123	7.87	0.55	3.2E-04	48	0.132	9.4	32.18	1.06	0.059	3.2	0.230	5.55	0.0309	1.09	0.197	1.00	196.2	2	195.3	2
S08-01-01	10266-73.1	347.49	0.35	368	10510	9.27	0.14	8.1E-05	429	0.134	8.9	32.15	1.24	0.055	3.1	0.229	10.11	0.0311	1.38	0.137	1.00	197.2	3	196.4	2
S08-01-01	10266-33.1	158.15	0.38	575	10369	4.23	1.31	7.5E-04	36	0.111	14.5	31.71	1.11	0.055	4.5	0.188	10.92	0.0311	1.21	0.111	1.00	197.6	2	199.0	2
S08-01-01	10266-2.1	597.20	0.40	689	10243	15.98	0.17	9.6E-05	58	0.141	6.2	32.05	1.14	0.053	2.3	0.222	3.04	0.0312	1.14	0.377	1.00	197.7	2	197.4	2
S08-01-01	10266-59.1	567.21	0.55	911	10541	15.19	0.92	5.3E-04	29	0.185	5.8	31.79	1.19	0.052	2.5	0.190	6.03	0.0312	1.22	0.202	1.00	197.9	2	199.2	2
S08-01-01	10266-29.1	298.12	0.30	420	10224	7.99	0.70	4.0E-04	59	0.122	9.6	31.84	1.06	0.052	3.3	0.199	8.57	0.0312	1.14	0.133	1.00	198.0	2	198.9	2
S08-01-01	10266-17.1	336.42	0.36	529	10312	9.02	0.17	9.9E-05	73	0.114	9.1	31.98	1.05	0.051	3.0	0.213	3.94	0.0312	1.06	0.269	1.00	198.2	2	198.3	2
S08-01-01	10266-45.1	370.25	0.34	483	10227	9.95	0.23	1.3E-04	145	0.106	13.6	31.89	1.12	0.056	2.8	0.233	6.01	0.0313	1.17	0.194	1.00	198.6	2	197.7	2
S08-01-01	10266-82.1	255.61	0.50	862	9444	6.88	0.66	3.8E-04	200	0.189	8.5	31.68	1.07	0.055	3.6	0.212	23.36	0.0314	1.71	0.073	1.00	199.0	3	199.3	2
S08-01-01	10266-66.1	359.54	0.54	817	10440	9.72	0.46	2.6E-04	18	0.211	6.9	31.61	1.21	0.054	3.0	0.218	3.77	0.0315	1.22	0.323	1.00	199.9	2	199.9	2
S08-01-01	10266-71.1	429.84	0.40	527	10390	11.70	1.30	7.5E-04	28	0.158	7.0	31.15	1.05	0.056	2.6	0.196	7.84	0.0317	1.11	0.142	1.00	201.1	2	202.3	2
S08-01-01	10266-54.1	185.66	0.28	259	10400	5.06	-0.43	-2.5E-04	198	0.082	15.3	31.67	1.10	0.059	4.0	0.272	12.06	0.0317	1.39	0.115	1.00	201.3	3	198.4	2
S08-01-01	10266-49.1	238.50	0.36	794	10142	6.50	0.21	1.2E-04	16	0.119	11.3	31.46	1.12	0.057	3.6	0.243	3.89	0.0317	1.12	0.287	1.00	201.3	2	200.0	2
S08-01-01	10266-80.1	528.79	0.59	480	10439	14.42	0.85	4.9E-04	34	0.192	6.2	31.24	1.04	0.053	3.2	0.201	6.67	0.0317	1.08	0.163	1.00	201.4	2	202.4	2
S08-01-01	10266-68.1	357.06	0.45	863	10444	9.74	0.42	2.4E-04	37	0.162	7.5	31.37	1.05	0.053	2.9	0.217	4.27	0.0317	1.06	0.249	1.00	201.5	2	201.6	2
S08-01-01	10266-31.1	348.65	0.60	1465	10545	9.51	0.78	4.5E-04	161	0.190	7.1	31.25	1.20	0.057	2.9	0.221	21.53	0.0317	1.75	0.081	1.00	201.5	3	201.4	2
S08-01-01	10266-63.1	305.62	0.33	434	10160	8.36	-0.46	-2.7E-04	2	0.112	10.5	31.54	1.07	0.054	3.4	0.256	3.30	0.0319	1.07	0.323	1.00	202.1	2	200.2	2
S08-01-01	10266-76.1	506.22	0.58	1078	10137	13.85	0.72	4.2E-04	64	0.211	5.5	31.17	1.15	0.055	2.4	0.214	8.65	0.0319	1.24	0.143	1.00	202.1	2	202.5	2
S08-01-01	10266-30.1	521.80	0.57	686	10503	14.29	0.56	3.2E-04	65	0.189	5.9	31.19	1.04	0.051	2.5	0.201	7.43	0.0319	1.10	0.148	1.00	202.3	2	203.4	2
S08-01-01	10266-25.1	311.28	0.40	512	10421	8.53	0.32	1.8E-04	34	0.139	8.6	31.23	1.06	0.056	3.0	0.235	3.78	0.0319	1.06	0.281	1.00	202.5	2	201.8	2
S08-01-01	10266-55.1	917.70	0.52	1336	10261	25.17	0.23	1.3E-04	134	0.180	8.9	31.24	1.02	0.053	1.8	0.224	5.60	0.0319	1.07	0.191	1.00	202.6	2	202.5	2
S08-01-01	10266-34.1	1014.23	0.44	1179	11181	27.90	1.48	8.5E-04	21	0.155	4.8	30.77	1.03	0.062	1.7	0.217	6.01	0.0320	1.08	0.179	1.00	203.2	2	203.4	2
S08-01-01	10266-70.1	605.83	0.44	920	10412	16.67	0.00	1.0E-32	100	0.129	9.9	31.22	1.08	0.051	2.2	0.225	2.45	0.0320	1.08	0.443	1.00	203.3	2	203.1	2
S08-01-01	10266-46.1	283.49	0.43	690	10580	7.85	0.73	4.2E-04	32	0.173	8.2	30.81	1.06	0.054	5.0	0.214	7.12	0.0322	1.09	0.153	1.00	204.4	2	204.9	2
S08-01-01	10266-74.1	512.70	0.76	1189	10257	14.20	0.20	1.2E-04	73	0.251	4.9	30.95	1.11	0.051	2.4	0.221	3.75	0.0322	1.12	0.298	1.00	204.6	2	204.7	2
S08-01-01	10266-75.1	1215.84	0.50	1044	10817	33.71	0.97	5.6E-04	22	0.154	4.2	30.68	1.10	0.052	1.6	0.197	4.72	0.0323	1.12	0.237	1.00	204.8	2	206.2	2
S08-01-01	10266-69.1	371.13	0.24	394	9758	10.40	3.52	2.0E-03	25	0.117	10.6	29.58	1.27	0.057	3.4	0.121	30.09	0.0326	1.56	0.052	1.00	206.9	3	212.5	3

Sample	Spot	ppm U	Th/U	Y ppm	Hf ppm	ppm 206*	% f206207	Atomic Ratios														Ages (Ma)			
								Uncorrected							204 Corrected (1)							206Pb/238U Calibration Error %	204	207	
								204Pb/206Pb	±%	208Pb/206Pb	±%	238U/206Pb	±%	207Pb/206Pb	±%	207Pb*/235U	±%	206Pb*/238U	±%	err corr					
S09-16-01A	10267-21.1	215.97	0.42	488	10830	4.84	4.85	2.8E-03	27	0.159	20.7	36.45	3.88	0.060	6.6	0.062	74.18	0.0261	4.12	0.055	1.27	166.1	7	172.3	7
S09-16-01A	10267-15.1	231.20	0.34	364	10555	5.71	2.22	1.3E-03	19	0.135	13.4	33.98	1.41	0.069	4.2	0.198	9.61	0.0288	1.48	0.154	1.27	182.9	3	182.8	3
S09-16-01A	10267-13.1	185.13	0.48	529	10423	4.66	1.55	8.9E-04	103	0.134	17.3	33.61	1.46	0.067	5.3	0.220	25.92	0.0293	2.18	0.084	1.27	186.1	4	185.1	3
S09-16-01A	10267-52.1	230.08	0.31	445	10531	5.84	2.86	1.7E-03	29	0.120	13.6	32.87	1.48	0.053	4.5	0.115	27.90	0.0296	1.71	0.061	1.27	187.7	3	192.5	3
S09-16-01A	10267-14.1	122.24	0.34	403	10806	3.13	2.56	1.5E-03	24	0.130	21.4	32.65	1.79	0.062	7.4	0.166	17.64	0.0298	1.90	0.107	1.27	189.6	4	191.7	4
S09-16-01A	10267-62.1	235.56	0.42	717	10354	6.08	1.19	6.8E-04	19	0.121	13.7	32.90	1.49	0.063	4.2	0.220	6.36	0.0300	1.51	0.238	1.27	190.8	3	190.1	3
S09-16-01A	10267-82.1	362.98	0.50	475	10774	9.39	1.53	8.9E-04	21	0.173	8.7	32.70	1.34	0.052	3.5	0.161	8.83	0.0301	1.39	0.157	1.27	191.2	3	193.7	3
S09-16-01A	10267-80.1	468.02	0.56	1094	10420	12.17	0.34	2.0E-04	29	0.191	7.2	32.92	1.50	0.055	3.0	0.216	3.87	0.0303	1.50	0.387	1.27	192.3	3	191.8	3
S09-16-01A	10267-33.1	368.37	0.53	900	10343	9.58	1.60	9.2E-04	35	0.179	9.1	32.50	1.33	0.058	3.6	0.185	11.94	0.0303	1.45	0.121	1.27	192.3	3	193.6	3
S09-16-01A	10267-70.1	360.48	0.36	484	10005	9.39	0.24	1.4E-04	263	0.119	11.1	32.88	1.54	0.050	3.8	0.199	12.27	0.0303	1.67	0.136	1.27	192.7	3	193.2	3
S09-16-01A	10267-58.1	184.88	0.34	542	10464	4.86	3.21	1.9E-03	32	0.135	13.9	31.61	1.49	0.057	4.8	0.124	33.19	0.0306	1.84	0.056	1.27	194.4	4	199.1	3
S09-16-01A	10267-57.1	357.67	0.44	422	10171	9.41	1.42	8.2E-04	36	0.143	9.5	32.20	1.33	0.054	3.5	0.176	11.47	0.0306	1.42	0.124	1.27	194.4	3	196.3	3
S09-16-01A	10267-1.1_A	233.75	0.54	495	10425	6.16	1.16	6.7E-04	24	0.195	10.7	32.23	1.49	0.054	4.5	0.189	7.90	0.0307	1.52	0.192	1.27	194.7	3	196.0	3
S09-16-01A	10267-29.1	180.13	0.49	537	9650	4.76	2.24	1.3E-03	35	0.200	12.3	31.76	1.47	0.053	5.4	0.145	21.91	0.0308	1.67	0.076	1.27	195.4	3	199.1	3
S09-16-01A	10267-77.1	164.09	0.33	521	10794	4.34	1.08	6.2E-04	63	0.117	16.6	32.12	1.65	0.058	5.0	0.206	13.50	0.0308	1.79	0.132	1.27	195.5	3	195.9	3
S09-16-01A	10267-74.1	219.82	0.38	687	10687	5.83	0.69	4.0E-04	26	0.121	15.4	32.16	1.37	0.053	4.7	0.200	6.40	0.0309	1.38	0.216	1.27	196.1	3	196.8	3
S09-16-01A	10267-81.1	350.34	0.53	729	10907	9.30	0.86	5.0E-04	39	0.195	8.5	32.07	1.81	0.052	3.7	0.189	7.93	0.0309	1.84	0.232	1.27	196.3	4	197.6	4
S09-16-01A	10267-16.1	281.00	0.55	760	10696	7.48	1.39	8.0E-04	73	0.205	12.3	31.81	1.74	0.050	5.3	0.164	24.04	0.0310	2.02	0.084	1.27	196.8	4	199.5	3
S09-16-01A	10267-18.1	479.13	0.49	370	10465	12.76	0.34	1.9E-04	32	0.168	8.1	32.15	1.34	0.053	3.1	0.215	4.03	0.0310	1.34	0.333	1.27	196.8	3	196.8	3
S09-16-01A	10267-111.1	152.55	0.42	477	9797	4.09	2.05	1.2E-03	42	0.111	17.3	31.41	2.26	0.056	5.4	0.165	21.12	0.0312	2.42	0.115	1.27	197.9	5	200.6	5
S09-16-01A	10267-65.1	234.98	0.44	760	10383	6.31	3.08	1.8E-03	29	0.120	13.1	30.98	1.55	0.054	6.6	0.119	31.60	0.0313	1.80	0.057	1.27	198.6	4	203.8	3
S09-16-01A	10267-91.1	474.44	0.37	643	9816	12.75	1.50	8.6E-04	30	0.127	8.8	31.48	1.33	0.051	3.1	0.166	11.20	0.0313	1.40	0.125	1.27	198.6	3	201.4	3
S09-16-01A	10267-71.1	367.32	0.43	494	10510	9.88	1.71	9.8E-04	34	0.145	9.6	31.39	1.33	0.057	3.4	0.182	13.00	0.0313	1.46	0.112	1.27	198.8	3	200.6	3
S09-16-01A	10267-11.1	438.51	0.55	840	10725	11.80	1.15	6.6E-04	68	0.160	10.9	31.56	1.86	0.060	3.9	0.216	14.35	0.0313	2.02	0.141	1.27	198.8	4	198.9	4
S09-16-01A	10267-69.1	362.14	0.57	903	10575	9.75	0.32	1.8E-04	36	0.184	8.5	31.81	1.97	0.057	3.4	0.233	4.45	0.0313	1.98	0.444	1.27	198.9	4	198.0	4
S09-16-01A	10267-10.1	317.85	0.39	946	10488	8.56	0.00	1.0E-32	100	0.109	12.8	31.90	1.37	0.051	4.2	0.219	4.38	0.0313	1.37	0.314	1.27	199.0	3	198.8	3
S09-16-01A	10267-88.1	274.75	0.33	219	10879	7.40	0.59	3.4E-04	33	0.154	11.6	31.70	1.62	0.063	4.0	0.252	5.44	0.0314	1.63	0.299	1.27	199.1	3	197.2	3
S09-16-01A	10267-1.1	364.34	0.49	730	10391	9.83	1.67	9.6E-04	24	0.200	9.4	31.31	1.35	0.051	4.1	0.161	11.06	0.0314	1.41	0.128	1.27	199.3	3	202.4	3
S09-16-01A	10267-9.1	572.79	0.66	613	10444	15.46	0.85	4.9E-04	25	0.226	6.4	31.55	1.36	0.057	2.8	0.214	5.14	0.0314	1.38	0.269	1.27	199.5	3	199.6	3
S09-16-01A	10267-110.1	224.37	0.39	479	10260	6.08	0.00	1.0E-32	100	0.110	15.6	31.69	1.39	0.055	4.8	0.239	5.04	0.0316	1.39	0.276	1.27	200.3	3	199.1	3
S09-16-01A	10267-31.1	441.85	0.58	843	10141	11.99	3.98	2.3E-03	20	0.239	7.1	30.39	1.56	0.070	2.9	0.158	20.86	0.0316	1.77	0.085	1.27	200.5	3	203.8	3
S09-16-01A	10267-87.1	176.98	0.40	459	11067	4.81	1.32	7.6E-04	21	0.153	12.8	31.16	1.57	0.051	6.0	0.172	10.00	0.0317	1.59	0.159	1.27	201.0	3	203.5	3
S09-16-01A	10267-37.1	413.10	0.47	818	10084	11.24	2.93	1.7E-03	30	0.210	10.3	30.64	1.84	0.067	3.9	0.182	19.68	0.0317	2.05	0.104	1.27	201.1	4	203.1	4
S09-16-01A	10267-25.1	319.65	0.51	579	10670	8.70	1.92	1.1E-03	38	0.187	10.7	30.95	1.39	0.059	4.2	0.185	16.20	0.0317	1.58	0.097	1.27	201.1	3	202.9	3
S09-16-01A	10267-85.1	399.51	0.44	514	10400	10.88	0.96	5.5E-04	45	0.177	8.4	31.23	1.47	0.062	3.2	0.236	7.84	0.0317	1.53	0.195	1.27	201.2	3	200.3	3
S09-16-01A	10267-72.1	254.16	0.39	296	10527	6.96	0.97	5.6E-04	19	0.145	11.2	31.09	1.43	0.050	4.2	0.182	6.52	0.0319	1.44	0.221	1.27	202.2	3	204.2	3
S09-16-01A	10267-86.1	466.26	0.54	325	10531	12.92	0.65	3.7E-04	35	0.199	10.3	30.81	1.38	0.057	4.3	0.230	6.18	0.0323	1.40	0.226	1.27	204.6	3	204.3	3

Sample	Spot	ppm U	Th/U	Y ppm	Hf ppm	ppm 206*	% f206207	Atomic Ratios														Ages (Ma)			
								Uncorrected							204 Corrected (1)							206Pb/238U Calibration Error %	204	207	
								204Pb /206Pb	±%	208Pb /206Pb	±%	238U/ 206Pb	±%	207Pb /206Pb	±%	207Pb* /235U	±%	206Pb* /238U	±%	err corr					
S09-16-01B	10268-20.1	499.74	0.21	813	10944	13.00	0.78	4.5E-04	35	0.078	10.0	32.76	1.36	0.050	2.8	0.181	6.49	0.0303	1.39	0.214	1.27	192.3	3	193.8	3
S09-16-01B	10268-36.1	292.55	0.32	1058	10770	7.66	1.40	8.1E-04	13	0.115	11.2	32.33	1.33	0.049	3.7	0.157	6.60	0.0305	1.34	0.203	1.27	193.7	3	196.5	3
S09-16-01B	10268-54.1	471.18	0.22	618	11359	12.35	0.62	3.6E-04	38	0.068	13.6	32.58	1.33	0.055	3.3	0.209	5.66	0.0305	1.35	0.238	1.27	193.7	3	193.8	3
S09-16-01B	10268-44.1	441.80	0.24	748	11353	11.60	0.64	3.7E-04	30	0.086	11.5	32.49	1.63	0.056	3.1	0.213	5.06	0.0306	1.64	0.325	1.27	194.2	3	194.0	3
S09-16-01B	10268-51.1	761.84	0.28	688	12712	20.13	0.22	1.2E-04	32	0.095	8.3	32.45	1.30	0.056	2.4	0.228	3.01	0.0308	1.30	0.433	1.27	195.3	3	194.4	3
S09-16-01B	10268-55.1	582.17	0.24	928	12466	15.39	-0.12	-7.2E-05	144	0.082	11.0	32.53	1.39	0.053	3.0	0.231	4.27	0.0308	1.41	0.329	1.27	195.5	3	194.5	3
S09-16-01B	10268-43.1	446.97	0.24	731	11805	11.83	0.72	4.2E-04	103	0.061	14.6	32.22	1.32	0.054	3.2	0.202	13.89	0.0308	1.52	0.109	1.27	195.7	3	196.2	3
S09-16-01B	10268-24.1	562.71	0.24	933	11160	14.90	0.30	1.7E-04	38	0.074	9.5	32.35	1.59	0.055	2.5	0.221	3.55	0.0308	1.59	0.449	1.27	195.7	3	195.2	3
S09-16-01B	10268-49.1	702.66	0.29	1286	11225	18.63	0.25	1.5E-04	141	0.089	9.2	32.32	1.32	0.055	2.6	0.226	6.45	0.0309	1.37	0.213	1.27	195.9	3	195.2	3
S09-16-01B	10268-22.1	281.64	0.39	844	11027	7.48	1.82	1.0E-03	24	0.178	10.2	31.76	1.35	0.057	3.8	0.176	10.74	0.0309	1.43	0.133	1.27	196.3	3	198.3	3
S09-16-01B	10268-35.1	855.25	0.37	701	11693	22.79	0.35	2.0E-04	60	0.127	5.9	32.12	1.32	0.051	2.1	0.207	4.54	0.0310	1.34	0.295	1.27	196.9	3	197.3	3
S09-16-01B	10268-46.1	702.97	0.29	1148	10851	18.81	0.20	1.1E-04	35	0.101	8.4	32.04	1.35	0.053	2.6	0.221	3.20	0.0312	1.35	0.421	1.27	197.8	3	197.5	3
S09-16-01B	10268-16.1	368.03	0.20	526	11058	9.88	0.00	1.0E-32	100	0.075	12.6	32.01	1.33	0.050	3.4	0.217	3.67	0.0312	1.33	0.362	1.27	198.3	3	198.2	3
S09-16-01B	10268-31.1	477.11	0.23	842	10887	12.84	0.97	5.6E-04	37	0.082	10.7	31.62	1.31	0.051	3.0	0.184	8.27	0.0313	1.36	0.165	1.27	198.8	3	200.5	3
S09-16-01B	10268-38.1	534.50	0.29	688	11930	14.40	0.17	9.7E-05	296	0.087	9.6	31.83	1.31	0.051	2.8	0.217	8.95	0.0314	1.40	0.156	1.27	199.1	3	199.1	3
S09-16-01B	10268-33.1	611.23	0.27	933	11461	16.47	0.25	1.4E-04	33	0.082	9.8	31.79	1.39	0.047	2.8	0.195	3.63	0.0314	1.39	0.384	1.27	199.2	3	200.3	3
S09-16-01B	10268-15.1	509.86	0.22	714	11600	13.75	0.18	1.1E-04	40	0.072	10.8	31.80	1.35	0.050	2.9	0.208	3.52	0.0314	1.35	0.382	1.27	199.2	3	199.7	3
S09-16-01B	10268-56.1	633.41	0.22	1056	10834	17.09	0.31	1.8E-04	48	0.093	9.9	31.73	1.31	0.053	2.9	0.219	4.18	0.0314	1.32	0.316	1.27	199.4	3	199.3	3
S09-16-01B	10268-32.1	586.22	0.34	1125	12260	15.82	0.71	4.1E-04	16	0.111	8.3	31.60	1.31	0.052	2.7	0.197	3.93	0.0314	1.32	0.335	1.27	199.4	3	200.5	3
S09-16-01B	10268-42.1	511.31	0.26	893	11366	13.80	0.45	2.6E-04	20	0.086	10.7	31.68	1.32	0.054	3.0	0.218	3.83	0.0314	1.32	0.345	1.27	199.5	3	199.4	3
S09-16-01B	10268-8.1	332.64	0.21	571	11143	8.98	0.92	5.3E-04	146	0.094	11.3	31.51	1.35	0.051	3.4	0.189	26.83	0.0314	1.91	0.071	1.27	199.6	4	201.1	3
S09-16-01B	10268-37.1	272.63	0.30	457	10322	7.37	0.00	1.0E-32	100	0.126	15.7	31.77	1.36	0.053	4.2	0.232	4.41	0.0315	1.36	0.308	1.27	199.8	3	199.0	3
S09-16-01B	10268-12.1	472.38	0.28	955	10802	12.99	1.03	5.9E-04	28	0.101	9.1	30.92	1.32	0.052	2.8	0.191	6.79	0.0320	1.35	0.199	1.27	203.1	3	204.8	3
S09-16-01B	10268-7.1	573.96	0.60	1311	11202	15.93	0.99	5.7E-04	31	0.205	5.7	30.64	1.30	0.052	2.5	0.193	6.92	0.0323	1.34	0.193	1.27	205.0	3	206.6	3
S09-16-01B	10268-11.1	596.12	0.29	1124	11721	16.94	0.35	2.0E-04	63	0.085	9.9	30.12	1.39	0.053	2.8	0.230	4.94	0.0331	1.41	0.286	1.27	209.8	3	209.8	3
S09-16-01B	10268-17.1	545.75	0.26	802	12093	16.54	0.73	4.2E-04	126	0.083	9.2	28.13	1.31	0.052	2.6	0.223	17.46	0.0353	1.60	0.092	1.27	223.6	4	224.8	3
S09-16-01B	10268-52.1	431.51	0.39	792	11238	20.70	0.23	1.3E-04	40	0.123	9.0	17.87	1.36	0.057	2.9	0.427	3.60	0.0558	1.36	0.378	1.27	350.3	5	349.5	5

Sample	Spot	ppm Σ	Th/U	Y ppm	Hf ppm	ppm 206 *	% 206 207	Atomic Ratios													Ages (Ma)				
								Uncorrected						204 Corrected (1)							204		207		
								204Pb/206Pb	$\pm\%$	208Pb/206Pb	$\pm\%$	238U/206Pb	$\pm\%$	207Pb/206Pb	$\pm\%$	207Pb*/235U	$\pm\%$	206Pb*/238U	$\pm\%$	err corr	206Pb/238U Calibration Error %	206Pb*/238U Age	206Pb*/238U Age		
S09-16-01C	10269-18.1	184.97	0.41	445	10734	4.54	2.93	1.7E-03	30	0.132	12.9	33.97	1.10	0.057	4.2	0.125	25.79	0.0286	1.42	0.055	1.0	181.6	3	185.5	2
S09-16-01C	10269-26.1	387.65	0.47	939	10281	9.76	0.36	2.1E-04	32	0.149	8.2	33.98	1.19	0.052	3.1	0.197	4.01	0.0293	1.20	0.299	1.0	186.3	2	186.5	2
S09-16-01C	10269-14.1	237.36	0.37	608	10168	5.99	1.68	9.7E-04	29	0.126	11.4	33.49	1.25	0.050	4.0	0.146	12.99	0.0294	1.34	0.103	1.0	186.5	2	189.6	2
S09-16-01C	10269-17.1	240.26	0.49	811	10066	6.12	1.62	9.3E-04	47	0.170	9.6	33.20	1.53	0.052	3.8	0.158	18.01	0.0296	1.72	0.095	1.0	188.2	3	190.7	3
S09-16-01C	10269-2.1	191.68	0.34	453	11522	4.93	1.08	6.2E-04	40	0.110	13.6	33.04	1.10	0.056	4.1	0.195	9.35	0.0299	1.18	0.126	1.0	190.2	2	190.8	2
S09-16-01C	10269-25.1	172.70	0.41	504	10652	4.45	0.00	1.0E-32	100	0.123	13.5	33.37	1.32	0.053	6.1	0.220	6.20	0.0300	1.32	0.213	1.0	190.3	2	189.6	3
S09-16-01C	10269-6.1	202.65	0.41	694	10296	5.27	0.54	3.1E-04	27	0.119	12.4	32.87	1.16	0.054	4.1	0.208	5.28	0.0303	1.17	0.221	1.0	192.2	2	192.2	2
S09-16-01C	10269-3.1	167.02	0.40	573	10138	4.37	1.90	1.1E-03	42	0.109	15.0	32.21	1.88	0.053	4.6	0.153	20.50	0.0305	2.05	0.100	1.0	193.4	4	196.5	4
S09-16-01C	10269-33.1	250.64	0.59	1075	10431	6.56	2.14	1.2E-03	13	0.214	8.5	32.10	1.08	0.055	3.7	0.153	8.88	0.0305	1.12	0.126	1.0	193.6	2	196.7	2
S09-16-01C	10269-38.1	351.99	0.64	746	10803	9.24	1.03	5.9E-04	28	0.204	7.6	32.39	1.29	0.054	3.2	0.190	6.79	0.0306	1.32	0.195	1.0	194.1	3	195.2	3
S09-16-01C	10269-32.1	401.90	0.72	1988	9685	10.57	0.53	3.0E-04	32	0.254	6.1	32.49	1.05	0.049	3.1	0.188	4.82	0.0306	1.06	0.221	1.0	194.4	2	195.7	2
S09-16-01C	10269-16.1	519.54	0.50	1601	10229	13.69	0.72	4.2E-04	23	0.175	6.2	32.36	1.15	0.053	2.5	0.196	4.30	0.0307	1.16	0.271	1.0	194.8	2	195.6	2
S09-16-01C	10269-43.1	443.97	0.45	1034	10365	11.79	0.77	4.5E-04	38	0.144	7.6	32.11	1.13	0.053	2.8	0.197	6.46	0.0309	1.17	0.181	1.0	196.2	2	197.1	2
S09-16-01C	10269-42.1	208.18	0.40	779	10026	5.53	2.44	1.4E-03	31	0.133	11.6	31.54	1.44	0.057	3.9	0.155	19.67	0.0309	1.64	0.084	1.0	196.4	3	199.5	3
S09-16-01C	10269-48.1	165.30	0.32	517	10518	4.40	0.72	4.1E-04	154	0.102	14.7	32.03	1.66	0.055	4.5	0.211	19.78	0.0310	2.00	0.101	1.0	196.8	4	196.9	3
S09-16-01C	10269-5.1	269.33	0.46	928	10154	7.17	0.77	4.4E-04	25	0.172	9.1	32.01	1.32	0.054	3.6	0.202	5.52	0.0310	1.34	0.242	1.0	196.8	3	197.4	3
S09-16-01C	10269-10.1	327.93	0.39	998	10195	8.74	0.18	1.1E-04	284	0.154	8.4	32.19	1.06	0.054	3.2	0.224	9.07	0.0310	1.18	0.130	1.0	196.9	2	196.3	2
S09-16-01C	10269-30.1	219.32	0.62	1107	9996	5.85	0.50	2.9E-04	147	0.260	9.7	32.03	1.24	0.050	4.1	0.195	14.45	0.0311	1.44	0.100	1.0	197.2	3	198.2	2
S09-16-01C	10269-20.1	564.70	0.56	1687	9627	15.07	-0.02	-1.2E-05	1785	0.201	5.6	32.20	1.03	0.053	2.4	0.227	6.23	0.0311	1.09	0.176	1.0	197.2	2	196.5	2
S09-16-01C	10269-45.1	306.84	0.48	723	10366	8.19	0.78	4.5E-04	40	0.144	11.2	31.92	1.75	0.049	4.7	0.182	8.61	0.0311	1.78	0.207	1.0	197.3	3	199.1	3
S09-16-01C	10269-27.1	245.25	0.38	730	10185	6.57	-0.04	-2.4E-05	1363	0.105	12.4	32.10	1.30	0.054	3.8	0.233	9.65	0.0312	1.41	0.147	1.0	197.8	3	196.9	3
S09-16-01C	10269-41.1	349.51	0.60	1122	10383	9.37	0.98	5.6E-04	53	0.210	7.4	31.73	1.30	0.049	3.4	0.175	11.79	0.0312	1.40	0.118	1.0	198.1	3	200.3	3
S09-16-01C	10269-44.1	217.86	0.45	971	9527	5.84	-0.34	-2.0E-04	249	0.123	19.3	32.15	1.56	0.050	4.3	0.229	14.05	0.0312	1.78	0.126	1.0	198.1	3	197.4	3
S09-16-01C	10269-13.1	224.77	0.31	628	10855	6.06	-0.17	-1.0E-04	150	0.119	11.8	31.91	1.08	0.056	3.9	0.247	5.45	0.0314	1.11	0.204	1.0	199.3	2	197.7	2
S09-16-01C	10269-4.1	430.04	0.37	790	11808	11.62	0.54	3.1E-04	72	0.128	8.2	31.61	1.05	0.049	2.9	0.194	8.25	0.0315	1.12	0.135	1.0	199.7	2	200.9	2
S09-16-01C	10269-22.1	588.63	0.54	1449	10410	15.93	0.00	1.0E-32	100	0.174	11.3	31.73	1.03	0.051	2.4	0.222	2.63	0.0315	1.03	0.393	1.0	200.0	2	199.8	2
S09-16-01C	10269-47.1	293.94	0.59	1246	10477	7.98	1.54	8.9E-04	28	0.190	9.3	31.16	1.10	0.058	3.7	0.197	9.64	0.0316	1.18	0.122	1.0	200.5	2	201.7	2
S09-16-01C	10269-11.1	307.80	0.60	1267	10323	8.39	1.15	6.6E-04	32	0.234	7.6	31.17	1.08	0.057	3.4	0.208	7.92	0.0317	1.14	0.144	1.0	201.3	2	201.9	2
S09-16-01C	10269-8.1	456.14	0.61	1661	10494	12.45	1.19	6.9E-04	33	0.213	6.0	31.11	1.06	0.053	2.7	0.187	8.61	0.0318	1.13	0.131	1.0	201.6	2	203.3	2
S09-16-01C	10269-7.1	677.39	0.73	2189	10345	18.58	0.30	1.7E-04	36	0.250	4.5	31.22	1.04	0.052	2.2	0.216	3.15	0.0319	1.05	0.333	1.0	202.6	2	202.9	2
S09-16-01C	10269-12.1	954.11	0.90	1714	10531	27.11	0.54	3.1E-04	34	0.300	3.5	30.07	1.03	0.051	1.9	0.211	4.13	0.0331	1.05	0.255	1.0	209.8	2	210.8	2

Sample	Spot	ppmU	Th/U	Y ppm	Hf ppm	ppm 206*	%f206207	Atomic Ratios														Ages (Ma)			
								Uncorrected							204 Corrected (1)							204	207		
								204Pb/206Pb	±%	208Pb/206Pb	±%	238U/206Pb	±%	207Pb/206Pb	±%	207Pb*/235U	±%	206Pb*/238U	±%	err corr	206Pb/238U Calibration Error %	206Pb*/238U Age	206Pb*/238U Age		
S09-16-01D	10270-39.1	591.35	0.23	911	11151	15.00	1.08	6.2E-04	20	0.086	9.4	33.50	1.04	0.052	2.6	0.175	5.49	0.0295	1.06	0.193	1.0	187.6	2	189.1	2
S09-16-01D	10270-81.1	355.08	0.22	558	11813	9.13	0.34	1.9E-04	32	0.077	12.1	33.31	1.06	0.052	3.3	0.201	4.08	0.0299	1.06	0.260	1.0	190.1	2	190.3	2
S09-16-01D	10270-95.1	224.37	0.40	450	11713	5.79	2.36	1.4E-03	24	0.137	11.3	32.53	1.83	0.054	4.0	0.140	16.17	0.0300	1.92	0.119	1.0	190.7	4	194.3	4
S09-16-01D	10270-105.1	444.62	0.35	816	11180	11.49	1.09	6.3E-04	28	0.125	8.2	32.88	1.05	0.057	2.7	0.198	6.52	0.0301	1.09	0.167	1.0	191.0	2	191.5	2
S09-16-01D	10270-69.1	667.58	0.26	1083	11396	17.45	0.71	4.1E-04	63	0.087	8.2	32.64	1.14	0.051	2.4	0.191	8.93	0.0304	1.23	0.137	1.0	193.2	2	194.2	2
S09-16-01D	10270-87.1	297.95	0.35	389	10012	7.86	1.24	7.2E-04	37	0.118	10.5	32.15	1.07	0.056	3.4	0.192	9.75	0.0307	1.16	0.119	1.0	195.0	2	196.1	2
S09-16-01D	10270-2.1	603.23	0.27	973	10880	15.94	0.38	2.2E-04	22	0.093	8.3	32.39	1.04	0.053	2.4	0.213	3.15	0.0308	1.04	0.330	1.0	195.3	2	195.2	2
S09-16-01D	10270-47.1	463.79	0.27	823	10878	12.26	1.22	7.1E-04	34	0.122	9.7	32.10	1.21	0.054	3.2	0.185	9.22	0.0308	1.28	0.139	1.0	195.4	2	196.8	2
S09-16-01D	10270-70.1	435.16	0.29	767	11171	11.58	1.02	5.9E-04	28	0.095	14.8	31.95	1.05	0.051	2.9	0.180	6.94	0.0310	1.09	0.157	1.0	196.6	2	198.4	2
S09-16-01D	10270-41.1	822.67	0.27	1131	12278	21.89	0.96	5.5E-04	17	0.090	7.2	31.98	1.03	0.052	2.1	0.187	4.14	0.0310	1.04	0.251	1.0	196.6	2	198.1	2
S09-16-01D	10270-44.1	405.98	0.26	519	10940	10.80	0.52	3.0E-04	18	0.098	10.0	32.11	1.05	0.056	3.0	0.220	3.75	0.0310	1.06	0.282	1.0	196.7	2	196.3	2
S09-16-01D	10270-51.1	432.88	0.15	438	12851	11.54	0.61	3.5E-04	127	0.056	13.3	32.02	1.05	0.052	3.0	0.202	14.35	0.0310	1.31	0.091	1.0	197.0	3	197.7	2
S09-16-01D	10270-29.1	883.77	0.32	1279	12263	23.59	0.36	2.1E-04	41	0.108	6.3	32.06	1.06	0.053	2.0	0.215	3.46	0.0311	1.07	0.310	1.0	197.3	2	197.3	2
S09-16-01D	10270-45.1	386.73	0.25	565	11684	10.47	0.88	5.1E-04	38	0.082	11.6	31.46	1.06	0.054	3.2	0.201	7.31	0.0315	1.11	0.152	1.0	200.0	2	200.8	2
S09-16-01D	10270-11.1	474.60	0.24	751	11846	12.89	0.49	2.8E-04	25	0.070	11.2	31.48	1.05	0.052	2.8	0.210	3.90	0.0316	1.06	0.271	1.0	200.6	2	201.1	2
S09-16-01D	10270-1.1	356.09	0.33	413	10770	9.67	0.39	2.3E-04	36	0.112	9.8	31.50	1.09	0.054	3.1	0.219	4.26	0.0316	1.10	0.258	1.0	200.7	2	200.6	2
S09-16-01D	10270-88.1	129.22	0.39	690	9407	3.52	1.84	1.1E-03	118	0.145	14.3	30.93	1.30	0.063	4.8	0.206	40.53	0.0317	2.57	0.063	1.0	201.4	5	202.1	3
S09-16-01D	10270-35.1	167.27	0.33	654	9991	4.61	0.77	4.4E-04	33	0.140	13.4	30.93	1.13	0.059	4.5	0.234	6.58	0.0321	1.16	0.176	1.0	203.6	2	202.9	2
S09-16-01D	10270-5.1	803.09	0.23	1654	11440	25.18	0.57	3.3E-04	33	0.064	12.7	27.24	1.36	0.054	2.2	0.246	4.28	0.0365	1.38	0.321	1.0	231.1	3	231.6	3
S09-16-01D	10270-19.1	412.08	0.42	1534	9924	16.56	0.07	3.9E-05	55	0.169	6.1	21.36	1.05	0.057	2.4	0.362	2.68	0.0468	1.05	0.393	1.0	294.8	3	293.5	3

Spot name follows the GSC SHRIMP laboratory convention x-y.z; where x = sample number, y = grain number and z = spot number. Multiple analyses in an individual spot are labelled as x-y.z.z

Uncertainties reported at 1s and are calculated by using SQUID 2.22.08.04.30, rev. 30 Apr 2008

f206₂₀₇ refers to mole fraction of total 206Pb that is due to common Pb, calculated using the 207Pb-method; common Pb composition used is the surface blank (4/6: 0.05770; 7/6: 0.89500; 8/6: 2.13840)

* refers to radiogenic Pb (corrected for common Pb) (1) based on 204 method; (2) based on 207 method

Discordance relative to origin = 100 * ((207/206 age -206/238 age)/(207Pb/206Pb age))

Calibration standard 6266; U = 910 ppm; Age = 559 Ma; 206Pb/238U = 0.09059

Error in ²⁰⁶Pb/²³⁸U calibration is 1.0% and 1.27% for Calibrations 1 and 2 respectively (included)

Standard Error in Standard calibration was 0.22% and 0.32 for calibrations 1 and 2 respectively (not included in above errors but required when comparing data from different mounts).

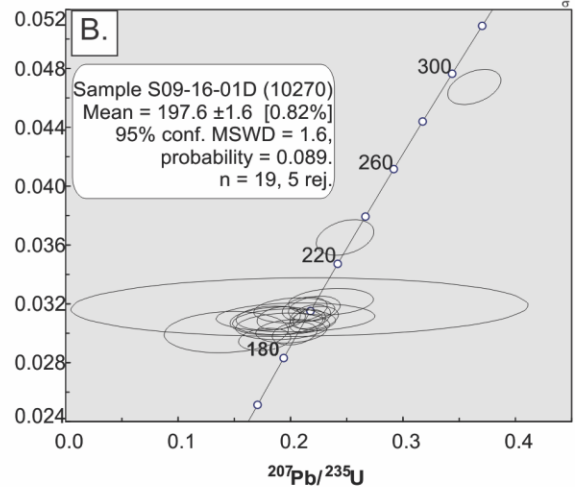
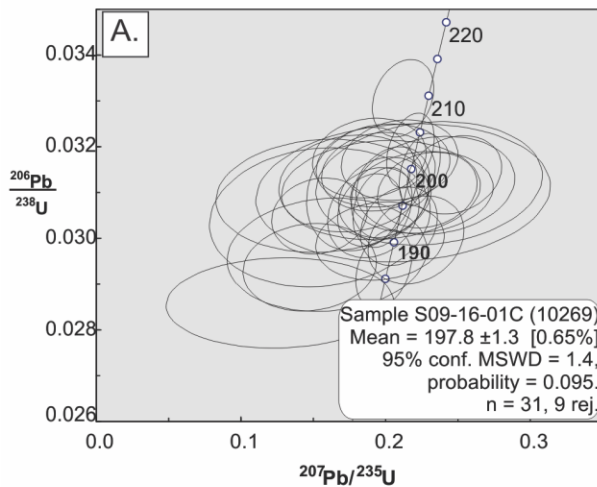
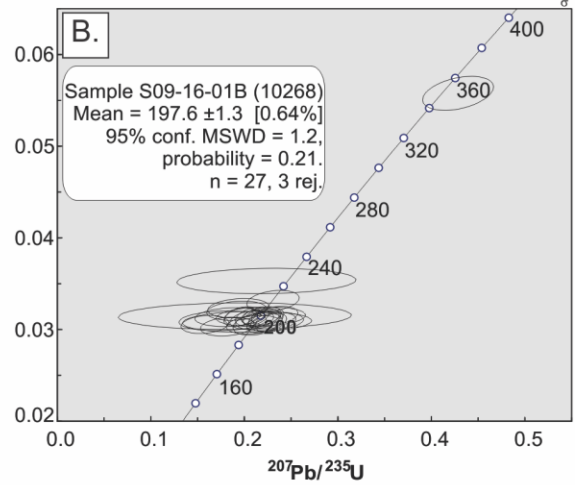
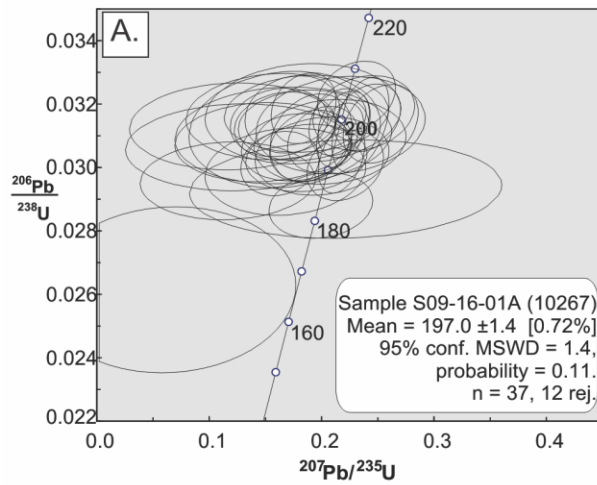
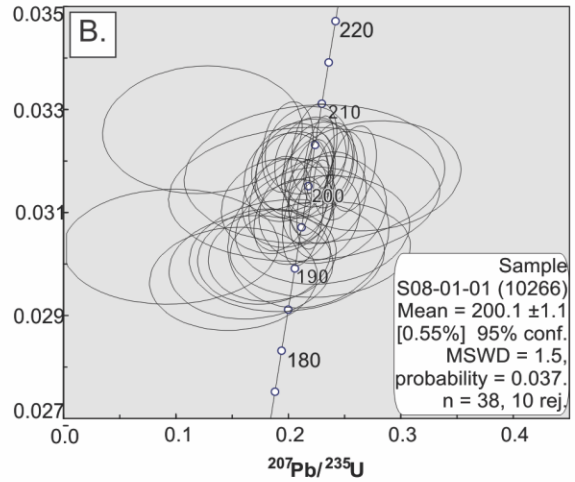
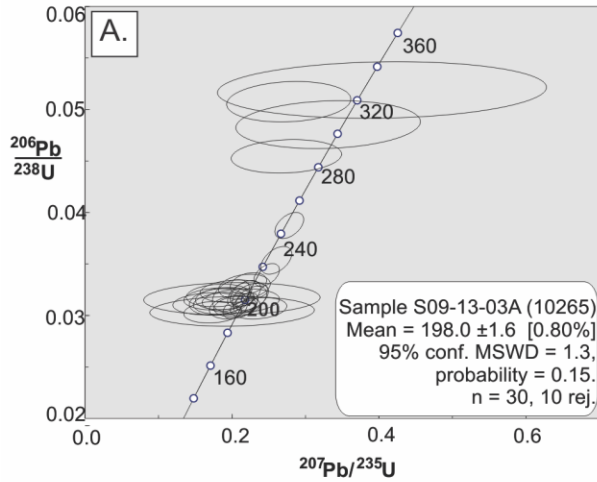


Figure 35: Concordia diagrams for U-Pb SHRIMP analysis of KGd zircons to examine relative cooling ages between variably deformed and altered samples in contact with one another. Data-point error ellipses are 2σ . A. Undeformed and unaltered KGd host rock (S09-13-03A, shown in Figure 6B) B. KGd enclave (S08-01-01, shown in Figure 6B). C. through F. Stacked sequence of variably altered and deformed KGd (from top to bottom: samples S09-16-01A, S09-16-01B, S09-16-01C, and S09-16-01D, shown in Figure 14C).

2.5.1.3 Results

2.5.1.3.1 Suite One

Sample S09-13-01A composes massive, unaltered KGd. Twenty-nine zircons were analysed by SHRIMP and the $^{207}\text{Pb}/^{206}\text{Pb}$ of eighteen of these is 198.0 ± 1.6 Ma (Table 4, Figure 35A), which is interpreted as the emplacement age of this granodiorite. The youngest (182 Ma) and oldest (208 Ma to 310 Ma) results were rejected from the calculation of the mean and are interpreted to represent minor Pb loss and inheritance, respectively.

Sample S08-01-01 composes altered granodiorite. Zircons for this sample were recovered by Apatite to Zircon, Inc. Forty-eight zircons were analysed by SHRIMP and the $^{207}\text{Pb}/^{206}\text{Pb}$ of 38 of these is 200 ± 1.1 Ma (Table 4; Figure 35B), which is interpreted as the emplacement age of this granodiorite. The youngest (189 Ma to 194 Ma) and oldest (206 Ma to 213 Ma) results were rejected from the calculation of the mean and are interpreted to represent minor Pb loss and inheritance, respectively.

2.5.1.3.2 Suite Two

Sample S09-16-03A comprises banded gneiss which is pervasively weathered and stained by hematite from weathered gossanous sulphides within the rock mass. Gneissic bands are tightly folded, with more felsic bands (volumetrically 75% of the rock) measuring 3 mm to 1 cm in thickness, and darker coloured magnetite-rich bands (25 vol.% of rock) measuring 2 mm to 5 mm. Forty-nine zircons were analysed by SHRIMP and the $^{207}\text{Pb}/^{206}\text{Pb}$ of thirty-seven of these is 197.0 ± 1.4 Ma (Table 4; Figure 35C), which is interpreted as the emplacement age of this granodiorite. The youngest (166 Ma to 190 Ma) and oldest (206 Ma) results were rejected from the calculation of the mean and are interpreted to represent minor Pb loss and inheritance, respectively.

Sample S09-16-03B comprises massive KGd. K-feldspar megacrysts (20 vol.%) are 1 to 2 centimetres in length and are well aligned, possibly due to magmatic lineation. Plagioclase (40 vol.%) grains are several millimetres in size, eu- to sub-hedral, and do not exhibit visible solid state recrystallization textures. Plagioclase appears blue-green, possibly due to argillization or malachite weathering from weathered Cu-sulphides. Biotite (35 vol.%) is randomly oriented black books at the centimetres scale. Quartz is present as quartz eyes (5 vol.%). Twenty-seven zircons were analysed by SHRIMP and the Pb^{207}/Pb^{206} of twenty-five of these is 197.6 ± 1.3 Ma (Table 4, Figure 35E), which is interpreted as the emplacement age of this granodiorite. The oldest (210-350 Ma) results were rejected from the calculation of the mean and are interpreted to represent inheritance.

Sample S09-16-03C composes stage 3 deformed KGd. K-feldspar megacryst augens (20 vol.%) measure 4-5 mm locally but are up to 1cm. Plagioclase (40 vol.%) is present as microlithons up to several centimetres in length and are aligned with weakly anastomosing S_P foliation. Plagioclase is blue-green in colour, either from argillization or malachite staining. Biotite (<5 vol.%) is present as weakly anastomosing S_P foliation. Trace fine-grained disseminated chalcopyrite and bornite are present as accessories. Thirty-one zircons were analysed by SHRIMP and the $^{207}Pb/^{206}Pb$ of twenty-two of these is 197.8 ± 1.3 Ma (Table 4, Figure 35E), which is interpreted as the emplacement age of this granodiorite. The youngest (182 Ma to 190 Ma) and oldest (210 Ma) results were rejected from the calculation of the mean and are interpreted to represent minor Pb loss and inheritance, respectively.

Sample S09-16-03D composes massive KGd. K-feldspar (10 vol.%) is present mainly as randomly oriented megacrysts up to 3 cm. Plagioclase (35 vol.%) is present as euhedral to subhedral crystals and is chalky white, possibly due to argillisation. Biotite (25-30 vol.%) is

present as randomly oriented books 1 to 2 mm in size. Quartz (5 vol.%) is present as quartz eyes up to 5 mm. Patchy fine to medium grained epidote (3-5 vol.%) is associated with biotite, but it is not clear whether it is igneous in origin or related to alteration. Nineteen zircons were analysed by SHRIMP and the $^{207}\text{Pb}/^{206}\text{Pb}$ of fourteen of these is 197.6 ± 1.6 Ma (Table 4, Figure 35F), which is interpreted as the emplacement age of this granodiorite. The youngest (188 Ma to 191 Ma) and oldest (231 Ma to 295 Ma) results were rejected from the calculation of the mean and are interpreted to represent minor Pb loss and inheritance, respectively.

2.5.2 Re-Os Molybdenite Geochronology

2.5.2.1 Samples

Three molybdenite-bearing samples were chosen to examine the absolute timing of mineralisation and assess its temporal relationship to the emplacement of the Minto pluton. Molybdenite associations and textures vary (see Appendix H), complicating interpretations of relative timing. For example, molybdenite is associated with pegmatite veinlets, quartz veinlets, or biotite foliation, a possible indication of numerous mineralisation generations. Contact relationships between molybdenite and Cu-sulphides also vary, further obscuring interpretations of relative timing. Samples contain molybdenite with inclusions of chalcopyrite and/or bornite (Figure 36A and B), a possible indication that molybdenite growth overprints or crosscuts pre-existing Cu-sulphides. However, molybdenite may also share grain boundaries with copper sulphides, or occur as discrete masses (Figure 36C).

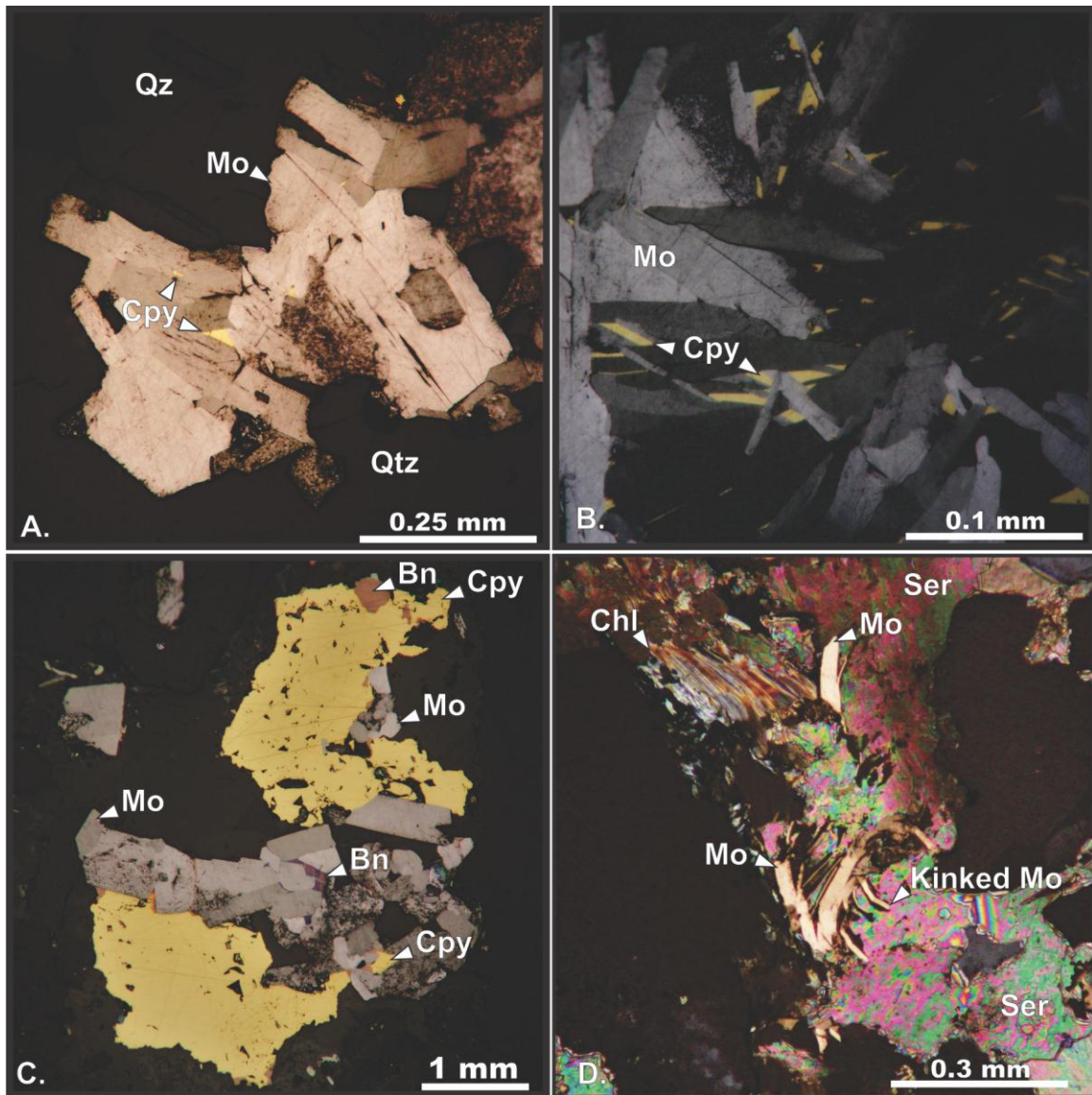


Figure 36: Photomicrographs showing textures in molybdenite samples suggestive of relative timing. A. Molybdenite along the margins of a quartz veinlet with chalcopyrite inclusions. Sample H510-276 from drill core at the north-west of the deposit. B. Close-up of chalcopyrite inclusions within euhedral molybdenite occurring in biotite foliation. It is not possible to determine whether Cu-sulphides have been crosscut by later molybdenite, have crystallized contemporaneously, or Cu-sulphides have intruded along grain margins. Sample H429-129 taken from drillcore from the south-east of the deposit. C. Kinked molybdenite from within a pegmatite dikelet indicating ductile deformation after emplacement. Dikelet is also folded. Rock is crosscut by fracture controlled propylitic alteration in the form of chloritized biotite and sericite growth in plagioclase. Sample H422-81.4 taken from drillcore in the southeast of the deposit.

Ductile deformation appears to have outlasted molybdenite mineralisation, as evidenced by kinked grains (Figure 36D). Propylitic alteration, controlled by brittle deformation, locally overprints ductilely deformed molybdenite (Figure 36D).

2.5.2.2 Analyses

Molybdenite separates from the three samples were prepared at Durham University. Whole rock samples were ground in a porcelain disk mill, collecting the +44 -210 μm (200–70 mesh) fraction. Molybdenite was then concentrated using heavy liquid techniques, and further purified by flotation using high purity water (MilliQ), magnetic separation, and/or removing impurities by hand under a microscope. After preparation, molybdenite from sample H510-276.5 was hand-picked using binocular microscope and tweezers at the University of British Columbia to separate it from abundant pyrite. The full analytical procedure for Re-Os age determinations at the University of Durham is described by Selby and Creaser (2001a; 2001b) and is only briefly noted here. Molybdenite samples were dissolved and equilibrated with a known amount of ^{185}Re and isotopically normal Os in inverse aqua regia (2:1 16 N HNO_3 and 12 N HCl , 3 mL) at 240°C for 24 h in a Carius-tube. Rhenium and Os were isolated and purified by solvent extraction, microdistillation, and anion exchange chromatography, and analysed by negative thermal ionization mass spectrometry on a Triton mass spectrometer using Faraday collectors. Total procedural blanks for Re and Os <2 pg and <0.5 pg, respectively, with an $^{187}\text{Os}/^{188}\text{Os}$ blank composition of 0.24 ± 0.02 (n = 2). Rhenium and Os concentrations and Re-Os molybdenite date uncertainties are reported in Table 5 and are presented at the 2σ level, which includes the uncertainties in Re and Os mass spectrometer measurement, spike and standard Re and Os isotopic compositions, and calibration uncertainties of ^{185}Re and ^{187}Os . Because a mixed

^{185}Re and Os tracer solution is used, uncertainties in weights of sample and tracer solution do not affect the calculated age, and are not considered. However, sample and tracer solution weight uncertainties are considered in determining the uncertainty in the Re and ^{187}Os concentrations. Uncertainty in the ^{187}Re decay constant (Smoliar et al., 1996) are included within errors within square brackets.

2.5.2.3 Results

Total rhenium contents of the three molybdenite samples ranged from 114.2 to 612.9 ppm. Osmium within molybdenite is predominantly radiogenic ^{187}Os (Stein et al., 1997; Selby and Creaser, 2001) and range between 242 and 1269 ppb (Table 5). Calculated model ages for molybdenite are 197.4 +/- 0.8 [1.0] Ma in sample H422-81.4, 201.8 +/- 0.8 Ma [1.0] in sample H429-129.5, and 196.0 +/- 0.8 [1.0] Ma in sample H510-276.5.

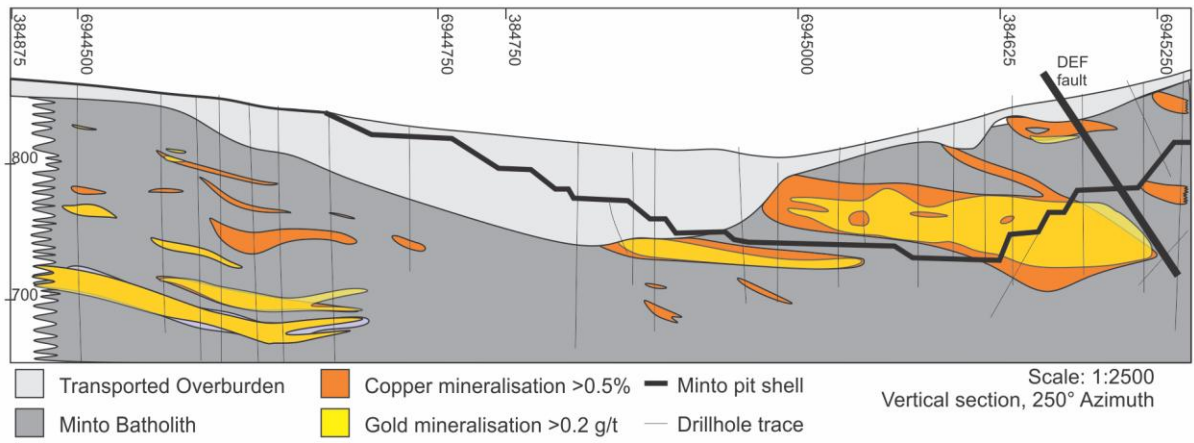
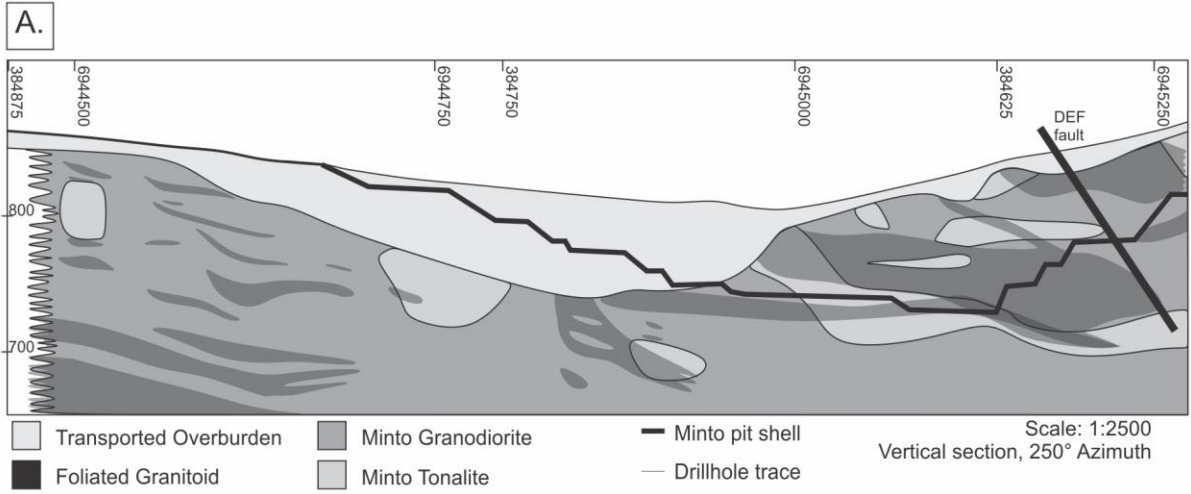
Table 5: Sample data from molybdenite

Sample no.	Sample Wt (mg)	Total Re (ppm)	±	^{187}Re (ppm)	±	^{187}Os (ppb)	±	Age (Ma)	±
H422-81.4	0.017	612.9	2.4	385.2	1.5	1269.1	4.3	197.4	0.8
H429-129.5	0.021	114.2	0.4	71.8	0.3	241.7	0.8	201.8	0.8
H510-276.5	0.030	265.1	0.9	166.6	0.6	545.0	1.5	196.0	0.8

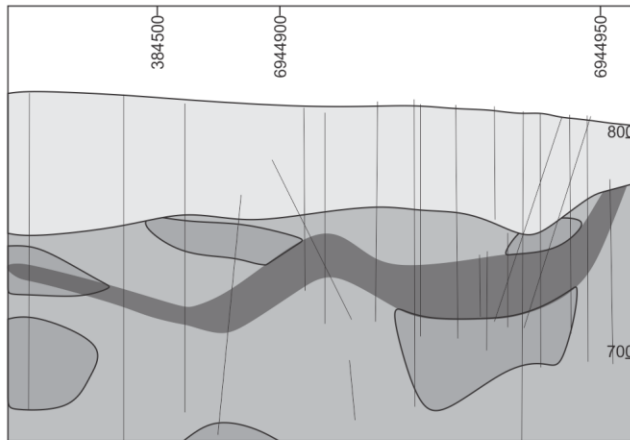
2.6 Summary

2.6.1 Relationship between Igneous Activity, Alteration, and Deformation

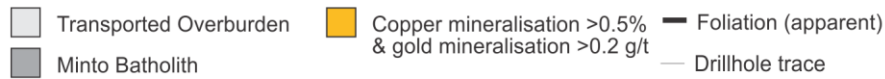
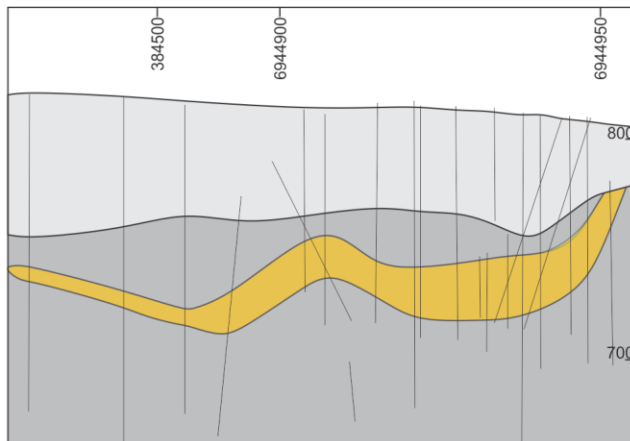
The Minto deposit is hosted entirely within the arc-granitoid rocks of the Minto pluton. This host pluton was emplaced as multiple pulses into a dynamic setting. Solid state deformation and the progressive development of a penetrative foliation, S_P , continued within the Minto pluton as different batches of magma were intruded and solidified. Copper-gold-silver mineralization is associated with potassic alteration in the form of biotite-magnetite, all hosted within the sheared granitoids. There is a weak correlation at the scale of individual shear zones between increased deformation intensity, folding of shear zones, potassic alteration, and copper grade (e.g., Figure 32, Appendix F). At open pit and regional scales (Figure 33 and Figure 34, respectively) there is a spatial coincidence between folded shear zones and copper mineralization, and the trend of highest grade mineralisation is approximately parallel to the strike of folded shear zone axial planes. These characteristics, along with structural character described in Section 2.4, are the basis for cross section interpretations of Minto ore zone geometry shown in Figure 37.



B.

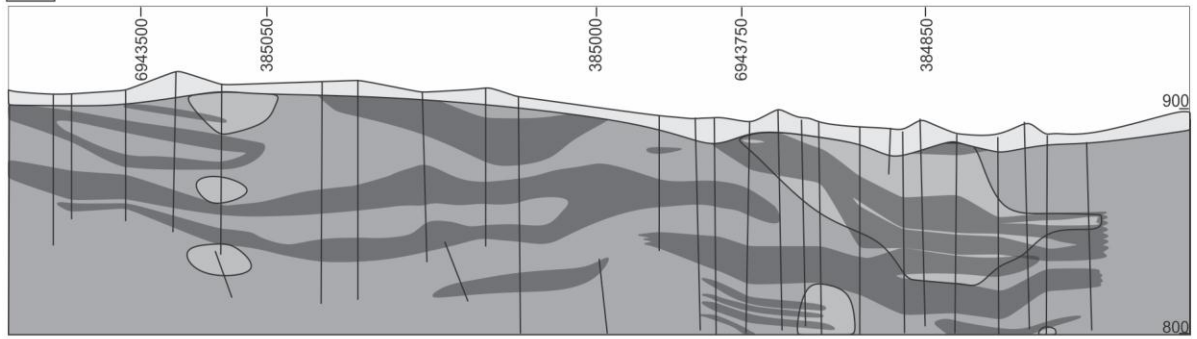


Scale: 1:1500
Vertical section, 340° Azimuth



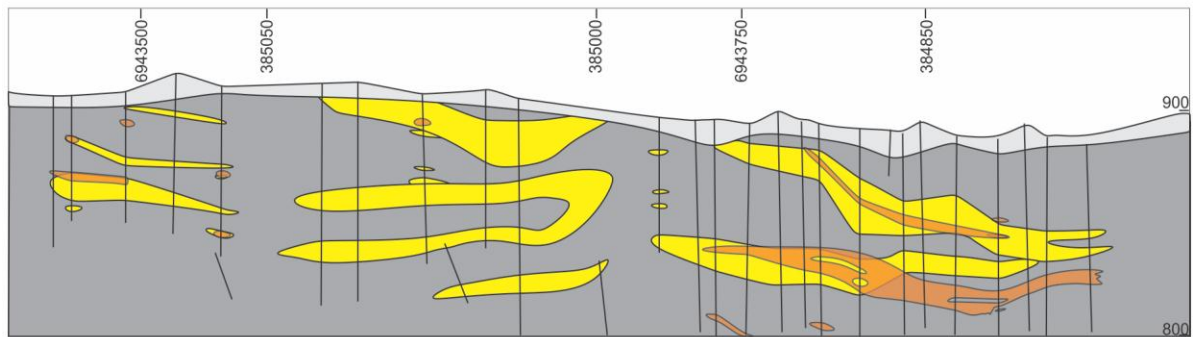
Scale: 1:1500
Vertical section, 340° Azimuth

C.



Scale: 1:1500
Vertical section, 250° Azimuth

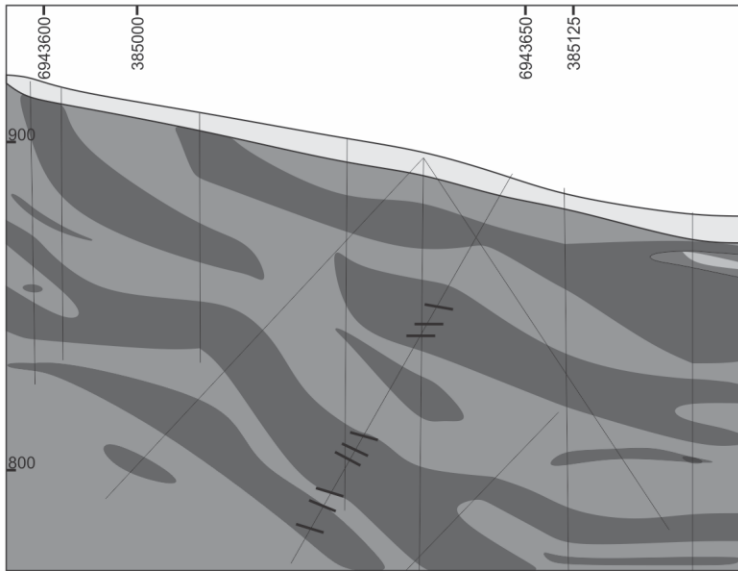
Legend:
Transported Overburden (light grey)
Minto Granodiorite (medium grey)
Foliated Granitoid (black)
Minto Tonalite (light grey)
Drillhole trace (vertical line)



Scale: 1:1500
Vertical section, 250° Azimuth

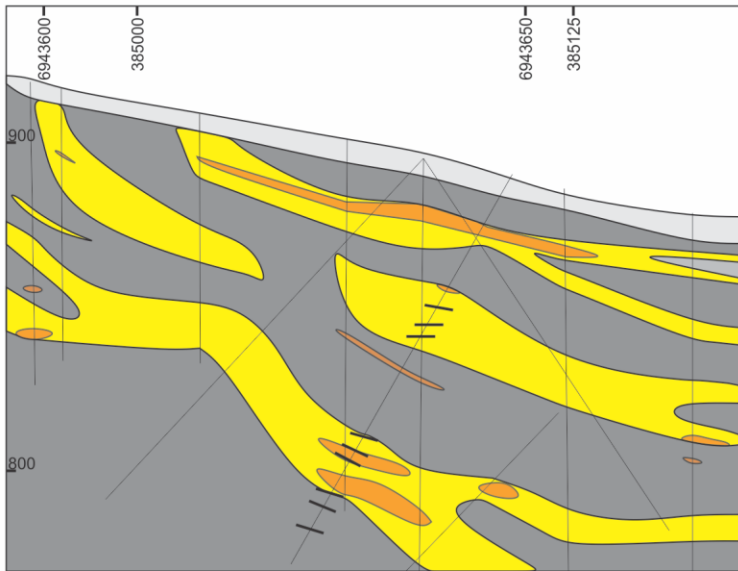
Legend:
Transported Overburden (light grey)
Minto Batholith (medium grey)
Copper mineralisation >0.5% (orange)
Gold mineralisation >0.2 g/t (yellow)
Drillhole trace (vertical line)

D.



- | | | |
|------------------------|--------------------|----------------------|
| Transported Overburden | Minto Granodiorite | Foliation (apparent) |
| Foliated Granitoid | Minto Tonalite | Drillhole trace |

Scale: 1:1000
Vertical section, 340° Azimuth



- | | | |
|------------------------|------------------------------|----------------------|
| Transported Overburden | Copper mineralisation >0.5% | Foliation (apparent) |
| Minto Batholith | Gold mineralisation >0.2 g/t | Drillhole trace |

Scale: 1:1000
Vertical section, 340° Azimuth

Figure 37: Cross sections from the Minto deposit showing the interpreted geometry of deformation zones and mineralization. Regions of foliation are modeled as anastomosing zones with discontinuities due to tapering out of the zones, stoping of deformed rock into younger intrusions, or late faulting. Mineralisation is hosted within deformed rocks only, although the degree of solid-state deformation can vary greatly. Additionally, not all deformed rocks are mineralized. Sections A. and B. are through the Minto pit, and sections C. and D. are proximal to oriented drill holes 09SWC427, 09SWC429, and 09SWC431. Sections envelopes are 20 metres in width.

2.6.2 Geochronology

The majority of Minto zircons yielded $^{206}\text{Pb}/^{238}\text{U}$ ages between approximately 197 Ma and 200 Ma, summarized in Figure 38. The first suite of samples represents the sample shown in Figure 6B and includes host Minto granodiorite (i.e., KGd, Sample S09-13-01A) and an enclave of altered KGd (Sample S08-01-01). Based on cross-cutting relationships, this enclave of propylitically altered granodiorite within unaltered granodiorite is older than its granodiorite host, consistent with the relative age dates for host rock and enclave.

The second suite of four samples (S09-16-03A, S09-16-03B, S09-16-03C, and S09-16-03D) were collected from a sequence of vertically stacked deformed and massive granodiorites (Figure 28C and D) outcropping on the hangingwall side of the DEF fault in the Minto open pit. This alternating sequence of massive and deformed KGd is interpreted as representing shear zones cross-cutting a single, relatively undeformed, phase of intrusion, although it is possible deformation has developed within separate intrusions of KGd. The timing of molybdenite mineralisation is broadly coincident with emplacement of the Minto pluton. These ages young northward as 201.8 +/- 0.8 Ma (H429-129.5), 197.4 +/- 0.8 Ma (H422-81.4), and 196.0 +/- 0.8 Ma (H510-276.5). Molybdenite in sample H429-129.5 is within uncertainty of the altered granodiorite enclave, sample S08-01-01, with an assigned age of 200.1 +/- 1.1 Ma. Samples H422-81.4 and H510-276.5 have different dates, but are within uncertainty of one-another. The similarity of dates between these two samples is noteworthy because the two samples represent differing mineralisation textures, i.e., the first is associated with a quartz veinlet, and the second with a medium grained quartz-feldspar dikelet. Also noteworthy is the northward-younging trend of molybdenite ages (see Appendix H).

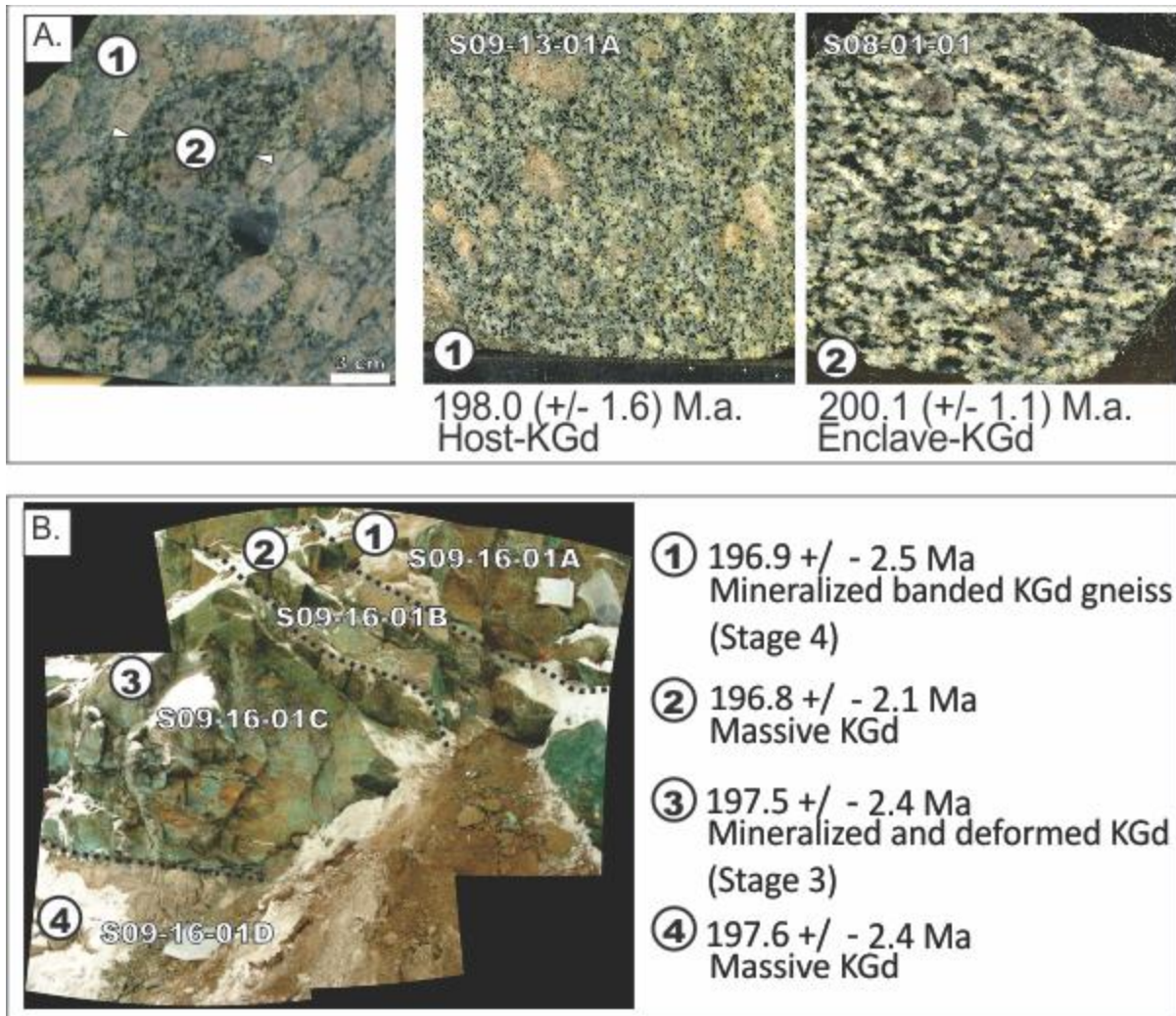


Figure 38: Annotated photograph of KGd samples showing summary of U-Pb SHRIMP zircon ages. A. Ages in Suite One, with an older enclave of KGd stopped into a younger KGd intrusion. B. Ages for Suite Two, with a vertically stacked sequence of variably deformed KGd with similar ages within error of one-another.

An additional interesting feature is the occurrence of molybdenite within the two samples on either side of the DEF fault, a feature that offsets the main Minto deposit from additional mineralisation to the north of the fault. The similarity in ages between the samples could indicate that both halves of mineralisation occurred more or less contemporaneously. These ages contrast with the older age calculated for sample H429-129.5, sampled within a kilometre of sample H422-81.4. This relationship is suggestive of several mineralisation events, at least an early biotite-foliation hosted event and a later vein/dikelet event.

2.7 Discussion

2.7.1 Petrogenesis and Emplacement Depth

Crosscutting relationships between KGd and Tlt indicate multiple stages of granitoid emplacement. Abundant fabrics within intrusions, e.g., K-feldspar alignment and clustering, mafic layering, and mafic magmatic enclaves are indicative of crystal movement within a melt, i.e., the Minto pluton was not fully crystallised during the development of these fabrics (Clemens and Wall, 1981; Vernon and Paterson, 2008).

Whole rock geochemical work indicates Minto granitoids are calc-alkaline, peraluminous, and sub-alkaline, consistent with existing work by Mortensen (1999) and Tafti (2005). These traits are typical of granitoids in porphyry Cu-Au-Mo deposits, i.e., calc-alkalic, oxidised magnetite-series granitoids (Ishihara, 1981; Blevin and Chappell, 1992, 1995).

Tectonic discrimination using Rb vs. Y+Nb (Figure 11A) suggests Minto granitoids are volcanic arc granitoids as defined by Pearce (1984), consistent with the current interpretation of the North American Coast Batholith belt, hosting the Aishihik batholith and Minto pluton, being a product of subduction (Anderson, 1990; Winter, 2001). KGd has molar ratios of $\text{Al}_2\text{O}_3/(\text{CaO}+\text{K}_2\text{O}+\text{Na}_2\text{O})$ (or A/CNK after Clarke, 1981) of approximately 1.25, indicating a strongly peraluminous nature. This contrasts slightly with the interpretation of Tafti (2005) that massive KGd is only weakly to moderately peraluminous. Peraluminous granitoids contain more Al than can be accommodated within feldspars, stabilizing other aluminous phases, typically muscovite, Al-rich biotite, cordierite, garnet, or an Al_2SiO_5 polymorph (Zen, 1988). In KGd, epidote and locally garnet are abundant and reflect the peraluminous nature of the melt. Strongly peraluminous melts are thought to originate from melting of a sedimentary source (e.g., Chappell and White, 1974), melting of biotite-bearing

metaluminous felsic rocks (Miller, 1985), or by water-excess melting of mafic rocks (Ellis and Thompson, 1986). It is not clear which of these processes were in effect at Minto, although contamination of the pluton by sedimentary country rocks of the Yukon-Tanana may be responsible. This hypothesis of contamination is supported by inherited cores of YTT age within KGd zircon, discussed in section 2.5.1, U-Pb geochronology.

Peraluminous rocks may be calcic, alkali-calcic, or calc-alkalic (Frost et al., 2001). KGd from Minto plots predominately within the calc-alkalic field, consistent with interpretations by Tafti (2005). The abundance of apatite, epidote and titanite, in addition to plagioclase, reflects the calcic nature of the melt. Several surface samples collected for this study plot within the calcic field, although this may be a reflection of Na, K, or Ca mobility during meteoric weathering. Primary variations in the MALI can be caused by either the sources or the differentiation history of magma. Frost et al. (2001) suggest that the MALI value for Cordilleran batholiths is related to the source region for the parent melts, with the plutons becoming progressively more potassic and alkalic away from the subduction zone.

Empirically, the oxidised nature of the Minto pluton magma can be inferred from the brown-green colour of biotite in crossed polars (Chinner, 1960; Ishihara, 1998), the presence of magmatic magnetite, and the lack of ilmenite (Ishihara, 1977; 2004). This second feature places granitoids within the magnetite series of Ishihara (1977), representing magmas with high-oxidizing potential and significantly associated with sulphide-rich Cu, Au, Mo, Pb, and/or Zn deposits (Ishihara, 1977; Lehmann, 1982; Blevin and Chappell, 1992; Candela, 1992; Blevin and Chappell, 2004). The oxidised character of the Minto pluton is also indicated by whole-rock geochemical plots of SiO_2 vs. calculated $\text{Fe}_2\text{O}_3/\text{FeO}$ by Tafti (2005) as per Kirkham and Sinclair (1996).

Frost et al. (2001) used an $[\text{FeO}^{\text{Tot}}/(\text{FeO}^{\text{Tot}} + \text{MgO})]$ index (Fe-index) to differentiate between rocks that are relatively Fe-enriched versus those that are relatively Fe-poor. KGd plots within the magnesian field (after Frost et al., 2001; Frost and Frost, 2008), indicating that Mg is relatively more abundant than Fe, consistent with Cordilleran granitoids in general (Frost et al., 2001).

Magmatic epidote is a common accessory mineral in KGd. For granodiorite at water-saturated conditions and at f_{O_2} equivalent to the NNO buffer, epidote has a wide magmatic stability field (Schmidt and Thompson, 1996; Schmidt and Poli, 2004a), crystallizing from intermediate magmas at pressures varying from 0.3 to 0.7 GPa (Zen and Hammarstrom, 1984; Schmidt and Poli, 2004a). However, stability at pressures as low as 0.2 GPa in water saturated conditions may be possible (Schmidt and Poli, 2004a). These pressures are consistent with the range of possible emplacement pressures for Minto granodiorites calculated by Tafti (2005) using Al in hornblende geobarometry between 0.27 GPa to 0.35 GPa (using the method of Blundy and Holland, 1990) or 0.62 GPa to 0.66 GPa (using the method of Holland and Blundy, 1994). These pressure calculations correspond to paleodepths of approximately 10 km to 13 km and 22 km to 23 km, respectively, based on an assumed baric gradient of 0.036 km/MPa (density 2.8 g/cm³) taken from McCausland et al. (2002), who reported emplacement depths for the Aishihik batholith of 16-20 km based on calculated pressures 0.426 GPa to 0.555 GPa.

Temperature calculations for Minto granodiorites by Tafti (2005) using the plagioclase-amphibole thermometer are 830 °C to 857 °C (using the method of Blundy and Holland, 1990) or 723 °C to 738 °C (using the method of Holland and Blundy, 1994). Temperatures of zircon crystallization for Minto granodiorites by Tafti (2005) are calculated as approximately

719 °C to 747 °C. These calculated temperatures are lower than predicted for calc-alkalic granitoid crystallization, but may be attributed to the effect of high activity of H₂O (e.g., Piwinskii, 1968; 1973). Similarly, the bulk of McCausland et al.'s (2002) data indicate temperatures ~720-750 °C for intruding granitoids in the Minto region, corresponding to depths around 20 km, with country rocks estimated to have an ambient temperature >480°C (assuming ~30°/km geothermal gradient).

2.7.2 Synopsis of the Crustal Environment During Emplacement of the Minto Pluton

Granodiorites of the Minto pluton are interpreted as a northern extension of the Granite Mountain batholith (Tafti, 2005), an Early Jurassic intrusion into the Yukon-Tanana Terrane (YTT; Mortensen, 1992). The YTT is an allochthonous pericratonic terrane accreted during the Mesozoic to the western margin of Laurentia, although the history of this event and of subduction-arc activity responsible for Early Jurassic intrusions is not well understood in the vicinity of the Minto deposit. Eastern movement of the YTT towards the Laurentian continental margin, along with consumption of the Slide Mountain ocean (Figure 38A), was initiated in the Late Permian (Mortensen, 1992; Colpron et al., 2006). However, subduction had likely ceased by the Middle Triassic (Beranek, 2006; Colpron et al., 2006; Colpron et al., 2007). Arc-subduction must have occurred between this time and the final assembly of the Intermontane belt during the Mid- to early-Jurassic (Mihalynuk et al., 1994) to account for the widespread mafic to felsic plutons of Late Triassic to Early Jurassic age intruding the metamorphic assemblages of YTT (Mortensen, 1992), including construction of the Minto pluton (Figure 38B). The tectonic event(s) responsible for deformation within the Minto pluton (Figure 38C, D) is also not known, although development of a regional orocline (Mihalynuk et al. 1994) could account for sufficient regional stresses. Also unclear are the

processes responsible for the rapid uplift of the pluton from at least 10-15 km depth (Mccausland et al., 2001; Tafti, 2005) to shallow crustal levels over ~10 My (Johnston et al., 1996b; Tafti, 2005) and exposure by the Upper Cretaceous (e.g., as depicted in Figure 39E).

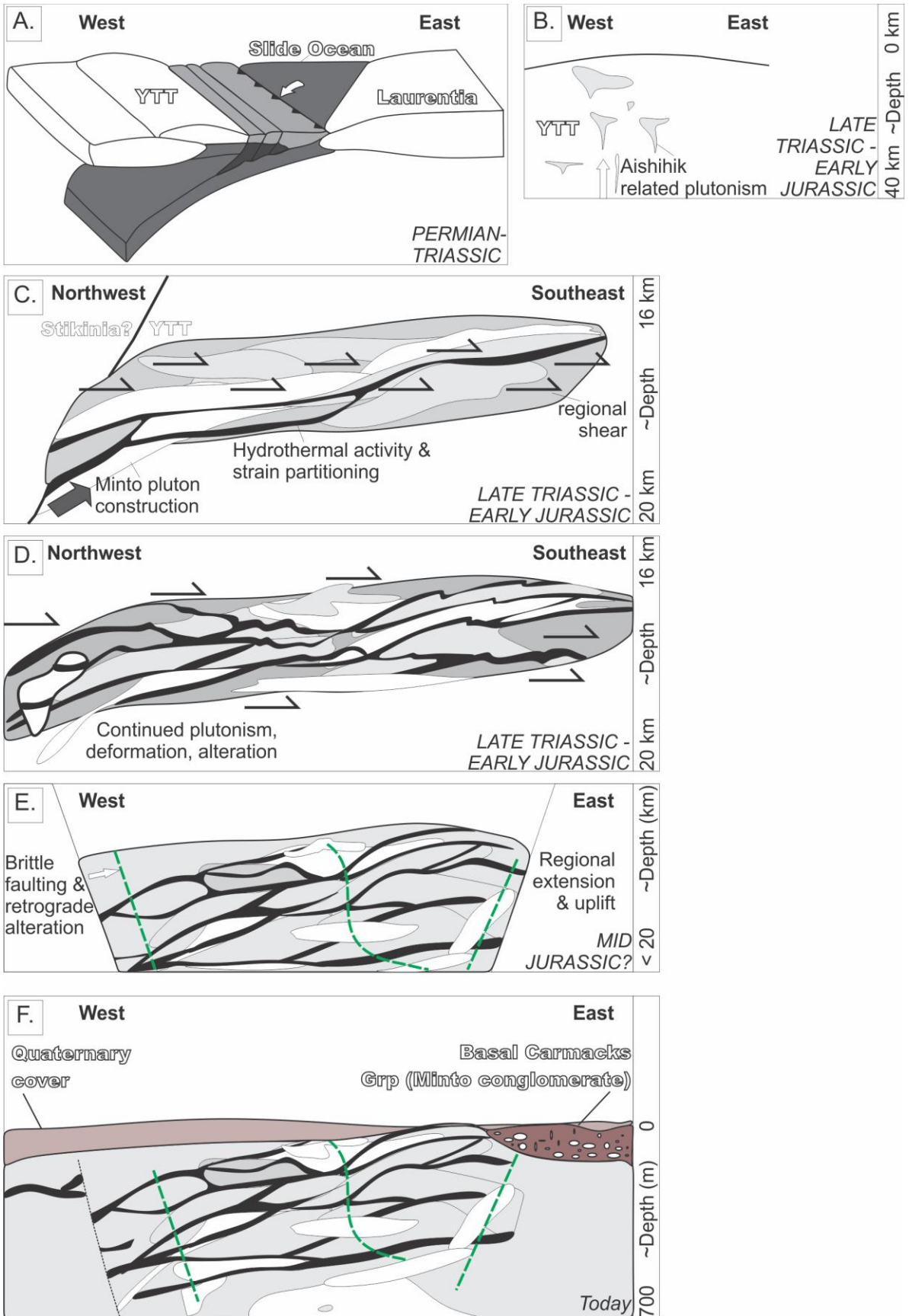


Figure 39: Schematic of Minto deposit paragenesis. A. The arc-subduction event responsible for Late-Triassic-Early Jurassic magmatism and emplacement within the Yukon-Tanana terrane (YTT) is not currently known. B. However, magmatism did occur, and resulted in the emplacement of the Minto pluton, interpreted as part of the Aishihik plutonic suite. C. Emplacement of the Minto pluton occurred in the ductile regime. Shear was accommodated within the pluton, with magmatic fluids and associated alteration confined to these discrete zones. D. Continued magmatic activity, deformation, and alteration developed, with corresponding cross cutting relationships. Continued deformation accommodated along shear zones led to folding of the zones and a resultant short-limb long-limb fold geometry. E. Cooling of the pluton and surrounding rocks allowed the development of brittle fractures. Retrograde alteration developed along fractures, possibly due to hydrothermal influx of previously exsolved fluids back into the cooled rock mass. F. Finally, rapid exhumation due to unroofing led to the exposure of the Minto pluton.

2.7.3 Pluton Emplacement and Ductile Deformation

Cross-cutting igneous relationships between granitoid intrusions of identical and contrasting composition observed in the Minto pluton are evidence that it was constructed through multiple intrusive stages. The size of granitic intrusions varies from sub-centimetre to at least tens of metres. Intrusions appear to have occurred both above and below the granodiorite solidus, as suggested by textures within and between intrusions. Intrusion into solidified rock is indicated by stoped enclaves of granitoid within younger intrusions, deformed mafic magmatic enclaves without solid state fabrics, intrusions that truncate pre-existing solid state foliation, and planar contacts between igneous bodies with magmatic alignment of K-feldspars along pre-existing solidified rock. Evidence that intrusions have been emplaced above solidus temperatures include accumulations of K-feldspar megacrysts, possibly the result of filter-pressed internal margins, and diffuse margins between intrusions.

The origin of pegmatite dikelets is not clear but could represent filter-pressed residual magma that builds up pressure and induces multiple episodes of fracturing within and out from magma batches (Hibbard, 1987). The general prevalence of pegmatite dikelets within shear zones, relative to undeformed/unaltered rock, could be related to shear zones providing a useful anisotropy for focussing fractures and related water-rich dikelets.

Deformation was partitioned into anastomosing shear zones that cut through intrusions, formed along contacts, and were possibly locally stoped by later emplaced slabs. The shear zones folded small dikelets creating further compositional banding in the gneiss. Shear zones and foliation have a shallowly dipping enveloping. Overprinting relationships between igneous intrusions and solid state foliations indicate an active shear zone during emplacement of magma during the construction of the Minto pluton. Magmatic fabric along the west margin of the Granite Mountain batholith has been suggested to indicate the nearby presence of the shear zone's

northwesterly trending wall within an Early Jurassic continental magmatic arc (McCausland et al., 2002). There is no evidence for significant tilting of Granite Mountain batholith (McCausland et al., 2002) meaning shear zone orientation may be close to orientation it formed at; however, further work must be done, especially regarding the interpreted dip of the Minto conglomerate from drillcore (Mortensen, pers. comm.).

Because country rock contacts were not observed in this study, it is not known whether ductile deformation was accommodated proximally in the Yukon Tanana Terrane. However, ductile deformation of granodiorites did occur within the Minto pluton during emplacement. Deformation could reflect intrusion into a regionally active crustal shear zone; or it might reflect emplacement related to heterogeneously partitioned strain associated with near vertical flattening and lateral expansion above an expanding magma chamber (de Saint-Blanquat et al., 2001; Pons et al., 2006; Stevenson, 2009). If it not intrinsically related to emplacement, the shear zones could represent a regional low angle shear zone system associated with regional shortening or lateral extrusion driven by far field kinematic boundary conditions larger than the Granite Mountain batholith itself. However, it could be that the thermal aureole of the growing batholith reduced the bulk competence of the crust surrounding the intrusion and this induced failure and lateral extrusion of a previously thickened crust by vertical shortening (Davis and Henderson, 1999; Arevalo et al., 2006). Either way, the Minto pluton could have been intruded as sheets into the active low angle shear zones. The rate of individual sheet emplacement and cooling, could be far shorter than the rate of ductile strain and hence they are almost like instantaneous brittle events within the longer lived shear zone.

Minto has a present surface area of approximately 170 km² (Figure 2), although it is fault bound within the surrounding Yukon Tanana Terrane, i.e., its original extents are not known. The thickness of the pluton is also not known, although drilling by Capstone indicates a thickness >

1 kilometre. The dimensions of the Minto pluton are within the order of magnitude as those described by Cruden (1998) in his models of timespans for arc pluton construction. Cruden (1998) predicts that tabular plutons 10 to 100 km wide and ~3 km thick can be emplaced between 100 years to 100 m.a. during tectonic deformation at rates of 10^{-10} to 10^{-15} s^{-1} .

Assuming a strain rate of about 10^{-13} - 10^{-13} s^{-1} , based on representations of strain rates in arc environments where granitoids are crystallizing (e.g., Paterson and Tobisch, 1992; Johnson et al., 2004), temperature during deformation of Minto rocks would have occurred at approximately 500 °C based on observed deformation microtextures summarized in Table 6. However, this temperature range serves as only a rough estimate, as texture development relies on rate of grain boundary migration, dislocation climb, and dislocation production; each of these is in turn dependent on temperature, pressure, strain rate and water availability (Hirth and Tullis, 1992). Interlobate grain boundaries involving plagioclase or quartz are indicative of grain boundary migration (GBM) (Guillope and Poirier, 1979; Urai, 1986; Stipp et al., 2002). This style of recrystallization is described as occurring at approximately 500 °C (Stipp et al., 2002). Regions of recrystallized quartz exhibits a shape-preferred orientation forming a continuous foliation indicative of sub grain rotation (SGR) (Nishikawa and Takeshita, 2000; Nishikawa et al., 2004; Passchier and Trouw, 2005). This feature is indicative of dislocation creep with a temperature range 400 – 500 °C. Tapered deformation twins within plagioclase indicate minor dislocation glide and a deformation temperature between 400° and 500° C (Pryer, 1993; Borg and Handin, 1966; Ji, 1998). The presence of prograde myrmekite and minor internal kinking, suggest recrystallization in the form of dislocation climb and a temperature range of 450 – 600 °C (Borges and White, 1980; Gapais, 1989; Gates and Glover III, 1989; Tullis and Yund, 1991).

Table 6: Temperature estimates based on observed microtextures

Temp °C / Microtexture	100	200	250	300	400	450	500	600	700	800	900	1000
Lobate plagioclase boundaries	Light Grey						Light Green					
Quartz lobate boundaries	Light Grey						Light Green					
Plagioclase deformation lamellae	Light Grey				Light Green			Light Grey				
Myrmekite	Light Grey					Light Green			Light Grey			
Quartz Sub grain rotation	Light Grey				Light Green			Light Grey				
Biotite ductile deformation	Light Grey		Light Green									

Myrmekite mantling K-feldspar is most commonly understood to arise during deformation (e.g., Simpson, 1983; Watts and Williams, 1983; Simpson, 1985) due to dissolution-precipitation creep (Tullis and Yund, 1985; Simpson and Wintsch, 1989; Wintsch and Yi, 2002; Menegon et al., 2008). Myrmekite growths rimming K-feldspar were commonly adjacent to small patches of undulose extinction within K-feldspar, in keeping with Simpson and Wintsch's (1989) model that myrmekite development during prograde metamorphism occurs at syn-tectonic stress concentration sites. Aligned biotite and/or chloritized biotite defines a tectonic foliation within deformed zones. This interpretation is based on criteria originally described by Trueman (1912; see also a review of foliation criteria by Williams, 1977), that biotite aggregate masses define a foliation which anastomose feldspar microlithons, and that folia are approximately co-planar. Although biotite foliation parallels the structural contact between zones, long axes of individual biotite books are poorly aligned and vary from neighbours by up to 30°. Biotite observed in samples commonly exhibits undulose extinction and kinking. These textures are described to occur at temperatures over 250 °C (Stesky et al., 1974; Stesky, 1978).

S_p is a penetrative, mesoscopically visible planar fabric developed with variable intensity at Minto. Feldspar, quartz, and biotite are recrystallized and earlier or syn-tectonic dikes are folded and have axial planes parallel to S_p . This fabric has developed separately in granitoids temporally, as intrusions are emplaced, or spatially, as zones of partitioned deformation. Gapais (1989) summarizes three typical varieties of structural patterns for strain partitioned into granitic rocks and operative at various scales: (i) homogeneously foliated domains, (ii) penetrative associations of foliation and small-scale shear bands, such as C-S structures, and (iii) discrete shear zones anastomosed around low-strain domains. Deformation zones at Minto are not homogeneously deformed, and C-S fabrics are not present. However, foliated zones of rock were observed with the open pit to anastomose more competent rock, especially in areas of high

contrast between unaltered and altered rock. The orientation of S_P is most commonly shallow and deformation intensity is weak to moderate. Local high strain and/or steep foliation observed in drill core may be indicative of anastomosing deformation zones (e.g., Bell, 1978; Mitra, 1978; White et al., 1980).

Shear zones within the Minto pluton and associated S_P foliation appear to have been folded with large sub-horizontal limbs and short, more steeply dipping limbs. This folding could have arisen due to a shortening event after pluton emplacement, while rocks were still hot, or regional shortening re-imposing itself after pluton emplacement.

2.7.4 Deformation, Permeability, and Hydrothermal Fluid Flow

The mineralised areas of the Minto pluton typically correspond to zones of deformation and foliation development. In addition, copper-gold-silver mineralisation is associated with metasomatism of host rocks. The relationship between deformation and hydrothermal alteration, i.e., preferential fluid flow along shear zones, is well known from metamorphic environments (Dipple and Ferry, 1992), with fluid flow in the direction of decreasing temperature likely increasing the ductility of silicate rocks by adding K^+ to the rocks and thereby driving mica-forming reactions (Dipple and Ferry, 1992). In addition, rocks in ductile shear zones are probably much more permeable during metasomatism (average permeability of 10^{-17} to 10^{-15} m^2) than rocks normally are during regional metamorphism (10^{-21} to 10^{-18} m^2) (Dipple and Ferry, 1992; Géraud et al., 1995). Mineralisation at Minto is restricted to shear zones that are deformed and altered versions of the massive non-mineralised granodiorite. At Minto, contacts between mineralisation zones and wallrock are typically sharp with only rare cases of sulphides present in massive rocks, and even then only up to several centimetres from the contacts. Granodiorite protoliths are so ubiquitously barren that they are used as “blank” unmineralized

material during assaying. The highly mineralized shear zones indicate that the hydrothermal fluid was not in chemical equilibrium with the host rocks.

In active shear zones at mid-crustal depths and temperatures $> \sim 500^{\circ}\text{C}$, increased permeability is likely inherently related to microdilateness through microfracturing. This deformation arises from heterogeneous strain between differently oriented crystals of the same mineral, minerals with different rheological properties, and different sized crystals (Kronenberg and Tullis, 1984; Wenk and Christie, 1991; Oliver, 2001; Oliver et al., 2006; Kolb, 2008). Strain softening and permeability enhancement can occur through positive feedback as hydrothermal fluids move through sites of microdilateness in developing shear zone (e.g., Yonkee et al., 2003).

Strain softening can also occur due to the growth of micas at the expense of other silicate phases; e.g., conversion of hornblende to biotite during hydrothermal alteration, as is observed at Minto. Biotite is the main alteration phase associated with mineralisation at Minto, and is interpreted to have played a major role in facilitating ductile deformation. Biotite is a weak mineral under shear (Dipple and Ferry, 1992; Shea and Kronenberg, 1993; Wintsch et al., 1995; Johnson et al., 2004; Holyoke III and Tullis, 2006) and micas segregated in foliation planes have a strain softening effect disproportionate to their modal volume and can lead to strain rates much higher than the bulk rate (e.g. Shea and Kronenberg, 1993; Wintsch et al., 1995; Johnson et al., 2004). In the specific context of plutons, biotite has been invoked as the weakest mineral in the deforming carapace of the San Jose tonalitic pluton in Baja California, Mexico and thus initiated localized microfractures in a stress-supporting plagioclase framework (Johnson et al., 2004). These microfractures evolved into ductile microshear zones, along which biotite grains coalesced to ultimately form a mylonitic foliation at the highest strains. Thus a progressive transition from small scale brittle to ductile flow can be controlled by biotite content with other weakening mechanisms further promoting ductile deformation. Strain softening can also occur

through hydrolytic weakening of minerals, particularly quartz, and easier intracrystalline slip (Griggs, 1967; Kronenberg and Tullis, 1984; Kronenberg, 1994; Gleason and DeSisto, 2008).

Fluid flow at Minto appears to have been pervasive through rocks undergoing shear and foliation development. The relative lack of brittle fractures and veins could be due to confining pressure during mineralisation, plus sufficient permeability within ductile shear zones to accommodate fluid flow. Rocks deforming by crystal-plastic processes are essentially inviscid and any pockets of fluid in the deforming rock mass will be constantly squeezed by the pressure of the rocks around them (Connolly and Podladchikov, 1998; Connolly and Podladchikov, 2004; Connolly, 2010). The length a pocket of fluid can reach (parallel to the external pressure gradient, approximately vertical in a non-deviatoric stress field) before significant squeezing occurs determines the maximum pressure that can develop at the top of the pinched fluid pocket, and hence the maximum effective stress in the rock surrounding it. This characteristic length scale of compaction is inversely proportional to temperature, and to the timescale of fluid generation and egress into the shear zone (Connolly, 2010). The lack of macroscopic veins could reflect insufficient fluid pressure generated at the end of a fluid pocket to lower the effective stress sufficiently to induce macroscopic tensile fracturing in the host rock, i.e., the fluid pockets are too short. This would suggest higher temperatures and less rapid fluid production than more highly veined hydrothermal systems like porphyry Cu deposits. Rather than travel via macroscopic fractures, the hydrothermal fluid at Minto likely moved pervasively through the shear zones as waves of vertically limited pockets that, at their upper ends, only reduced the effective stress sufficiently to promote microdilacy and enhanced permeability through increased levels of microfracturing and grain boundary sliding (as per Connolly, 2010). Rather than moving vertically through the shallow dipping shear zones, it is likely that the strong fabric anisotropy favoured microfracturing and fluid flow along the S_P foliation at Minto.

This is similar to situations described by Pollard et al. (1998), where shear zones distractive during emplacement of mid-crustal intrusions (~14 km) are likely conduits for the egress of magmatic fluids as the magma cooled below the solidus.

In summary, following the initiation of deformation at Minto, hydrothermal fluid infiltrated and altered the rock setting up a positive feedback mechanism where zones of strong alteration focussed fluid flow, leading to further alteration. Deformation was heterogeneously distributed and extensive fluid flow either did not follow all shear zone branches, or some shear zone branches developed after the cessation of hydrothermal fluid flow. Folding and the development of step shear zones likely outlasted hydrothermal fluid flow, as suggested by the ductile deformation of Cu-sulphides into and around fold hinges.

2.7.5 Hydrothermal Alteration

Magmatic hydrothermal fluids responsible for metasomatism and economic mineralization at Minto are evidenced in several ways. For example, (1) mineralization is hosted within the Minto pluton and was emplaced during the span of its emplacement, indicating ore is spatially and temporally coincident with intrusions. (2) Isocon analysis indicates that K₂O, Fe₂O₃, P₂O₃, U, Th, Pb, Cu, Au, and Ag have been added ore-bearing rocks, and SiO₂, Al₂O₃, CaO, Na₂O, and Sr have been depleted. This element mobility can be attributed to metasomatism, provided the assumptions for isocon analysis are valid for these rocks. (3) The abundant potassic alteration associated with mineralization, K-metasomatism with biotite after hornblende plus magnetite, is a typical high temperature product of cooling magmatic fluids in feldspar bearing host rocks (e.g., Seedorff et al., 2005). (4) Sulphur isotope compositions of $\delta^{34}\text{S}$ (‰) values of 0.65 to -3.27. (+/- 0.2) (‰) for Cu-Fe-sulphides at Minto reported by Tafti (2005) are within the typical range of sulphides in porphyry deposits and are consistent with a magmatic derived fluid (Ohmoto, 1986; Taylor, 1987; Hattori and Keith, 2001; Simon and Ripley, 2011). (5) The

zonation of sulphide types as mapped by Pearson (1979) are interpreted to reflect changing redox conditions during mineralization, possibly due to the cooling of hydrothermal fluids.

Based on the current understanding of constraints for mineralization at Minto fluid was not likely to have been generated by intrusions emplaced at the level of the Minto deposit itself, but rather by a deeper part of the magmatic chamber that was molten longer and more able to exsolve larger volumes of fluid. At Minto emplacement depths of ~16-19 km (corresponding to ~0.45 – 0.50 GPa (McCausland et al., 2002), an aqueous fluid will not exsolve from an intermediate magma with typical H₂O contents of 4-6wt% until ~40-60% crystallization (see Cloos, 2001). At these pressures (and at temperatures of <800-1000°C) Cl will be strongly partitioned into an aqueous phase to produce a saline parental magmatic-hydrothermal fluid (Cline and Bodnar, 1991; Webster, 1992). Magmatic S will also partition preferentially into the exsolved fluid phase (Webster and Botcharnikov, 2011). Based on metal partitioning coefficients for S-Cl bearing aqueous fluids, metal will strongly partition into the fluid phase (Candela and Holland, 1984; Cline and Bodnar, 1991; Harris et al., 2003; Hack and Mavrogenes, 2006; Simon et al., 2006; Simon and Ripley, 2011). Consequently, crystallization of the Minto Pluton should have been capable of producing a metal-rich hydrothermal fluid.

Molybdenite appears to post-date Cu-mineralisation based on its crosscutting relationship with Cu-sulphides and pyrite. Propylitic alteration is widespread, but is controlled predominately by fracture permeability, in contrast with the ductile controls on high temperature assemblages. The propylitic assemblages likely reflect an influx of lower temperature fluids after the main mineralising event. Multiple magmatic-hydrothermal cycles can play a role in modifying grade and contained metal of intrusion-related either by superposition of multiple mineralizing cycles, or through dilution by the emplacement of weakly-mineralized intrusions, e.g., in gold-rich porphyry copper deposits (Braxton and Cooke, 2005). Hydrothermal fluid events at Minto have

added Fe, K, S, Cu, Au, and Ag to the existing bulk composition. Al, Ca, and Na are reduced in sulphide bearing rocks. Hydrothermal mass transfer is responsible for zoned high temperature assemblages, most notably the transition from bornite-chalcopyrite mineralisation to pyrite only. Biotite-magnetite and Mo-sulphide development are important associated assemblages. Molybdenite is observed to crosscut chalcopyrite, bornite, and pyrite. Age dates based on Re-Os contents of three molybdenite samples suggests two, possibly three, Mo-sulphide events. Based on the observation of multiple intrusions and distinct Cu-Fe-sulphide cutting molybdenite, it is reasonable to invoke episodic hydrothermal activity in the deposit. However, it should be noted that chalcopyrite, bornite, or pyrite were not locally recognized as cross-cutting one-another, although emplacement textures have been completely overprinted by later deformation and thermal re-equilibration.

Hydrothermal biotite and magnetite are spatially associated with sulphide development. These phases represent an enrichment through mass transfer of K and Fe. Such potassic metasomatism associated with granitoid intrusions is described to occur as juvenile waters cool away from intrusions (e.g., Warren et al., 2007). This alteration is in turn accompanied by silicification and dissolution of Ca-, Mg-, and Na-bearing phases (Giggenbach, 1984).

At Minto, there is a zoning of bornite, bornite-chalcopyrite, chalcopyrite-pyrite, and pyrite (see mapping by Pearson, 1977). Similar zoning is known from the alkali Ridgeway deposit in Australia, where Cu grades are very similar to Minto (Wilson et al., 2003). This zoning could reflect progressive rock buffering of the fluid. Cooling leads to increased reduced sulphur owing to disproportionation; higher T = more oxidized fluid (more SO₂) and get bornite stable over chalcopyrite. Cooling also leads to increased dissociation and lower pH. Progressive reduction of ore fluid by interaction with Fe-bearing minerals in host rock also releases H and lowers pH. Cooling fluid reduces Cu solubility so it is lost early. SO₂ in porphyry-style deposits originates

from granitic melts and when dissolved in water disproportionates to give sulfate and reduced sulfur. This reaction continues as fluids cool and is the main control achieving sufficient H₂S saturation to precipitate sulphide. As fluid alters wall rock and releases Fe²⁺, the Fe will drive the reaction to the right by removing H₂S from solution to precipitate sulphide. Early magnetite reflects the oxidized nature of S in the fluid and most Fe in equilibrium with the fluid precipitates as magnetite rather than sulphide. This reaction could be responsible for the abundant magnetite observed at Minto. The most important mineral reaction during potassic alteration is the conversion of igneous hornblende, or in some cases pyroxene, to hydrothermal biotite. Thus the outermost reaction is preserved at the interface with fresh rock, and occurred first. At Minto, magnetite-biotite alteration is more widespread than Cu-mineralisation, and could represent the margins of individual mineralizing fluid events.

The hypothesized deep, high-temperature origin for hydrothermal ore fluids at Minto would come with caveats. At the high degree of crystallization needed to exsolve an aqueous fluid, the expectation exists of more fractionated (more fluid rich) phases intruding late into the level of the Minto pluton exposed over the Minto property, or perhaps rising of these late fractionated melts higher in the crust taking fluids with them. CO₂ is orders of magnitude more insoluble than water in a melt and will exsolve at higher pressures and lower levels of crystallization than H₂O (Lowenstern, 2001; Baker, 2002). In felsic magmatic systems CO₂ should form a fluid phase first and then H₂O, Cl and S will preferentially dissolve into it. At the depth the Minto pluton was emplaced, the initial fluids exsolved are likely to be CO₂-rich (Baker, 2002). There is no mineralogical evidence for the hydrothermal ore stage fluid at Minto having been CO₂-rich. Perhaps the early CO₂-rich fluid phase separated from the magma early and was not involved in the ore-stage event; or perhaps fluids more fully exsolved to the H₂O-rich end-member prior to separating from the magma. Perhaps the CO₂ that should be present in deeply

exsolved magmatic fluids underwent phase separation into a CO₂-rich lower density phase and a denser H₂O-Cl-S fluid that carried much of the copper and Au. The lower density phase may have separated from the magma and not significantly interacted with the overlying rocks.

Early, high temperature hydrothermal fluids derived from intrusions are commonly only in slight disequilibrium with igneous host rocks, hence large water volumes are needed to produce large scale volumes of potassic alteration (Dilles, in press). Potassic alteration at high temperature tends to occur with limited H⁺ availability, i.e., conditions of relatively limited acid supply, leading to the formation of hydrothermal biotite and local K-feldspar (Dilles, in press). Such assemblages are produced both from low salinity parental magmatic-hydrothermal fluids and brine-vapor mixtures (Dilles, in press).

2.7.6 Comparisons with Other Cu-Au-Magmatic Related Ore Systems

The Minto deposit type has been previously interpreted as a sedimentary copper deposit, orthomagmatic sulphide cumulate deposit, porphyry deposit, and IOCG deposit. The linkage between hydrothermal Cu-Fe-sulphides at Minto and a magmatic hydrothermal source was first proposed by Pearson (1979) based on sulphur isotope values, although he noted that the phases were in disequilibrium. Tafti (2005) also examined sulphur isotope compositions for Cu-Fe-sulphides and reported $\delta^{34}\text{S}$ (‰) values of 0.65 to -3.27. (+/- 0.2) (‰). These values, $\delta^{34}\text{S} = 2$ and -4‰, are within the typical range of sulphides in porphyry deposits (e.g., Ohmoto, 1986; Taylor, 1987). Geochemical interpretations of Minto granodiorites show that they are oxidized (i.e., magnetite series) I-type, and peraluminous, broadly compatible with published granitoid compositions associated with Cu-Au-Mo generating rocks (Blevin, 2004).

This study shows that construction of the Minto pluton occurred from ~197 to 202 Ma, contemporaneous with multiple phases of intrusion, continued ductile deformation, and mineralization. This interpretation contrasts with that of Tafti (2005) who suggests that

mineralization predates emplacement of the Granite Batholith, citing sharp intrusive contacts between unmineralized, massive quartz diorite of the Granite Batholith, strongly deformed, mineralized rock units, and a range of interpreted crystallization ages. Tafti (2005) classifies the Minto deposit as an “arrested” porphyry deposit, and suggests that the lack of symmetry for the mineral zonation to the west indicates that this ore zone is not in its original position and in fact is a piece of a deposit embedded in the intrusive phase as a raft. However, no evidence of large-scale rafts or roof-pendants was observed during this study. Stoping of earlier rock was uncommon and at scales less than ~one metres, and alteration was observed both in early and late intrusions. Certain features of the Minto deposit are, however, similar to definitions of “classic” porphyry deposits. For example, ore mineral zonation can occur with bornite dominating the core of an orebody, especially at deeper crustal levels (Sillitoe, 2010). The size of the pluton hosting mineralization is variable from <1 km to >4 km. (Sillitoe, 2010), which could account for the size of the Minto pluton. Potassic alteration, specifically biotite alteration, is a common feature of hydrothermal alteration associated with porphyry mineralization (Sillitoe, 2010). However, one of the most distinctive features of porphyry deposits, veining, is rare in the Minto deposit (Titley, 1966; Sillitoe, 1973; Sillitoe, 2010). Thermobarometric data from Tafti (2005) and this study indicate emplacement depths of >15 km. Such depths are incompatible with the definition of porphyry deposits in current literature, with maximum depths described as <9 km (e.g., Sillitoe, 2010). Therefore, although the Minto deposit shares certain characteristics of a porphyry deposit, the conditions of formation are not compatible with the classic definition of a porphyry deposit.

Workers at the Minto deposit have also interpreted the deposit as an IOCG, mainly due to an abundance of magnetite associated with mineralisation. However, Minto does not exhibit the essential characteristics of IOCG deposits described in current literature, e.g., brittle

deformation as the control on mineralizing fluids, local large scale hydrothermal breccias, depleted SiO₂ contents in altered wall rocks, and the presence of abundant low Ti iron oxides or iron silicates (Sillitoe, 2003; Pollard, 2006; Groves et al., 2010). At Minto, none of these key characteristics are present, except for mineralisation being related to magmatic-hydrothermal activity. Alteration characteristic of IOCG deposits includes either calcic alteration (amphibole, epidote, and/or carbonate) and/or potassic alteration (biotite, K-feldspar, or white mica in high level, hydrolytic systems) (Groves et al., 2010). Both of these alteration types are observed at Minto, although such alteration also occurs in relation to porphyry deposits. Direct petrological and geochemical evidence, plus indirect isotopic evidence, implicate the devolatilization of deep, volatile-rich mantle-derived magmas as the primary energy- and fluid-driving force for IOCG systems (Groves et al., 2010); no such evidence has yet been discovered at Minto.

The ductile shear-related permeability inferred at Minto is not typical of copper-gold deposits occurring in similar environments, i.e., porphyry or IOCG deposits where ore fluids are derived from convergent margin related granitoid intrusions. Porphyry and IOCG deposits are recorded as occurring in the upper crust with ore fluids generating fracture related permeability (e.g., Norton and Knight, 1977; Haynes and Titley, 1980; Sillitoe, 2003; Cathles and Shannon, 2007) including even the most deeply emplaced porphyry deposits as deep as 10 km (Seedorff et al., 2005). Pollard (2006) does describe deeply occurring IOCG deposits where magma–fluid systems cannot generate sufficient mechanical energy to fracture the host rocks; however, these deposits utilize a variety of existing fault-related structural traps for fluid permeability and do not initiate ductile deformation.

Potassic alteration in the form of biotite-magnetite has been noted in the high temperature portion of porphyry deposits. In these environments, initial potassic alteration and minor metal precipitation occur from a metalliferous single-phase liquid or coexisting hypersaline liquid and

vapour as porphyry Cu systems cool through the 700 °C to 550 °C temperature range (e.g., Eastoe, 1978; Bodnar, 1995; Frei, 1995; Ulrich and Heinrich, 2001).

Minto is a unique deposit because it is similar to porphyry deposits, e.g., mineralisation related to hydrothermal activity from granitic intrusions and biotite-magnetite alteration associated with sulphides, yet fundamental and defining characteristics set it apart, e.g., the depth of emplacement and importance of ductile deformation as a permeability pathway. Given the understandings of how the Minto deposit formed described in this thesis, in addition to earlier work, this deposit is believed to represent an entity within the continuum of hydrothermal deposits possible in the continental crust above arc subduction zones (Figure 39). These zones, i.e., regions below porphyry deposits, have been identified as prospective areas for over 40 years. Sillitoe (1973) proposed a genetic relationships between porphyry copper deposits and calc-alkaline intrusives, their relationship to convergent margins and magma production, and the potential for mineralisation below the observed bases of porphyry deposits. More recently, Seedorff (2008) refers to the region below the porphyry ore deposits as rarely described even though metallogenic hydrothermal fluids are widely believed to originate from below such deposits (e.g., Gustafson and Hunt, 1975; Burnham, 1979; Dilles, 1987; Carten et al., 1988; Redmond et al., 2004). Furthermore, Seedorff (2008) rationalises that magmatic systems likely continue for many kilometres beneath the orebody, into and perhaps beneath a cogenetic batholith, and that “these zones constitute an important source region of ore fluids and other components, and in certain geologic terrains the characteristics of root zones may point to previously undiscovered deposits.” That Minto Cu-Au-Ag mineralisation is coeval with the construction of a large plutonic granodiorite body, and that emplacement of mineralisation and igneous bodies occurred within the ductile regime at depths more than 10 kilometres, points

strongly to Minto representing a predicted but hitherto undiscovered deposit type beneath porphyry deposits.

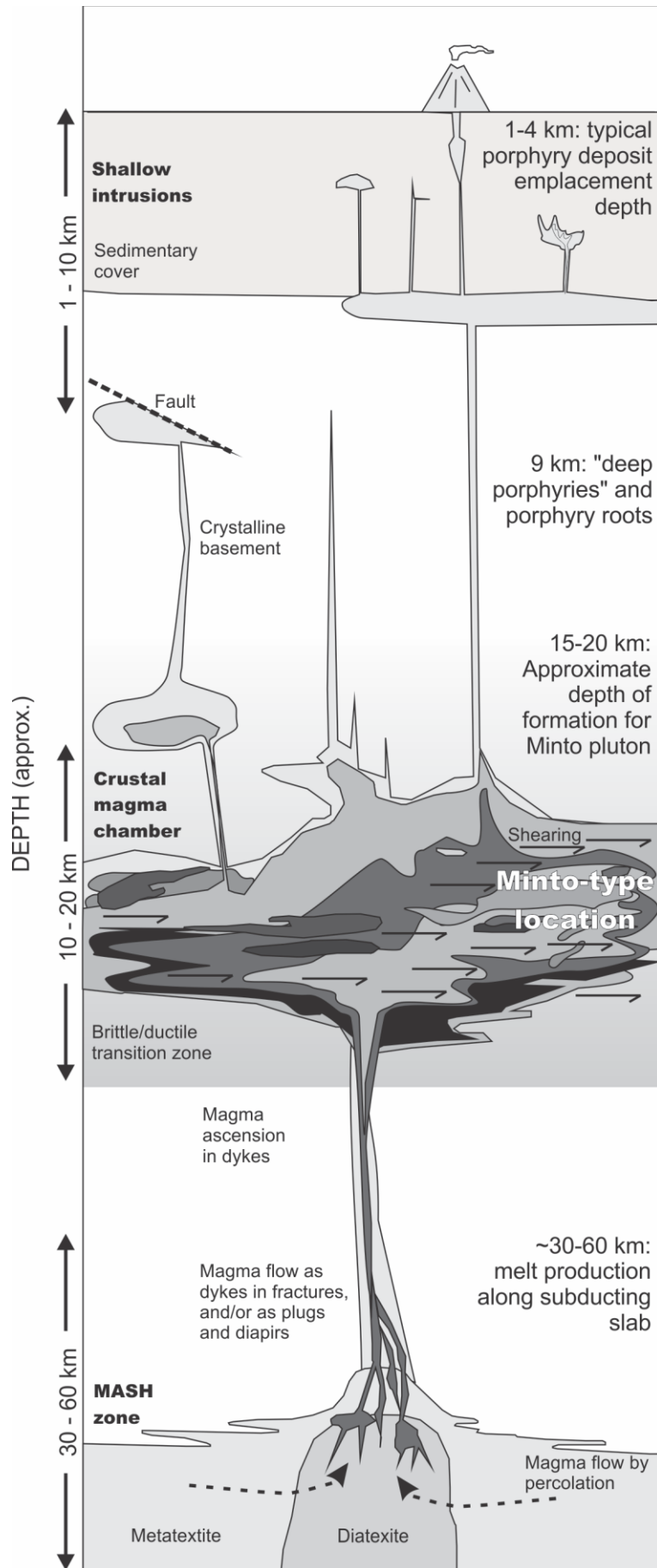


Figure 40: Simplified schematic diagram of magma generation and emplacement within a subduction arc environment. The Minto deposit is interpreted as the product of normal geologic processes, i.e., created as the consequence of felsic magma emplacement and associated hydrothermal activity (as described by Richards, 2003). Although the deposit characteristics of Minto are unique, it is interpreted as part of the magmatic-hydrothermal continuum of deposits occurring in arc environments (as described by Robert, 2000). Deposit genesis at depth and within the ductile deformation regime is the unique feature of this deposit that separates it from more common varieties occurring in subduction environments, e.g., porphyry and epithermal deposits.

Chapter 3: Conclusion

Cu-Au-Ag mineralisation at the Minto Deposit, YT, Canada, is hosted within ductilely deformed and altered granitoids of the Minto pluton. Variably foliated mineralized granodiorites and associated minor variants are juxtaposed with barren rocks by sharp contacts.

On average, deformation zones observed in the open pit dip $< 30^\circ$ towards the northeast and are continuous over tens of metres with $> 60^\circ$ dipping margins; these margins are commonly truncated by much younger faults. The enveloping surface of the deformation zones can be mapped based on drill core and Cu-Au-Ag grade as sub-horizontal and laterally continuous over tens to hundreds of metres, although in reality the interface between deformed mineralized rocks and barren massive rocks vary on a sub-metre scale. Mineral foliation within deformation zones is typically parallel to structural contacts near said contacts, but internally varies in orientation and is locally strongly folded. . The contact between massive and deformed rocks is commonly cusp and lobate, or mullioned, also due to continued deformation accommodated by deformation zones. Cusp and piercement geometry have also developed for analogous reasons of rheological contrast within individual deformation zones between massive sulphides and adjacent internally deformed granodiorites.

Deformation-related recrystallization of quartz, feldspar, and biotite is present to some degree in all Minto granodiorites, even those that appear undeformed in hand specimen. Biotite-magnetite (potassic) alteration is strongly correlated with mineralisation and deformation zones.

Several hypotheses to explain the geometry of the deposit were proposed at the beginning of this thesis: (i) that contacts between massive and foliated rocks represent igneous contacts, and mineralisation predates the intrusive units, i.e., a “raft and roof pendant” model wherein a pre-existing deposit was partially incorporated into a pluton, (ii) that contacts between massive and foliated rocks represent strain accommodation within a plutonic mass and mineralizing fluids

were focussed along deformation pathways, i.e., “a shear-hosted hydrothermal deposit” model, or (iii) some combination of igneous activity, hydrothermal fluid flow, and ductile deformation, i.e., a “plutonism and mineralisation in an active shear zone” model. The data presented in this thesis are most consistent with the third option. Deformation zones observed during study are the result of partitioned strain into Minto granitoids and are preferentially localized in zones of hydrothermal alteration, especially the assemblage biotite + magnetite +/- sulphides. Magmatic anisotropies such as igneous contacts and K-feldspar megacryst-rich layering also aided strain partitioning. The presence of biotite during alteration promoted strain softening and continued deformation consistent with the work of Shea and Kronenburg (1993) and Johnson (2004), and created positive feedback link with hydrothermal fluid flow (as described by Dipple and Ferry, 1992).

Granitoid magmas hosting mineralization were intruded as batches between at least 200.1 Ma to 197.0 Ma based on U-Pb SHRIMP geochronology of zircons. This timing is broadly contemporaneous with molybdenite mineralisation dates calculated for a separate suite of rocks at 202 (+/- 0.8) Ma to ~197. Molybdenite occurs with a variety of textures and associations with Cu-sulphides, and locally molybdenite appears to crosscut copper sulphides. This relationship thus locally constrains the timing of Cu-Au-Ag mineralization to that of the host intrusions, approximately 202 to 197 Ma.

References

- Anderson, J. L., 1990, The nature and origin of Cordilleran magmatism, Geological Society of America. Memoir 174, 414 pp, 1990.
- Annual Technical Report, December 15, 2009. Annual Report. *SEDAR*. Web. Accessed December 4, 2010.
- Arevalo, C., Grocott, J., Martin, W., Pringle, M., and Taylor, G., 2006, Structural Setting of the Candelaria Fe Oxide Cu-Au Deposit, Chilean Andes (27° 30'S): *Economic Geology*, v. 101, p. 819.
- Baker, T., 2002, Emplacement depth and carbon dioxide-rich fluid inclusions in intrusion-related gold deposits: *Economic Geology*, v. 97, p. 1111.
- Barbarin, B., 1999, A review of the relationships between granitoid types, their origins and their geodynamic environments: *Lithos*, v. 46, p. 605-626.
- Bas, M. J. L. E., Maitre, R. W. L., Streckeisen, A., and Zanettin, B., 1986, A chemical classification of volcanic rocks based on the total alkali-silica diagram: *Journal of Petrology*, v. 27, p. 745.
- Baumgartner, L., and Olsen, S., 1995, A least-squares approach to mass transport calculations using the isocon method: *Economic Geology*, v. 90, p. 1261.
- Bea, F., 2010, Crystallization Dynamics of Granite Magma chambers in the Absence of Regional Stress: Multiphysics Modeling with Natural Examples: *Journal of Petrology*, v. 51, p. 1541.
- Becker, J., Siegesmund, S., and Jelsma, H., 2000, The Chinamora batholith, Zimbabwe: structure and emplacement-related magnetic rock fabric: *Journal of Structural Geology*, v. 22, p. 1837-1853.
- Bell, T., 1978, Progressive deformation and reorientation of fold axes in a ductile mylonite zone: the Woodroffe thrust: *Tectonophysics*, v. 44, p. 285-298.
- Beranek, L. P., 2006, A Triassic link between Yukon-Tanana terrane and North America: New detrital zircon age, geochemical, and biostratigraphic data: Geological Society of America, Abstracts with programs, Cordilleran Section, 2006, p. 5.
- Brimhall, G. H., C. N. Alpers, and A. B. Cunningham (1985) Analysis of supergene ore-forming processes and ground-water solute transport using mass balance principles. *Economic Geology*, 80, 1227-1256.
- Blevin, P., 2004, Redox and Compositional Parametres for Interpreting the Granitoid Metallogeny of Eastern Australia: Implications for Gold rich Ore Systems: *Resource Geology*, v. 54, p. 241-252.
- Blevin, P., and Chappell, B., 1992, The role of magma sources, oxidation states and fractionation in determining the granite metallogeny of eastern Australia: *Transactions of the Royal Society of Edinburgh. Earth sciences*, v. 83, p. 305-316.
- Blevin, P., and Chappell, B., 1995, Chemistry, origin, and evolution of mineralized granites in the Lachlan fold belt, Australia; the metallogeny of I- and S-type granites: *Economic Geology*, v. 90, p. 1604.
- Blundy, J. D., and Holland, T. J. B., 1990, Calcic amphibole equilibria and a new amphibole-plagioclase geothermometer: *Contributions to Mineralogy and Petrology*, v. 104, p. 208-224.
- Bodnar, R., 1995, Fluid-inclusion evidence for a magmatic source for metals in porphyry copper deposits: in Thompson, JFH, ed., *Magma, fluids, and ore deposits*: Mineralogical Association of Canada Short Course Series, v. 23, p. 139-152.

- Bodorkos, S., Cawood, P. A., and Oliver, N. H. S., 2000, Timing and duration of syn-magmatic deformation in the Mabel Downs Tonalite, northern Australia: *Journal of Structural Geology*, v. 22, p. 1181-1198.
- Borg, I., and Handin, J., 1966, Experimental deformation of crystalline rocks: *Tectonophysics*, v. 3, p. 249-367.
- Borges, F., and White, S., 1980, Microstructural and chemical studies of sheared anorthosites, Roneval, South Harris: *Journal of Structural Geology*, v. 2, p. 273-280.
- Bostock, H. S., 1936, Carmacks district, Yukon. Geological Survey of Canada, Memoir 189, 67 p.
- Boudreau, A., 2011, The evolution of texture and layering in layered intrusions: *International Geology Review*, v. 53, p. 330-353.
- Braxton, D., and Cooke, D., 2005, The Boyongan porphyry Cu-Au deposit: Repeated hydrothermal cycles tied to discrete intrusive events, 2005, p. 357-360.
- Brett, R., 1964, Experimental data from the system Cu-Fe-S and their bearing on exsolution textures in ores: *Economic Geology*, v. 59, p. 1241-1269.
- Brown, G., Thorpe, R., and Webb, P., 1984, The geochemical characteristics of granitoids in contrasting arcs and comments on magma sources: *Journal of Geological Society*, v. 141, p. 413.
- Brown, M., 2007, Crustal melting and melt extraction, ascent and emplacement in orogens: mechanisms and consequences: *Journal of the Geological Society*, v. 164, p. 709.
- Brown, M., and Solar, G. S., 1998, Granite ascent and emplacement during contractional deformation in convergent orogens: *Journal of Structural Geology*, v. 20, p. 1365-1393.
- Brown, M., and Solar, G. S., 1999, The mechanism of ascent and emplacement of granite magma during transpression: a syntectonic granite paradigm: *Tectonophysics*, v. 312, p. 1-33.
- Burnham, C., 1979, Magmas and Hydrothermal Fluids, in Barnes, H., ed., *Geochemistry of Hydrothermal Ore Deposits*, Wiley-Interscience, p. 71-136.
- Candela, P. A., and Holland, H. D., 1984, The partitioning of copper and molybdenum between silicate melts and aqueous fluids: *Geochimica et Cosmochimica Acta*, v. 48, p. 373-380.
- Carten, R. B., Geraghty, E. P., Walker, B. M., and Shannon, J. R., 1988, Cyclic development of igneous features and their relationship to high-temperature hydrothermal features in the Henderson porphyry molybdenum deposit, Colorado: *Economic Geology*, v. 83, p. 266.
- Cathles, L., and Shannon, R., 2007, How potassium silicate alteration suggests the formation of porphyry ore deposits begins with the nearly explosive but barren expulsion of large volumes of magmatic water: *Earth and Planetary Science Letters*, v. 262, p. 92-108.
- Chappell, B., and White, A., 1974, Two contrasting granite types: *Pacific Geology*, v. 8, p. 173-174.
- Chappell, B., White, A., and Wyborn, D., 1987, The importance of residual source material (restite) in granite petrogenesis: *Journal of Petrology*, v. 28, p. 1111.
- Chinner, G., 1960, Pelitic gneisses with varying ferrous/ferric ratios from Glen Clova, Angus, Scotland: *Journal of Petrology*, v. 1, p. 178.
- Clarke, D., 1981, The mineralogy of peraluminous granites: a review: *Canadian Mineralogist*, v. 19, p. 3.
- Clemens, J., and Benn, K., 2010, Anatomy, emplacement and evolution of a shallow-level, post-tectonic laccolith: the Mt Disappointment pluton, SE Australia: *Journal of the Geological Society*, v. 167, p. 915.
- Clemens, J. D., and Wall, V. J., 1981, Origin and crystallization of some peraluminous (S-type) granitic magmas: *Canadian Mineralogist*, v. 19, p. 111.

- Cline, J., and Bodnar, R., 1991, Can economic porphyry copper mineralization be generated by a typical calc-alkaline melt?: *Journal of Geophysical Research*, v. 96, p. 8113-8126.
- Cloos, M., 2001, Bubbling magma chambers, cupolas, and porphyry copper deposits: *International Geology Review*, v. 43, p. 285-311.
- Collins, W., and Sawyer, E., 1996, Pervasive granitoid magma transfer through the lower-middle crust during non coaxial compressional deformation: *Journal of Metamorphic Geology*, v. 14, p. 565-579.
- Colpron, M., (compiler), 2006, Tectonic Assemblage map of Yukon-Tanana and related terranes in Yukon and British Columbia (1: 1 000 000 scale). Open File 2006-1, Yukon Geological Survey.
- Colpron, M., Nelson, J., and Murphy, D., 2006, A tectonostratigraphic framework for the pericratonic terranes of the northern Cordillera: *Paleozoic Evolution and Metallogeny of Pericratonic Terranes at the Ancient Pacific Margin of North America*, Canadian and Alaskan Cordillera, M. Colpron and JL Nelson (eds.), Geological Association of Canada, Special Paper, v. 45, p. 1-23.
- Colpron, M., Nelson, J. A. L., and Murphy, D. C., 2007, Northern Cordilleran terranes and their interactions through time: *GSA Today*, v. 17, p. 4-10.
- Connolly, J., 1997, Devolatilization-generated fluid pressure and deformation-propagated fluid flow during prograde regional metamorphism: *Journal of Geophysical Research*, v. 102, p. 18149-18,173.
- Connolly, J., and Podladchikov, Y., 2004, Fluid flow in compressive tectonic settings: Implications for midcrustal seismic reflectors and downward fluid migration: *Journal of Geophysical Research*, v. 109, p. B04201.
- Connolly, J., and Podladchikov, Y. Y., 1998, Compaction driven fluid flow in viscoelastic rock: *Geodinamica Acta*, v. 11, p. 55-84.
- Connolly, J. A. D., 2010, The mechanics of metamorphic fluid expulsion: *Elements*, v. 6, p. 165.
- Corfu, F., Hanchar, J. M., Hoskin, P. W. O., and Kinny, P., 2003, Atlas of zircon textures: *Reviews in Mineralogy and Geochemistry*, v. 53, p. 469.
- Cox, K., Bell, J., and Pankhurst, R., 1979, *The interpretation of igneous rocks*, George Allen and Unwin, London.
- Cox, S. F., 2002, Fluid flow in mid-to deep crustal shear systems: Experimental constraints, observations on exhumed high fluid flux shear systems, and implications for seismogenic processes, J.W. Hedenquist, J.F.H. Thompson, R.J. Goldfarb, and J.P. Richards (eds.), *Earth Planets and Space*, v. 54, p. 1121-1126.
- Cox, S. F., 2005, Coupling between deformation, fluid pressures and fluid flow in ore-producing hydrothermal systems at depth in the crust: *Economic Geology 100th Anniversary Volume*, p. 1-35.
- Cruden, A., 1998, On the emplacement of tabular granites: *Journal of the Geological Society*, v. 155, p. 853.
- Cruden, A., and McCaffrey, K., 2001, Growth of plutons by floor subsidence: implications for rates of emplacement, intrusion spacing and melt-extraction mechanisms: *Physics and Chemistry of the Earth, Part A: Solid Earth and Geodesy*, v. 26, p. 303-315.
- Davis, B., and Henderson, R., 1999, Syn-orogenic extensional and contractional deformation related to granite emplacement in the northern Tasman Orogenic Zone, Australia: *Tectonophysics*, v. 305, p. 453-475.
- de Saint-Blanquat, M., Law, R. D., Bouchez, J. L., and Morgan, S. S., 2001, Internal structure and emplacement of the Papoose Flat pluton: An integrated structural, petrographic, and

- magnetic susceptibility study: Geological Society of America Bulletin, v. 113, p. 976-995.
- DePaolo, D., and Wasserburg, G., 1977, The sources of island arcs as indicated by Nd and Sr isotopic studies: Geophysical Research Letters, v. 4, p. 465-468.
- Didier, J., 1991, The various types of enclaves in the Hercynian granitoids of the Massif Central, France, *in* Didier, J., and Barbarin, B., eds., Enclaves and Granite Petrology. Developments in Petrology 13, p. 47 - 60.
- Dilles, J., 1987, Petrology of the Yerington Batholith, Nevada; evidence for evolution of porphyry copper ore fluids: Economic Geology, v. 82, p. 1750.
- Dipple, G. M., and Ferry, J. M., 1992, Metasomatism and fluid flow in ductile fault zones: Contributions to Mineralogy and Petrology, v. 112, p. 149-164.
- Durazzo, A., and Taylor, L., 1982, Experimental exsolution textures in the system bornite-chalcopyrite: Genetic implications concerning natural ores: Mineralium Deposita, v. 17, p. 79-97.
- Eastoe, C., 1978, A fluid inclusion study of the Panguna porphyry copper deposit, Bougainville, Papua New Guinea: Economic Geology, v. 73, p. 721.
- Ellis, D. J., and Thompson, A. B., 1986, Subsolvus and partial melting reactions in the quartz-excess $\text{CaO}+\text{MgO}+\text{Al}_2\text{O}_3+\text{SiO}_2+\text{H}_2\text{O}$ system under water-excess and water-deficient conditions to 10 kb: some implications for the origin of peraluminous melts from mafic rocks: Journal of Petrology, v. 27, p. 91.
- Finlow-Bates, T., and Stumpfl, E., 1981, The behaviour of so-called immobile elements in hydrothermally altered rocks associated with volcanogenic submarine-exhalative ore deposits: Mineralium Deposita, v. 16, p. 319-328.
- Frei, R., 1995, Evolution of mineralizing fluid in the porphyry copper system of the Skouries Deposit, Northeast Chalkidiki (Greece); evidence from combined Pb-Sr and stable isotope data: Economic Geology, v. 90, p. 746.
- Frost, B. R., Barnes, C., Collins, W., Arculus, R., Ellis, D., and Frost, C., 2001, A geochemical classification for granitic rocks: Journal of Petrology, v. 42, p. 2033.
- Frost, B. R., and Frost, C., 2008, A geochemical classification for feldspathic igneous rocks: Journal of Petrology, v. 49, p. 1955 - 1969.
- Furman, T., and Spera, F. J., 1985, Co-mingling of acid and basic magma with implications for the origin of mafic I-type xenoliths: field and petrochemical relations of an unusual dike complex at Eagle Lake, Sequoia National Park, California, USA: Journal of Volcanology and Geothermal Research, v. 24, p. 151-178.
- Gale, R. E., 1976, Origin of the Minto copper deposit. Yukon Territory (abstract). Bulletin of the Canadian Institute of Mining and Metallurgy, v. 69, p. 61.
- Gapais, D., 1989, Shear structures within deformed granites; mechanical and thermal indicators: Geology, v. 17, p. 1144-1147.
- Gates, A., and Glover III, L., 1989, Alleghanian tectono-thermal evolution of the dextral transcurrent hylas zone, Virginia Piedmont, USA: Journal of Structural Geology, v. 11, p. 407-419.
- Géraud, Y., Caron, J., and Faure, P., 1995, Porosity network of a ductile shear zone: Journal of Structural Geology, v. 17, p. 1757-1769.
- Giggenbach, W., 1984, Mass transfer in hydrothermal alteration systems: A conceptual approach: Geochimica et Cosmochimica Acta, v. 48, p. 2693-2711.
- Gill, J., 1969, Experimental deformation and annealing of sulphides and interpretation of ore textures: Economic Geology, v. 64, p. 500.

- Glazner, A., and Ussler III, W., 1988, Trapping of magma at midcrustal density discontinuities: *Geophysical Research Letters*, v. 15, p. 673-675.
- Glazner, A. F., and Bartley, J. M., 1991, Volume loss, fluid flow and state of strain in extensional mylonites from the central Mojave Desert, California: *Journal of Structural Geology*, v. 13, p. 587-594.
- Gleason, G. C., and DeSisto, S., 2008, A natural example of crystal-plastic deformation enhancing the incorporation of water into quartz: *Tectonophysics*, v. 446, p. 16-30.
- Gordey, S. P., and Makepeace, A. J., 2001, *Bedrock Geology, Yukon Territory*. Geological Survey of Canada, Open File 3754 and Exploration and Geological Services Division, Yukon Region, Indian and Northern Affairs Canada, Open File 2001-1, 1:1 000 000 scale map.
- Grant, J., 1986, The isocon diagram; a simple solution to Gresens' equation for metasomatic alteration: *Economic Geology*, v. 81, p. 1976.
- Grant, J., 2005, Isocon analysis: A brief review of the method and applications: *Physics and Chemistry of the Earth, Parts A/B/C*, v. 30, p. 997-1004.
- Gresens, R., 1967, Composition-volume relationships of metasomatism: *Chemical Geology*, v. 2, p. 47-65.
- Griggs, D., 1967, Hydrolytic Weakening of Quartz and Other Silicates: *Geophysical Journal of the Royal Astronomical Society*, v. 14, p. 19-31.
- Gromet, L. P., and Silver, L. T., 1983, Rare earth element distributions among minerals in a granodiorite and their petrogenetic implications: *Geochimica et Cosmochimica Acta*, v. 47, p. 925-939.
- Groves, D. I., Bierlein, F. P., Meinert, L. D., and Hitzman, M. W., 2010, Iron oxide copper-gold (IOCG) deposits through Earth history: Implications for origin, lithospheric setting, and distinction from other epigenetic iron oxide deposits: *Economic Geology*, v. 105, p. 641.
- Guillope, M., and Poirier, J., 1979, Dynamic recrystallization during creep of single-crystalline halite: an experimental study: *J. geophys. Res.*, v. 84.
- Gustafson, L., and Hunt, J., 1975, The porphyry copper deposit at El Salvador, Chile: *Economic Geology*, v. 70, p. 857.
- Hack, A. C., and Mavrogenes, J. A., 2006, A synthetic fluid inclusion study of copper solubility in hydrothermal brines from 525 to 725 C and 0.3 to 1.7 GPa: *Geochimica et Cosmochimica Acta*, v. 70, p. 3970-3985.
- Harris, A. C., Kamenetsky, V. S., White, N. C., Van Achtebergh, E., and Ryan, C. G., 2003, Melt inclusions in veins: Linking magmas and porphyry Cu deposits: *Science*, v. 302, p. 2109.
- Hattori, K. H., and Keith, J. D., 2001, Contribution of mafic melt to porphyry copper mineralization: evidence from Mount Pinatubo, Philippines, and Bingham Canyon, Utah, USA: *Mineralium Deposita*, v. 36, p. 799-806.
- Hawkesworth, C., 1982, Isotope characteristics of magmas erupted along destructive plate margins, in Thorpe, R., ed., *Andesites: Orogenic Andesites and Related Rocks*, p. 549-571.
- Haynes, F. M., and Titley, S., 1980, The evolution of fracture-related permeability within the Ruby Star Granodiorite, Sierrita porphyry copper deposit, Pima County, Arizona: *Economic Geology*, v. 75, p. 673.
- Helwig, J., 1974, Eugeosynclinal basement and a collage concept of orogenic belts: Helwig, J. *Modern and ancient geosynclinal sedimentation*. Tulsa: Society of Economic Paleontologists and Mineralogists, p. 359-376.

- Hibbard, M., 1987, Deformation of incompletely crystallized magma systems: granitic gneisses and their tectonic implications: *Journal of Geology*, p. 543-561.
- Hickey, K. A., and Bell, T. H., 1996, Syn-deformational grain growth; matrix coarsening during foliation development and regional metamorphism rather than by static annealing: *European Journal of Mineralogy*, v. 8, p. 1351.
- Hildreth, W., and Moorbath, S., 1988, Crustal contributions to arc magmatism in the Andes of central Chile: *Contributions to Mineralogy and Petrology*, v. 98, p. 455-489.
- Hirth, G., and Tullis, J., 1992, Dislocation creep regimes in quartz aggregates: *Journal of Structural Geology*, v. 14, p. 145-159.
- Holland, T., and Blundy, J., 1994, Non-ideal interactions in calcic amphiboles and their bearing on amphibole-plagioclase thermometry: *Contributions to Mineralogy and Petrology*, v. 116, p. 433-447.
- Holyoke III, C. W., and Tullis, J., 2006, Formation and maintenance of shear zones: *Geology*, v. 34, p. 105.
- Huppert, H. E., and Sparks, R. S. J., 1988, The generation of granitic magmas by intrusion of basalt into continental crust: *Journal of Petrology*, v. 29, p. 599.
- Ishihara, S., 1977, The magnetite-series and ilmenite-series granitic rocks: *Mining Geology*, v. 27, p. 293-305.
- Ishihara, S., 1981, The granitoid series and mineralization: *Economic geology*, Seventy-fifth Anniversary Volume, 1905-1980, p. 458.
- Ishihara, S., 1998, Granitoid Series and Mineralization in the Circum Pacific Phanerozoic Granitic Belts: *Resource Geology*, v. 48, p. 219-224.
- Ishihara, S., 2004, The redox state of granitoids relative to tectonic setting and earth history: The magnetite-ilmenite series 30 years later: *Transactions of the Royal Society of Edinburgh-Earth Sciences*, v. 95, p. 23-33.
- Ji, S., 1998, Deformation microstructure of natural plagioclase, *in* Snoke, A., Tullis, J., and Todd, V., eds., *Fault-related rocks: A photographic atlas*, Princeton Univ Pr.
- Johnson, S., Fletcher, J., Fanning, C., Vernon, R., Paterson, S., and Tate, M., 2003, Structure, emplacement and lateral expansion of the San José tonalite pluton, Peninsular Ranges batholith, Baja California, México: *Journal of Structural Geology*, v. 25, p. 1933-1957.
- Johnson, S., Vernon, R., and Upton, P., 2004, Foliation development and progressive strain-rate partitioning in the crystallizing carapace of a tonalite pluton: microstructural evidence and numerical modeling: *Journal of Structural Geology*, v. 26, p. 1845-1865.
- Johnston, S., Mortensen, J., and Erdmer, P., 1996a, Igneous and metaigneous age constraints for the Aishihik metamorphic suite, southwest Yukon: *Canadian Journal of Earth Sciences*, v. 33, p. 1543-1555.
- Johnston, S. T., Mortensen, J. K., and Erdmer, P., 1996b, Igneous and metaigneous age constraints for the Aishihik metamorphic suite, southwest Yukon: *Canadian Journal of Earth Sciences*, v. 33, p. 1543-1555.
- Kirkham, R., and Sinclair, W., 1996, Porphyry copper, gold, molybdenum, tungsten, tin, silver: *Geology of the Canadian Mineral Deposit types*: Geologic Survey of Canada, *Geology of Canada*, v. 8, p. 421-446.
- Kolb, J., 2008, The role of fluids in partitioning brittle deformation and ductile creep in auriferous shear zones between 500 and 700° C: *Tectonophysics*, v. 446, p. 1-15.
- Koukouvelas, I., Pe-Piper, G., and Piper, D. J. W., 2002, The role of dextral transpressional faulting in the evolution of an early Carboniferous mafic-felsic plutonic and volcanic complex: Cobequid Highlands, Nova Scotia, Canada: *Tectonophysics*, v. 348, p. 219-246.

- Kronenberg, A. K., 1994, Hydrogen speciation and chemical weakening of quartz: Reviews in Mineralogy and Geochemistry, v. 29, p. 123.
- Kronenberg, A. K., and Tullis, J., 1984, Flow strengths of quartz aggregates: grain size and pressure effects due to hydrolytic weakening: Journal of Geophysical Research, v. 89, p. 4281-4297.
- Le Maitre, R. W., 1989, A Classification of Igneous Rocks and Glossary of Terms (Recommendations of the International Union of Geological Sciences Sub-Commission on the Systematics of Igneous Rocks). Blackwell, Oxford. .
- Lehmann, B., 1982, Metallogeny of tin: magmatic differentiation versus geochemical heritage: Economic Geology, v. 77, p. 50-59.
- Leitch, C., and Lentz, D., 1994, The Gresens approach to mass balance constraints of alteration systems: methods, pitfalls, examples, Alteration and Alteration Processes Associated with Ore-Forming Systems, 11, Geological Association of Canada, p. 161–192.
- Lister, G., and Price, G., 1978, Fabric development in a quartz-feldspar mylonite: Tectonophysics, v. 49, p. 37-78.
- Liu, X., Dong, S., Xue, H., and Zhou, J., 1999, Significance of allanite-(Ce) in granitic gneisses from the ultrahigh-pressure metamorphic terrane, Dabie Shan, central China: Mineralogical Magazine, v. 63, p. 579.
- Lowenstern, J. B., 2001, Carbon dioxide in magmas and implications for hydrothermal systems: Mineralium Deposita, v. 36, p. 490-502.
- Ludwig, K., 2003, User's manual for Isoplot 3.00: a geochronological toolkit for Microsoft Excel: Berkeley Geochronology Center Special Publication, v. 4, p. 70.
- Maiden, K. J., Chimimba, L. R., and Smalley, T. J., 1986, Cuspate ore-wall rock interfaces, piercement structures and the localization of some sulphide ores in deformed sulphide deposits: Economic Geology, v. 81, p. 1464-1472.
- Maniar, P., and Piccoli, P., 1989, Tectonic discrimination of granitoids: Bulletin of the Geological Society of America, v. 101, p. 635.
- Marquer, D., and Burkhard, M., 1992, Fluid circulation, progressive deformation and mass-transfer processes in the upper crust: the example of basement-cover relationships in the External Crystalline Massifs, Switzerland: Journal of Structural Geology, v. 14, p. 1047-1057.
- McCausland, P., Symons, D., Hart, C., and Blackburn, W., 2002, Paleomagnetism and geobarometry of the Granite Mountain batholith, Yukon: Minimal geotectonic motion of the Yukon-Tanana Terrane relative to North America: Yukon Exploration and Geology, p. 163-177.
- McDonough, W., and Sun, S., 1995, The composition of the Earth: Chemical Geology, v. 120, p. 223-253.
- Menegon, L., Pennacchioni, G., and Spiess, R., 2008, Dissolution-precipitation creep of K-feldspar in mid-crustal granite mylonites: Journal of Structural Geology, v. 30, p. 565-579.
- Middlemost, E. A. K., 1994, Naming materials in the magma/igneous rock system: Earth Science Reviews, v. 37, p. 215-224.
- Mihalynuk, M. G., Nelson, J. A., and Diakow, L. J., 1994, Cache Creek terrane entrapment: Oroclinal paradox within the Canadian Cordillera: Tectonics, v. 13, p. 575-595.
- Miller, C. F., 1985, Are strongly peraluminous magmas derived from pelitic sedimentary sources?: Journal of Geology, v. 93, p. 673-689.
- Miller, C. F., Furbish, D. J., Walker, B. A., Claiborne, L. L., Koteas, G. C., Bleick, H. A., and Miller, J. S., 2009, Growth of plutons by incremental emplacement of sheets in crystal-

- rich host: Evidence from Miocene intrusions of the Colorado River region, Nevada, USA: *Tectonophysics*, v. 500, p. 65-77.
- Mitra, G., 1978, Ductile deformation zones and mylonites; the mechanical processes involved in the deformation of crystalline basement rocks: *American Journal of Science*, v. 278, p. 1057.
- Miyashiro, A., 1974, Volcanic rock series in island arcs and active continental margins: *American Journal of Science*, v. 274, p. 321.
- Morgan, S. S., Law, R. D., and Nyman, M. W., 1998, Laccolith-like emplacement model for the Papoose Flat pluton based on porphyroblast-matrix analysis: *Geological Society of America Bulletin*, v. 110, p. 96.
- Mortensen, J., 1992, Pre-mid-Mesozoic tectonic evolution of the Yukon-Tanana terrane, Yukon and Alaska: *Tectonics*, v. 11, p. 836-853.
- Mortensen, J., Emon, K., Johnston, S., and Hart, C., 1999, Age, geochemistry, paleotectonic setting and metallogeny of Late Triassic-Early Jurassic intrusions in the Yukon and eastern Alaska: A preliminary report: *Yukon Exploration and Geology*, p. 139-144.
- Mortensen, J., and Tafti, R., 2002, Nature and origin of copper-gold mineralization at the Minto and Williams Creek deposits, west-central Yukon: Preliminary investigations: *Yukon Exploration and Geology*, p. 175-182.
- Mortensen, J. K., Emon, K., Johnston, S. T., and Hart, C. J. R., 2000, Age, geochemistry, paleotectonic setting and metallogeny of Late Triassic-Early Jurassic intrusions in the Yukon and eastern Alaska: A preliminary report, *in* Emond, D. S., and Weston, L. H., eds., *Yukon Exploration and Geology 1999*, Exploration and Geological Services Division, Yukon Region, Indian and Northern Affairs Canada, p. 139-144.
- Nishikawa, O., Saiki, K., and Wenk, H., 2004, Intra-granular strains and grain boundary morphologies of dynamically recrystallized quartz aggregates in a mylonite: *Journal of Structural Geology*, v. 26, p. 127-141.
- Nishikawa, O., and Takeshita, T., 2000, Progressive lattice misorientation and microstructural development in quartz veins deformed under subgreenschist conditions: *Journal of Structural Geology*, v. 22, p. 259-276.
- Norton, D., and Knight, J., 1977, Transport phenomena in hydrothermal systems: cooling plutons: *American Journal of Science*, v. 277.
- O'Hara, K., and Blackburn, W. H., 1989, Volume-loss model for trace-element enrichments in mylonites: *Geology*, v. 17, p. 524.
- Ohmoto H., Rye R.O., 1979, Isotopes of sulfur and carbon. In: Barnes H.L., ed., *Geochemistry of hydrothermal ore deposits*, 2nd edition, Wiley, New York, p. 509-567.
- Ohmoto, H., 1986, Stable isotope geochemistry of ore deposits: *Reviews in Mineralogy and Geochemistry*, v. 16, p. 491.
- Oliver, N. H. S., 2001, Linking of regional and local hydrothermal systems in the mid-crust by shearing and faulting: *Tectonophysics*, v. 335, p. 147-161.
- Oliver, N. H. S., McLellan, J. G., Hobbs, B. E., Cleverley, J. S., Ord, A., and Feltrin, L., 2006, Numerical models of extensional deformation, heat transfer, and fluid flows across basement-cover interfaces during basin-related mineralization: *Economic Geology*, v. 101, p. 1-31.
- Osterman, C., and Hutchinson, R. W., 1994, Sulphide piercement structures in the Selebi-Phikwe nickel-copper deposits, Botswana: *Exploration and Mining Geology*, v. 3, p. 285.
- Passchier, C. W., and Trouw, R. A. J., 2005, *Microtectonics*. 2nd edition, New York, Springer.
- Paterson, S., 1989, Are syntectonic granites truly syntectonic?: *EOS Transactions*, v. 70, p. 762.

- Paterson, S., and Tobisch, O., 1992, Rates of processes in magmatic arcs: implications for the timing and nature of pluton emplacement and wall rock deformation: *Journal of Structural Geology*, v. 14, p. 291-300.
- Paterson, S. R., 2009, Magmatic tubes, pipes, troughs, diapirs, and plumes: Late-stage convective instabilities resulting in compositional diversity and permeable networks in crystal-rich magmas of the Tuolumne batholith, Sierra Nevada, California: *Geosphere*, v. 5, p. 496.
- Paterson, S. R., Vernon, R. H., and Tobisch, O. T., 1989, A review of criteria for the identification of magmatic and tectonic foliations in granitoids: *Journal of Structural Geology*, v. 11, p. 349-363.
- Pearce, J., Harris, N., and Tindle, A., 1984, Trace element discrimination diagrams for the tectonic interpretation of granitic rocks: *Journal of Petrology*, v. 25, p. 956.
- Pearce, J. A., and Norry, M. J., 1979, Petrogenetic implications of Ti, Zr, Y, and Nb variations in volcanic rocks: *Contributions to Mineralogy and Petrology*, v. 69, p. 33-47.
- Pearson, W. N., 1977, The Minto copper deposit, Yukon Territory: a metamorphosed orebody in the Yukon Crystalline Terrane, Queen's University, 193 p.
- Pearson, W. N., and Clark, A. H., 1979, The Minto copper deposit, Yukon Territory: A metamorphosed orebody in the Yukon Crystalline Terrane: *Economic Geology*, v. 74, p. 1577-1599.
- Petford, N., 1996, Dikes or diapirs?: *Geological Society of America Special Papers*, v. 315, p. 105.
- Petford, N., Cruden, A., McCaffrey, K., and Vigneresse, J., 2000a, Granite magma formation, transport and emplacement in the Earth's crust: *Nature*, v. 408, p. 669-673.
- Petford, N., Cruden, A. R., McCaffrey, K. J. W., and Vigneresse, J. L., 2000b, Granite magma formation, transport and emplacement in the Earth's crust: *Nature*, v. 408, p. 669-673.
- Pignotta, G. S., Paterson, S. R., Coyne, C. C., Anderson, J. L., and Onezime, J., 2010, Processes involved during incremental growth of the Jackass Lakes pluton, central Sierra Nevada batholith: *Geosphere*, v. 6, p. 130-159.
- Pitcher, W., 1982, Granite type and tectonic environment: *Mountain Building Processes*: 19-40. Academic Press. London.
- Piwinskii, A., 1973, Experimental studies of igneous rock series, central Sierra Nevada batholith, California: Part II: *Neues Jahrbuch für Mineralogie*, v. 5, p. 193-215.
- Piwinskii, A. J., 1968, Experimental studies of igneous rock series central Sierra Nevada batholith, California: *The Journal of Geology*, p. 548-570.
- Poirier, J. P., and Guillopé, M., 1979, Deformation induced recrystallization of minerals: Mécanismes de déformation des minéraux et des roches *Colloques internationaux du centre national de la recherche scientifique*, 102. p. 67-74.
- Pollard, P., 2006, An intrusion-related origin for Cu–Au mineralization in iron oxide–copper–gold (IOCG) provinces: *Mineralium Deposita*, v. 41, p. 179-187.
- Pollard, P., Mark, G., and Mitchell, L., 1998, Geochemistry of post-1540 Ma granites in the Cloncurry district, northwest Queensland: *Economic Geology*, v. 93, p. 1330.
- Pons, J., Barbey, P., Nachit, H., and Burg, J. P., 2006, Development of igneous layering during growth of pluton: The Tarcouate Laccolith (Morocco): *Tectonophysics*, v. 413, p. 271-286.
- Prochaska, W., Bechtel, A., and Klötzli, U., 1992, Phyllonite formation and Alteration of Gneisses in Shear Zones (Gleinalmkristallin, Eastern Alps/Austria): *Mineralogy and Petrology*, v. 45, p. 195-216.

- Pryer, L., 1993, Microstructures in feldspars from a major crustal thrust zone: the Grenville Front, Ontario, Canada: *Journal of Structural Geology*, v. 15, p. 21-36.
- Redmond, P., Einaudi, M., Inan, E., Landtwing, M., and Heinrich, C., 2004, Copper deposition by fluid cooling in intrusion-centered systems: New insights from the Bingham porphyry ore deposit, Utah: *Geology*, v. 32, p. 217.
- Ree, J., Kim, H., Han, R., and Jung, H., 2005, Grain-size reduction of feldspars by fracturing and neocrystallization in a low-grade granitic mylonite and its rheological effect: *Tectonophysics*, v. 407, p. 227-237.
- Richards, J., 2003, Tectono-magmatic precursors for porphyry Cu-(Mo-Au) deposit formation: *Economic Geology*, v. 98, p. 1515.
- Richards, J., 2005, Cumulative factors in the generation of giant calc-alkaline porphyry Cu deposits, *in* Porter, T., ed., *Super Porphyry Copper and gold deposits: A global perspective*, 1: Linden Park, Porter GeoConsultancy (PGC) Publishing, p. 7-25.
- Roser, B., and Korsch, R., 1988, Provenance signatures of sandstone-mudstone suites determined using discriminant function analysis of major-element data: *Chemical Geology*, v. 67, p. 119-139.
- Rubin, A., 1993, Dikes vs. diapirs in viscoelastic rock: *Earth and Planetary Science Letters*, v. 117, p. 653-670.
- Schilling, F., and Partzsch, G., 2001, Quantifying partial melt fraction in the crust beneath the central Andes and the Tibetan Plateau: *Physics and Chemistry of the Earth, Part A: Solid Earth and Geodesy*, v. 26, p. 239-246.
- Schmidt, M. W., and Poli, S., 2004b, Magmatic epidote: *Reviews in Mineralogy and Geochemistry*, v. 56, p. 399-430.
- Schmidt, M. W., and Thompson, A. B., 1996, Epidote in calc-alkaline magmas: An experimental study of stability, phase relationships, and the role of epidote in magmatic evolution: *American Mineralogist*, v. 81, p. 462-474.
- Scott, D., and St-Onge, M., 1995, Constraints on Pb closure temperature in titanite based on rocks from the Ungava orogen, Canada: Implications for U-Pb geochronology and PTt path determinations: *Geology*, v. 23, p. 1123.
- Seedorff, E., Barton, M. D., Stavast, W. J. A., and Maher, D. J., 2008, Root zones of porphyry systems: Extending the porphyry model to depth: *Economic Geology*, v. 103, p. 939.
- Seedorff, E., Dilles, J., Proffett Jr, J., Einaudi, M., Zurcher, L., Stavast, W., Johnson, D., and Barton, M., 2005, Porphyry deposits: Characteristics and origin of hypogene features: *Economic Geology 100th Anniversary Volume*, v. 29, p. 251-298.
- Selby, D., and Creaser, R., 2001a, Late and mid-Cretaceous mineralization in the northern Canadian Cordillera: Constraints from Re-Os molybdenite dates: *Economic Geology*, v. 96, p. 1461.
- Selby, D., and Creaser, R. A., 2001b, Re-Os Geochronology and Systematics in Molybdenite from the Endako Porphyry Molybdenum Deposit, British Columbia, Canada: *Economic Geology*, v. 96, p. 197-204.
- Shea, W., and Kronenberg, A., 1993, Strength and anisotropy of foliated rocks with varied mica contents: *Journal of Structural Geology*, v. 15, p. 1097-1121.
- Shinohara, H., and Hedenquist, J., 1997, Constraints on magma degassing beneath the Far Southeast porphyry Cu-Au deposit, Philippines: *Journal of Petrology*, v. 38, p. 1741.
- Shinohara, H., Kazahaya, K., and Lowenstern, J. B., 1995, Volatile transport in a convecting magma column: implications for porphyry Mo mineralization: *Geology*, v. 23, p. 1091.

- Siegesmund, S., and Becker, J., 2000, Emplacement of the Ardara pluton (Ireland): new constraints from magnetic fabrics, rock fabrics and age dating: *International Journal of Earth Sciences*, v. 89, p. 307-327.
- Sillitoe, R., 1973, The tops and bottoms of porphyry copper deposits: *Economic Geology*, v. 68, p. 799.
- Sillitoe, R. H., 2003, Iron oxide-copper-gold deposits: an Andean view: *Mineralium Deposita*, v. 38, p. 787-812.
- Sillitoe, R. H., 2010, Porphyry copper systems: *Economic Geology*, v. 105, p. 3.
- Sillitoe, R. H., and Hedenquist, J. W., 2003, Linkages between volcanotectonic settings, ore-fluid compositions, and epithermal precious metal deposits, in Graham, I., and Simmons, S., eds., *Volcanic, Geothermal, and Ore-forming Fluids: Rulers and Witnesses of Processes Within the Earth*, Society of Economic Geologists, Inc. p. 315-343.
- Simon, A. C., Pettke, T., Candela, P. A., Piccoli, P. M., and Heinrich, C. A., 2006, Copper partitioning in a melt-vapor-brine-magnetite-pyrrhotite assemblage: *Geochimica et Cosmochimica Acta*, v. 70, p. 5583-5600.
- Simon, A. C., and Ripley, E. M., 2011, The role of magmatic sulfur in the formation of ore deposits: *Reviews in Mineralogy and Geochemistry*, v. 73, p. 513.
- Simpson, C., 1983, Strain and shape-fabric variations associated with ductile shear zones: *Journal of Structural Geology*, v. 5, p. 61-72.
- Simpson, C., 1985, Deformation of granitic rocks across the brittle-ductile transition: *Journal of Structural Geology*, v. 7, p. 503-511.
- Simpson, C., and Wintsch, R., 1989, Evidence for deformation-induced K-feldspar replacement by myrmekite: *Journal of Metamorphic Geology*, v. 7, p. 261-275.
- Singer, B., Myers, J., Linneman, S., and Angevine, C., 1989, The thermal history of ascending magma diapirs and the thermal and physical evolution of magmatic conduits: *Journal of Volcanology and Geothermal Research*, v. 37, p. 273-289.
- Singer, D. A., Berger, V. I., and Moring, B. C., 2008, Porphyry copper deposits of the world: Database and grade and tonnage models, U.S. Geological Survey Open-File Report 2008-1155.
- Skelton, A., Valley, J., Graham, C., Bickle, M., and Fallick, A., 2000, The correlation of reaction and isotope fronts and the mechanism of metamorphic fluid flow: *Contributions to Mineralogy and Petrology*, v. 138, p. 364-375.
- Smoliar, M., Walker, R., and Morgan, J., 1996, Re-Os ages of group IIA, IIIA, IVA, and IVB iron meteorites: *Science*, v. 271, p. 1099.
- Sokoutis, D., 1987, Finite strain effects in experimental mullions: *Journal of Structural Geology*, v. 9, p. 233-242.
- Sokoutis, D., 1990, Experimental mullions at single and double interfaces: *Journal of Structural Geology*, v. 12, p. 365-373.
- Stern, R., 1997, The GSC sensitive high resolution ion microprobe (SHRIMP): analytical techniques of zircon U-Th-Pb age determinations and performance evaluation: *Radiogenic age and isotopic studies: Report*, v. 10, p. 1-31.
- Stern, R., and Amelin, Y., 2003, Assessment of errors in SIMS zircon U-Pb geochronology using a natural zircon standard and NIST SRM 610 glass: *Chemical Geology*, v. 197, p. 111-142.
- Stesky, R., 1978, Mechanisms of high temperature frictional sliding in Westerly granite: *Canadian Journal of Earth Sciences*, v. 15, p. 361-375.
- Stesky, R., Brace, W., Riley, D., and Robin, P., 1974, Friction in faulted rock at high temperature and pressure: *Tectonophysics*, v. 23, p. 177-203.

- Stevenson, C., 2009, The relationship between forceful and passive emplacement: The interplay between tectonic strain and magma supply in the Rosses Granitic Complex, NW Ireland: *Journal of Structural Geology*, v. 31, p. 270-287.
- Stipp, M., StuÈnitz, H., Heilbronner, R., and Schmid, S., 2002, The eastern Tonale fault zone: a 'natural laboratory' for crystal plastic deformation of quartz over a temperature range from 250 to 700 8C: *Journal of Structural Geology*, v. 24, p. 1861–1884. P. 287.
- Streckeisen, A., 1974, Classification and nomenclature of plutonic rocks recommendations of the IUGS subcommission on the systematics of Igneous Rocks: *Geologische Rundschau*, v. 63, p. 773-786.
- Streit, J., and Cox, S., 2002, Evolution of fracture networks in shear zones: insights from see-through experiments on biphenyl aggregates: *Journal of Structural Geology*, v. 24, p. 107-122.
- Tafti, R., 2005, Nature, Age and Origin of Cu-Au mineralization at the Minto and Williams Creek Deposits, Yukon, University of British Columbia, 213 p.
- Talbot, C. J., and Sokoutis, D., 1992, The importance of incompetence: *Geology*, v. 20, p. 951-953.
- Taylor, B., 1987, Stable isotope geochemistry of ore-forming fluids: *Short Course in Stable Isotope Geochemistry of Low Temperature Fluids*, v. 13, p. 337–445.
- Tempelman-Kluit, D. J., 1974. *Geology of the Carmacks map-area*. Geological Survey of Canada, Open File Report 200.
- Tempelman-Kluit, D., Wanless, R., Wilson, M., Schafer, C., Mudie, P., Fyson, W., Ray, G., Wintle, A., Huntley, D., and Terasmae, J., 1980, Zircon ages for the Pelly Gneiss and Klotassin granodiorite in western Yukon: *Canadian Journal of Earth Sciences*, v. 17, p. 297-306.
- Tempelman-Kluit, D. J., 1984, *Geology, Laberge (105E) and Carmacks (115I), Yukon Territory*, Open File Report 1101, Geological Survey of Canada.
- Titley, S., and Wilson, E., 1966, *Geology of the porphyry copper deposits: southwestern North America*, University of Arizona Press.
- Tobisch, O., Barton, M., Vernon, R., and Paterson, S., 1991, Fluid-enhanced deformation: transformation of granitoids to banded mylonites, western Sierra Nevada, California, and southeastern Australia: *Journal of Structural Geology*, v. 13, p. 1137-1156.
- Trueman, J., 1912, The value of certain criteria for the determination of the origin of foliated crystalline rocks. I: *Journal of Geology*, v. 20, p. 228-258.
- Tullis, J., and Yund, R., 1985, Dynamic recrystallization of feldspar: a mechanism for ductile shear zone formation: *Geology*, v. 13, p. 238.
- Tullis, J., and Yund, R., 1991, Diffusion creep in feldspar aggregates: experimental evidence: *Journal of Structural Geology*, v. 13, p. 987-1000.
- Ulrich, T., and Heinrich, C. A., 2001, Geology and alteration geochemistry of the porphyry Cu-Au deposit at Bajo de la Alumbrera, Argentina: *Economic Geology*, v. 96, p. 1719–1742.
- Urai, J., 1986, Dynamic recrystallization of minerals. In: Heard HC, Hobbs BE (eds). *Mineral and Rock Deformation: laboratory studies, the Paterson volume*. Geophysical Monograph 36: 161-200, American Geophysical Union, Washington DC.
- Urai, J. L., Means, W. D., and Lister, G. S., 1986, Dynamic recrystallization of minerals: *Mineral and Rock Deformation: Laboratory Studies*, p. 166–199.
- Vernon, R., Etheridge, M., and Wall, V., 1988, Shape and microstructure of microgranitoid enclaves: indicators of magma mingling and flow: *Lithos*, v. 22, p. 1-11.

- Vernon, R., and Paterson, S., 2008, How late are K-feldspar megacrysts in granites?: *Lithos*, v. 104, p. 327-336.
- Vernon, R., Williams, V., and D'arcy, W., 1983, Grain-size reduction and foliation development in a deformed granitoid batholith: *Tectonophysics*, v. 92, p. 123-145.
- Vigneresses, J., 1995, Control of granite emplacement by regional deformation: *Tectonophysics*, v. 249, p. 173-186.
- Watts, M., and Williams, G., 1983, Strain geometry, microstructure and mineral chemistry in metagabbro shear zones: a study of softening mechanisms during progressive mylonitization: *Journal of Structural Geology*, v. 5, p. 507-517.
- Webster, J. D., 1992, Fluid-melt interactions involving Cl-rich granites: Experimental study from 2 to 8 kbar: *Geochimica et Cosmochimica Acta*, v. 56, p. 659-678.
- Webster, J. D., and Botcharnikov, R. E., 2011, Distribution of sulfur between melt and fluid in SOHC-Cl-bearing magmatic systems at shallow crustal pressures and temperatures: *Reviews in Mineralogy and Geochemistry*, v. 73, p. 247.
- Weinberg, R. F., Mark, G., and Reichardt, H., 2009, Magma ponding in the Karakoram shear zone, Ladakh, NW India: *Geological Society of America Bulletin*, v. 121, p. 278-285.
- Weinberg, R. F., and Podladchikov, Y., 1994, Diapiric ascent of magmas through power law crust and mantle: *Journal of Geophysical Research*, v. 99, p. 9543-9560.
- Weinberg, R. F., Sial, A., and Mariano, G., 2004, Close spatial relationship between plutons and shear zones: *Geology*, v. 32, p. 377-380.
- Wenk, H. R., and Christie, J., 1991, Comments on the interpretation of deformation textures in rocks: *Journal of Structural Geology*, v. 13, p. 1091-1110.
- White, S., 1975, Tectonic deformation and recrystallisation of oligoclase: *Contributions to Mineralogy and Petrology*, v. 50, p. 287-304.
- White, S., Burrows, S., Carreras, J., Shaw, N., and Humphreys, F., 1980, On mylonites in ductile shear zones: *Journal of Structural Geology*, v. 2, p. 175-187.
- Wiebe, R., Blair, K., Hawkins, D., and Sabine, C., 2002, Mafic injections, in situ hybridization, and crystal accumulation in the Pyramid Peak granite, California: *Bulletin of the Geological Society of America*, v. 114, p. 909.
- Wiebe, R., and Collins, W., 1998, Depositional features and stratigraphic sections in granitic plutons: implications for the emplacement and crystallization of granitic magma: *Journal of Structural Geology*, v. 20, p. 1273-1289.
- Wiebe, R., Jellinek, M., Markley, M., Hawkins, D., and Snyder, D., 2007, Steep schlieren and associated enclaves in the Vinalhaven granite, Maine: possible indicators for granite rheology: *Contributions to Mineralogy and Petrology*, v. 153, p. 121-138.
- Williams, P., 1977, Foliation: a review and discussion: *Tectonophysics*, v. 39, p. 305-328.
- Wilson, A. J., Cooke, D. R., and Harper, B. L., 2003, The Ridgeway gold-copper deposit: A high-grade alkalic porphyry deposit in the Lachlan Fold Belt, New South Wales, Australia: *Economic Geology*, v. 98, p. 1637.
- Winter, J. D. N., 2001, *An introduction to igneous and metamorphic petrology*, Prentice Hall.
- Wintsch, R., Christoffersen, R., and Kronenberg, A., 1995, Fluid-rock reaction weakening of fault zones: *Journal of Geophysical Research*, v. 100, p. 13021.
- Wintsch, R., and Yi, K., 2002, Dissolution and replacement creep: a significant deformation mechanism in mid-crustal rocks: *Journal of Structural Geology*, v. 24, p. 1179-1193.
- Yonkee, W., Parry, W., and Bruhn, R., 2003, Relations between progressive deformation and fluid-rock interaction during shear-zone growth in a basement-cored thrust sheet, Sevier orogenic belt, Utah: *American Journal of Science*, v. 303, p. 1.

- Yund, R. A., and Tullis, J., 1980, The effect of water, pressure, and strain on Al/Si order-disorder kinetics in feldspar: *Contributions to Mineralogy and Petrology*, v. 72, p. 297-302.
- Zak, J., and Paterson, S. R., 2006, Roof and walls of the Red Mountain Creek pluton, eastern Sierra Nevada, California (USA): implications for process zones during pluton emplacement: *Journal of Structural Geology*, v. 28, p. 575-587.
- Žák, J., and Paterson, S. R., 2005, Characteristics of internal contacts in the Tuolumne Batholith, central Sierra Nevada, California (USA): implications for episodic emplacement and physical processes in a continental arc magma chamber: *Geological Society of America Bulletin*, v. 117, p. 1242.
- Zen, E., 1988, Phase relations of peraluminous granitic rocks and their petrogenetic implications: *Annual Review of Earth and Planetary Sciences*, v. 16, p. 21-51.
- Zen, E., and Hammarstrom, J., 1984, Magmatic epidote and its petrologic significance: *Geology*, v. 12, p. 515.

Appendices

Appendix A Field Measurements

Table A1: Axial planes measured in oriented drillcore

HoleID	Depth	theta	phi	alpha	beta	gamma	azimuth	plunge	strike	dip	dipdirection
09SWC422	53.9	240	60	50	170	40	233	-20	323	70	53
09SWC422	57.35	240	60	30	20	60	93	-57	183	33	273
09SWC424	170.6	236	57	50	20	40	124	-76	214	14	304
09SWC424	125.6	234	59	40	0	50	54	-71	144	19	234

Table A2: Axial planes measured in outcrop. NR = not recorded

Feature	Trav	Easting	Northing	Elev	AxialPlane Dip	AxialPlane DipAz	Hinge Trend	Hinge Plunge	Opening_Dir
Fold_Kink	80708	384549	6943858	950	90	230			up
Fold_Open	S09-25	384633	6944928	730	35	60	125	5	
Fold_Open		384548	6945070	730	60	60	150	5	
Fold_Kink	S09-25	384633	6944928	730	30	220	165	40	up
Fold_S1		384463	6945098	730	35	335	165	35	Tight, opens to NE
Fold_S1		384640	6944938	730	60	270	175	20	up
Fold_S1		384640	6944938	730	60	270	180	25	down
Fold_S1		384640	6944938	730	70	255	185	30	down
Fold_S1		384640	6944938	730	60	270	190	25	up
Fold_Open		384463	6945098	730	30	340	315	20	open, opens to S
Fold_Open	S09-25	384633	6944928	730	30	40	315	0	
Fold_S1		384463	6945098	730	30	350	315	30	Tight, opens to NE
Fold_Kink	80708	384552	6943866	950	70	228	NR	NR	
Fold_Open		384372	6945297	868	26	222	NR	NR	

Table A3: Regional foliation measurements.

Category	Trav	UTM_E	UTM_N	Elev	Dip	Dip Azimuth	Note
Foliation		392382	6948710	472	68	92	In altered pG
Foliation	S09-21	384582	6944970	725	20	100	'gneissic' bands parallel, local openly
Foliation	S09-15	384600	6945161	728	50	35	
Foliation	S09-15	384600	6945161	728	50	60	
Foliation	S09-15	384600	6945161	728	50	75	
Foliation	S09-24	384460	6945088	730	45	280	Banded Gneiss
Foliation	S09-24	384460	6945088	730	55	295	Banded Gneiss
Foliation	S09-24	384490	6945122	730	30	265	Banded Gneiss, common complex internal deformation
Foliation	S09-24	384490	6945122	730	45	265	Banded Gneiss, common complex internal deformation
Foliation	S09-24	384490	6945122	730	35	285	Banded Gneiss, common complex internal deformation
Foliation	S09-24	384515	6945030	730	80	45	bGn- high grade cpy, bn
Foliation	S09-24	384515	6945030	730	90	220	bGn- high grade cpy, bn
Foliation	S09-24	384515	6945030	730	75	230	bGn- high grade cpy, bn
Foliation	S09-24	384518	6945128	730	40	300	Partially recrystallized KM; some carlsbad twins intact.
Foliation	S09-24	384518	6945128	730	30	315	Partially recrystallized KM; some carlsbad twins intact.
Foliation	S09-24	384518	6945128	730	20	325	Partially recrystallized KM; some carlsbad twins intact.
Foliation	S09-22	384538	6945022	730	35	0	Gneissic Foliation of compositional banding
Foliation	S09-25	384626	6944926	730	50	225	S1 axial planar to isoclinal folds
Foliation	S09-25	384626	6944926	730	60	250	S1 axial planar to isoclinal folds
Foliation	S09-25	384626	6944926	730	65	250	S1 axial planar to isoclinal folds
Foliation	S09-25	384626	6944926	730	60	260	S1 axial planar to isoclinal folds
Foliation	S09-25	384637	6944932	730	30	105	Continuous foliation
Foliation	S09-25	384637	6944932	730	35	205	Continuous foliation
Foliation	S09-25	384637	6944932	730	45	215	Continuous foliation
Foliation	S09-25	384638	6944927	730	25	40	S1? Polyphase def'n? Folded bGn
Foliation	S09-25	384638	6944927	730	20	50	S1? Polyphase def'n? Folded bGn
Foliation	S09-25	384638	6944927	730	40	75	S1? Polyphase def'n? Folded bGn
Foliation	S09-25	384638	6944927	730	15	80	S1? Polyphase def'n? Folded bGn
Foliation	S09-25	384638	6944927	730	50	100	S1? Polyphase def'n? Folded bGn
Foliation	S09-25	384638	6944927	730	20	120	S1? Polyphase def'n? Folded bGn
Foliation	S09-25	384638	6944927	730	10	130	S1? Polyphase def'n? Folded bGn
Foliation	S09-25	384638	6944927	730	50	200	S1? Polyphase def'n? Folded bGn
Foliation	S09-25	384638	6944927	730	50	205	S1? Polyphase def'n? Folded bGn
Foliation	S09-25	384638	6944927	730	50	215	S1? Polyphase def'n? Folded bGn
Foliation	S09-25	384638	6944927	730	60	215	S1? Polyphase def'n? Folded bGn
Foliation	S09-25	384638	6944927	730	55	250	S1? Polyphase def'n? Folded bGn

Category	Trav	UTM_E	UTM_N	Elev	Dip	Dip Azimuth	Note
Foliation	S09-25	384638	6944927	730	60	250	S1? Polyphase def'n? Folded bGn
Foliation	S09-25	384638	6944927	730	80	255	S1? Polyphase def'n? Folded bGn
Foliation	S09-22	384530	6945018	730	60	55	Gneissic Foliation of compositional banding
Foliation	S09-22	384530	6945018	730	65	60	Gneissic Foliation of compositional banding
Foliation	S09-22	384530	6945018	730	65	70	Gneissic Foliation of compositional banding
Foliation	S09-22	384530	6945022	730	65	50	Gneissic Foliation of compositional banding
Foliation		386543	6945651	735	84	70	pG with possible flow orientation or foliation. Oriented sample taken
Foliation	S09-27-05	384540	6944954	736	70	180	NA
Foliation	S09-27-05	384540	6944954	736	80	190	NA
Foliation	S09-20	384603	6944925	736	30	60	Rock poorly foliated moderately foliated (continuous folia).
Foliation	S09-20	384603	6944925	736	0	355	Rock poorly foliated moderately foliated (continuous folia).
Foliation	S09-27-04	384605	6944941	736	60	235	Very weathered; difficult to see fol'n. Abundant KM at contact
Foliation	S09-20	384617	6944920	736	30	245	Rock poorly foliated moderately foliated (continuous folia).
Foliation	S09-20	384617	6944920	736	5	275	Rock poorly foliated moderately foliated (continuous folia).
Foliation	S09-20	384620	6944910	736	10	165	Rock poorly foliated moderately foliated (continuous folia).
Foliation	S09-20	384620	6944910	736	5	170	Rock poorly foliated moderately foliated (continuous folia).
Foliation	S09-23	384640	6944909	736	50	65	Typical foliation
Foliation	S09-23	384644	6944923	736	5	70	Typical foliation
Foliation	S09-23	384645	6944923	736	80	40	Typical foliation
Foliation	S09-23	384645	6944923	736	40	70	Typical foliation
Foliation	S09-23	384645	6944923	736	50	80	Typical foliation
Foliation	S09-23	384645	6944923	736	30	95	Typical foliation
Foliation		384517	6944979	745	85	25	near sample S09-13-01D
Foliation		384517	6944979	745	80	35	near sample S09-13-01D
Foliation		384517	6944979	745	75	245	near sample S09-13-01D
Foliation		384522	6944978	745	60	250	Dragged down by local fault (fault ~60->110)
Foliation		384525	6944978	745	35	300	Dragged down by local fault (fault ~60->110)
Foliation	S09-12-01	384439	6945074	747	60	270	
Foliation	S09-12-01	384439	6945074	747	40	275	

Category	Trav	UTM_E	UTM_N	Elev	Dip	Dip Azimuth	Note
Foliation	S09-12-01	384439	6945074	747	20	280	
Foliation	S09-12-01	384439	6945074	747	60	280	
Foliation	S09-12-01	384439	6945074	747	30	290	
Foliation	S09-14-02	384500	6944987	747	40	240	
Foliation	S09-13-01	384519	6944978	748	85	25	
Foliation	S09-13-01	384519	6944978	748	80	35	
Foliation	S09-13-01	384519	6944978	748	30	140	
Foliation	S09-13-01	384519	6944978	748	85	225	
Foliation	S09-13-01	384519	6944978	748	75	245	
Foliation	S09-13-01	384519	6944978	748	60	250	
Foliation	S09-13-01	384519	6944978	748	35	300	
Foliation	S09-13-01	384519	6944978	748	20	350	
Foliation	s09-27-03	384707	6945028	748	70	0	Foliation veers suddenly upward. Foliated KMGD. Measurement is of contact
Foliation	s09-27-03	384707	6945028	748	50	20	Foliation veers suddenly upward. Foliated KMGD. Measurement is of contact
Foliation	s09-27-03	384707	6945028	748	80	175	Foliation veers suddenly upward. Foliated KMGD. Measurement is of contact
Foliation	S09-12-01	384440	6945088	750	25	0	
Foliation	S09-12-01	384440	6945088	750	30	10	
Foliation	S09-12-01	384440	6945088	750	20	20	
Foliation	S09-12-01	384440	6945088	750	30	355	
Foliation	S09-26	384702	6945033	750	45	55	Folded Q-F gneiss
Foliation	S09-26	384702	6945033	750	50	80	Folded Q-F gneiss
Foliation	s09-27-02	384719	6945040	757	30	65	Foliated eG
Foliation	s09-27-02	384719	6945040	757	50	70	Foliated eG
Foliation	s09-27-02	384711	6945038	760	20	30	Foliated eG
Foliation	s09-27-02	384711	6945038	760	40	85	Foliated eG
Foliation	s09-27-02	384711	6945038	760	40	95	Foliated eG
Foliation	s09-27-02	384711	6945038	760	75	50	Foliated eG
Foliation		384711	6945048	762	10	60	
Foliation		384711	6945048	762	20	90	
Foliation		384711	6945048	762	20	100	
Foliation		384711	6945048	762	45	80	
Foliation		384711	6945048	762	30	110	
Foliation		384714	6945056	762	40	5	***CROSSCUTS MAIN FOLIATION*** Small zone, ~10cm
Foliation		384714	6945060	762	60	35	***CROSSCUTS MAIN FOLIATION*** Small zone, ~10cm

Category	Trav	UTM_E	UTM_N	Elev	Dip	Dip Azimuth	Note
Foliation		384714	6945060	762	80	45	***CROSSCUTS MAIN FOLIATION*** Small zone, ~10cm
Foliation		384714	6945060	762	50	45	***CROSSCUTS MAIN FOLIATION*** Small zone, ~10cm
Foliation	s09-27-01	384716	6945053	775	50	40	Continuous folia, recrystallized feld
Foliation	s09-27-01	384716	6945053	775	40	40	Continuous folia, recrystallized feld
Foliation	s09-27-01	384716	6945053	775	45	70	Continuous folia, recrystallized feld
Foliation	s09-27-01	384716	6945053	775	50	70	Continuous folia, recrystallized feld
Foliation	S09-11-02	384772	6945118	779	15	80	
Foliation	S09-11-02	384772	6945118	779	20	135	
Foliation	S09-11-02	384680	6945105	781	15	30	
Foliation	S09-11-02	384680	6945105	781	25	125	
Foliation		384827	6945009	795	55	35	Fol'd GD-K
Foliation		384827	6945009	795	40	110	Fol'd GD-K
Foliation		384782	6945050	805	75	60	More intense foliation in narrow zone cutting weak foliation
Foliation		384782	6945050	805	15	65	Fol'd tonalite
Foliation	S09-26	384700	6945270	808	30	70	Western Hinge portion - contacts (blue dots)
Foliation	S09-26	384700	6945270	808	40	240	Western Hinge portion - contacts (blue dots)
Foliation	S09-26	384700	6945270	808	30	270	Western Hinge portion - contacts (blue dots)
Foliation	S09-26	384700	6945270	808	50	275	Western Hinge portion - contacts (blue dots)
Foliation	S09-26	384700	6945270	808	40	285	Western Hinge portion - contacts (blue dots)
Foliation	S09-26	384700	6945270	808	30	310	Western Hinge portion - internal foliation (blue crosses)
Foliation	S09-26	384700	6945270	808	20	350	Western Hinge portion - internal foliation (blue crosses)
Foliation	S09-26	384728	6945252	808	40	30	Middle portion of interval - contacts (Red dots)
Foliation	S09-26	384728	6945252	808	25	55	Middle portion of interval - internal foliation (red crosses)
Foliation	S09-26	384730	6945250	808	44	40	Middle portion of interval - contacts (Red dots)
Foliation		384769	6945111	820	25	20	pseudogneiss
Foliation		384769	6945111	820	10	30	pseudogneiss
Foliation		384769	6945111	820	15	70	pseudogneiss

Category	Trav	UTM_E	UTM_N	Elev	Dip	Dip Azimuth	Note
Foliation		384773	6945144	825	20	50	Fol'd GD-KQ
Foliation		384769	6945111	820	20	85	pseudogneiss
Foliation		384769	6945111	820	15	110	pseudogneiss
Foliation		384764	6945132	825	20	5	Fol'd diorite
Foliation		384764	6945132	825	20	315	Fol'd diorite
Foliation		384764	6945132	825	25	325	Fol'd diorite
Foliation		384773	6945144	825	20	45	Fol'd GD-KQ
Foliation		384773	6945144	825	30	50	Fol'd GD-KQ
Foliation		384773	6945144	825	40	65	Fol'd GD-KQ
Foliation		384773	6945144	825	30	220	Fol'd GD-KQ
Foliation	80810	384530	6945300	834	40	126	At sample P017. Foln in small lenses-truncated by small faults?
Foliation	80810	384390	6945200	834	50	36	
Foliation	80810	384415	6945250	834	40	36	
Foliation	80810	384415	6945260	834	25	12	
Foliation		384785	6945181	835	30	110	
Foliation		383927	6948433	838	20	163	More intense foliation in narrow zone cutting weak foliation
Foliation		383965	6948371	838	65	40	At Manana, crosscut by a more intense foliation (see cross cutting foliations)
Foliation		383965	6948371	838	75	70	At Manana, crosscut by a more intense foliation (see cross cutting foliations)
Foliation		383965	6948371	838	20	80	More intense foliation in narrow zone cutting weak foliation
Foliation		383965	6948371	838	60	240	At Manana, crosscut by a more intense foliation (see cross cutting foliations)
Foliation		383965	6948371	838	70	240	At Manana, crosscut by a more intense foliation (see cross cutting foliations)
Foliation		384960	6944525	840	60	36	Foliation near gossen abundant siliceous 'layer' trending 304 deg. Foliation strike/dip = 306/60
Foliation		384962	6944528	840	32	20	Looks like a fracture which follows foliation, could be a joint
Foliation		384350	6945144	841	50	266	could be fault related but looks like fold eG
Foliation		384966	6944519	843	28	14	

Category	Trav	UTM_E	UTM_N	Elev	Dip	Dip Azimuth	Note
Foliation		384977	6944498	845	24	50	Foliation in fG. Displacement of about 1.4m with foliation below
Foliation		384408	6945141	855	110	84	Sample SBH-08-002. Foliation @ 110/84. Lt green anhedral foliated plagioclase and black books of bt defining disjunctive cleavage. Sulphide bearing.
Foliation		384977	6944498	845	14	58	Foliation in fG. Displacement of about 1.4m with foliation above. Moderate mch staining
Foliation	80804	384400	6945250	850	60	335	
Foliation		384590	6945310	850	60	40	
Foliation		383976	6948351	853	35	210	foliation in outcrop from Manana with xenolith of fG
Foliation		384611	6945251	860	65	45	Fol'd tonalite
Foliation		384588	6945310	861	64	40	Foliation in fG. Anastomizing cleavage of f.gr. platy bt. Microlithons of qz + plag up to 8mm or so in long axis diameter, plag milky white. Scattered kspar up to 1cm. No real obvious weathering, large amount of staining from mch, some tn.
Foliation		384397	6945252	864	60	334	fG w dk green mafics
Foliation		384419	6945260	875	20	350	SBH-P018. An easy to grab slab of slightly folded fG. Foliation on SW side @ 20/350 NW
Foliation		385159	6943445	887	40	50	Foliation in fG.
Foliation		385159	6943445	887	22	70	Foliation in fG
Foliation		385159	6943445	887	70	232	Weak foliation in massive granitoid (pG)
Foliation		386170	6943762	887	70	105	Trench with great foliated rock exposure + Mch
Foliation		386170	6943762	887	60	265	Trench with great foliated rock exposure + Mch
Foliation		384888	6943798	903	50	50	Foliation in fG. Trench trends 050, mch staining common, some az. Trench walls are extremely weathered, although measurements are still possible
Foliation		384889	6943796	903	30	74	Foliation in fG; strongly weathered, very ms rich and limonitic
Foliation		385029	6943635	903	24	72	Foliation in fG

Category	Trav	UTM_E	UTM_N	Elev	Dip	Dip Azimuth	Note
Foliation		385029	6943635	903	20	80	Foliation in fG
Foliation		384876	6943785	905	39	30	SW trending foliation in bt rich fg
Foliation		384876	6943785	905	39	30	Foliation in bt rich fG (dip/dip dir = 39/030 SW)
Foliation		384692	6945420	910	50	40	
Foliation		384710	6945417	910	40	70	
Foliation		385032	6943592	910	39	56	Foliation in fG
Foliation		385032	6943592	910	38	88	Foliation in fG
Foliation		384692	6944027	913	49	226	Patch of exposed fG light mch staining. Contact ~ parallel to foliation. fG ~ 1m thick towards S. Bounded on S by peg
Foliation		383256	6943521	915	55	70	
Foliation		384678	6944027	915	60	218	Foliation
Foliation		384678	6944027	915	60	278	Weak foliation; dip/dir = 60/278
Foliation		384881	6943702	920	64	210	Foliation? dip/dir = 64/210
Foliation		384882	6943701	920	36	52	Foliation in fG
Foliation		384882	6943701	920	36	82	Foliation in fG dip/dir = 42/082
Foliation		384635	6943410	937	60	35	Trench, contact btwn DI1 and DI4. Fold hinges in float
Foliation		384635	6943410	937	50	40	Trench, contact btwn DI1 and DI4. Fold hinges in float
Foliation		384635	6943410	937	75	210	Trench, contact btwn DI1 and DI4. Fold hinges in float
Foliation		384635	6943410	937	75	245	Trench, contact btwn DI1 and DI4. Fold hinges in float
Foliation		384635	6943410	937	80	260	Trench, contact btwn DI1 and DI4. Fold hinges in float
Foliation		384635	6943410	937	60	260	Trench, contact btwn DI1 and DI4. Fold hinges in float
Foliation		384635	6943410	937	60	285	Trench, contact btwn DI1 and DI4. Fold hinges in float
Foliation		384552	6943866	952	78	254	Foliation in fG
Foliation		384549	6943858	953	70	314	fG with mch and rare f.gr. cpy. There's a steep anastomosing cleavage here, though difficult to tell whether it parallels foliation of fG. sbh-0807-01
Foliation		383754	6945737	955	50	265	Foliated showing near Marlboro Woman
Foliation		383754	6945737	955	55	275	Foliated showing near Marlboro Woman
Foliation		384845	6945852	955	55	60	Malachite Knob

Category	Trav	UTM_E	UTM_N	Elev	Dip	Dip Azimuth	Note
Foliation		384845	6945852	955	60	100	Malachite Knob, higher strain zone
Foliation		384456	6943815	957	60	50	Foliation in burned look rock (probably fG).
Foliation		384456	6943815	957	64	230	Foliation in burned look rock (probably fG).
Foliation		384515	6943830	957	64	252	Foliation. Rock looks like eG; about 30% bt, 15% qz, plag 25%, limonite 5%. Moderate alignment of phenos. Just to the SW there's uncommon, mod mch and az in same looking rock
Foliation		384469	6943812	960	22	44	Foliation in burned look rock (probably fG). Looks like a switch in foliation - possible fold hinge. SAMPLE THIS TRENCH
Foliation		384469	6943812	960	40	50	Foliation in burned look rock (probably fG). Looks like a switch in foliation - possible fold hinge. SAMPLE THIS TRENCH
Foliation		384653	6943533	960	50	40	Trench with bt rich foliated T
Foliation		384653	6943533	960	25	145	Trench with bt rich foliated T
Foliation		384653	6943533	960	70	210	Trench with bt rich foliated T
Foliation		384092	6945731	975	75	270	Fol'd GD and gneissic stuff
Foliation		384127	6945752	975	80	50	slightly fol'd GD. KM fewer and smaller than usual (<1cm)
Foliation	90622	384732	6945077	760	30	350	5 measurements from outcrop
Foliation	90622	384732	6945077	760	30	345	5 measurements from outcrop
Foliation	90622	384732	6945077	760	30	0	5 measurements from outcrop
Foliation	90622	384732	6945077	760	25	0	5 measurements from outcrop
Foliation	90622	384732	6945077	760	25	345	5 measurements from outcrop
Foliation	90622	384732	6945080	760	35	110	Shallow foln observed to be defd by cross cutting steep foln. Pic 290-1778
Foliation	90622	384732	6945080	760	10	40	Shallow foln observed to be defd by cross cutting steep foln. Pic 290-1779
Foliation	90622	384732	6945080	760	15	120	Shallow foln observed to be defd by cross cutting steep foln. Pic 290-1780
Foliation	90622	384732	6945080	760	5	10	Shallow foln observed to be defd by cross cutting steep foln. Pic 290-1781

Category	Trav	UTM_E	UTM_N	Elev	Dip	Dip Azimuth	Note
Foliation	90622	384733	6945093	760	10	320	Poor Bt foln, difficult to measure (crenulated?). Pic 290-1784
Foliation	90622	384732	6945080	760	15	0	Shallow foln observed to be defd by cross cutting steep foln. Pic 290-1782
Foliation	90622	384733	6945093	760	30	240	Poor Bt foln, difficult to measure (crenulated?). Pic 290-1784
Foliation	90622	384733	6945093	760	20	340	Poor Bt foln, difficult to measure (crenulated?). Pic 290-1784
Foliation	90622	384733	6945093	760	20	350	Poor Bt foln, difficult to measure (crenulated?). Pic 290-1784
Foliation	90622	384733	6945093	760	10	10	Poor Bt foln, difficult to measure (crenulated?). Pic 290-1784
Foliation	90622	384733	6945105	760	60	50	North of steep shear zone
Foliation	90622	384733	6945105	760	20	22	North of steep shear zone
Foliation	90622	384733	6945105	760	20	355	North of steep shear zone
Foliation	90622	384733	6945105	760	30	350	North of steep shear zone
Foliation	90622	384631	6945167	760	90	240	Small fol'd intrusion bounded by cataclasite. Steep foln zone or fol'd intrusion/horse? Foln // contact.
Foliation	90622	384625	6945170	760	30	85	Foln E of intrusion/horse
Foliation	90622	384571	6945202	760	90	250	High strain zone with sulfides. 2m region between high strain zones is very "milled" with poor foln, no minzn. Siliceous zone+sulfides along outside margin
Foliation	90622	384571	6945202	760	80	80	High strain zone with sulfides. 2m region between high strain zones is very "milled" with poor foln, no minzn. Siliceous zone+sulfides along outside margin
Foliation	90622	384571	6945202	760	70	255	High strain zone with sulfides. 2m region between high strain zones is very "milled" with poor foln, no minzn. Siliceous zone+sulfides along outside margin
Foliation	90622	384569	6945202	760	70	120	High strain zone with sulfides. 2m region between high strain zones is very "milled" with poor foln, no minzn. Siliceous zone+sulfides along outside margin

Foliation	90622	384569	6945202	760	70	110	High strain zone with sulfides. 2m region between high strain zones is very "milled" with poor foln, no minzn. Siliceous zone+sulfides along outside margin
Foliation	90622	384569	6945202	760	80	110	High strain zone with sulfides. 2m region between high strain zones is very "milled" with poor foln, no minzn. Siliceous zone+sulfides along outside margin
Foliation	90622	384569	6945202	760	80	120	High strain zone with sulfides. 2m region between high strain zones is very "milled" with poor foln, no minzn. Siliceous zone+sulfides along outside margin
Foliation	90622	384569	6945202	760	80	120	High strain zone with sulfides. 2m region between high strain zones is very "milled" with poor foln, no minzn. Siliceous zone+sulfides along outside margin
Foliation	90622	384560	6945250	760	70	240	v.weak foln in Gd
Foliation	90622	384560	6945250	760	90	240	v.weak foln in Gd
Foliation	90622	384570	6945201	760	80	120	Ccp+Bn in 20 cm high strain zone
Foliation	Bench780-1	384780	6945142	780	40	60	10 interval of deformed Gd- fault bounded? Sharp contact with Gd below.
Foliation	Bench780-2	384775	6945145	780	45	40	Sharp contact with Gd, above
Foliation	Bench778	384781	6945415	778	20	25	
Foliation	Bench778	384765	6945153	778	30	55	foln // contact
Foliation	90805	384442	6945330	847	25	290	foln// contact
Foliation	90805	384443	6945331	848	20	270	foln// contact
Foliation	90805	384444	6945332	847	60	35	Steep short limb
Foliation	90805	384445	6945333	846	30	270	See also sample S12-05-01A & pic 2396.
Foliation	90805	384446	6945334	847	25	225	foln// contact
Foliation	90805	384388	6945298	874	55	300	Defd zone above irma's Bn. Truncated to N by 55-->045 fault at 384400, 6945311
Foliation	90805	384398	6945302	869	22	280	Defd zone above irma's Bn. Truncated to N by 55-->045 fault at 384400, 6945311

Category	Trav	UTM_E	UTM_N	Elev	Dip	Dip Azimuth	Note
Foliation	90805	384398	6945304	869	20	215	Defd zone above irma's Bn. Truncated to N by 55-->045 fault at 384400, 6945311

Table A4: Foliation measured in oriented drill core.

HoleID	Depth	theta	phi	alpha	beta	gamma	Pole Az	Pole Plg	Notes
09SWC420	134	210	-61	20	240	70	265	-4	High strain zone
09SWC420	142	214	-61	40	330	50	339	-62	High strain zone
09SWC420	148	214	-61	65	80	25	167	-56	High strain zone
09SWC420	148	214	-61	55	275	35	272	-48	High strain zone
09SWC420	149	214	-61	60	170	30	209	-31	High strain zone
09SWC420	149	214	-61	60	340	30	300	-80	High strain zone
09SWC420	151	214	-61	60	350	30	309	-85	High strain zone
09SWC420	157	214	-61	25	350	65	19	-54	High strain zone
09SWC420	157	214	-61	35	345	55	7	-62	High strain zone
09SWC420	159	214	-61	60	260	30	259	-46	High strain zone
09SWC420	171	214	-61	60	0	30	34	-89	High strain zone
09SWC420	172	214	-61	45	310	45	310	-57	High strain zone
09SWC420	179	214	-61	60	340	30	300	-80	High strain zone
09SWC420	181	214	-61	40	220	50	245	-16	High strain zone
09SWC420	181	214	-61	60	225	30	240	-36	High strain zone
09SWC420	54	208	-61	55	290	35	275	-54	
09SWC420	67	208	-61	55	70	35	141	-54	
09SWC420	68	208	-61	55	90	35	153	-46	
09SWC420	108	210	-61	55	0	35	30	-84	
09SWC420	110	210	-61	50	90	40	150	-42	
09SWC420	112	210	-61	55	70	35	143	-54	
09SWC420	113	210	-61	60	45	30	138	-68	
09SWC420	154	214	-61	50	255	40	265	-36	
09SWC420	162	214	-61	60	140	30	191	-35	
09SWC420	163	214	-61	45	200	45	229	-17	
09SWC420	169	214	-61	55	320	35	302	-68	
09SWC420	191	214	-61	70	115	20	186	-49	
09SWC420	191	214	-61	65	100	25	175	-49	
09SWC420	192	214	-61	70	300	20	258	-65	
09SWC420	198	214	-61	60	120	30	180	-39	
09SWC420	216	218	-61	60	255	30	260	-44	
09SWC420	285	214	-61	65	40	25	155	-72	
09SWC420	286	214	-61	75	265	15	241	-56	
09SWC420	307	214	-61	50	50	40	126	-60	
09SWC420	308	214	-61	40	30	50	89	-62	
09SWC420	308	214	-61	45	35	45	103	-64	
09SWC420	309	214	-61	55	40	35	127	-68	
09SWC420	310	214	-61	75	35	15	187	-71	
09SWC420	311	214	-61	75	40	15	185	-70	
09SWC420	312	214	-61	70	25	20	177	-76	
09SWC420	314	214	-61	60	10	30	121	-85	
09SWC420	315	214	-61	65	20	25	158	-80	
09SWC420	316	214	-61	70	20	20	181	-78	
09SWC420	319	214	-61	45	345	45	357	-72	
09SWC420	320	214	-61	60	30	30	135	-75	

HoleID	Depth	theta	phi	alpha	beta	gamma	Pole Az	Pole Plg	Notes
09SWC420	321	214	-61	55	340	35	323	-78	
09SWC420	323	214	-61	50	0	40	34	-79	
09SWC420	323	214	-61	50	40	40	117	-65	
09SWC420	328	214	-61	70	30	20	174	-75	
09SWC420	332	216	-60	60	25	30	136	-78	
09SWC420	333	216	-60	65	25	25	160	-78	
09SWC420	335	216	-60	60	25	30	136	-78	
09SWC420	338	216	-60	55	20	35	109	-78	
09SWC420	345	216	-60	80	340	10	226	-69	
09SWC420	347	216	-60	75	255	15	241	-54	
09SWC420	348	216	-60	65	235	25	244	-42	
09SWC422	54	240	-60	50	170	40	233	-20	Axial Plane
09SWC422	57	240	-60	30	20	60	93	-57	Axial Plane
09SWC422	58	237	-60	70	210	20	250	-42	
09SWC422	62	237	-60	60	180	30	237	-30	
09SWC422	62	237	-60	75	275	15	266	-58	
09SWC422	65	237	-60	65	0	25	237	-85	
09SWC422	68	237	-60	51	180	39	237	-21	
09SWC422	69	237	-60	60	320	30	310	-70	
09SWC422	152	239	-58	75	290	15	268	-60	
09SWC422	152	239	-58	65	260	25	277	-47	
09SWC422	165	239	-58	65	250	25	273	-44	
09SWC422	170	239	-58	55	310	35	314	-63	
09SWC422	226	240	-58	70	270	20	274	-52	
09SWC422	227	240	-58	60	0	30	240	-88	
09SWC422	229	240	-58	60	345	30	306	-82	
09SWC422	232	240	-58	40	210	50	263	-11	
09SWC422	233	240	-58	40	170	50	232	-8	
09SWC422	234	240	-58	40	145	50	214	-12	
09SWC422	245	240	-58	60	170	30	235	-28	
09SWC422	245	240	-58	75	330	15	262	-69	
09SWC422	246	240	-58	65	235	25	267	-39	
09SWC422	264	239	-57	55	50	35	167	-63	
09SWC422	264	239	-57	60	0	30	239	-87	
09SWC424	65	233	-60	45	295	45	314	-50	[cms] bands of increased strain
09SWC424	78	233	-60	65	330	25	290	-75	[cms] bands of increased strain
09SWC424	79	233	-60	60	315	30	303	-68	[cms] bands of increased strain
09SWC424	79	233	-60	40	30	50	110	-63	[cms] bands of increased strain
09SWC424	126	234	-59	40	0	50	54	-71	Axial Plane
09SWC424	171	236	-57	50	20	40	124	-76	Axial Plane
09SWC424	58	233	-60	55	180	35	233	-25	
09SWC424	95	234	-59	50	220	40	261	-23	

HoleID	Depth	theta	phi	alpha	beta	gamma	Pole Az	Pole Plg	Notes
09SWC424	109	234	-59	55	265	35	285	-42	
09SWC424	125	234	-59	20	245	70	293	-5	
09SWC424	125	234	-59	70	355	20	243	-79	
09SWC424	141	234	-59	65	180	25	234	-34	
09SWC424	170	236	-57	40	125	50	195	-18	
09SWC424	171	236	-57	80	125	10	223	-51	
09SWC424	210	236	-57	65	310	25	287	-65	
09SWC424	214	236	-57	65	260	25	273	-46	
09SWC424	217	237	-56	65	340	25	276	-77	
09SWC424	313	238	-55	60	230	30	264	-31	
09SWC424	315	236	-54	60	270	30	281	-45	
09SWC424	317	236	-54	50	240	40	275	-26	
09SWC427	49	244	-60	65	330	25	301	-75	
09SWC427	59	244	-60	55	10	35	115	-83	
09SWC427	70	244	-60	70	20	20	212	-77	
09SWC427	107	245	-59	65	330	25	300	-75	
09SWC427	111	245	-59	65	330	25	300	-75	
09SWC427	113	245	-59	80	320	10	261	-66	
09SWC427	116	245	-59	75	285	15	275	-60	
09SWC427	127	245	-59	70	310	20	287	-67	
09SWC427	147	245	-59	65	180	25	245	-34	
09SWC427	149	245	-59	70	110	20	216	-48	
09SWC427	154	245	-59	45	35	45	137	-65	
09SWC427	164	245	-59	65	340	25	295	-79	
09SWC427	215	245	-59	50	290	40	317	-50	
09SWC429	149	59	-60	35	180	55	59	-5	-5 folding at 146.70?
09SWC429	143	59	-60	50	250	40	105	-33	local peglets- fol'n trustworthy?
09SWC429	56	56	-61	5	180	85	236	-24	
09SWC429	63	56	-61	25	15	65	259	-53	
09SWC429	64	56	-61	45	130	45	20	-23	
09SWC429	68	56	-61	40	10	50	257	-68	
09SWC429	71	56	-61	20	340	70	208	-47	
09SWC429	101	59	-60	35	190	55	67	-5	
09SWC429	101	59	-60	35	180	55	59	-5	
09SWC429	129	59	-60	30	110	60	1	-16	
09SWC429	130	59	-60	60	110	30	20	-41	
09SWC429	131	59	-60	60	130	30	31	-36	
09SWC429	144	59	-60	55	285	35	122	-52	
09SWC429	148	59	-60	60	340	30	139	-80	
09SWC429	171	60	-59	20	115	70	1	-5	
09SWC431	46	237	-61	70	0	20	237	-81	
09SWC431	51	237	-61	65	0	25	237	-86	
09SWC431	55	237	-61	60	0	30	57	-89	
09SWC431	91	242	-60	70	325	20	283	-73	
09SWC431	90	242	-60	70	0	20	242	-80	

HoleID	Depth	theta	phi	alpha	beta	gamma	Pole Az	Pole Plg	Notes
09SWC431	91	242	-60	75	325	15	268	-71	
09SWC431	96	242	-60	75	300	15	273	-64	
09SWC431	98	242	-60	80	0	10	242	-70	
09SWC431	110	242	-60	76	0	15	242	-75	
09SWC431	115	242	-60	70	0	20	242	-80	
09SWC431	116	242	-60	70	345	20	267	-78	
09SWC431	117	242	-60	60	290	30	300	-57	
09SWC431	122	242	-60	70	10	20	223	-79	
09SWC431	125	242	-60	60	285	30	298	-55	
09SWC431	140	236	-59	60	0	30	236	-89	
09SWC431	141	236	-59	55	340	35	339	-78	
09SWC431	148	236	-59	70	270	20	271	-54	
09SWC431	150	236	-59	75	295	15	266	-62	
09SWC495	41	195	-61	65	145	25	177	-39	
09SWC495	135	195	-60	55	45	35	113	-66	
09SWC495	136	195	-59	55	10	35	70	-83	
09SWC495	137	195	-59	45	50	45	102	-57	
09SWC495	138	195	-59	80	0	10	195	-69	
09SWC495	140	195	-59	65	135	25	172	-39	
09SWC495	142	195	-59	55	120	35	158	-34	
09SWC495	146	195	-59	70	70	20	155	-60	
09SWC495	147	195	-59	45	235	45	234	-24	
09SWC495	148	195	-59	60	85	30	144	-50	
09SWC495	149	195	-59	70	20	20	165	-77	
09SWC497	74	45	-56	50	0	40	225	-84	at 73.75, heavy Bt + Ccp - hinge?
09SWC497	76	45	-56	40	100	50	347	-27	at 76.7 - fold hinge?
09SWC497	74	45	-56	70	5	20	38	-76	Beta rotation
09SWC497	74	45	-56	40	100	50	347	-27	Beta rotation
09SWC497	80	45	-56	50	150	40	25	-19	Diffuse Peg, Bt defines no folia. Hinge?
09SWC497	81	45	-56	70	310	20	82	-64	Possible folding PIC 2003-2007
09SWC497	107	45	-56	45	165	45	34	-11	Small shear zone
09SWC497	69	45	-56	55	0	35	225	-89	
09SWC497	70	45	-56	60	180	30	45	-26	
09SWC497	71	45	-56	65	170	25	40	-31	
09SWC497	72	45	-56	70	60	20	8	-61	
09SWC497	73	45	-56	60	110	30	8	-38	
09SWC497	74	45	-56	70	60	20	8	-61	
09SWC497	75	45	-56	70	5	20	38	-76	
09SWC497	77	45	-56	80	340	10	53	-65	
09SWC497	78	45	-56	65	90	25	5	-48	
09SWC497	79	45	-56	65	60	25	358	-60	
09SWC497	80	45	-56	50	150	40	25	-19	
09SWC497	81	45	-56	60	260	30	86	-42	
09SWC497	82	45	-56	35	5	55	237	-69	

Appendix B Pit Maps

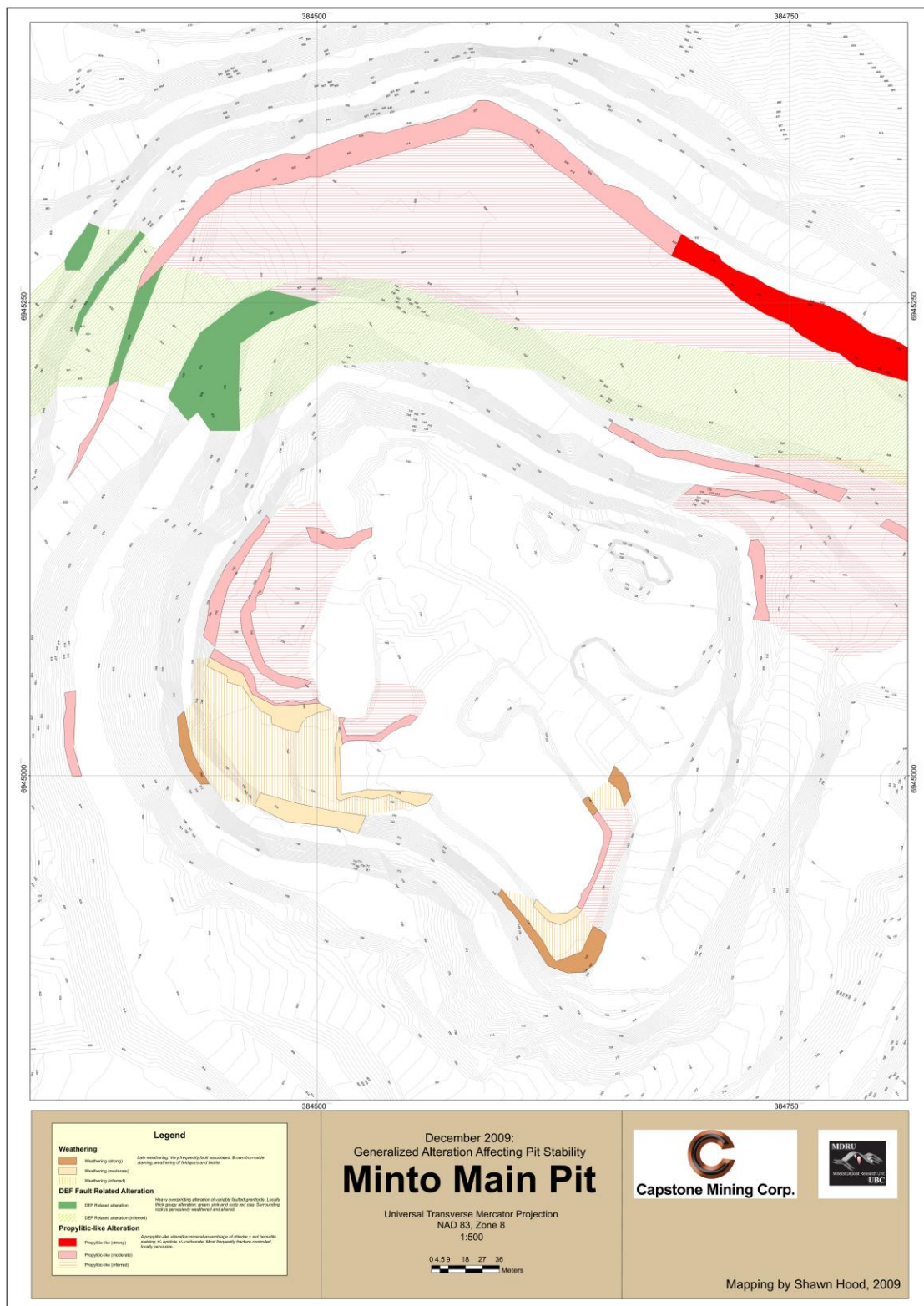
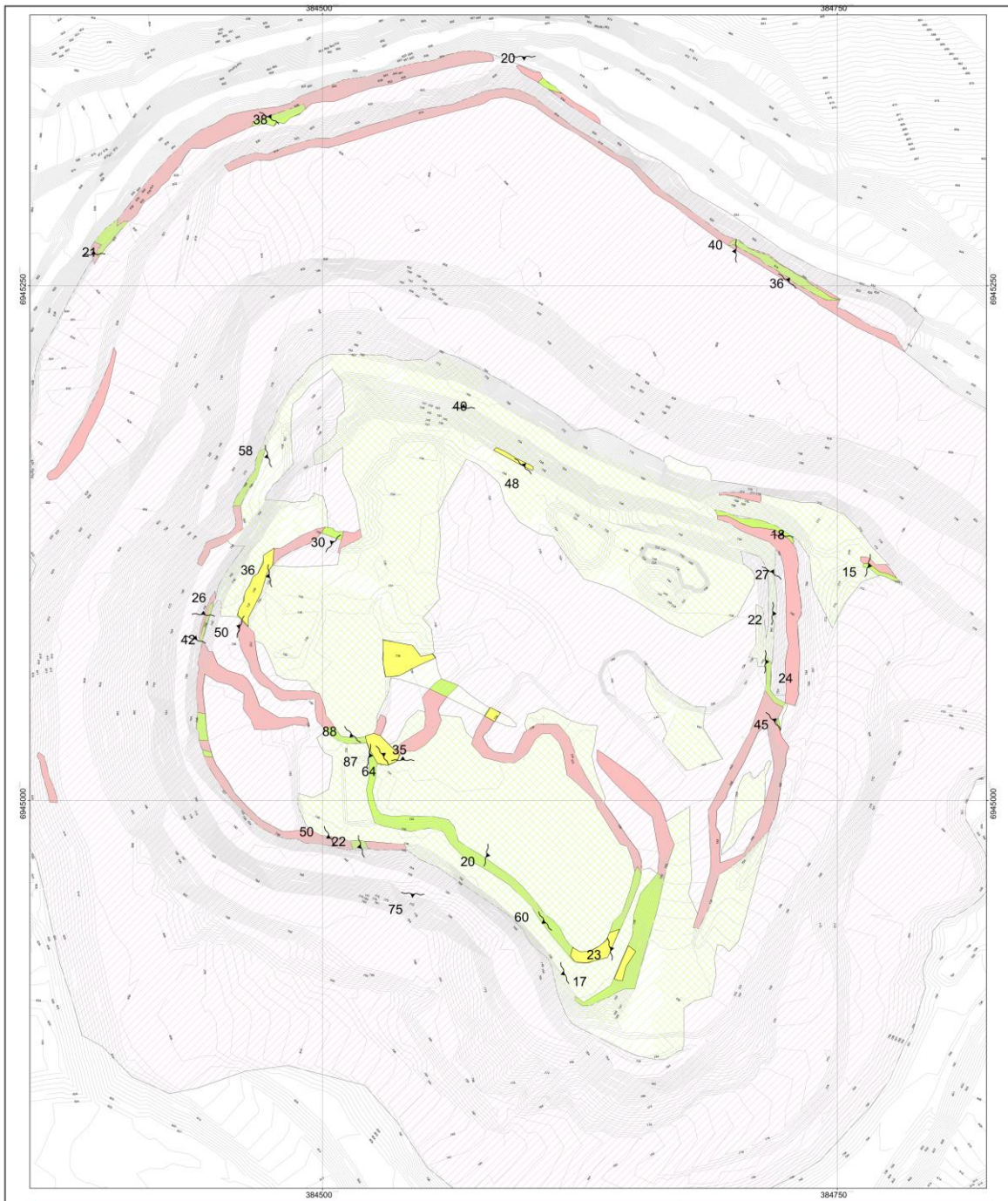


Figure B1: Map showing propylitic alteration and weathering mapped in the Minto pit during 2009.



Legend	
	Fillstone
	Deformation

December 2009 Foliation

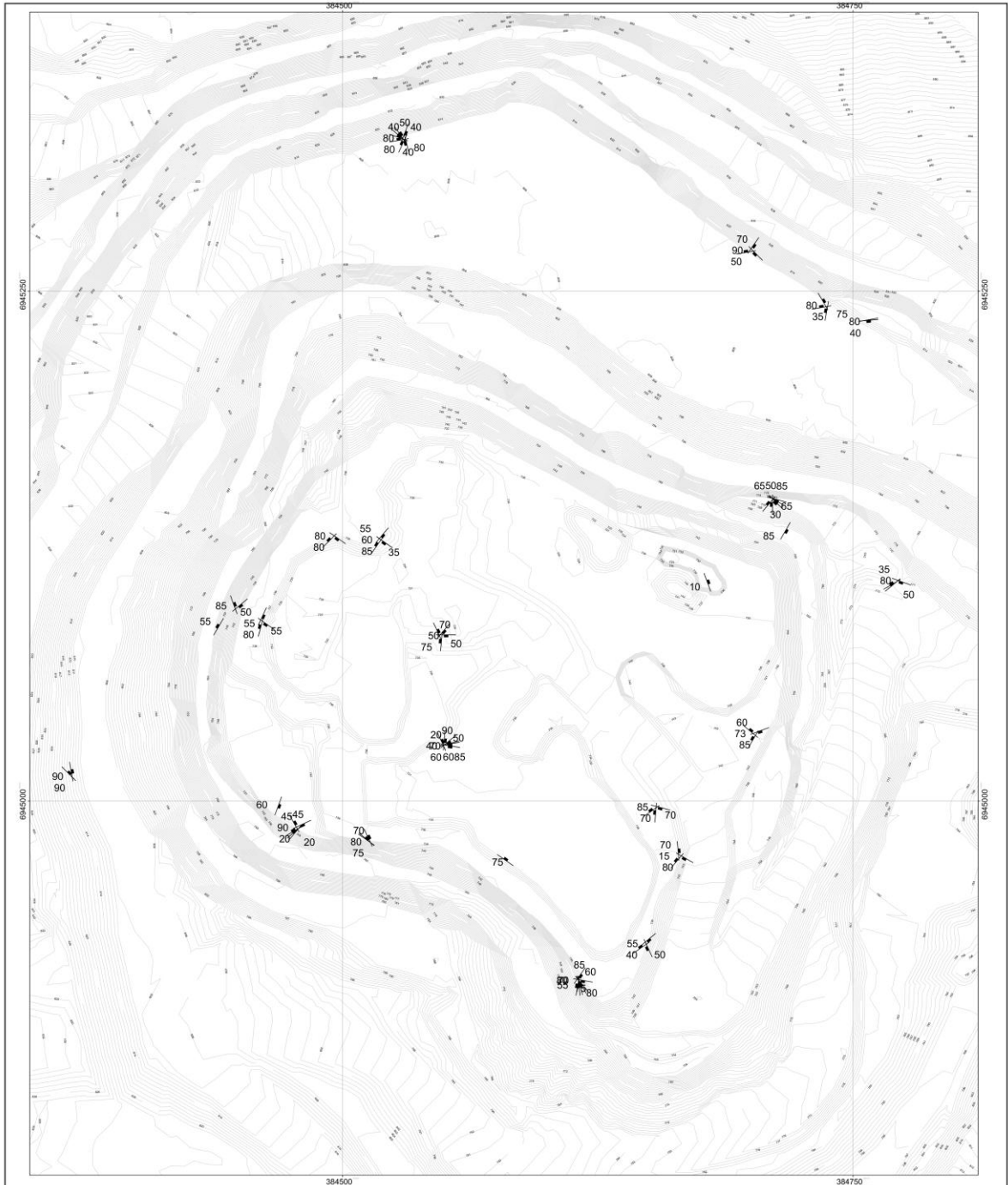
Minto Main Pit

Universal Transverse Mercator Projection
NAD 83, Zone 8
1:500



Mapping by Shawn Hood, 2009
Block model data from Minto Exploration

Figure B3: Map showing the distribution of deformed rocks and orientations of faults observed during 2009 field work.



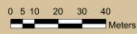
<p>Legend</p> <p>Fractures Continuous on a scale >= bench</p>	<p>December 2009: Distribution of Joints/Fractures</p>	 <p>Capstone Mining Corp.</p>	 <p>MDRU Mineral Development Research Unit UBC</p>
<h1>Minto Main Pit</h1>		<p>Universal Transverse Mercator Projection NAD 83, Zone 8 1:500</p>	
 <p>0 5 10 20 30 40 Meters</p>		<p>Mapping by Shawn Hood, 2009 Block model data from Minto Exploration</p>	

Figure B4: Map of joints/fractures observed during 2009 mapping. Measurements shown are for structures continuous at approximately bench scale, i.e., greater in length than 6m.

Appendix C Whole-Rock Geochemical Sample Locations

Table C1: Location and descriptions of whole-rock geochem samples analysed at ALS Chemex. Sample of format Hxxx-yyy equate to Capstone exploration hole SWC-xxx, depth yyy metres. KGd = Minto granodiorite, Tlt = tonalite, Cpy = chalcopyrite, Bn = bornite, Mag = magnetite, Kfs = K-feldspar, KM = K-feldspar megacryst, Hem = hematite, Pl = plagioclase, Hbl = hornblende, Epi = Epidote, Bt = biotite, Qz = quartz, bGn = banded gneiss, FeOx = iron oxide, phlog = phlogopite, Gnt = garnet, cms = centimetres, mms = millimetres.

Sample	PkgCode	UTM_E	UTM_N	Depth	Description
H424-212	4Lithoresearch	384531	6944491	212	Massive KGd adjacent to foliated KGd (sample H424-224).
H424-224	4LithoresearchQuant	384531	6944491	224	Deformed KGd between intervals of massive KGd (sample H424-212 above and H424-252 below).
H424-252	4Lithoresearch	384531	6944491	252	Massive KGd below foliated KGd (sample H424-224).
H424-314	4LithoresearchQuant	384531	6944491	314	Deformed KGd.
H424-323	4Lithoresearch	384531	6944491	323	Massive KGd
H427-115	4LithoresearchQuant	384956	6943813	115	Deformed KGd with disseminated Cpy; compare with H427-125
H427-124	4Lithoresearch	384956	6943813	124	Adjacent samples of massive KGd, foliated KGd, massive KGd. This sample is massive
H427-125	4LithoresearchQuant	384956	6943813	125	Adjacent samples of massive KGd, foliated KGd, massive KGd. This sample is deformed
H427-131	4Lithoresearch	384956	6943813	131	Adjacent samples of massive KGd, foliated KGd, massive KGd. This sample is massive
H427-70	4LithoresearchQuant	384956	6943813	70	With Cpy+Bn; compare with H427-125
H510-64	4Lithoresearch	383202	6945821		KGd; nice and crystalline looking. Nice epidote.
H587-141	4Lithoresearch	384141	6945938	141	~Massive KGd. Blotchy textured, adjacent to deformed KGd and massive KGd
H587-233	4LithoresearchQuant	384141	6945938	233	Deformed KGd adjacent to blotchy textured Tonalite, and KGd. KGd below is protolith?
H587-253	4Lithoresearch	384141	6945938	253	Massive KGd.
H666-68	4LithoresearchQuant	-	-	-	MDRU reference sample: QGRM-101
H666-70	4Lithoresearch	-	-	-	Duplicate of S09-22-01A
S09-02-9A	4Lithoresearch	383776	6945758	Surface	Outcrop just E of trench. Outcrop ~16m trending 170 deg; 'boulder' weathering. Kfs as KM (25-35%) very pale, almost grey. Good and tabular [2.5cm]. Pl (55%) [3-5mm]. Qz (10%) eyes. Bt (5%) pseudomorphing Hbl? Epi (3%) patchy but crystalline in mafic sites [1mm
S09-04-06A	4Lithoresearch	383197	6944378		Rubby outcrop of felsic intrusive rock in contact with Qtz-eye tonalite (KGd without KM?) and Tlt. Greenish tinge to plagioclase. Cleavage planes at 60-000 and 70-010.
S09-08-01A	4Lithoresearch	382654	6944715	1007	Massive KGd from regional trav. Patchy Epi.
S09-08-04A	4Lithoresearch	381289	6944784	Surface	Massive KGd. Moderate patchy eEpi.

S09-10-03B	4Lithoresearch	391014	6947669	Surface	Another great roadside exposure. Very fresh looking, broken apart as blocks. Hbl and minor Bt granodiorite. KGd (20%) as euhedral KM [2 cm]. Pl (30%) sub- to euhedral. Hbl (20-30%) blotchy, subhedral stubby crystals up to [1cm], long crystals up to [1cm], average size [5 mm]. Epi (5%) associated with Hbl/Bt. Bt (<2%) black and in equilibrium or replacing Hbl; possibly pseudomorphing Hbl. Qz (5%) anhedral. Possible weak foliation. Minor mafic magmatic enclaves.
S09-13-03A	4Lithoresearch	386926	6946023	Surface	Massive KGd
S09-13-03B	4Lithoresearch	386926	6946023	Surface	Crowded Kfs porphyry variety of KGd
S09-13-03C	4Lithoresearch	386926	6946023	Surface	KGd with abundant mafic xenoliths
Sample	PkgCode	UTM_E	UTM_N	Depth	Description
S09-14-01Bi	4LithoresearchQuant	384590	6945165	730	BGn; so-called "siliceous ore"
S09-14-01Bii	4LithoresearchQuant	384590	6945165	730	BGn. Hem altered feldspars
S09-15-04A	4Lithoresearch	387024	6946222	767	Massive KGd with possible flow banding.
S09-16-01A	4LithoresearchQuant	384724	6945250	825	BGn. Pervasively weathered and FeOx stained. 30->080, 45->065, 35->070. parallel banding. Qz-Feldspar 3mm->1cm. Mag bands 2mm to 5mm. Magnetic.
S09-16-01B	4Lithoresearch	384724	6945250	825	Near massive KGd w slight fabric; flow banding?. KM 20% porph. Well aligned [1-2cm]. Emplacement aligned? Pl 40% eu-subhedral, no recrystallization, stained grn from Mch or argillization. Bt 35% generally as randomly oriented blk books [cms].
S09-16-01C	4LithoresearchQuant	384724	6945250	825	Def'd KGd. KM 20%, 4-5mm locally 1cm, some recrystallization-grain sized reduced. Pl 40% micro-lith [cm-cms] well aligned. Commonly stained Gnt. Bt 30%, black books [1mm], folia [cms] & anastomosing, almost continuous. Qz (<5%) as [mms] bands. Trace diss Cpy+Bn
S09-16-01D	4Lithoresearch	384724	6945250	825	Massive KGd. KM randomly oriented [->3cm]. Pl [35%] eu-sub-hedral, chalky white -> clay altered. Bt(25-30%) randomly oriented, books [1-2mm] altered to phlog? Qtz (5%) eyes [5mm] with visible subgrains? Epi (3-5%) w Bt, patchy alteration.
S09-17-05A	4Lithoresearch	388739	6947539	747	Massive KGd
S09-22-01A	4LithoresearchQuant	384535	6945018	730	Parallel banded Tonalite
S09-22-01B	4LithoresearchQuant	384535	6945018	730	Green-plagioclase (illitized?) tonalite which seems commonly "swirled" or mixed in with Bt+Cpy+Bn lithology (tonalite-porphyroclast bt-mag-gneiss); evidence of magma intrusions into un-solidified host?
S09-22-01C	4Lithoresearch	384535	6945018	730	Massive KGd adjacent to strongly deformed and altered rock. Contact rel'p with S09-22-01B unclear. Potential shear or fault contact? Steep limb of folding?
S09-24-02Ai	4LithoresearchQuant	384539	6945075	730	Tonalite "porphyroclast" in contact with siliceous Cpy-Bn-mag-gneiss
S09-24-02Aii	4LithoresearchQuant	384539	6945075	730	Siliceous Cpy-Bn-Mag-gneiss
S09-25-02B	4LithoresearchQuant	384633	6944928	730	fold hinge of bGn
S09-69	4LithoresearchQuant	-	-	-	Ref sample: QGRM-101
S09-71	4Lithoresearch	-	-	-	Dup 2: S09-13-03B

Appendix D Whole-Rock Lithochemical Data

Table D1: Analytical precision for geochemical analysis by Actlabs Ltd. See Table C1 for method used per sample.

Lithochemistry

Lithochemistry for Exploration and Research

All elements are in PPM except where noted.



Code	INAA	INAA	WRA-ICP	Trace Element	WRA+trace	Trace Element	WRA+trace	WRA-XRF	XRF pressed pellet 4C1
	4A-expl	4A-research	4B	4B2-std	4Litho	4B2-research	4Lithoresearch	4C	
Al ₂ O ₃			0.01%		0.01%		0.01%	0.01%	
CaO			0.01%		0.01%		0.01%	0.01%	
Cr ₂ O ₃			0.01%					0.01%	
Fe ₂ O ₃			0.01%		0.01%		0.01%	0.01%	
K ₂ O			0.01%		0.01%		0.01%	0.01%	
MgO			0.01%		0.01%		0.01%	0.01%	
MnO			0.001%		0.001%		0.001%	0.001%	
Na ₂ O			0.01%		0.01%		0.01%	0.01%	
P ₂ O ₅			0.01%		0.01%		0.01%	0.01%	
SiO ₂			0.01%		0.01%		0.01%	0.01%	
TiO ₂			0.001%		0.001%		0.001%	0.01%	
LOI			0.01%		0.01%		0.01%	0.01%	
Ag	5	2	(0.5+)	0.5	0.5	0.5	0.5		
As	2	1	(0.5++)	5 (0.5++)	5 (0.5+)	5 (0.5++)	5 (0.5++)		
Au	5 ppb	2 ppb	(2 ppb++)	(2 ppb++)	(2 ppb++)	(2 ppb++)	(2 ppb++)		
Ba	100	20	3	3	3	3	3		5*
Be			1		1		1		
Bi			(10+)	0.4	0.4		0.1		
Br	1	0.5	(0.5++)	(0.5++)	(0.5++)	(0.5++)	(0.5++)		
Ca	0.5%	0.2%							
Cd			(0.5+)	(0.5+)	(0.5+)	(0.5+)	(0.5+)		
Co	1	0.1	(1+)	1	1	1	1		5**
Cr	2	0.5	(5+)	20 (5+)	20 (5+)	20 (5+)	20 (5+)		5**
Cs	0.5	0.2	(1+)	0.5	0.5	0.1	0.1		
Cu			(1+)	10 (1+)	10 (1+)	10 (1+)	10 (1+)		5**
Fe	0.02%	0.005%		(0.01++)		(0.01++)			
Ga			1		1		1		5*
Ge				1	1	0.5	0.5		
Hf	0.5	0.2	(1+)	0.2	0.2	0.1	0.1		
In				0.2	0.2	0.1	0.1		
Ir	5 ppb	2 ppb	(5 ppb++)	(5 ppb++)	(5 ppb++)	(5 ppb++)	(5 ppb++)		
Mo	5	2	(5+)	2	2	2	2		
Na	0.01%	0.001%		(0.01++)		(0.01++)			
Nb			1		1		0.2		1*
Ni	100	50	(1+)	20 (1+)	20 (1+)	20 (1+)	20 (1+)		4**
Pb			(5+)	5	5	5	5		5**
Rb	20	10	(20+)	2	2	1	1		2*
S			(100+)	(100+)	(100+)	(100+)	(100+)		
Sb	0.2	0.1	(0.2++)	0.5 (0.2++)	0.5 (0.2+)	0.2	0.2		
Sc	0.1	0.01	1	(0.1++)	1 (0.1++)	(0.1++)	1 (0.1++)		
Se	3	0.5	(3+)	(3+)	(3+)	(3+)	(3+)		
Sn			1		1		1		5
Sr	500	100	2	2	2	2	2		2*
Ta	1	0.3	(0.5++)	0.1	0.1	0.01	0.01		
Th	0.5	0.1	(0.2++)	0.1	0.1	0.05	0.05		
Ti				0.1	0.1	0.05	0.05		
U	0.5	0.1	(0.5++)	0.1	0.1	0.01	0.01		
V			5	5	5	5	5		5**
W	3	1	(1+)	1	1	0.5	0.5		
Y			2	1	1	0.5	0.5		2*
Zn	40	10	(1+)	30 (1+)	30 (1+)	30 (1+)	30 (1+)		5**
Zr			4	5	5	1	1		5*
La	0.2	0.05	(0.5++)	0.1	0.1	0.05	0.05		
Ce	3	1	(3+)	0.1	0.1	0.05	0.05		
Pr			(10.01)	0.05	0.05	0.01	0.01		
Nd	5	1	(5+)	0.1	0.1	0.05	0.05		
Sm	0.1	0.01	(0.1++)	0.1	0.1	0.01	0.01		
Eu	0.1	0.05	(0.2++)	0.05	0.05	0.005	0.005		
Gd			(10.01)	0.1	0.1	0.01	0.01		
Tb	0.5	0.1	(0.5++)	0.1	0.1	0.01	0.01		
Dy			(10.01)	0.1	0.1	0.01	0.01		
Ho			(10.01)	0.1	0.1	0.01	0.01		
Er			(10.01)	0.1	0.1	0.01	0.01		
Tm			(10.01)	0.05	0.05	0.005	0.005		
Yb	0.1	0.05	(0.2++)	0.1	0.1	0.01	0.01		
Lu	0.05	0.01	(0.05++)	0.01	0.01	0.002	0.002		

(1) Optional elements, see Code 4A
 (+) Optional elements by INAA, Code 4B1NAA
 (++) Optional elements by multiacid digestion ICP, Code 4B1

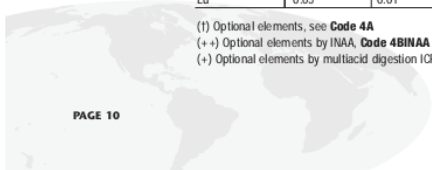


Table D2: Table of whole rock geochemical data for samples listed in Table C1.

Sample	SiO ₂ (%)	Al ₂ O ₃ (%)	Fe ₂ O ₃ (%)	MnO (%)	MgO (%)	CaO (%)	Na ₂ O (%)	K ₂ O (%)	TiO ₂ (%)	P ₂ O ₅ (%)	LOI (%)	Total (%)	Ag (ppm)	As (ppm)	Au (ppb)
H424-212	67.21	16.14	3.77	0.085	1.16	3.97	4.46	1.89	0.35	0.15	0.49	99.68	< 0.5	< 0.5	< 2
H424-224	65.77	15.13	4.35	0.136	1.28	3.83	3.36	3.23	0.38	0.21	0.55	98.22	< 0.5	< 0.5	< 2
H424-252	65.09	16.76	4.02	0.088	1.35	4.37	4.41	2.16	0.32	0.15	0.46	99.18	< 0.5	< 0.5	< 2
H424-314	62.78	15.52	4.94	0.051	1.52	4.19	3.41	3.07	0.43	0.25	2.35	98.52	1	< 0.5	59
H424-323	64.13	16.77	3.91	0.139	1.26	4.51	4.17	1.9	0.33	0.16	1.07	98.34	< 0.5	< 0.5	< 2
H427-115	68.22	14.66	3.93	0.039	1.22	2.71	3.68	3.29	0.33	0.18	1.04	99.3	< 0.5	2.3	14
H427-124	65.01	16.17	3.95	0.070	1.31	3.79	4.32	2.13	0.36	0.17	0.93	98.22	< 0.5	< 0.5	< 2
H427-125	63.53	15.28	6.05	0.072	1.69	3.07	3.73	2.9	0.45	0.25	1.22	98.24	< 0.5	< 0.5	9
H427-131	64.16	16.67	4.21	0.091	1.43	4.58	4.54	1.56	0.37	0.18	0.58	98.37	< 0.5	< 0.5	< 2
H427-70	65.41	14.71	5.43	0.072	1.45	3.02	3.41	3.2	0.39	0.22	1.58	98.88	1.6	< 0.5	99
H510-64	64.75	16.50	4.22	0.104	1.43	4.71	4.49	1.93	0.39	0.18	0.47	99.17	< 0.5	< 0.5	4
H587-141	65.20	15.67	4.55	0.080	1.4	4.23	3.47	3.68	0.39	0.22	0.62	99.51	< 0.5	< 0.5	< 2
H587-233	61.61	13.84	6.36	0.467	1.44	3.61	2.97	3.61	0.38	0.2	2.54	97.02	3.5	< 0.5	450
H587-253	63.84	16.49	4.24	0.093	1.32	4.58	4.56	2.04	0.35	0.16	0.98	98.64	< 0.5	< 0.5	< 2
S09-02-9A	64.92	16.79	4.48	0.102	1.56	4.90	4.54	1.63	0.42	0.2	0.53	100.1	< 0.5	< 0.5	< 2
S09-08-01A	64.82	16.96	4.26	0.126	1.45	4.76	4.69	1.72	0.38	0.17	0.43	99.78	< 0.5	< 0.5	< 2
S09-08-04A	66.28	16.72	3.42	0.061	1.05	3.93	4.84	1.31	0.32	0.12	0.59	98.63	< 0.5	1.7	< 2
S09-10-03B	63.98	15.89	4.64	0.120	1.59	4.50	4.10	2.59	0.40	0.23	0.51	98.54	< 0.5	< 0.5	< 2
S09-13-03A	64.97	16.48	3.88	0.100	1.25	4.10	4.65	2.07	0.37	0.16	0.69	98.71	< 0.5	< 0.5	< 2
S09-13-03B	63.11	16.43	4.90	0.106	1.21	3.19	3.54	4.66	0.40	0.14	0.76	98.45	< 0.5	< 0.5	< 2
S09-13-03C	68.4	15.19	3.82	0.080	0.94	2.51	3.57	4.26	0.33	0.07	0.5	99.67	< 0.5	< 0.5	< 2
S09-14-01Bi	79.64	0.68	15.55	0.060	0.28	0.40	0.05	0.13	0.27	0.04	0.22	97.33	7.8	0.9	693
S09-14-01Bii	57.09	11.48	13.92	0.147	1.95	1.44	1.21	5.42	0.62	0.25	2.37	95.89	11.6	1.9	1050
S09-15-04A	66.71	16.76	3.27	0.065	0.94	3.77	4.47	1.96	0.31	0.11	0.91	99.28	< 0.5	< 0.5	< 2
S09-16-01A	77.70	4.73	8.45	0.032	0.05	0.07	0.46	3.08	0.09	< 0.01	1.75	96.42	28.2	5.7	4160
S09-16-01B	65.43	16.47	3.85	0.079	1.23	3.31	4.11	2.18	0.35	0.15	1.1	98.28	1.5	< 0.5	< 2
S09-16-01C	64.54	14.73	6.57	0.104	1.57	2.28	2.58	4.95	0.42	0.31	1.41	99.44	3.1	5.5	409
S09-16-01D	65.16	16.67	3.68	0.064	1.19	3.46	4.35	1.81	0.39	0.15	1.19	98.12	< 0.5	< 0.5	< 2
S09-17-05A	66.51	16.44	2.95	0.064	0.84	2.76	4.86	2.61	0.28	0.11	0.88	98.29	< 0.5	< 0.5	< 2
S09-22-01A	51.37	12.67	16.99	0.150	1.69	3.85	2.47	2.86	0.90	0.3	3.53	96.77	5.5	< 0.5	5210
S09-22-01B	56.03	12.91	13.39	0.164	1.58	4.30	2.94	1.93	0.77	0.22	3.55	97.79	3.5	3.8	865
S09-22-01C	65.64	16.69	3.71	0.073	1.34	3.97	4.28	2.39	0.34	0.16	0.93	99.55	< 0.5	< 0.5	< 2
S09-24-02Ai	52.64	16.72	11.29	0.166	1.97	4.53	4.77	1.45	0.48	0.16	1.84	96.02	11.1	< 0.5	13300
S09-24-02Aii	57.83	0.69	22.87	0.097	0.36	0.78	0.10	0.21	0.24	0.03	4.56	87.76	9.2	< 0.5	1530
S09-25-02B	62.14	11.60	14.01	0.107	1.36	1.10	2.01	4.58	0.41	0.14	1.24	98.69	3.9	< 0.5	1150

Sample	Ba (ppm)	Be (ppm)	Bi (ppm)	Br (ppm)	Ce (ppm)	Co (ppm)	Cr (ppm)	Cs (ppm)	Cu (%)	Cu (ppm)	Dy (ppm)	Er (ppm)	Eu (ppm)	Ga (ppm)	Gd (ppm)
H424-212	1164	2	< 0.1	< 0.5	26.6	5	13	0.2	NA	< 10	1.28	0.74	0.602	21	1.56
H424-224	1322	2	< 0.1	< 0.5	38.4	6	56	1	NA	30	2.19	1.32	0.804	18	2.51
H424-252	1985	1	< 0.1	< 0.5	37.0	6	< 5	0.4	NA	< 10	1.59	0.93	0.686	20	1.86
H424-314	1514	1	0.2	< 0.5	34.3	6	< 5	0.8	NA	2440	1.93	1.14	0.763	18	2.38
H424-323	1597	2	< 0.1	< 0.5	23.5	6	36	0.4	NA	< 10	2.30	1.28	0.708	20	2.30
H427-115	1168	2	< 0.1	< 0.5	26.9	5	9	0.7	NA	1170	1.74	1.05	0.615	18	1.92
H427-124	1565	2	< 0.1	< 0.5	39.2	6	< 5	0.3	NA	< 10	0.94	0.54	0.613	20	1.42
H427-125	1275	2	< 0.1	< 0.5	43.7	8	11	1.5	NA	450	2.24	1.27	0.856	20	2.78
H427-131	1245	2	< 0.1	< 0.5	29.4	6	11	0.2	NA	< 10	2.10	1.26	0.722	20	2.27
H427-70	1081	2	1	< 0.5	29.0	8	57	1.1	NA	3370	1.75	1.04	0.632	20	1.96
H510-64	1762	2	< 0.1	< 0.5	29.8	7	56	< 0.1	NA	< 10	2.30	1.38	0.863	20	2.66
H587-141	1540	1	< 0.1	< 0.5	39.4	7	5	0.3	NA	30	2.39	1.42	0.844	18	2.61
H587-233	1247	1	0.3	< 0.5	33.6	7	10	0.9	1.69	NA	2.16	1.23	0.653	18	2.38
H587-253	2001	2	< 0.1	< 0.5	21.1	6	14	< 0.1	NA	10	2.05	1.24	0.711	20	2.23
S09-02-9A	1239	2	< 0.1	< 0.5	29.4	7	40	0.2	NA	< 10	2.84	1.64	0.895	20	2.99
S09-08-01A	1080	2	< 0.1	< 0.5	26.8	6	10	0.2	NA	10	2.18	1.27	0.731	20	2.34
S09-08-04A	2049	1	< 0.1	< 0.5	24.4	4	15	0.1	NA	< 10	1.63	0.87	0.627	19	1.80
S09-10-03B	1181	2	< 0.1	< 0.5	34.3	7	10	1	NA	20	2.11	1.24	0.785	20	2.34
S09-13-03A	1660	1	< 0.1	< 0.5	36.3	5	11	0.2	NA	< 10	2.64	1.59	0.809	20	2.96
S09-13-03B	4880	1	< 0.1	< 0.5	37.7	6	56	0.4	NA	< 10	2.63	1.51	0.840	19	2.81
S09-13-03C	2569	1	< 0.1	< 0.5	37.2	4	13	0.3	NA	< 10	2.00	1.21	0.605	17	2.11
S09-14-01Bi	84	< 1	3.9	< 0.5	1.2	7	25	< 0.1	1.91	NA	0.14	0.08	0.041	11	0.18
S09-14-01Bii	5259	< 1	6	< 0.5	3.8	13	67	0.8	2.52	NA	0.54	0.28	0.183	19	0.75
S09-15-04A	1786	1	< 0.1	< 0.5	28.8	4	16	0.3	NA	< 10	1.89	1.06	0.637	19	2.07
S09-16-01A	587	< 1	15.9	< 0.5	0.3	5	9	< 0.1	2.52	NA	< 0.01	< 0.01	0.065	11	< 0.01
S09-16-01B	1074	1	< 0.1	< 0.5	18.1	5	61	0.7	NA	3230	0.58	0.31	0.405	21	0.76
S09-16-01C	1434	1	2	< 0.5	15.1	6	12	0.8	NA	4740	1.75	1.02	0.537	20	1.89
S09-16-01D	1579	1	< 0.1	< 0.5	55.8	6	14	0.5	NA	1210	0.84	0.46	0.522	20	1.25
S09-17-05A	2051	2	< 0.1	< 0.5	30.7	4	19	0.3	NA	< 10	1.91	1.14	0.649	20	2.08
S09-22-01A	2175	1	0.7	< 0.5	13.9	17	17	0.6	3.06	NA	0.95	0.51	0.526	23	1.29
S09-22-01B	1105	1	0.4	< 0.5	6.78	15	< 5	0.6	1.71	NA	0.65	0.36	0.356	23	0.84
S09-22-01C	2468	1	< 0.1	< 0.5	24.8	5	69	0.4	NA	< 10	1.66	0.94	0.616	19	1.83
S09-24-02Ai	818	2	4	< 0.5	6.2	12	16	0.5	1.95	NA	2.70	1.57	0.611	24	2.56
S09-24-02Aii	158	< 1	3.5	< 0.5	8.9	16	19	0.2	9.59	NA	0.81	0.45	0.209	7	0.87
S09-25-02B	1997	< 1	0.8	< 0.5	8.3	8	22	0.4	1.21	NA	0.42	0.20	0.255	20	0.52

Sample	Ge (ppm)	Hf (ppm)	Ho (ppm)	In (ppm)	Ir (ppb)	La (ppm)	Lu (ppm)	Mo (ppm)	Nb (ppm)	Nd (ppm)	Ni (ppm)	Pb (ppm)	Pr (ppm)	Rb (ppm)	Sb (ppm)
H424-212	0.8	2.6	0.25	< 0.1	< 5	13.50	0.126	< 2	10	10.8	< 20	19	2.89	52	< 0.2
H424-224	1.5	3.5	0.44	< 0.1	< 5	19.90	0.248	5	9.9	15.1	< 20	25	4.1	92	< 0.2
H424-252	1.3	2.8	0.32	< 0.1	< 5	19.30	0.16	< 2	5.3	14.1	< 20	17	3.91	47	< 0.2
H424-314	1.4	3.3	0.39	< 0.1	< 5	17.50	0.168	< 2	10	14.7	< 20	24	3.83	77	0.3
H424-323	1.2	2.8	0.45	< 0.1	< 5	12.80	0.202	3	5.1	10.4	< 20	33	2.66	50	< 0.2
H427-115	1.5	2.9	0.35	< 0.1	< 5	13.70	0.181	< 2	9.7	11.8	< 20	11	3	67	< 0.2
H427-124	0.9	2.7	0.18	< 0.1	< 5	21.90	0.098	< 2	7.9	14.2	< 20	12	4.02	60	< 0.2
H427-125	1.6	3.4	0.44	< 0.1	< 5	23.40	0.223	< 2	11.9	17.4	< 20	18	4.7	95	0.3
H427-131	1.4	3.6	0.42	< 0.1	< 5	14.70	0.237	< 2	7.8	12.6	< 20	12	3.32	31	< 0.2
H427-70	1.5	3.3	0.35	< 0.1	< 5	15.00	0.187	7	10.9	12.2	< 20	20	3.16	77	< 0.2
H510-64	0.9	2.5	0.46	< 0.1	< 5	13.90	0.224	7	8	14.8	< 20	14	3.65	42	< 0.2
H587-141	1.5	2.9	0.48	< 0.1	< 5	20.20	0.298	< 2	12	15.7	< 20	17	4.28	61	< 0.2
H587-233	1.1	3.1	0.42	< 0.1	< 5	17.30	0.239	5	9.9	14	< 20	79	3.66	90	0.3
H587-253	0.9	2.9	0.42	< 0.1	< 5	9.83	0.204	< 2	7.6	11.2	< 20	10	2.62	41	< 0.2
S09-02-9A	1.3	3.6	0.56	< 0.1	< 5	13.40	0.279	4	10	15.4	< 20	10	3.7	36	< 0.2
S09-08-01A	1.4	3.3	0.43	< 0.1	< 5	13.60	0.216	< 2	7	11.6	< 20	11	3.03	38	< 0.2
S09-08-04A	1.0	2.6	0.31	< 0.1	< 5	13.50	0.123	< 2	3.4	10.1	< 20	6	2.66	22	< 0.2
S09-10-03B	1.5	2.9	0.41	< 0.1	< 5	17.60	0.247	< 2	9.4	14.2	< 20	9	3.77	62	< 0.2
S09-13-03A	1.3	3.2	0.53	< 0.1	< 5	17.30	0.256	< 2	10.1	15.8	< 20	8	4.16	38	< 0.2
S09-13-03B	1.3	3.9	0.51	< 0.1	< 5	18.40	0.267	5	11.3	16.7	< 20	11	4.3	75	< 0.2
S09-13-03C	1.3	3.8	0.40	< 0.1	< 5	19.90	0.237	< 2	11	13.7	< 20	11	3.88	71	< 0.2
S09-14-01Bi	0.8	1.1	0.03	< 0.1	< 5	0.52	0.011	< 2	0.2	0.72	< 20	5	0.15	3	< 0.2
S09-14-01Bii	0.7	3.4	0.10	< 0.1	< 5	1.87	0.057	9	7.8	2.72	< 20	33	0.54	85	< 0.2
S09-15-04A	1.1	3.3	0.36	< 0.1	< 5	14.70	0.178	< 2	7.7	11.8	< 20	8	3.15	36	< 0.2
S09-16-01A	1.2	1.1	< 0.01	< 0.1	< 5	0.27	0.003	12	< 0.2	0.13	< 20	16	0.04	45	< 0.2
S09-16-01B	1.2	3.1	0.11	< 0.1	< 5	11.10	0.059	6	6	7.68	< 20	12	2.23	66	< 0.2
S09-16-01C	1.5	3.6	0.34	< 0.1	< 5	8.19	0.158	< 2	8.5	8.31	< 20	40	2.04	100	< 0.2
S09-16-01D	1.1	2.4	0.16	< 0.1	< 5	32.70	0.079	< 2	4.3	17.3	< 20	9	5.26	44	< 0.2
S09-17-05A	1.2	3.2	0.39	< 0.1	< 5	15.30	0.195	< 2	9.5	12.7	< 20	9	3.36	51	< 0.2
S09-22-01A	1.1	5.0	0.18	< 0.1	< 5	6.69	0.084	< 2	12	7.28	< 20	11	1.71	83	< 0.2
S09-22-01B	1.1	3.9	0.13	< 0.1	< 5	3.23	0.072	< 2	8.3	3.95	< 20	8	0.87	71	< 0.2
S09-22-01C	1.2	3.3	0.32	< 0.1	< 5	12.10	0.164	6	6	11.2	< 20	14	2.84	50	< 0.2
S09-24-02Ai	1.3	3.2	0.53	< 0.1	< 5	2.44	0.261	5	7.2	5.92	< 20	19	1.1	39	< 0.2
S09-24-02Aii	0.6	0.9	0.16	0.3	< 5	4.69	0.063	6	5.4	3.95	< 20	13	0.99	9	< 0.2
S09-25-02B	1.2	2.9	0.08	< 0.1	< 5	4.42	0.036	< 2	6.3	3.55	< 20	13	0.9	90	< 0.2

Sample	Sc (ppm)	Se (ppm)	Sm (ppm)	Sn (ppm)	Sr (ppm)	Ta (ppm)	Tb (ppm)	Th (ppm)	Ti (ppm)	Tm (ppm)	U (ppm)	V (ppm)	W (ppm)	Y (ppm)	Yb (ppm)
H424-212	4.9	< 3	1.88	< 1	783	0.28	0.23	3.2	0.25	0.108	1.74	69	< 0.5	7.2	0.72
H424-224	6.7	< 3	2.95	< 1	701	0.49	0.38	8.93	0.57	0.205	1.57	80	< 0.5	13.2	1.42
H424-252	7.1	< 3	2.49	< 1	847	0.14	0.28	3.26	0.24	0.141	0.52	74	< 0.5	9.2	0.96
H424-314	7	< 3	2.87	< 1	735	0.4	0.34	6.82	0.49	0.17	1.15	95	< 0.5	11.5	1.1
H424-323	9.8	< 3	2.4	< 1	824	0.24	0.38	3.02	0.33	0.188	0.6	69	< 0.5	13.1	1.24
H427-115	5.9	< 3	2.27	< 1	603	0.48	0.3	9.02	0.47	0.162	0.76	71	< 0.5	10.4	1.13
H427-124	3.9	< 3	2.08	< 1	780	0.24	0.18	5.43	0.3	0.081	0.53	70	< 0.5	5.4	0.55
H427-125	7.6	< 3	3.37	2	653	0.67	0.4	10.4	0.59	0.199	1.47	105	< 0.5	12.9	1.35
H427-131	7.1	< 3	2.64	< 1	887	0.38	0.36	2.36	0.14	0.2	0.69	75	< 0.5	12.9	1.43
H427-70	6.8	< 3	2.56	< 1	615	0.6	0.31	9.02	0.46	0.167	1.46	84	< 0.5	10.3	1.12
H510-64	7.2	< 3	3.1	< 1	933	0.4	0.4	2.42	0.17	0.209	0.83	82	< 0.5	13.7	1.39
H587-141	6.1	< 3	3.19	< 1	781	0.77	0.42	6	0.22	0.233	1.88	89	< 0.5	15.1	1.76
H587-233	6.9	< 3	2.89	< 1	504	0.53	0.37	8.11	0.52	0.198	1.35	94	< 0.5	13.2	1.43
H587-253	6.9	< 3	2.49	< 1	920	0.36	0.35	1.51	0.14	0.186	0.56	74	< 0.5	12.6	1.23
S09-02-9A	7.7	< 3	3.4	< 1	905	0.52	0.48	1.82	0.14	0.252	0.7	88	< 0.5	16.5	1.73
S09-08-01A	7.3	< 3	2.65	< 1	901	0.27	0.38	2.25	0.16	0.193	0.6	81	< 0.5	12.8	1.34
S09-08-04A	5.1	< 3	2.02	< 1	985	0.11	0.29	1.54	0.08	0.131	0.25	54	< 0.5	8.9	0.84
S09-10-03B	8.7	< 3	2.81	< 1	827	0.51	0.38	5.08	0.22	0.198	1.38	84	< 0.5	13.3	1.41
S09-13-03A	8.4	< 3	3.37	< 1	728	0.59	0.46	2.74	0.13	0.249	0.67	59	< 0.5	16.6	1.64
S09-13-03B	7.6	< 3	3.39	< 1	822	0.7	0.46	3.48	0.27	0.239	1.03	92	< 0.5	15.9	1.66
S09-13-03C	5.6	< 3	2.57	< 1	659	0.58	0.35	3.55	0.25	0.202	0.87	61	< 0.5	13.1	1.45
S09-14-01Bi	1.1	18	0.19	< 1	15	0.03	0.03	0.17	< 0.05	0.013	0.09	210	< 0.5	0.8	0.09
S09-14-01Bii	4.1	22	0.67	1	417	0.17	0.1	0.6	0.37	0.044	0.35	174	0.5	3.1	0.34
S09-15-04A	5.3	< 3	2.42	< 1	859	0.41	0.33	2.55	0.14	0.164	0.66	51	< 0.5	11.3	1.14
S09-16-01A	0.6	28	< 0.01	< 1	137	< 0.01	< 0.01	3.28	0.23	< 0.005	0.38	59	< 0.5	< 0.5	0.03
S09-16-01B	3.4	< 3	1.17	< 1	672	0.16	0.11	6.62	0.38	0.048	0.62	62	< 0.5	3.6	0.35
S09-16-01C	7.1	< 3	1.97	< 1	676	0.37	0.3	8.31	0.68	0.151	1	93	< 0.5	10.9	0.98
S09-16-01D	2.9	< 3	2.15	< 1	931	0.19	0.16	6.29	0.18	0.069	0.45	62	< 0.5	4.9	0.47
S09-17-05A	4.5	< 3	2.54	< 1	825	0.44	0.33	2.65	0.19	0.174	0.79	48	< 0.5	11.8	1.2
S09-22-01A	2.7	26	1.56	1	537	0.23	0.18	1.32	0.41	0.077	0.78	343	< 0.5	6	0.51
S09-22-01B	2.5	11	0.91	< 1	562	0.21	0.12	0.6	0.34	0.056	0.69	264	< 0.5	4.4	0.41
S09-22-01C	6.8	< 3	2.29	< 1	963	0.19	0.29	2.08	0.23	0.146	0.56	69	< 0.5	10	1
S09-24-02Ai	14.7	< 3	2.14	3	948	0.28	0.44	0.5	< 0.05	0.241	0.61	110	1.5	14.6	1.64
S09-24-02Aii	1.5	114	0.87	2	28	0.22	0.14	1.52	< 0.05	0.066	0.57	162	3.3	5.1	0.42
S09-25-02B	2.9	10	0.63	< 1	506	0.17	0.07	2.85	0.41	0.029	0.27	120	< 0.5	2.4	0.2

Sample	Zn (ppm)	Zr (ppm)	Mass (g)
H424-212	110	116	34.4
H424-224	110	125	31
H424-252	80	110	32.1
H424-314	50	120	30.2
H424-323	130	118	34.4
H427-115	40	103	27
H427-124	70	123	29.3
H427-125	80	124	28.9
H427-131	60	145	31.4
H427-70	80	118	31.2
H510-64	90	119	34.4
H587-141	40	111	33.5
H587-233	400	116	27.1
H587-253	80	139	31.3
S09-02-9A	70	142	33.8
S09-08-01A	90	130	30.9
S09-08-04A	40	114	29.3
S09-10-03B	70	112	30.3
S09-13-03A	60	131	30.9
S09-13-03B	70	154	30.6
S09-13-03C	50	150	32.1
S09-14-01Bi	110	45	37.2
S09-14-01Bii	280	163	34.3
S09-15-04A	50	133	29.7
S09-16-01A	30	35	30.9
S09-16-01B	100	129	29.9
S09-16-01C	160	132	29.2
S09-16-01D	70	95	27.8
S09-17-05A	50	130	30.5
S09-22-01A	240	203	30.1
S09-22-01B	240	161	26.8
S09-22-01C	70	135	34.1
S09-24-02Ai	270	145	30.9
S09-24-02Aii	520	32	36.6
S09-25-02B	160	112	27.2

Appendix E Isocon Calculations

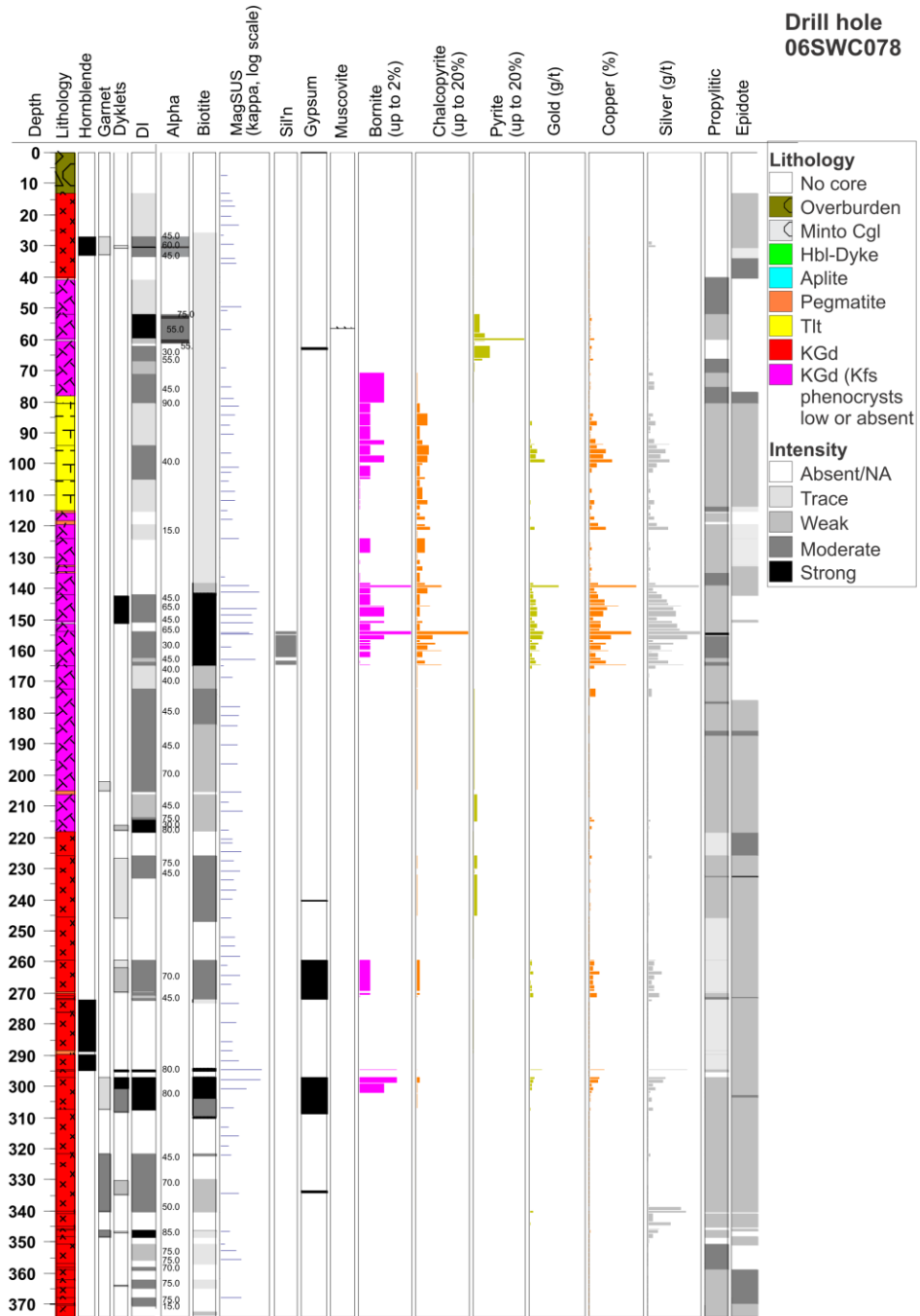
Table E1: Geochemical data from Table D1 scaled here for use in isocon diagrams. KGd = Minto granodiorite. Bt = biotite, Mag = magnetite, Cpy = chalcopyrite, Bn = bornite, Py = pyrite, weath BGn = weathered banded gneiss. CO_Suite represents an averaged protolith of KGd.

Sample	CO_Suite	H424-212	H424-252	H424-323	H424-314	H424-224	H427-124	H427-131	H427-70	H427-115	H427-125	S09-16-01A	S09-16-01B	S09-16-01C	S09-16-01D
Protolith	KGd	KGd	KGd	KGd	KGd	KGd	KGd	KGd	KGd	KGd	KGd	KGd	KGd	KGd	KGd
Alteration	NONE	NONE	NONE	NONE	Bt-Mag, Cpy-Bn	Bt-Mag, Cpy	NONE	NONE	Bt-Mag, Cpy-Bn	Bt-Mag, Cpy	Bt-Mag, Cpy-Py	Bn-Cpy (weath BGn)	NONE	Bn-Cpy	NONE
SiO2	20	20.61	19.96	19.66	19.25	20.17	19.93	19.67	20.06	20.92	19.48	23.82	20.05	19.79	19.98
Al2O3	18	17.45	18.12	18.13	16.78	16.35	17.48	18.02	15.9	15.85	16.52	5.11	17.83	15.92	18.02
Fe2O3	2	1.91	2.03	1.98	2.5	2.2	2	2.13	2.75	1.99	3.06	4.27	1.95	3.32	1.86
MnO	14	12.67	13.12	20.72	7.6	20.28	10.44	13.57	10.73	5.81	10.73	4.77	11.93	15.51	9.54
MgO	12	10.71	12.46	11.63	14.03	11.82	12.09	13.2	13.38	11.26	15.6	0.46	11.35	14.49	10.98
CaO	16	14.77	16.26	16.78	15.59	14.25	14.1	17.04	11.24	10.08	11.42	0.26	12.32	8.48	12.87
Na2O	8	8.03	7.94	7.51	6.14	6.05	7.78	8.18	6.14	6.63	6.72	0.83	7.4	4.65	7.83
K2O	5	4.86	5.56	4.89	7.9	8.31	5.48	4.01	8.23	8.47	7.46	7.93	5.61	12.74	4.66
TiO2	22	21.67	19.46	20.26	26.4	23.02	22.28	22.59	23.88	20.13	27.62	5.22	21.48	25.54	23.82
P2O5	10	9.43	9.43	10.06	15.72	13.21	10.69	11.32	13.84	11.32	15.72	-	9.43	19.5	9.43
Ce	16	14.02	19.5	12.38	18.08	20.24	20.66	15.49	15.28	14.18	23.03	0.17	9.54	7.96	29.41
Ga	20	21.11	20.1	20.1	18.09	18.09	20.1	20.1	20.1	18.09	20.1	11.06	21.11	20.1	20.1
Gd	12	8.88	10.58	13.09	13.54	14.28	8.08	12.92	11.15	10.92	15.82	-	4.32	10.75	7.11
Hf	25	22.03	23.73	23.73	27.97	29.66	22.88	30.51	27.97	24.58	28.81	9.32	26.27	30.51	20.34
La	18	15.59	22.29	14.79	20.21	22.99	25.3	16.98	17.33	15.82	27.03	0.31	12.82	9.46	37.77
Lu	10	6.88	8.73	11.03	9.17	13.54	5.35	12.94	10.21	9.88	12.17	0.16	3.28	8.62	4.31
Pb	6	7.86	7.03	13.66	9.93	10.34	4.97	4.97	8.28	4.55	7.45	6.62	4.97	16.55	3.72
Sc	14	10.41	15.08	20.82	14.87	14.23	8.29	15.08	14.45	12.53	16.15	1.27	7.22	15.08	6.16
Sr	24	21.2	22.93	22.31	19.9	18.98	21.11	24.01	16.65	16.32	17.68	3.71	18.19	18.3	25.2
Th	4	4.51	4.59	4.25	9.61	12.58	7.65	3.32	12.7	12.7	14.65	4.62	9.32	11.7	8.86
U	2	4.82	1.44	1.66	3.19	4.35	1.47	1.91	4.04	2.11	4.07	1.05	1.72	2.77	1.25
V	7	6.72	7.2	6.72	9.25	7.79	6.82	7.3	8.18	6.91	10.22	5.74	6.04	9.05	6.04
Zr	4	3.75	3.56	3.82	3.88	4.04	3.98	4.69	3.82	3.33	4.01	1.13	4.17	4.27	3.07

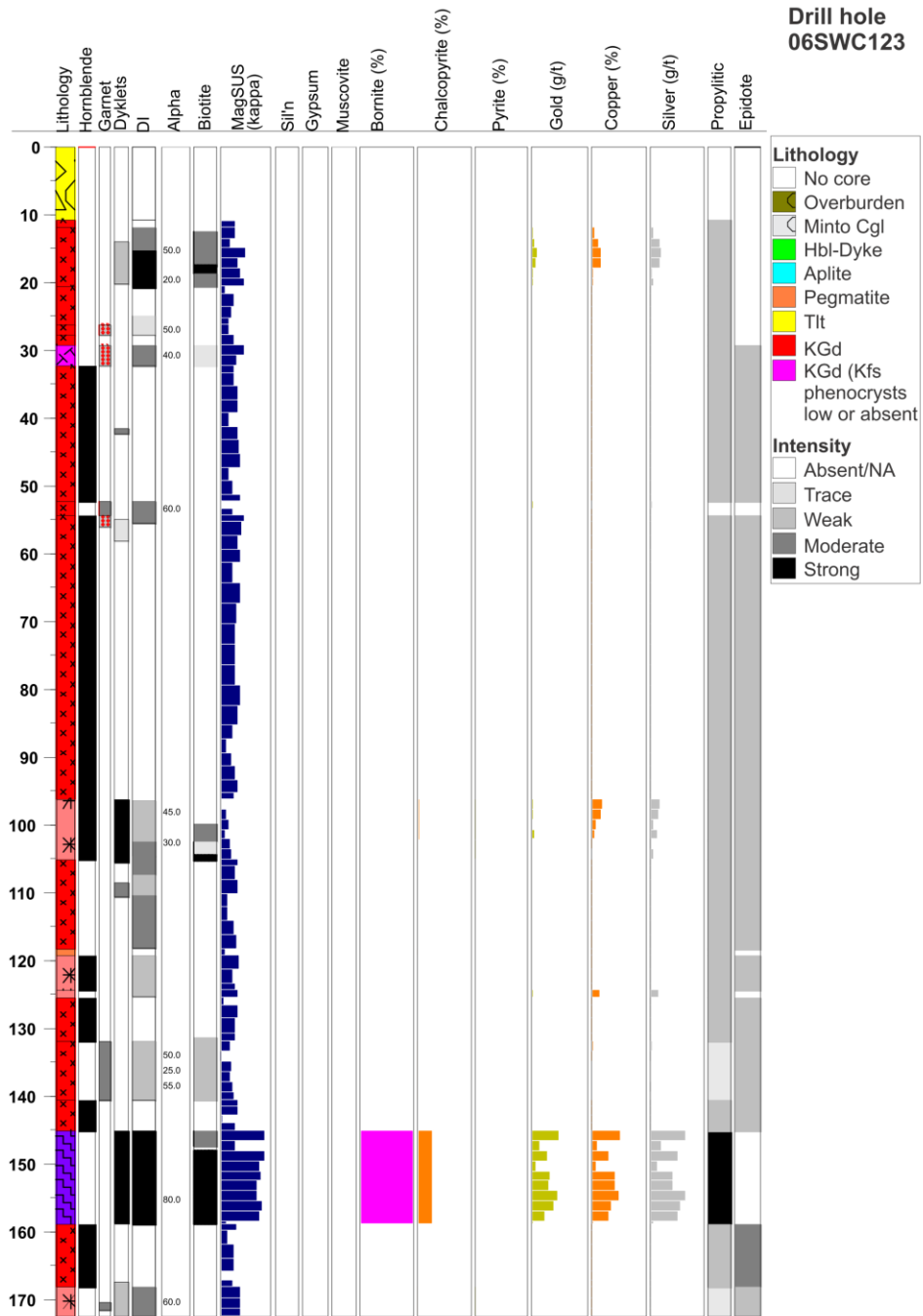
Appendix F Graphical Logs

The following graphical logs represent lithological, mineral, structural, and alteration observations for logged holes indicated in Figure 28.

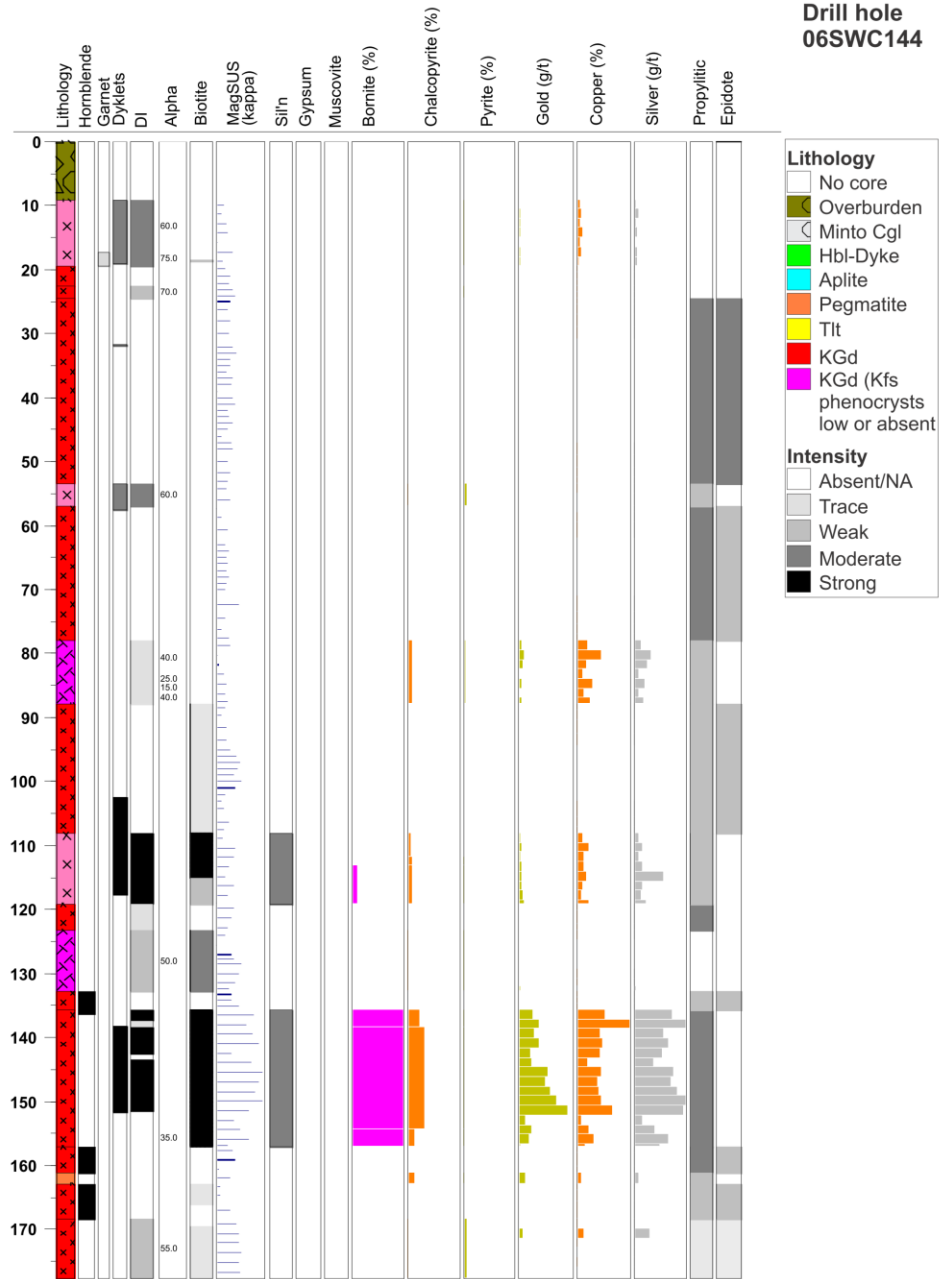
**Drill hole
06SWC078**



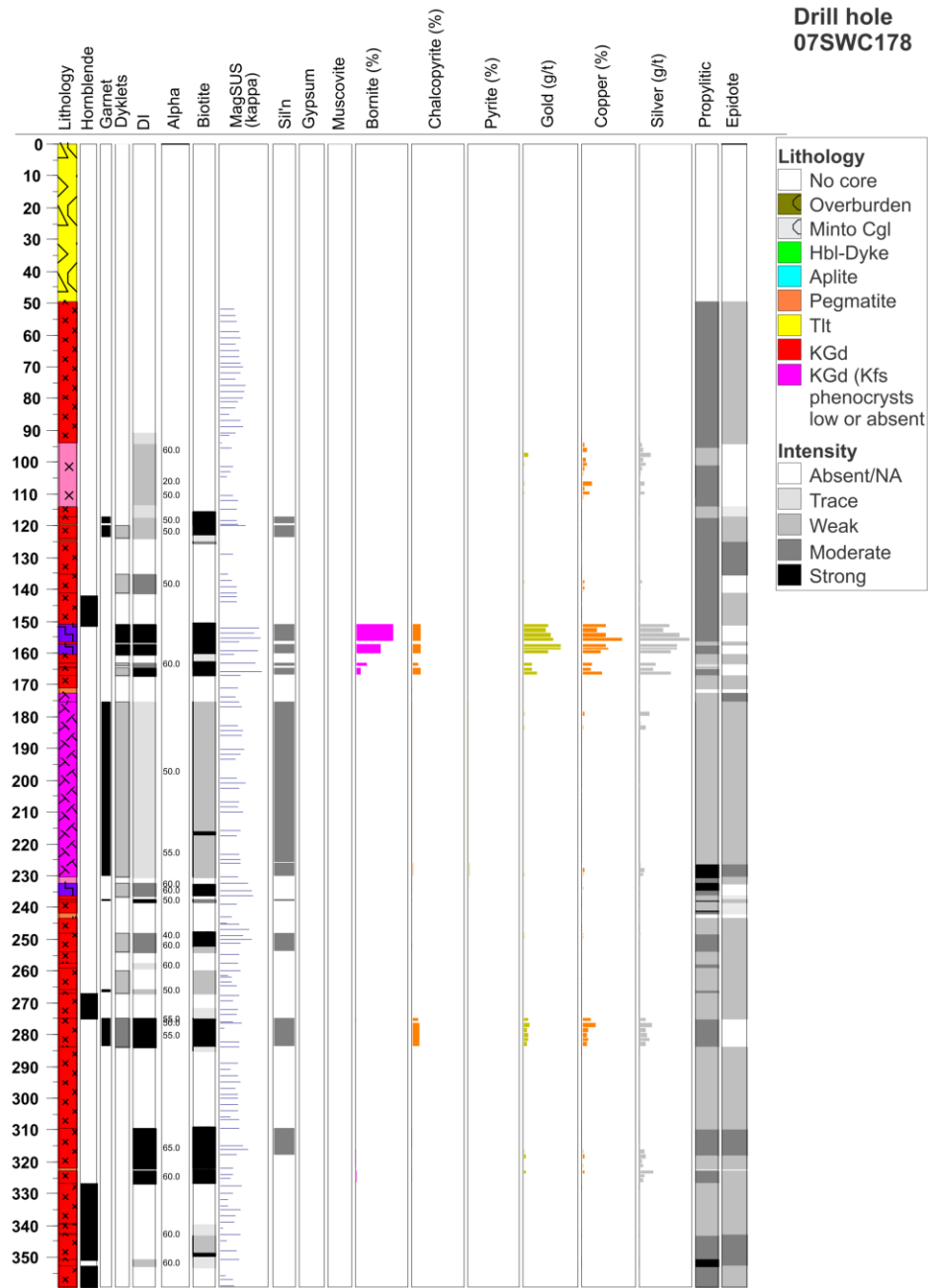
**Drill hole
06SWC123**



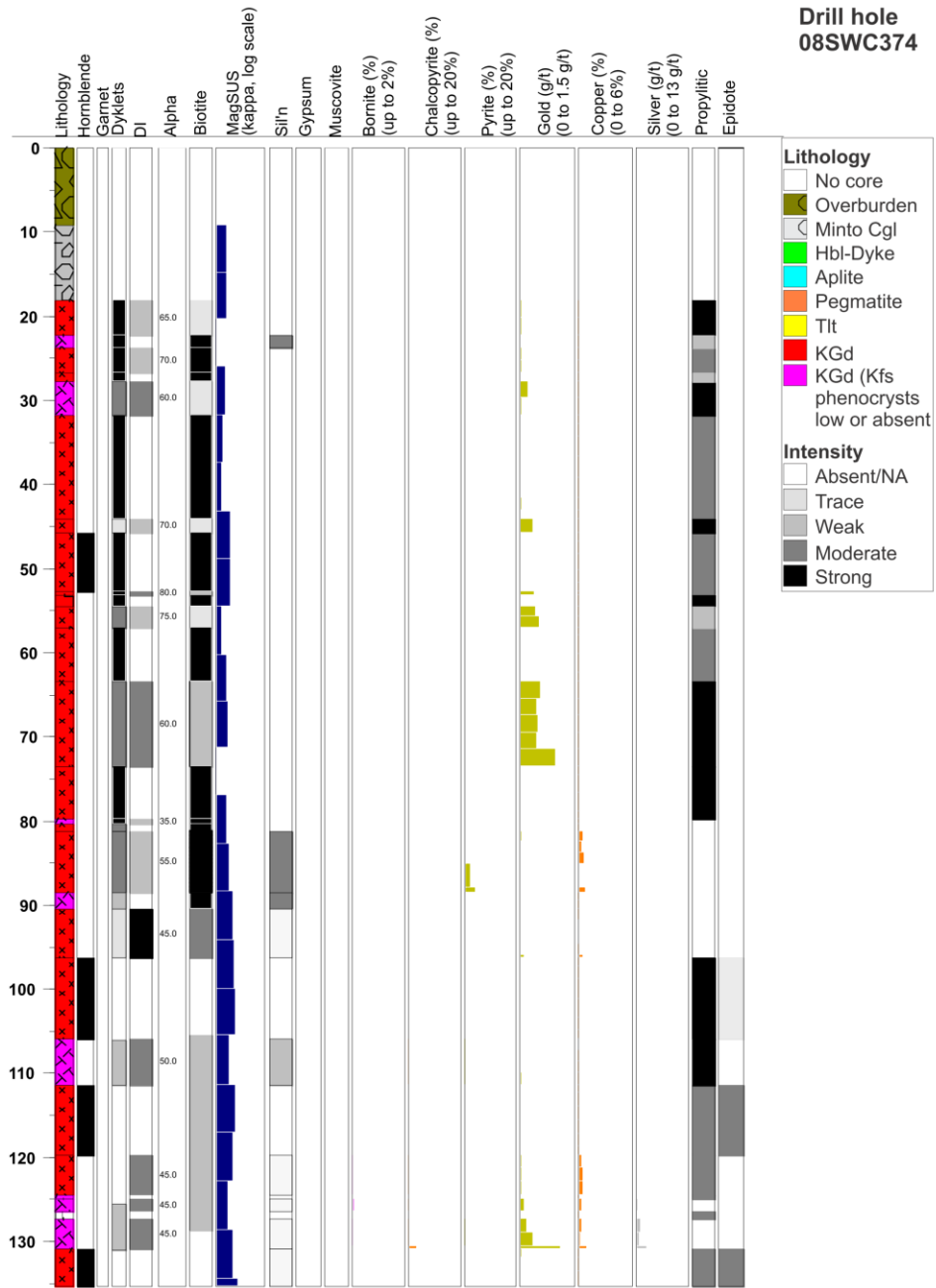
**Drill hole
06SWC144**



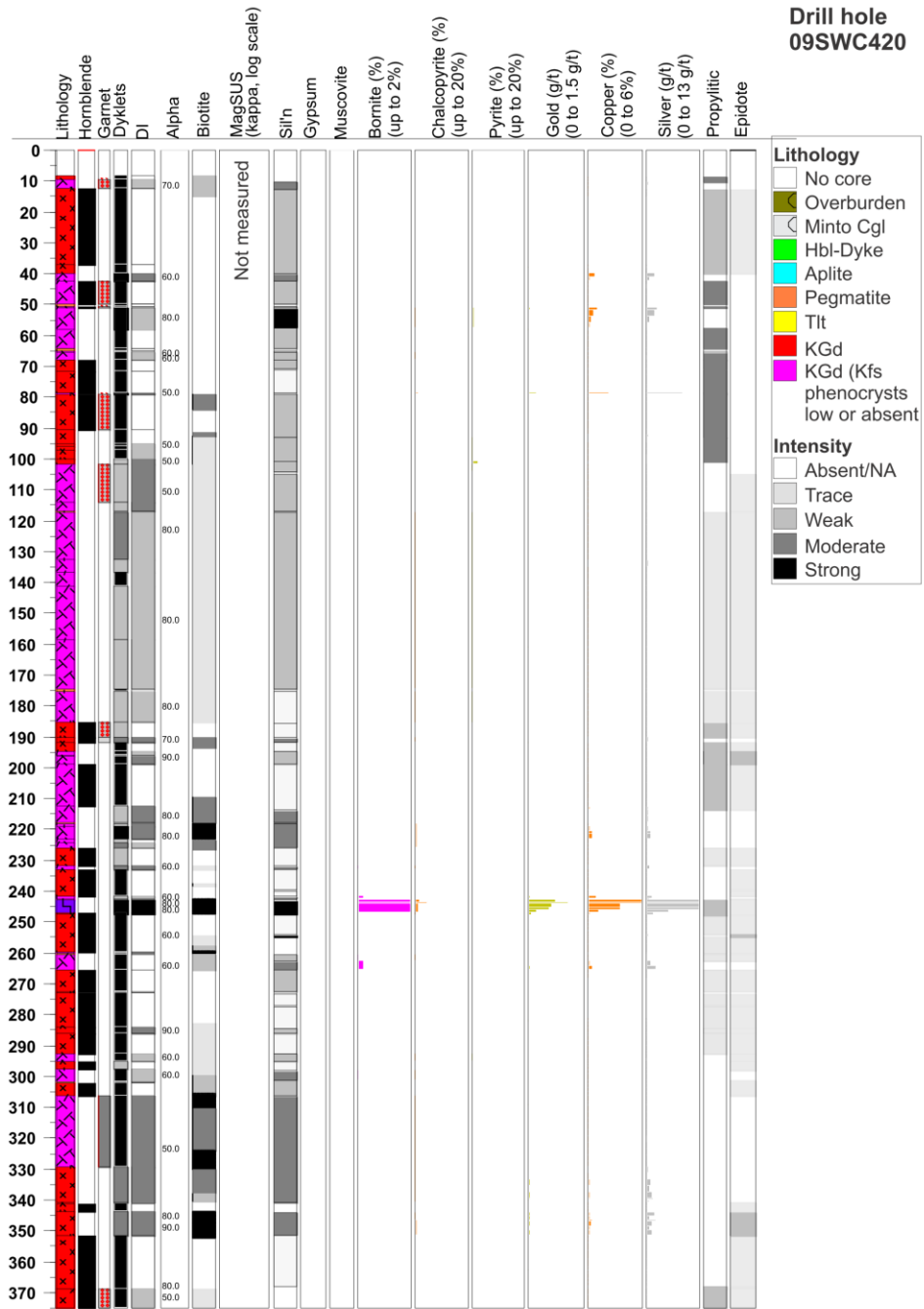
**Drill hole
07SWC178**



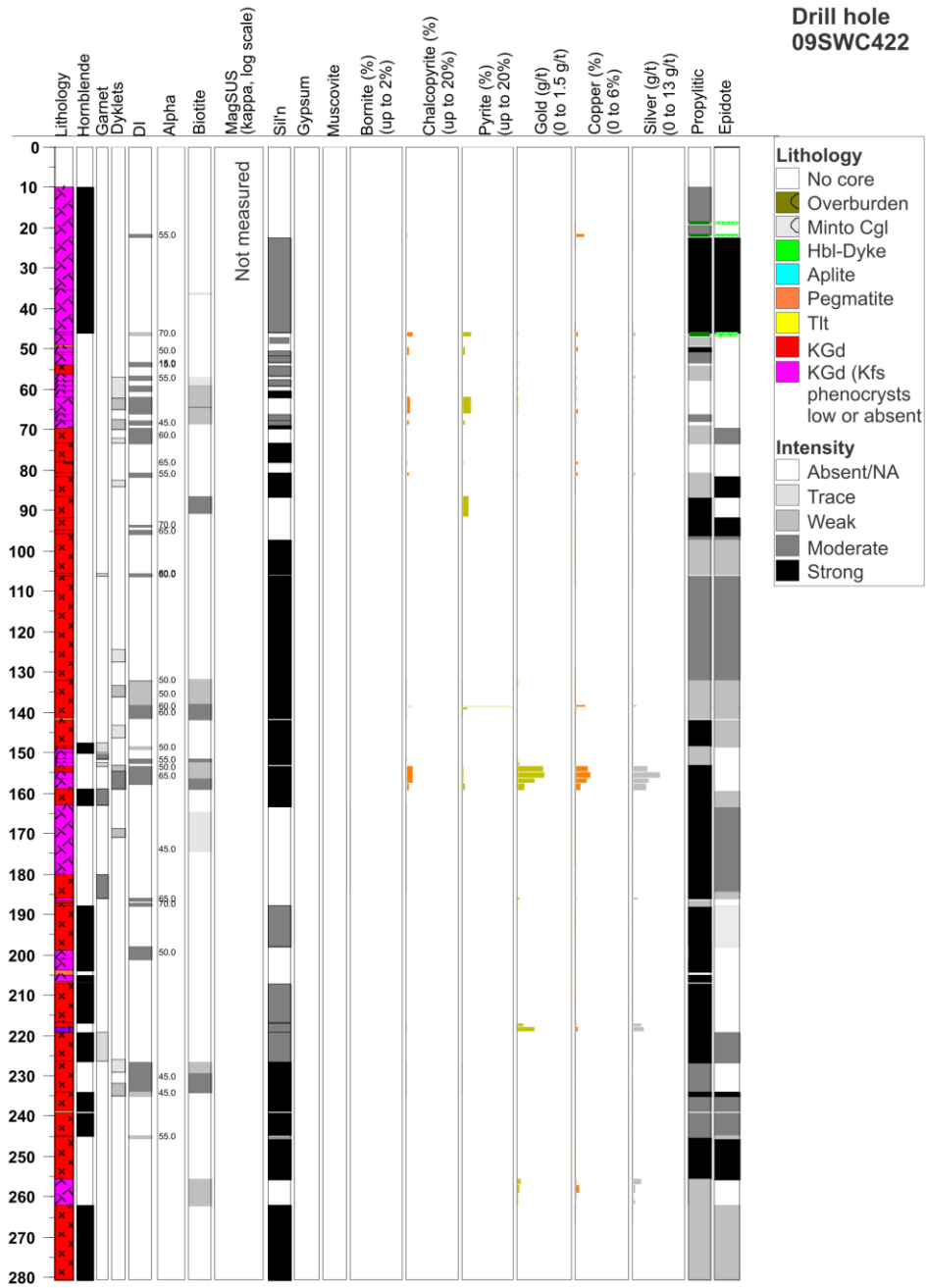
**Drill hole
08SWC374**



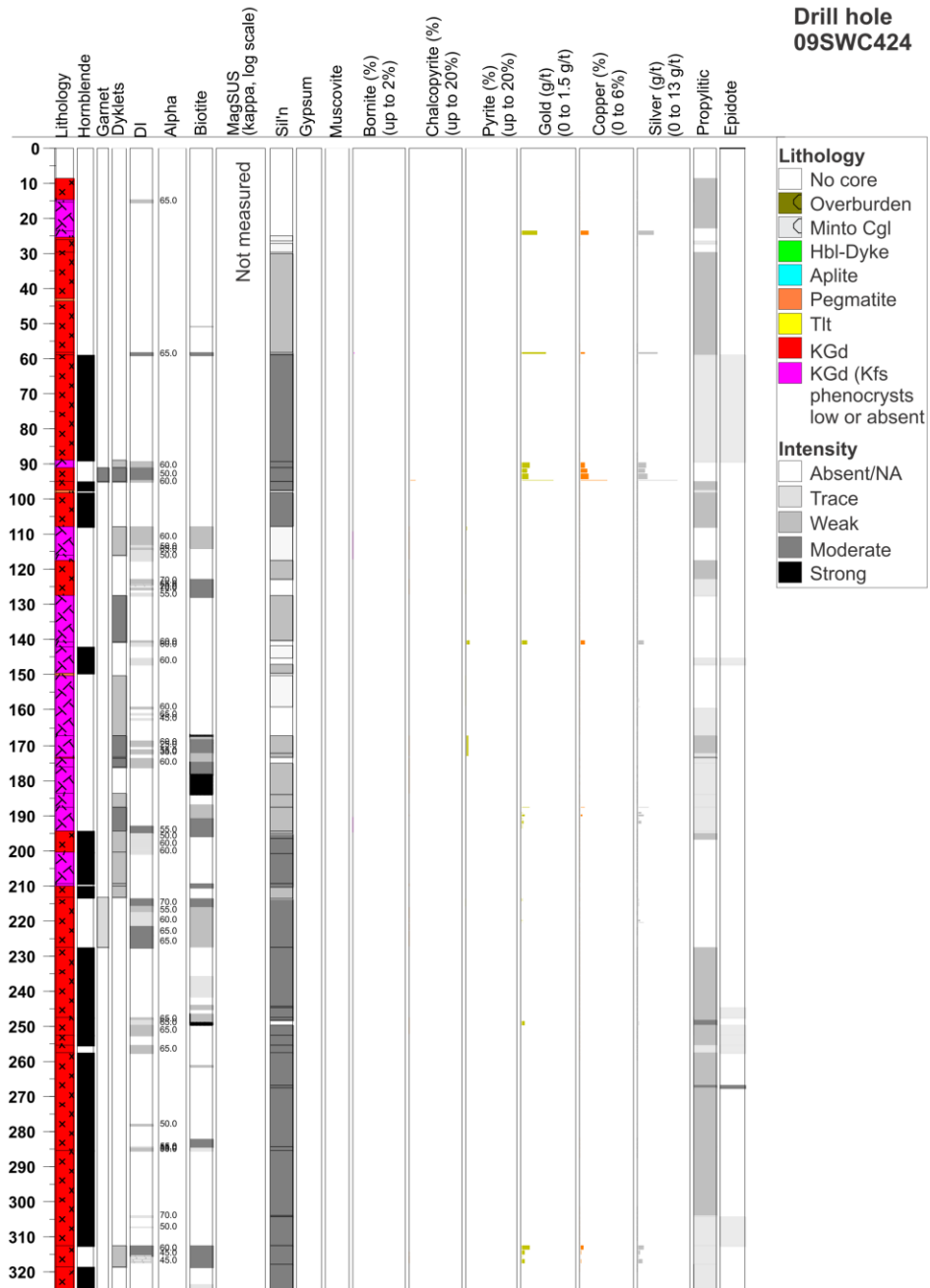
**Drill hole
09SWC420**



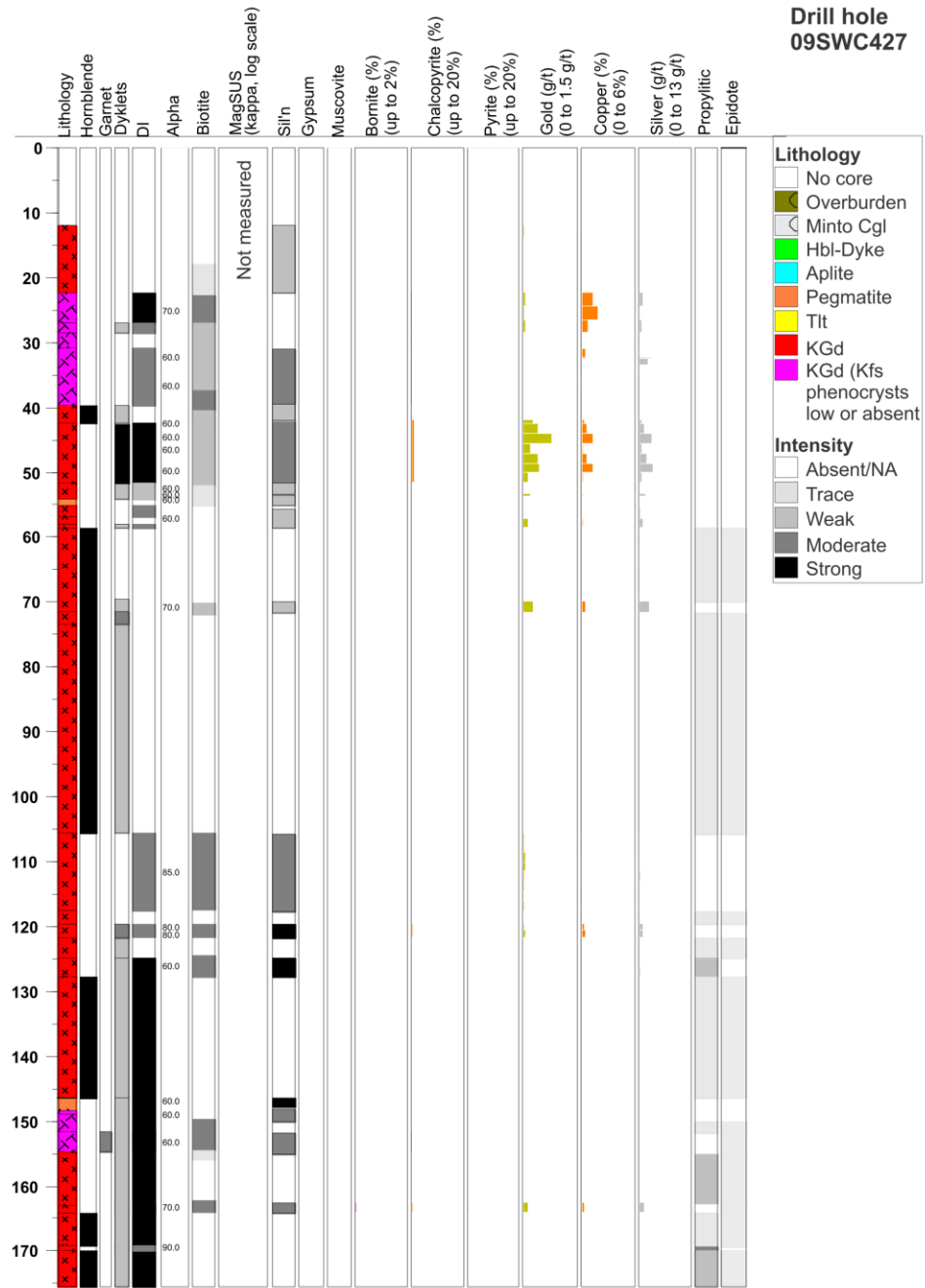
**Drill hole
09SWC422**



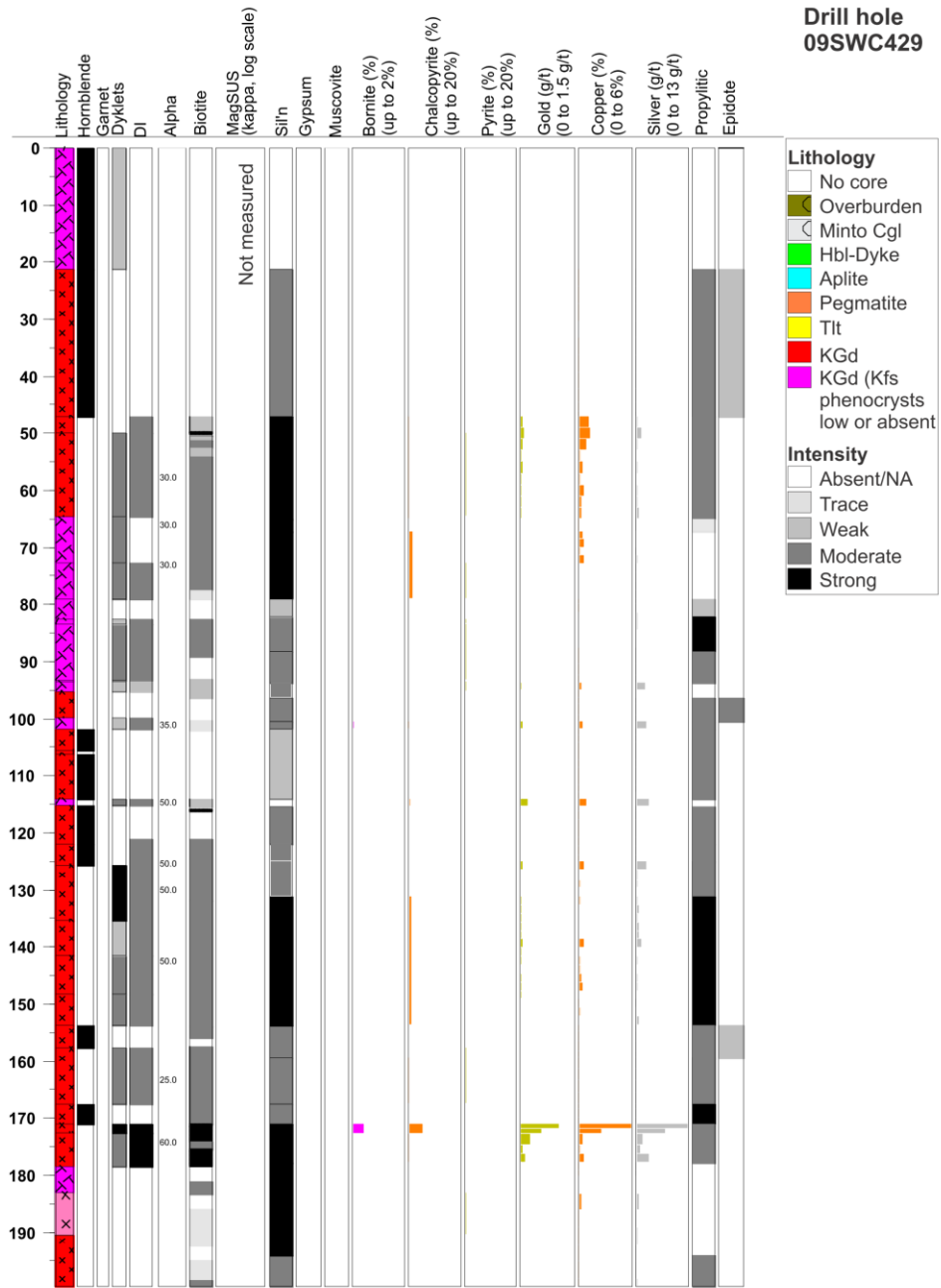
**Drill hole
09SWC424**



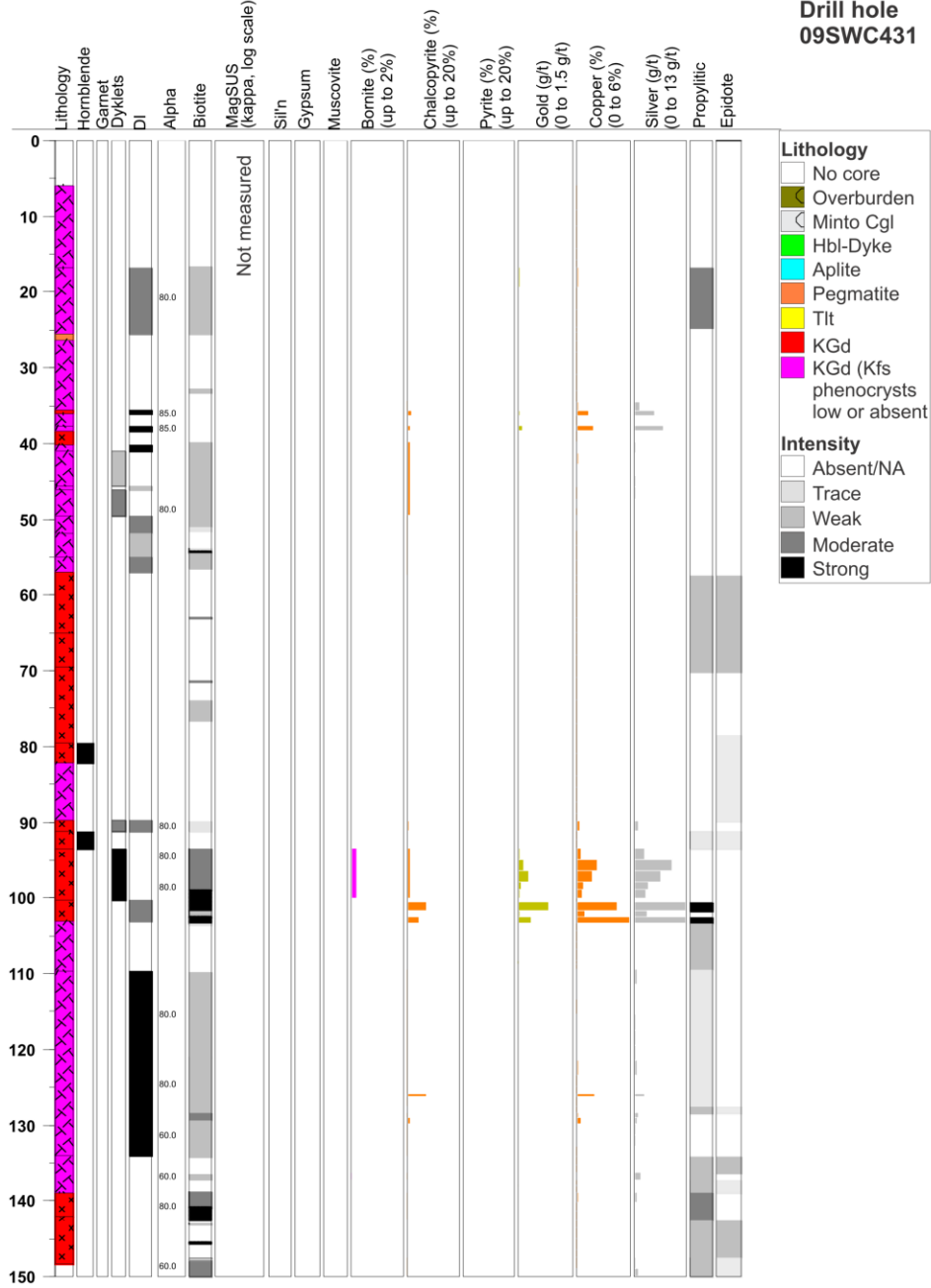
**Drill hole
09SWC427**



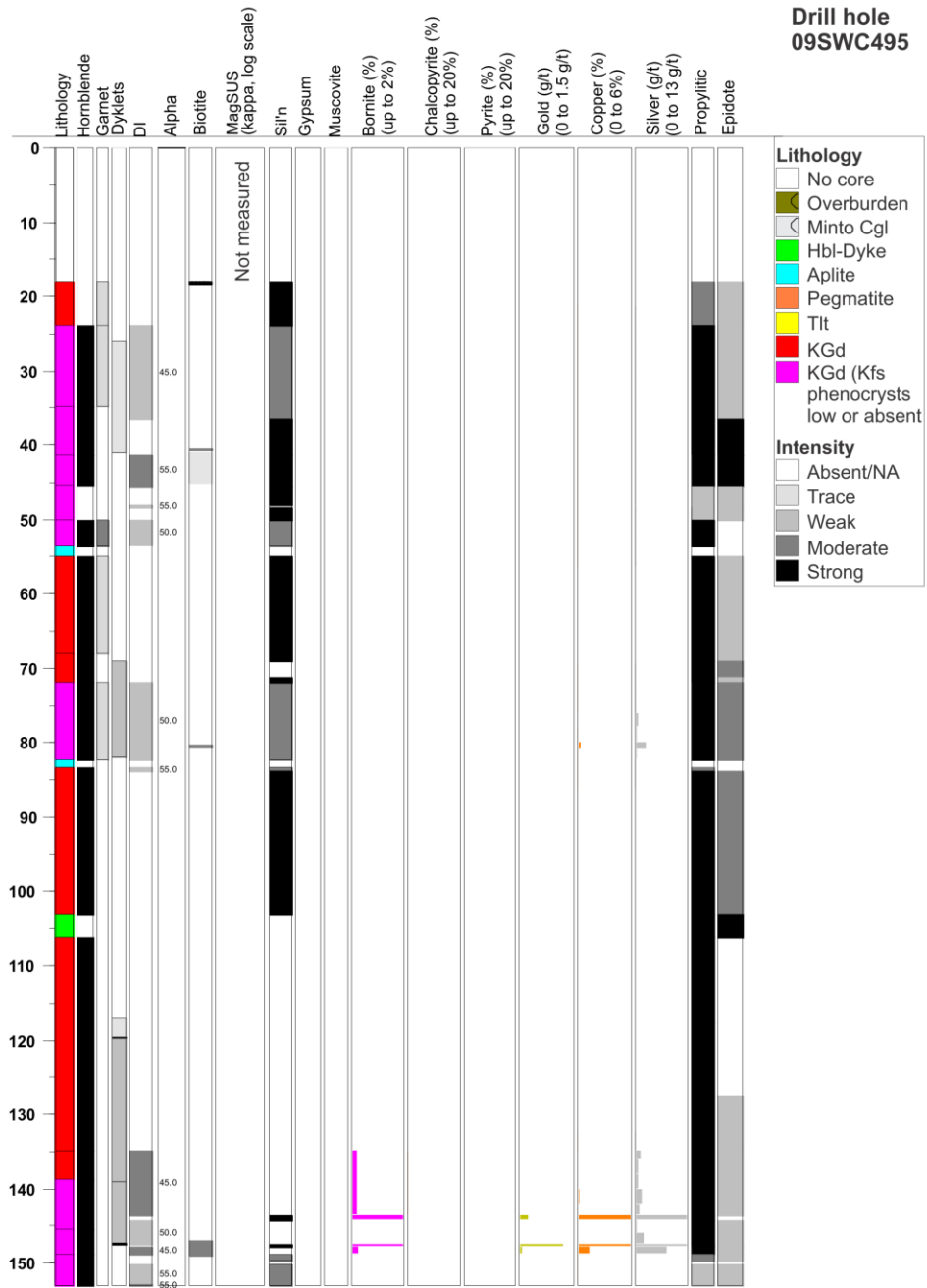
**Drill hole
09SWC429**



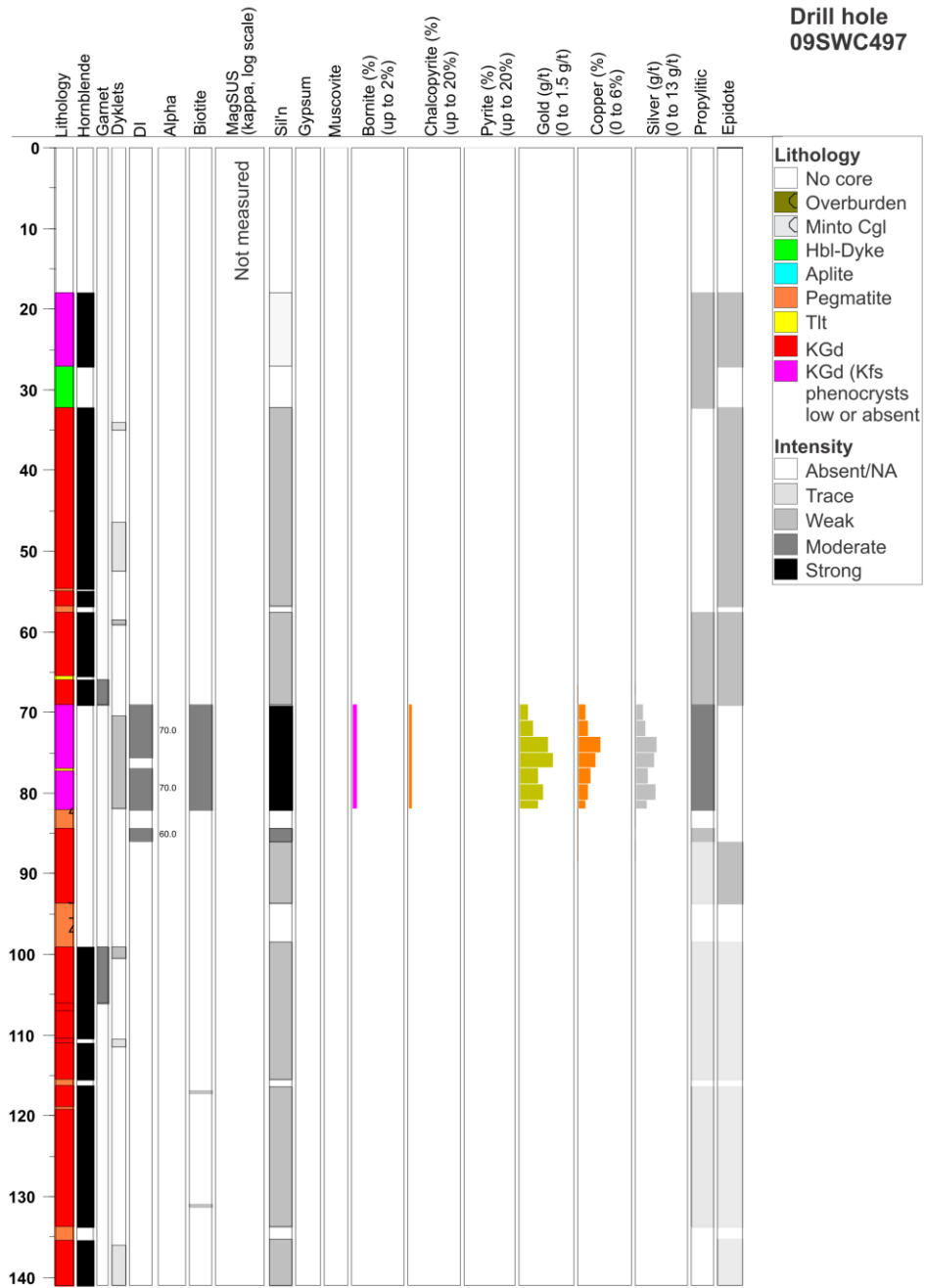
**Drill hole
09SWC431**



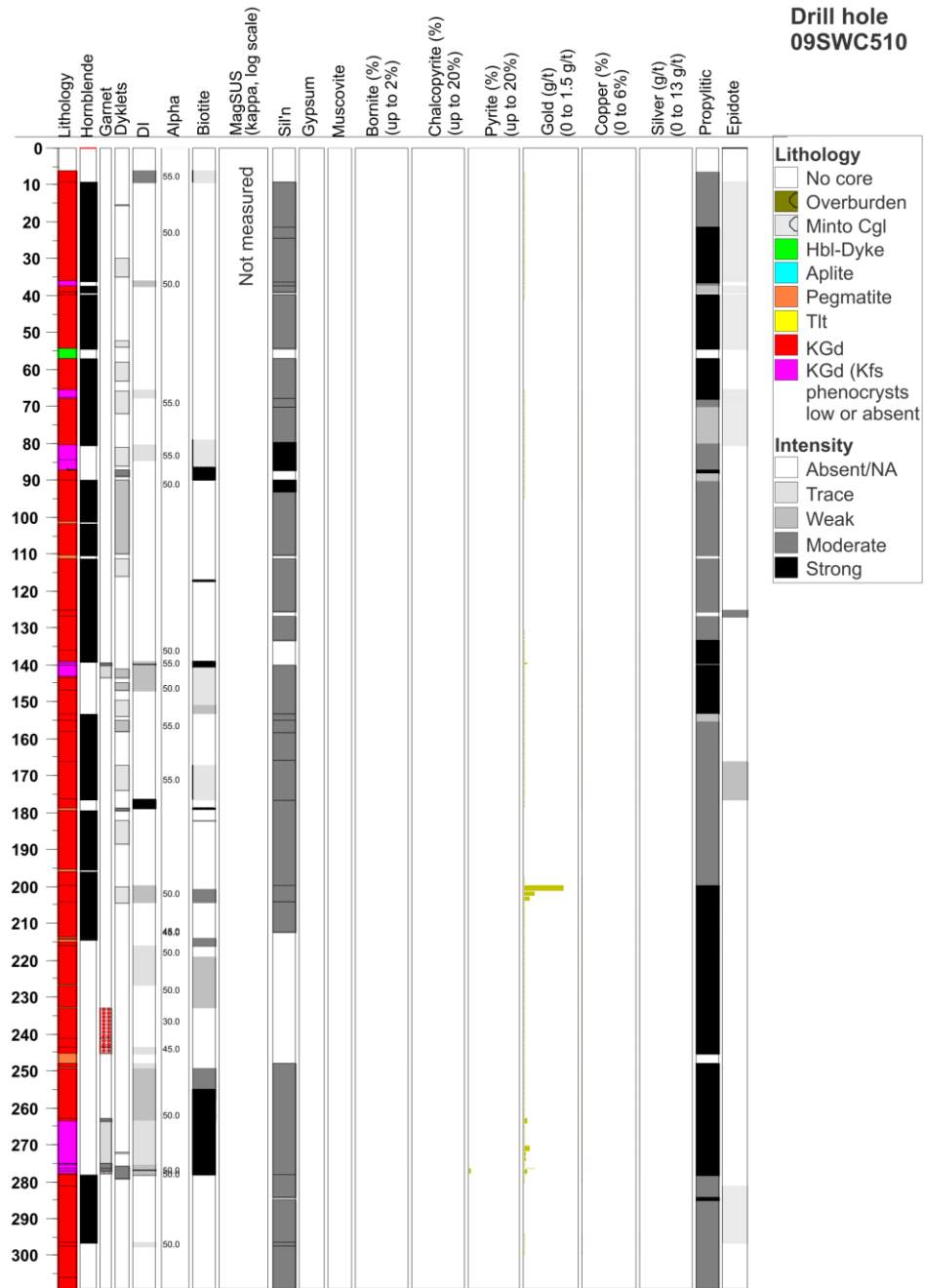
**Drill hole
09SWC495**



**Drill hole
09SWC497**



**Drill hole
09SWC510**



Appendix G U-Pb Geochronology

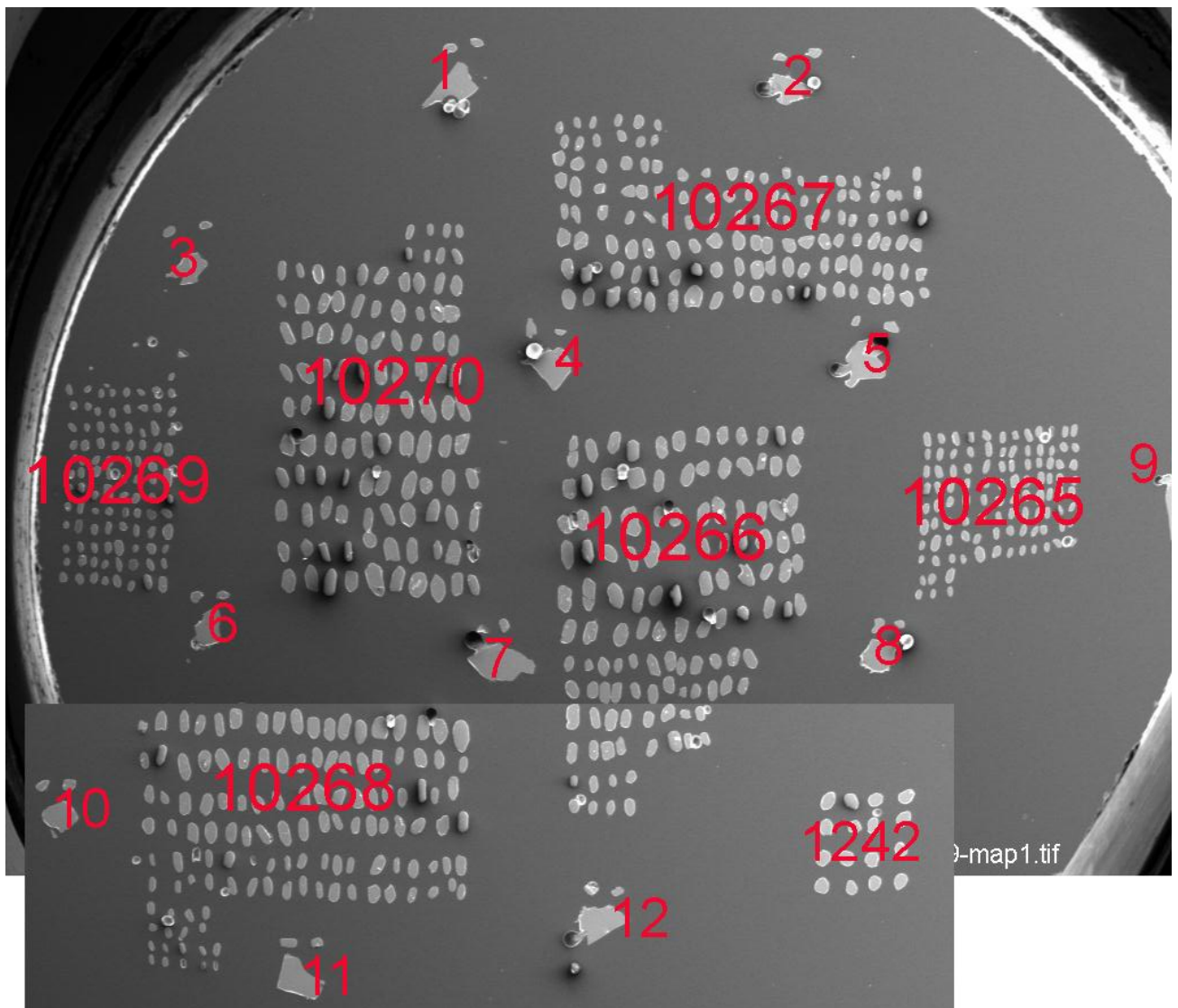


Figure G1: Map of zircons analysed using SHRIMP II. 10265 = sample S09-13-03A, 10266 = sample S08-01-01, 10267 = sample S09-16-01A, 10268 = sample sample S09-16-01B, 10269 = sample S09-16-01C, 10270 = sample S09-16-01D, 6266 = GSC laboratory standard ($^{206}\text{Pb}/^{238}\text{U}$ age = 559 Ma), numbers 1 through 12 = Temora standard ($^{206}\text{Pb}/^{238}\text{U}$ age 417 Ma).

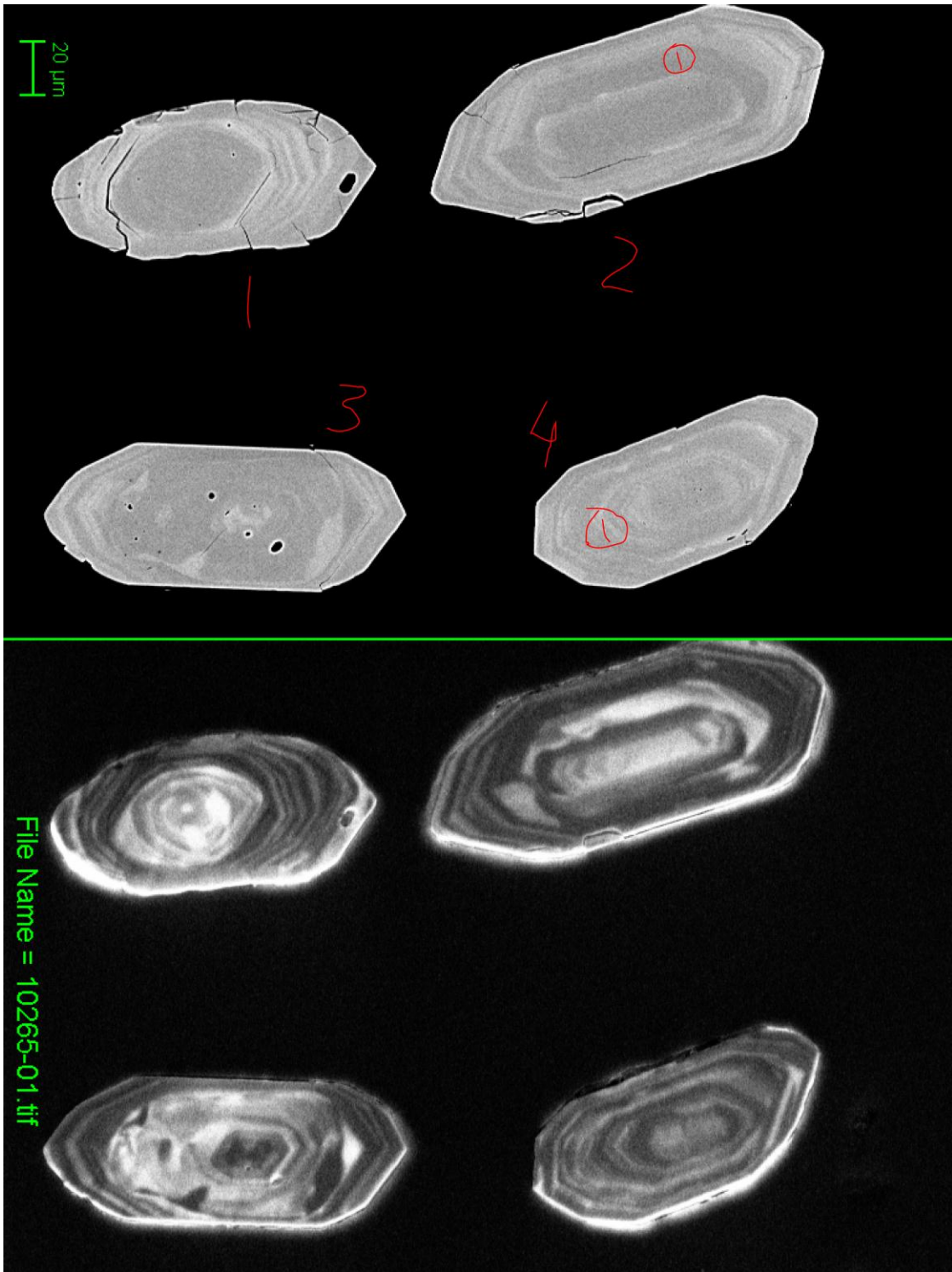


Figure G2: Example of reflected light (top half of image) and SEM backscatter (bottom half) imaging for four KGd zircons taken from sample S09-13-03A (10265). Circled numbers in red denote the location of SHRIMP probe points, checked visually after sample runs. Imaging for each zircon shown in Figure G1 is available as a separate digital appendix.

Appendix H Molybdenite Study

Sample Locations

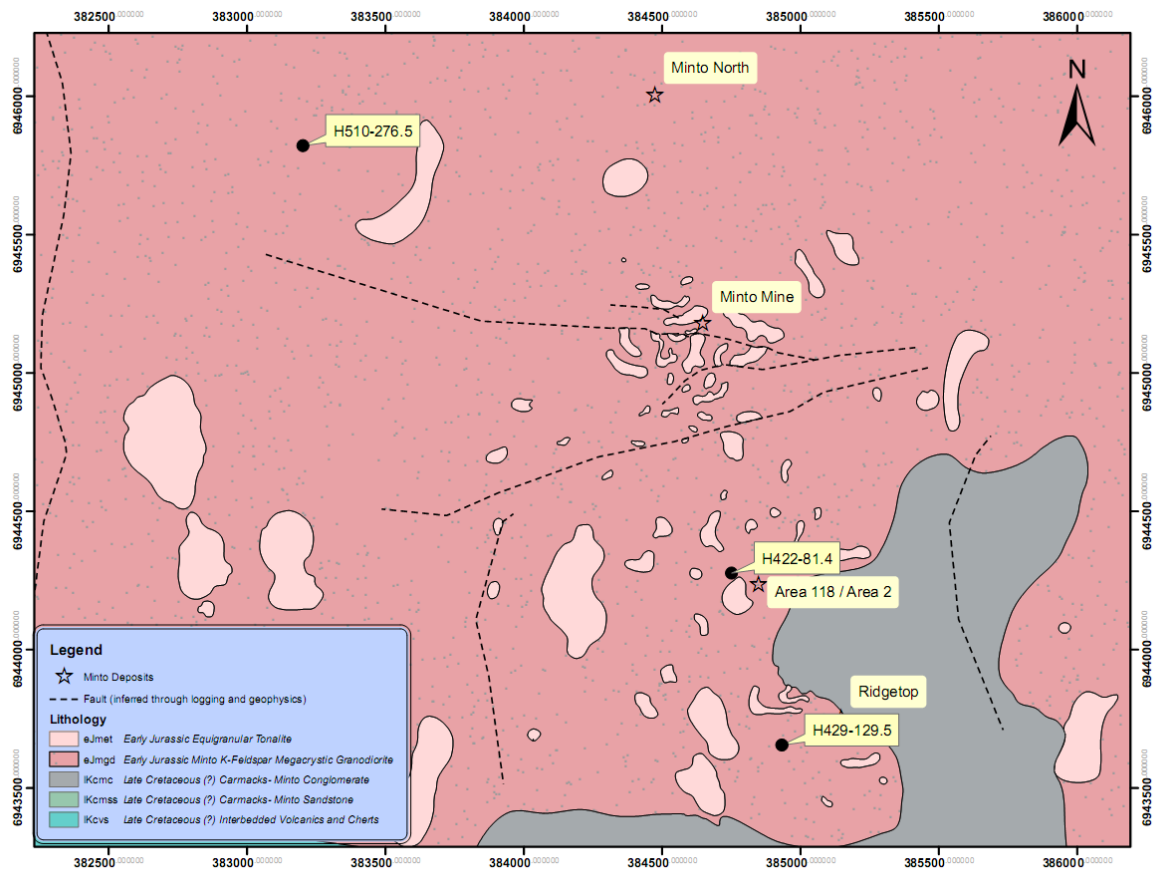


Figure H1: Map showing the location of molybdenite geochronology samples described in Section 2.5.2. Calculated model ages for molybdenite young northwards: 201.8 +/- 0.8 Ma [1.0] in sample H429-129.5, 197.4 +/- 0.8 [1.0] Ma in sample H422-81.4, and 196.0 +/- 0.8 [1.0] Ma in sample H510-276.5.

Detailed Sample Descriptions

Sample H510-276.5

Table H1: Mineral descriptions for sample H510-276.5

Mineral	Volume % Estimation	Description
Biotite	5 - 45	Black books in hand specimen; dark green in xpl. Grain size up to 1 mm long. Most frequently books share common alignment occur together, representing a discontinuous foliation. Isolated books are similarly aligned. Biotite foliation locally contains magnetite, pyrite, chalcopyrite, and garnet.
Plagioclase	25-40	Grainsize varies and is larger in areas with less biotite: 1 mm to 5 mm in higher grainsize portion of sample, 0.5 mm to 1 mm in more fine grained portion. POSSIBLE parallel growth twins- crosscutting oscillatory zoning [ask KEN HICKEY]? Stepped and tapered twins are uncommon. Rounded inclusions of quartz up to 0.5 mm are common. Patchy saussuritization is very rare.
Magnetite	20	Disseminated subhedral to anhedral grains more prevalent in finer grained section of sample. Masses up to 4 mm. Magnetite generally associated with biotite, also as individual grains. Shares sharp boundaries with all other minerals. Generally 'scrappy' looking. Rare inclusions of chalcopyrite and pyrite (fig); however, also observed as an inclusion within pyrite (fig)
Quartz	3	Predominately in larger grainsize portion of sample. Anhedral, up to 2 mm, and interstitial to feldspar. Very clear. Patchy subgrains are poorly defined- re-equilibration? Amoeboid intermineral boundaries. Weak sweeping undulose extinction is common.
Garnet	1; locally 20	red-orange euhedral to subhedral grains 1/5 mm to 1mm. Localized zones of abundance, either as disseminated or "vein-disseminated", pseudo veinlets of individual grains. Occurs near magnetite and sulfides in this sample. Sharp boundaries with epidote. Very fractured. Chalcopyrite commonly within garnet.
Molybdenite	Accessory	disseminated and at margins of quartz-plagioclase dykelet. Grains anhedral and up to 0.5 mm. Uncommon inclusions of chalcopyrite; molybdenite post-dates chalcopyrite?
Epidote	5	Anhedral grains up to 1 mm. Common inclusions of chalcopyrite and pyrite when in association with these minerals. Sharp intermineral boundaries.
Anhydrite or Gypsum	Accessory	One discontinuous vein less than 1mm in thickness. After sample was polished for examination, became rough looking after about a week. Uncommon chalcopyrite and pyrite grains up to 1 mm disseminated within vein and along vein margins. Crosscut by quartz vein.
Carbonate	Accessory	Anhedral masses up to 5mm, interstitial to other minerals.

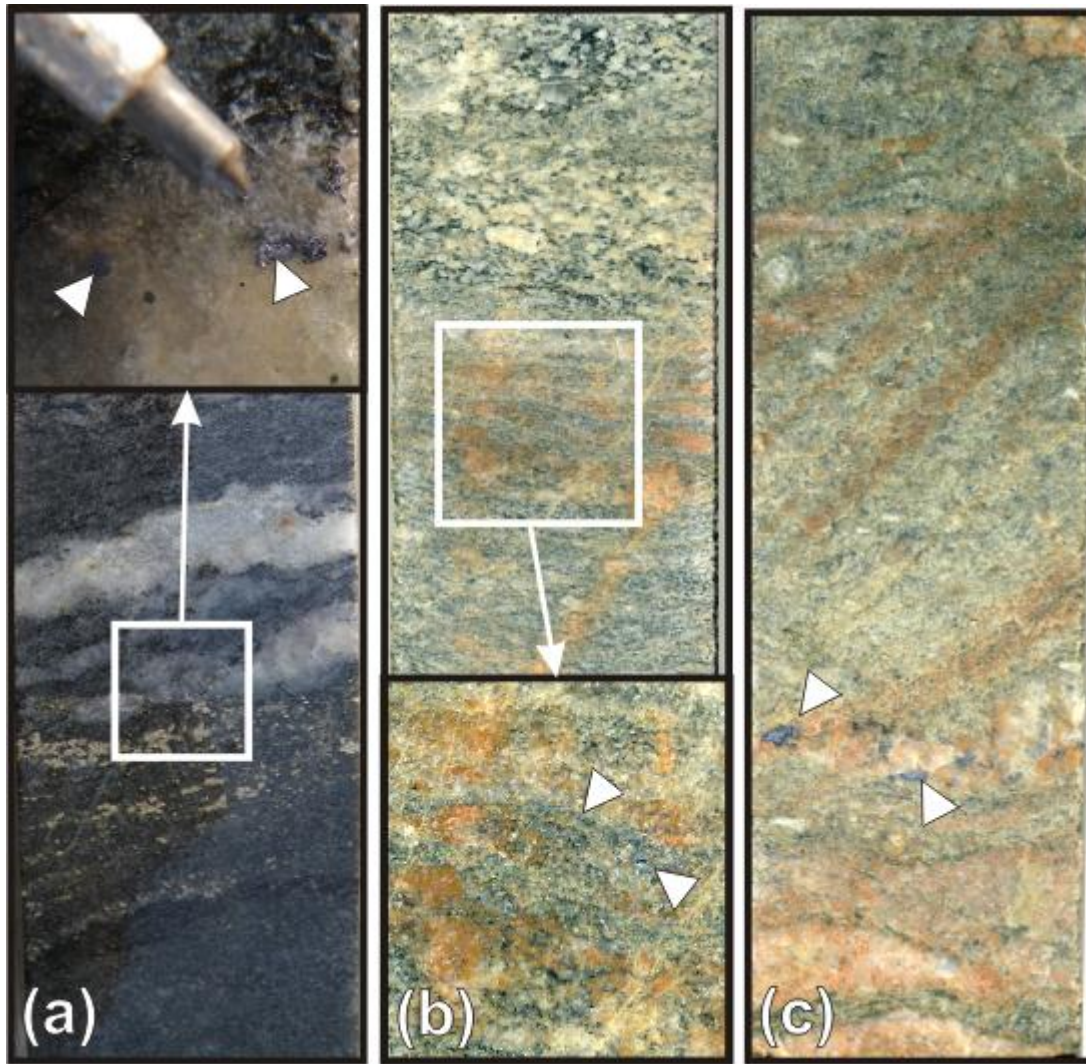


Figure H2: Minto diamond drill core sampled for Re-Os dating of molybdenite. Various textural occurrences of molybdenite are sampled from “separate” Minto deposits interpreted to have common origin. (a) Sample H510-276.5: molybdenite and proximal gypsum or anhydrite hosted in quartz vein or quartz-rich portion of pegmatite dyke. (b) Sample H422-81.4: disseminated molybdenite occurring parallel to mica foliation (biotite altered to chlorite). Small diffuse pegmatite dyklets occur parallel to foliation. Crosscutting orange-pink feature is fracture controlled hematite staining of plagioclase. (c) Sample H429-129.5: molybdenite occurring within deformed pegmatite dyket.

Table H2: Mineral description for sample H422-81.4. Sample contains both massive and deformed zones.

Mineral	Volume % Estimation	Description
Plagioclase	30-50	Anhedral phenocrysts 1 - 2 mm on average. Parallel and tapered twins are common and overprinted by ubiquitous patchy saussuritization. Grain boundaries with quartz are interlobate and deeply sutured.
Quartz	10	Anhedral and interstitial to feldspar, up to several millimeters. Very clear in hand specimen. Parallel subgrain boundaries are common. Fluid inclusion trails are ubiquitous.
Biotite	2, locally 15	Black books 1 - 3mm. Books are very well aligned. Light brown in xpl. In thin sections biotite as individual books; in core sample defines a discontinuous foliation where enough biotite is present and wraps plagioclase phenocrysts.
Fe-Carbonate	3-5	Small pale orange veinlets up to 0.25 mm. Veinlets are continuous and typically follow intergrain boundaries. Also occurs between "jacked open" books of biotite.
Chalcopyrite	3-5	Disseminated anhedral blebs up to 1 mm. Uncommon intergrowths of bornite.
Bornite	Accessory	Fine grained anhedral growths typically within or along margins of chalcopyrite
Molybdenite	Accessory	Very fine grained. Disseminated but occurring parallel to foliation along intermineral boundaries. Occurs in association with sericite.
Sericite	Accessory	Up 1 mm. Common "ragged" boundaries with plagioclase. Distinguished visually from muscovite based on the lack of tabular habit.
Magnetite	Accessory	Very fine grained disseminated anhedral grains.
Carbonate	Accessory	White veinlets less than 0.25 mm in diameter. Veinlets crosscut orange-pink carbonates and chalcopyrite. Most visible after application of dilute HCl acid.

Table H3: Mineral descriptions for sample H429-129.5

Mineral	Volume % Estimation	Description
Plagioclase	40	Anhedral to subhedral phenocrysts up to 3 mm. Heavily saussuritized; relict stepped and tapered twins are uncommon.
K-Feldspar	20	Subhedral to anhedral grains up to 4 mm. Microcline twinning (?) is common (Figure X). Uncommon inclusions of quartz.
Quartz	25	Anhedral, seriate up to 1 mm, interstitial to feldspar. Deeply sutured subgrain boundaries. Interlobate boundaries with plagioclase.
Chlorite	10	Biotite with grain size up to 1 mm. Disseminated and moderately aligned. Very commonly altered to chlorite.
Chalcopyrite	3	Disseminated anhedral blebs up to 0.5 mm. Uncommon intergrowths of bornite. In hand specimen is commonly mantled with dark grey, sooty mineral; possibly fine grained chlorite as observed in thin section. Chalcopyrite is a common inclusion within molybdenite (Figure X). Occurs in both host rock and pegmatite dyklet.
Molybdenite	3	Disseminated blebs up to 5mm. Occurs only within pegmatite dykelet.
Pyrite	Accessory	Anhedral, disseminated grains up to 0.3 mm. Occurs in both host rock and pegmatite dyklet.
Dyklets	NA	Quartzofeldspathic dykelets cross sample and appear to be partially deformed. Roughly 1/3 each of quartz, K-feldspar and plagioclase
Fe-Carbonate	5-10	Veins up to 0.2 mm infilling fractures.